ANISOTROPIC PHENOMENA IN STRONGLY CORRELATED ELECTRON SYSTEMS

by

EDWIN CHRISTOPHER CARTER

A thesis submitted to
The University of Birmingham
for the degree of
DOCTOR OF PHILOSOPHY

School of Physics and Astronomy
The University of Birmingham

September 2004

Abstract

This thesis is concerned with momentum anisotropy in strongly correlated electron systems, and explores its origin and its consequences through two contrasting projects. The first is a study of the temperature dependences of magnetotransport quantities in the normal state of the cuprate high-temperature superconductors. A phenomenological anisotropic small-angle scattering model is investigated; Hall effect measurements can be reproduced for parameters sufficiently close to particle-hole symmetry, but the experimentally observed magnetoresistance cannot be explained. The second project studies the phase diagram and quasiparticle properties of the square lattice Hubbard model within two-site cluster dynamical mean-field theory (DMFT), at zero temperature. The "two-site" approach provides a drastically simplified but physically-motivated self-consistency scheme for DMFT. This is combined for the first time with cluster DMFT, within which different magnetic orders and momentum anisotropy may be represented consistently. The extent of antiferromagnetism is determined; phases are discovered where the Fermi surface consists of small hole pockets, and the Mott transition happens as these pockets shrink to points. Anisotropic phenomena observed in the cuprates are reproduced by the theory; a pseudogap destroys the Fermi surface in some places, leaving behind Fermi arcs that closed into hole pockets by lines with very small quasiparticle residue.

Acknowledgements

Contents

List of Figures

Chapter 1

INTRODUCTION

Party is Nature too, and you shall see
By force of Logic how they both agree:
The Many in the One, the One in Many;
All is not Some, nor Some the same as Any...

GEORGE ELIOT
Middlemarch [1]

This thesis is an investigation of the behaviour of electrons in solids. In the vast majority of materials, the electrons moving within a lattice of atoms can be considered to behave independently. The behaviour of a single electron can be extrapolated to all, and electronic properties as a whole are well-understood. However, circumstances can conspire such that this framework breaks down, and certain materials exhibit peculiar phenomena which defy explanation. The behaviour of many electrons *collectively* can be quite different from what one would expect for electrons individually — and, more surprisingly, the resultant phases are often completely stable, protected by higher organizational principles. Generally, the phenomena are apparent at *low temperature*, where the relevant physical laws are from *many-body quantum mechanics*.

Superconductivity is a familiar and unmissable example of a phenomenon whose underlying physics is the collective behaviour of many electrons. In conventional superconductors, the superconductivity is well-understood, and seeded by the influence of lattice vibrations (phonons); however, the focus of this thesis will instead be upon instabilities of the electron gas caused by the interactions of electrons just with one other. In the so-called "high-temperature" superconductors, the origin of the superconductivity remains mysterious, but it is widely believed that magnetic fluctuations, due to the interactions between electrons, seed the superconducting instability. It is not just the high superconducting transition temperature (T_c) that makes these materials peculiar; the *"normal" state* of the cuprate high-temperature superconductors, existing at temperatures above T_c, has many anomalous properties. Several of these will be studied in this thesis; understanding the normal state of the cuprates is widely believed to be a prerequisite to understanding their superconductivity.

The *Mott insulator* is another dramatic instance of the effects of electron correlations. Materials which are predicted to be metals by band theory turn out to be insulators, and the cause is electrons blocking each others' motions. There are unanswered questions concerning the *Mott transition* between such an insulator and a metal — and indeed the high temperature superconductors are often regarded as a doped Mott insulator. Later in this thesis the Mott transition will be discussed in detail, and I present calculations that aid our understanding of it.

Unfortunately, there is no way of observing directly what the electrons in a material are actually doing; experimental probes are limited and sophisticated, and it is often difficult to disentangle the underlying physics. The job of the theorist is to invent and investigate models for materials, and provide clues to understanding of their strange properties. Such models could be microscopic (such as the *Hubbard model* discussed below), modelling the behaviour of the electrons from first principles; or constructed *phenomenologically* from the results of experiments. In either case, the models should pro-

duce results which can be compared with experiments, and ideally predict the results of future experiments. Ultimately, with sufficient insight, conscious design of materials can become possible; perhaps to increase the superconducting transition temperature, or capitalize upon unusual properties to construct novel devices.

In the next part of this introduction I will discuss in more detail the conventional framework for electron fluids (Fermi liquid theory), and the Hubbard model. I will then describe why strongly correlated electron systems are so difficult — but rewarding — to study, and the progress made with a modern technique (dynamical mean-field theory). Finally, I will give an overview of the specific investigations made in this thesis.

1.1 Fermi liquids

A metal contains a sea of mutually-repelling electrons in close proximity to each other; yet, strangely, their interactions are usually unimportant, and merely manifest themselves solely as a renormalization of the electron's mass. Effective electron masses vary from close to the vacuum value (in s-electron metals, such as sodium), to being hundreds or thousands of times the bare mass in "heavy-fermion" materials such as $CeCu_{6-x}Au_x$, where there is a large effective electronic interaction in the tight f-electron orbitals. The ordinary behaviour of these electrons is described by the *Fermi liquid theory* of Landau [2]; non-interacting electrons fill up modes in momentum space, yielding a *Fermi surface* — the locus of points in momentum-space that are filled last. At low temperature, the properties of the system depend only on small excitations around this surface.

Such excitations are robust; if interactions are turned on adiabatically, and we can keep track of the numbering of eigenstates, electronic properties are merely renormalized.[1] But we should not now think in terms of the original electrons, but instead of *quasiparticles*, many-particle superpositions containing a fraction z (the *quasiparticle residue*) of the original electron. Quasiparticles have a finite lifetime as they are not exact eigenstates.

There are special situations, however, where the Fermi liquid breaks down, giving a *non-Fermi liquid* [4]. In one spatial dimension, the destruction of a Fermi liquid giving the dramatically different Luttinger liquid (where the charge and spin degrees of the electron can separate) is well-understood [5]. The focus for this thesis is *two-dimensional* systems, which are not understood — perhaps one layer of a compound, where inter-layer coupling is sufficiently weak, such as the CuO_2 plane in many high-temperature

---

[1]The Fermi liquid is a "quantum protectorate" [3] — intricate details can be entirely neglected.

superconducting materials.

There are many possible mechanisms for the breakdown of a Fermi liquid. The lifetime of the quasiparticles could become so small that the concept of a quasiparticle ceases to be meaningful; the *marginal Fermi liquid* seen in the normal state of the cuprates (see Chapter 2) is believed to be an example of such as state. Alternatively, the quasiparticle residue z could tend towards zero — or the quasiparticle gets so heavy, that it dies [6]. The Mott transition to an insulating state occurs like this (see Chapter 3). A further possibility is superconductivity: an instability to an utterly different lower energy state;[2] interactions can be so large that the ground state of the interacting system is no longer connected with that of the original system.

In other cases, all we know is that there is experimental evidence that the single electron-like quasiparticle is no longer the right description of the physics. Transport measurements in the cuprates show that the electron appears to exhibit two distinctly different scattering rates [7, 8]; Chapter 2 is concerned with this phenomenon. Breakdown of the Wiedemann–Franz law has been observed in a cuprate [9], implying that there are somehow different types of electron involved in thermal and electrical transport. Outside the cuprates, itinerant ferromagnets [10] and the bilayer strontium ruthenate $Sr_3Ru_2O_7$ [11] are examples of materials where non-Fermi liquid behaviour has been observed. Proximity to a quantum critical point [12] is thought to be an underlying feature of many of these materials. Non-Fermi liquid behaviour can also be induced artificially — for example, the fractional quantum Hall effect seen with extreme magnetic fields.

1.2 The Hubbard model

To investigate physics beyond the Fermi liquid a comprehensive but simple microscopic model is required, for which the Hubbard model is commonly utilized. Electrons are assumed to exist on a set of independent sites (Wannier orbitals, perhaps); they have kinetic energy from hopping between sites, and potential energy from the interaction between the electrons. The latter is represented in the Hubbard model by a simple energy penalty U for any site which is doubly-occupied (*i.e.* containing both an ↑-spin electron and a ↓-spin electron). The Hamiltonian $\hat{H}_{\mathrm{Hubbard}} = \hat{T} + \hat{V}$, where

$$\hat{T} = -\sum_{ij} t_{ij} \hat{c}^\dagger_{i,\sigma} \hat{c}_{j,\sigma} = \sum_{\mathbf{k},\sigma} \epsilon_\mathbf{k} \hat{c}^\dagger_{\mathbf{k},\sigma} \hat{c}_{\mathbf{k},\sigma} \quad \text{and} \quad \hat{V} = U \sum_i \hat{c}^\dagger_{i\uparrow} \hat{c}_{i\uparrow} \hat{c}^\dagger_{i\downarrow} \hat{c}_{i\downarrow} . \tag{1.1}$$

The Hubbard model is parametrized by the dispersion $\epsilon_\mathbf{k}$, the Hubbard interaction

---

[2]Although superconductivity is to some extent based upon the original Fermi surface.

energy U, and the number of electrons per site n. Clearly, in real materials the local chemistry of multiple atomic orbitals etc. will mean that this is not an accurate representation of the situation, but in many cases such features will be irrelevant. Further sophistication can be added subsequently if necessary. We are mainly interested in the copper oxide plane, where it can be shown that the Hubbard model is a good representation of the low energy physics [13].

Despite its simplicity and many years of study, much of the physics of the Hubbard model remains unknown;[3] surprisingly simple facts, such as whether it hosts a ferromagnetic ground state, are still not resolved. Recently, the limit of *infinite* dimensions has allowed considerable progress, and provided insight into its behaviour in lower dimensions (see discussion of dynamical mean-field theory below). The focus here is the 2D Hubbard model, and we aim to survey its phase diagram, concentrating on magnetism, as U and n are varied. A particular material, such as a high-temperature superconductor at a specific doping level, will fall at a single point on this phase diagram; the general picture will be relevant to our understanding a wide variety of materials and how their states relate to each other.

In two limits the Hubbard model is easily understood. For $U = 0$, it is solvable when Fourier-transformed, and the **k**-modes are filled up one by one, giving a non-interacting Fermi liquid. In the opposite limit $t_{ij} = 0$, the sites are decoupled and can be solved independently; the system is clearly an insulator. In the intermediate regime, the Hubbard model is tough and the electrons have a character somewhere between localized and itinerant: a *strongly correlated electron system*.

1.3 Strongly correlated electron systems

When the potential energy of electrons from interactions becomes comparable to their kinetic energy, the system may be described as strongly correlated; typically, this occurs in materials where d-electrons are active (*e.g.* cuprates, ruthenates). There is likewise a balance between itinerant and localized nature of the electrons, which manifests itself as the boundary between wave- and particle-like nature: at low temperatures quantum mechanics is important and wave-particle duality plays an important rôle. Non-interacting electrons in a crystalline solid fall into eigenmodes of momentum, defining a clean Fermi surface in momentum space, but the electron-electron interaction is fundamentally point-like in space. As this interaction increases, so does the influence of local, particle-like physics and the Fermi liquid description is called into

---

[3]In one dimension the Hubbard model has been solved exactly, although it is still not fully understood.

question.

A strongly correlated regime is finely balanced: small changes in parameters can have dramatic effects on the system, so there is a wide variety of fascinating phenomena and a real possibility of intelligent engineering. Another characteristic of such systems is the simultaneous presence of a large range of energy scales, which means perturbation theory becomes useless — there is no small parameter to use. It is difficult to know where to start; simple model Hamiltonians are useful for describing regimes (perhaps protectorates) whose low energy behaviour is understood, but drastic approximations to the Hubbard model Hamiltonian have often been misleading: their results have been specific to the reduced model implemented and have not necessarily reflected genuine Hubbard model physics.

In the last 15 years, *dynamical mean-field theory (DMFT)* has emerged as a well-justified, non-perturbative approach to strongly correlated electron systems. Inspired by the limit of infinite spatial dimensions, where physics is simplified by being *local*, DMFT encompasses from the outset both localized and itinerant physics. Within the theory, particles are effectively localized on short timescales but itinerant over long time scales; technically, this corresponds to a local but fully frequency-dependent *self-energy*. DMFT can be derived analytically in the infinite dimensional limit, giving it a rigorous basis; when applying it to finite dimensional real systems, we know exactly what approximation is being made. If its results turn out to be different from an experiment, they are still informative: one could ask at what dimension there is a transition — and whether it could be accessed in crystals with high coordination number. Most of this thesis is concerned with the use of DMFT to survey the phase diagram of the Hubbard model.

1.4   Overview of Thesis

This thesis comprises two contrasting and complementary approaches to strongly correlated electron systems. The first is a phenomenological study of magnetotransport in the cuprates; the starting point is not a microscopic model like the Hubbard model, but instead a proposal is put forward inspired by experimental observations. Calculations with the phenomenological model predict the results of other experiments, which tests the veracity of the hypothesis. If it is successful, the form of such a model can provide hints as to the microscopic physical processes which give rise to it, and considerable insight into the important physics.

In contrast, the second part of the thesis is an investigation into the properties of a particular microscopic model across a wide range of parameters. The results are rel-

evant to a variety of experimental circumstances; the phase diagram contains points corresponding to individual compounds (including hopefully the normal state of the superconducting cuprates), and so gives insight into the relationships between different materials. Any experimentally relevant quantity may be calculated from the model, and the details and origin of a phenomenon may be investigated further if comparison to real observations is favourable.

There turn out to be surprising connections between the two projects, most notably that of *anisotropy*: Chapter 6 and Chapter 7 give insight into possible mechanisms that cause anisotropy, whereas Chapter 2 describes effects that anisotropy might have on a system.

1.4.1   Magnetotransport

In the normal state of the cuprate superconductors, transport quantities under the influence of a magnetic field exhibit peculiarly non-concordant properties. The Hall coefficient has a marked temperature dependence, at odds with the conventional theory of metals according to which it should be constant; and the temperature dependence of the magnetoresistance breaks the prediction of conventional theory, Kohler's rule. Together these seem to imply that the electron simultaneously exhibits two different lifetimes. The normal state is certainly peculiar — the resistivity shows a linear temperature dependence — and many believe all these phenomena are symptoms of a non-Fermi liquid of an as yet unascertained nature.

Many have tried to explain the Hall effect measurements within the framework of Fermi liquid theory, generally by invoking *anisotropic* scattering processes. One such proposal is that of Varma and Abrahams [14], involving a small-angle scattering model inspired by photoemission observations. In Chapter 2 I investigate this model in detail using a numerical approach; this work has been published [15]. The calculations aim to provide an independent verification of the work of Varma and Abrahams on the Hall effect, and more importantly to calculate the expected behaviour of the magnetoresistance according to the small-angle scattering model — a quantity they do not themselves calculate. In the past, the magnetoresistance has often proved the definitive quantity for discriminating between transport theories.

1.4.2   Cluster study of the Hubbard model

Little is known definitively about the Hubbard model away from half-filling (the case where there is exactly one electron per site), yet many fascinating materials such as the superconducting cuprates are believed to lie within its phase diagram. In this thesis, I

investigate the Hubbard model using an implementation of dynamical mean-field theory adapted so that calculations are relatively quick, so that the entire phase diagram may be explored with access to complete spectral information. The technique is also modified so that it is able to represent antiferromagnetic order and broad features in momentum space. We concentrate on the 2D Hubbard model on a square lattice at zero temperature, and do not allow the possibility of superconductivity.

Chapter 3 contains a detailed description of dynamical mean-field theory. There are many methods for solving the self-consistent equations of DMFT, but they generally require huge amounts of computational power. The approach within this thesis is to represent the DMFT equations in a highly restricted, minimal way, which enables computational resources to be rechannelled towards extending DMFT. "Two-site" DMFT, discussed in Chapter 4, effectively consists of Hartree–Fock mean-field theory together with a single dynamical degree of freedom, that is self-consistently constrained with physically well-justified criteria. It is probably the simplest model that is capable of reproducing the key features of the Mott transition — proven many-body capabilities that make it a useful kernel for other calculations.

In this thesis I combine two-site DMFT, for the first time, with "cluster DMFT" (Chapter 5), where the single-site basis of conventional DMFT is extended to a cluster of sites. Whilst neither two-site DMFT nor cluster DMFT maintain the rigorous infinite-dimensional basis of pure DMFT, we can regard two-site cluster DMFT as a sophisticated boundary condition that becomes exact in the limit of infinite cluster size. A cluster enables a consistent approach to different magnetic orders such as antiferromagnetism; also local lattice effects may play a rôle, and features can be resolved in momentum space. This flexibility will turn out to be critical for our understanding of the Mott transition in the neighbourhood of antiferromagnetism, and for modelling anisotropic features in the cuprates.

Before introducing a cluster, I present results for ferromagnetic and antiferromagnetic phases within ordinary two-site DMFT in Chapter 4, and subsequently I present the phase diagram and quasiparticle properties for the Hubbard model under several implementations of two-site cluster DMFT. The DMFT approach ensures that sophisticated many-body processes are included and so a large cluster is not required. The first cluster results are contained in Chapter 6, where a 2×1 site "pair-cluster" is utilized; this work was the subject of a published paper [16]. Finally, I increase the cluster size and investigate a 2×2 site "quad-cluster" in Chapter 7.

1.5 Notes

- Vectors are written like $\mathbf{k}$, and matrices like A. I shall use the symbol $\doteq$ to denote that the quantities should become equal for self-consistency.

- Hamiltonians are denoted $\mathcal{H}$, and will often include the $-\mu\hat{N}$ term of the grand canonical ensemble.

- The expectation of an operator $\hat{O}$ in a system with Green's function G is

$$\langle\hat{O}\rangle = \int_{-\infty}^{+\infty} d\omega\, n_F(\omega)\frac{1}{\pi}\lim_{\delta\to0}\text{Im tr}\left[\mathsf{O}\cdot\mathsf{G}(\omega+\mu-i\delta)\right],\tag{1.2}$$

where the trace is over the basis in which O and G are matrices, and $n_F(\omega)$ is the Fermi function; generally I work at zero temperature ($T = 0$) where this becomes the step function $\theta(\omega)$.

- I shall use the word "finitesimal" to mean greater than infinitesimal (the word "finite" is often used for this, but zero is finite).

- Please note the distinction between "two-site" and "pair-cluster" in later chapters. These correspond to very different concepts, despite both referring to objects consisting of two adjacent sites.

Chapter 2

MAGNETOTRANSPORT IN THE CUPRATES: PHENOMENOLOGY

And there he plays extravagant matches
In fitless finger-stalls
On a cloth untrue
With a twisted cue
And elliptical billiard balls!

WILLIAM S. GILBERT
The Mikado [17]

2.1 Introduction

The cuprate materials that superconduct at high temperatures turn out to exhibit many bizarre properties in their *normal state* (*i.e.* at temperatures above the superconducting transition). Understanding the peculiar nature of the electronic excitations in this phase is widely believed to be a prerequisite to understanding the mechanism for its superconductivity. In this chapter, I shall concentrate upon several measurements made of electrical transport in these compounds, under the influence of a magnetic field. How these conductivities vary with temperature, and in relation to each other, turn out to be significantly different from that of a conventional metal, and shed light on the nature of the electronic excitations. We will investigate the small-angle scattering model proposed by Varma and Abrahams [14] to account for the anomalous temperature dependences.

The approach of this chapter is *phenomenological*. Experiments cannot directly reveal the nature of electron scattering processes, which underlie many important properties of materials. Instead, hypothetical scattering models may be constructed, and their consequences compared with experimental observations. Recent angle-resolved photoemission spectroscopy (ARPES) experiments inspired the phenomenological model of Varma and Abrahams; ARPES observations revealed an *anisotropic* part to the electronic lifetime, and the essence of Varma and Abrahams' idea is to allocate this feature to *small-angle scattering* processes, wherein the momentum of an electron is not changed significantly. Temperature dependences of the conductivities may be calculated from the phenomenological scattering model including such a small-angle scattering term, and compared with the experimental results. If the model proves correct, attention may then be turned to speculate on possible microscopic causes of the scattering processes, which may provide insight into details of the electronic properties of the normal state of the cuprates.

The remainder of this thesis implements a microscopic approach to understanding materials, in contrast to the phenomenology of this chapter. Although the phenomena investigated are largely separate, Chapter 7 will provide a possible microscopic explanation of the anisotropy observed in ARPES experiments.

The original paper by Varma and Abrahams [14] contained serious calculational errors [18, 19, 20], meaning that they overestimated the effects of small-angle scattering by several orders of magnitude. In a second paper [21] they maintained the veracity of their idea and recalculated using a different method. We investigated the model numerically, an entirely independent approach; the results were published [15] although disputed by Abrahams and Varma [21]. In fact, our calculations did generally agree

well with their results, but additionally focused upon the *magnetoresistance*, a quantity that they never calculated directly. The magnetoresistance is a sensitive test of any transport theory (see for example Ref. [22]), and we shall see (in §2.5.2) that it is the definitive discriminator for the small-angle scattering model.

All quantities shall be regarded as solely two-dimensional; the important physics of the high-temperature superconducting cuprates lies in the CuO_2 plane that they have in common, and the inter-plane coupling is known to be weak. In §2.2 I shall detail transport and ARPES experiments on the cuprates, and explain why the temperature dependences of the conductivities are apparently inconsistent. §2.3 describes theoretical approaches to transport calculations. I show in §2.3.1 how the Drude theory is inadequate for the cuprates, and in §2.3.2 how Anderson proposed altering the standard picture to fit experimental observations, and the attempts by other researchers to give his picture some foundation. §2.3.3 details what is meant by small-angle scattering in the proposal of Varma and Abrahams. My calculations are described in §2.4, beginning with Boltzmann transport theory and how the standard solution is altered to include the particular features of the Varma–Abrahams model, and ending up with an analytical framework to understand numerical results. The numerical method is presented in §2.4.3, and I present an overview of the results (§2.4.4) together with detailed graphs for the specific model studied in Abrahams and Varma's later paper [21] (§2.4.5). Finally, I discuss and interpret the findings (§2.5).

2.2 Experiments

The transport quantities that underlie the study contained in this chapter are the resistance, Hall effect and magnetoresistance. In this section I will outline the conventional theory for each of the three quantities, and compare with the anomalous behaviour in the cuprates, focusing upon their temperature dependences. We are interested in the cuprates in their normal state, *i.e.* at relatively high temperatures, above the superconducting transition; and near *optimal doping* (the concentration of dopant atom that gives the highest superconducting transition temperature). This is the "strange metal" phase indicated on the phase diagram of the cuprates in Fig. 2.1(a). The cone above the superconducting dome is believed to be characterized by fluctuations from a quantum critical point; the strange metal may have the universal properties of a protectorate [3], and indeed $CeCoIn_5$ near a quantum critical point exhibits the same set of transport properties as the cuprates [23].

Angle-resolved photoemission spectroscopy (ARPES) gives an independent set of information about the nature of the quasiparticles in the strange metal; §2.2.4 contains
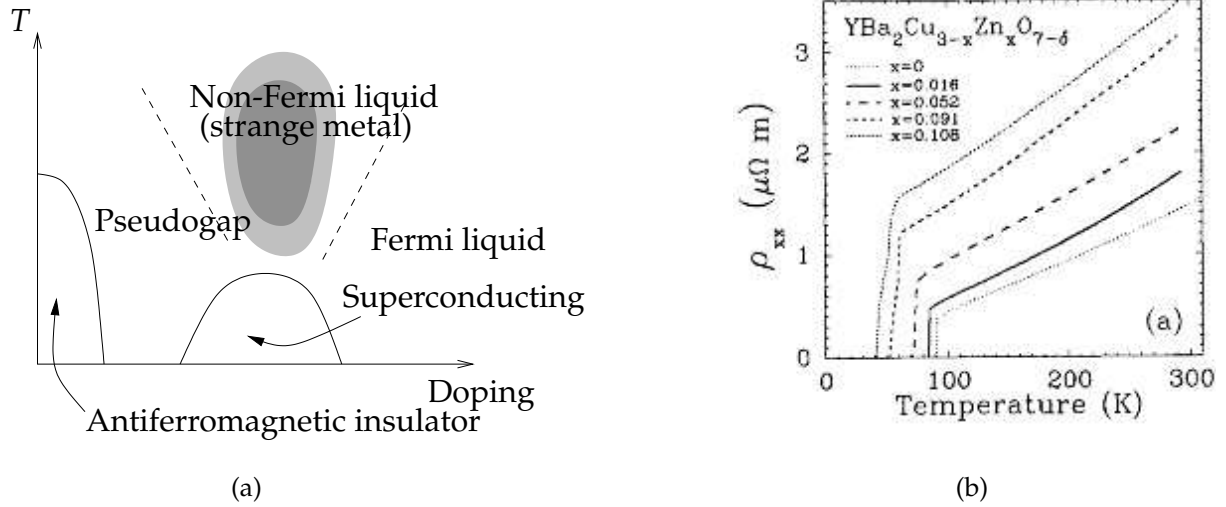
Figure 2.1: (a) Phase diagram of the cuprates. Here we study the temperature dependence transport properties of the "strange metal" phase near optimal doping (shaded). (b) Temperature dependence of the resistance taken from Chien *et al.* [8]. It obeys a law $\rho \sim A + BT$ where the residual resistivity A depends on the in-plane Zn doping and B is a constant of the marginal Fermi liquid.

a rationalization of some of the ARPES observations.

2.2.1 Resistance

In metals, the acceleration of electrons by an electric field is reduced to equilibrium by scattering, from impurities and lattice vibrations for example. As long as the electric field **E** is small, the current **J** will be proportional to it, and the longitudinal resistivity is defined $\rho = |\mathbf{E}|/|\mathbf{J}|$. A conventional Fermi liquid of electrons is expected to have a temperature variation $\rho \sim T^2$ at the lowest temperatures, but usually this is obscured by phonon scattering, for which one would expect $\rho \sim T^5$ at low T and $\rho \sim T$ at high T [24].

In the cuprates near optimal doping (see Fig. 2.1(a)), however, a very good linear-T law $\rho = A + BT$ is observed for a wide range of temperatures — see Fig. 2.1(b) and Refs [25, 8] for example. This behaviour has defied explanation: it is neither a conventional Fermi liquid nor phononic in origin. Other experiments on the cuprates (such as ARPES [26]) have confirmed that the T-linearity is intrinsic to the single-electron relaxation rate, and is consistent with a hypothesis of a scale-invariant fluctuation spectrum and proximity to a quantum critical point [26]; Varma *et al.* [27] termed this state a *marginal Fermi liquid*. It seems that at the Fermi surface, the quasiparticle residue goes to zero: quasiparticles have very short lifetimes and are constantly flittering in and out of existence. However, I am not concerned here with the origin of marginal Fermi liquid behaviour, but just the *relationships* between the resistance and the transport

13

properties under the influence of a magnetic field, that are discussed in the succeeding sections.

2.2.2 Hall effect

If a magnetic field is introduced perpendicular to the plane of a sample, a electric field E_y is generated transverse to the applied electric field E_x. This is because the magnetic field causes electrons to curl to one side and charge builds up (until the electric field generated cancels the effect of the magnetic field). The Hall coefficient R_H is defined as E_y/J_x. For free electrons, and experimentally in almost all materials, R_H is a constant that depends only on the electron density ($R_H = 1/ne$). However, the cuprate superconductors show a marked monotonic decline in R_H with increasing temperature, continuing up to very high temperatures.

The physics needs to be formulated with tensors for conductivity $\boldsymbol{\sigma}$ and resistivity $\boldsymbol{\rho}$, related by matrix inversion, defined by

$$\mathbf{J} = \boldsymbol{\sigma}\mathbf{E}, \quad i.e. \quad \begin{pmatrix} J_x \\ 0 \end{pmatrix} = \begin{pmatrix} \sigma^{xx} & \sigma^{xy} \\ -\sigma^{xy} & \sigma^{xx} \end{pmatrix} \begin{pmatrix} E_x \\ E_y \end{pmatrix}; \quad \text{and} \quad \begin{pmatrix} E_x \\ E_y \end{pmatrix} = \begin{pmatrix} \rho^{xx} & \rho^{xy} \\ -\rho^{xy} & \rho^{xx} \end{pmatrix} \begin{pmatrix} J_x \\ 0 \end{pmatrix}$$

$$(2.1)$$

(if the material has x-y symmetry). The *Hall angle* Θ_H, defined by

$$\cot\Theta_H = \frac{\sigma^{xx}}{\sigma^{xy}} = \frac{\rho^{xy}}{\rho^{xx}}, \qquad (2.2)$$

is a better quantity to consider than R_H, as longitudinal effects are factored out (see §2.3.1). Intuitively, Θ_H is the angle by which an electron deviates from the straight-on path, due to the magnetic field, and in conventional metals $\cot\Theta_H$ has the same temperature dependence as the resistivity ρ. In the cuprates, the decline in R_H alerted researchers to the fact that Θ_H exhibits a different temperature dependence to ρ: $\cot\Theta_H \sim C + DT^2$. Surprisingly and significantly, this rule is even more robust than the linear-T resistivity. The offset C changes with in-plane zinc-doping, as shown in Fig. 2.2(a): this is a similar effect to that seen in the residual resistivity A, and implies that $\cot\Theta_H$ also measures an electronic scattering inverse lifetime, to which impurity scattering would give such an additive constant. The gradient D, on the other hand, varies with the carrier doping (see Fig. 2.2(b).

These results seems to imply that the electronic quasiparticles have two different lifetimes for the processes which contribute to the resistance and the Hall effect respectively. This bizarre situation, where the electron appears to split into particles with different character, has been taken as evidence for spin-charge separation in the CuO_2
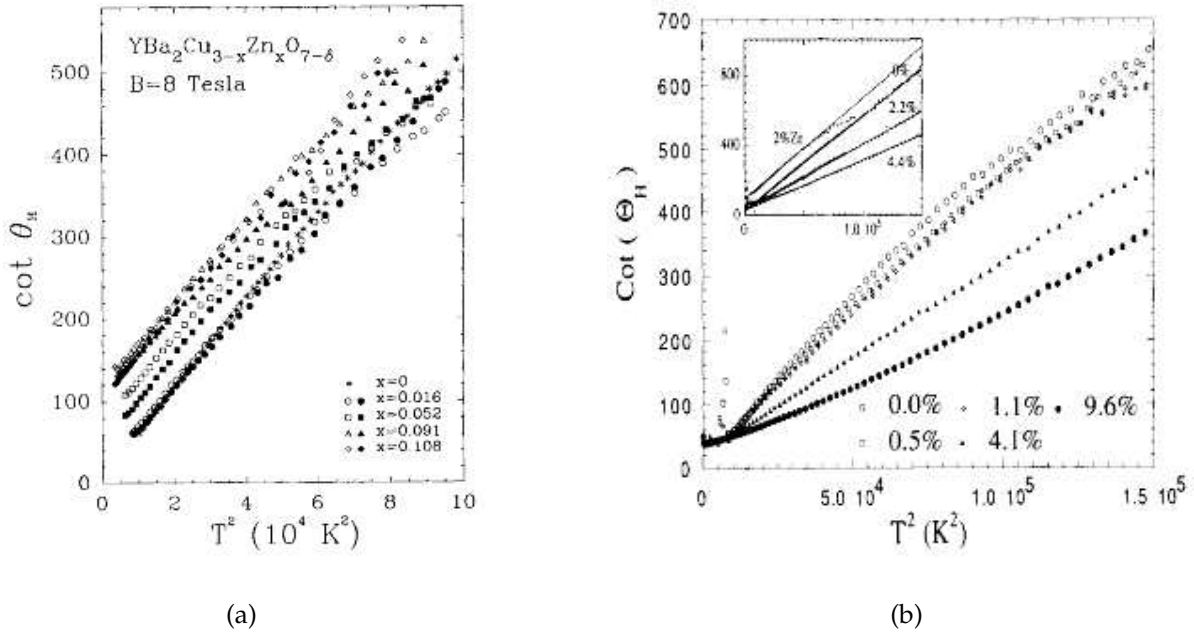
Figure 2.2: (a) Temperature dependence of the Hall angle in in-plane zinc-doped $YBa_2Cu_3O_{7-\delta}$, taken from Chien *et al.* [8]. (b) Temperature dependence of the Hall angle in out-of-plane cobalt-doped $YBa_2Cu_3O_{7-\delta}$ taken from Carrington *et al.* [28]. Cobalt changes the hole concentration in the CuO_2 plane. The Hall angle is believed to obey a law $\cot \Theta_H \sim C + DT^2$ where C depends on the in-plane impurity doping and D on the carrier doping.

plane — analagously to 1D systems wherein it is known that the electron splits into two different components, the holon and the spinon. The breakdown of the Wiedemann–Franz law observed at low temperature in a cuprate [9], adds further credence to this view. However, we shall not explore these ideas further here; the small-angle scattering model of Varma and Abrahams that we investigate is one of many attempts to explain the observations whilst staying within the conventional Fermi liquid picture (see §2.3).

2.2.3 Magnetoresistance

The magnetic field also causes an increase in the resistance of a sample, known as the *magnetoresistance*. It is defined

$$\frac{\Delta\rho}{\rho} = \frac{\rho(B) - \rho(0)}{\rho(0)} = \frac{\Delta\rho^{xx}}{\rho^{xx}} = -\frac{\Delta\sigma^{xx}}{\sigma^{xx}} - \left(\frac{\sigma^{xy}}{\sigma^{xx}}\right)^2 , \qquad (2.3)$$

and is proportional to B^2, for small fields. Intuitively the origin of the magnetoresistance is the curving of electron paths away from the straight-on direction, thus reducing conductance. It is more subtle than this, however: in an isotropic metal, the magnetoresistance can be shown to be zero [24], because the Hall field restores the straight-on

(a)

(b)
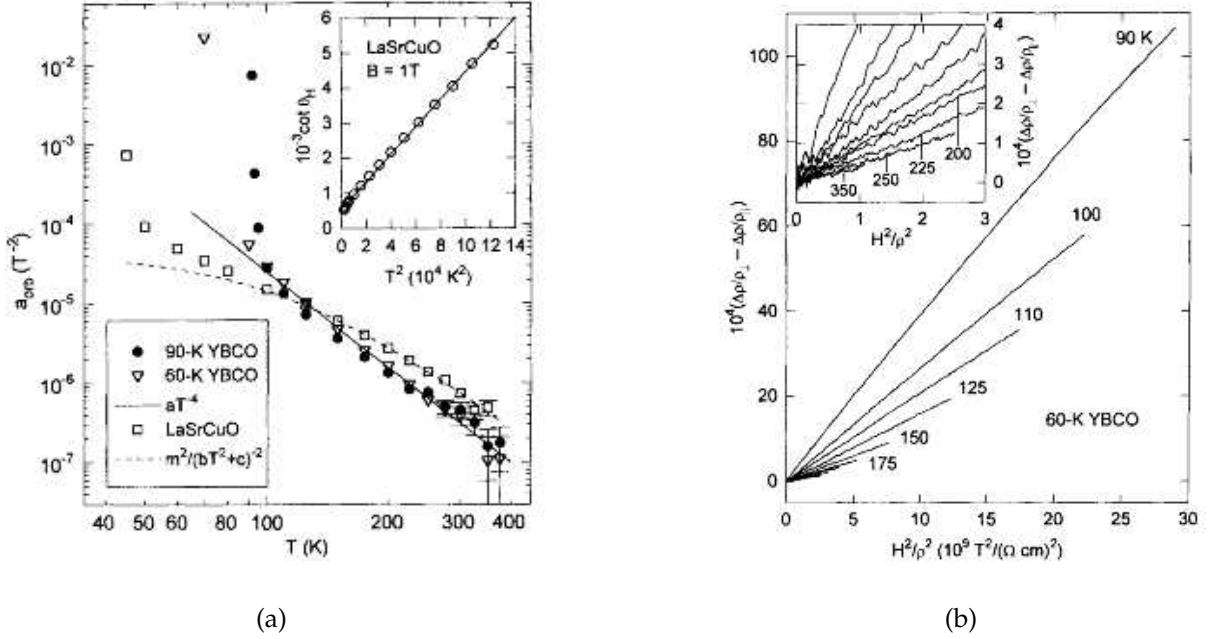
Figure 2.3: (a) Temperature dependence of the magnetoresistance $\Delta\rho/\rho$ in YBa$_2$Cu$_3$O$_{7-\delta}$ and La$_{2-x}$Sr$_x$CuO$_4$ ($\bullet,\triangledown$; $\square$) taken from Harris *et al.* [30], fitted to $(C + DT^2)^{-2}$ (dashed line) and T^{-4} (solid line). The inset shows $\cot\Theta_H \sim C + DT^2$ with only slightly different values of C and D. (b) Kohler plot for a YBa$_2$Cu$_3$O$_{7-\delta}$ sample, showing plots for temperatures between 90K and 175K. If Kohler's rule were obeyed, all lines would coincide. The inset is a zoom showing higher temperatures.

path for an electron. The case where there is an observable magnetoresistive effect is when the Fermi surface is not circular; the magnetoresistance in effect probes the variance of the Hall angle around the Fermi surface. In a conventional metal $\Delta\rho/\rho \propto B^2/\rho^2$ (see §2.3.1). On a *Kohler plot* of $\Delta\rho/\rho$ vs B^2/ρ^2, points fall on a straight line that has a gradient independent of temperature — this is *Kohler's rule*. [29]

However, in the cuprates Kohler's rule is strongly violated [30]. It is believed that (for temperature dependences) the magnetoresistance in cuprates is no longer proportional to the inverse square of the resistivity ρ^{-2}. Instead, it is proportional to the square of the Hall angle $\Delta\rho/\rho \sim \cot^{-2}\Theta_H \sim (C + DT^2)^{-2}$, creating a "modified Kohler's rule." However, magnetoresistance is a very sensitive experiment and this relationship is somewhat controversial — for example, Malinowski *et al.* [31] provide evidence suggesting that a different relaxation rate (see §2.3.1) is associated with the magnetoresistance than that for the Hall effect.

2.2.4   Photoemission

More recently, angle-resolved photoemission spectroscopy (ARPES) experiments have shed light on the detailed properties of the electronic quasiparticle. ARPES measures

the distribution, with angle and energy, of electrons emitted when a sample is bombarded with photons; a density $A(\omega, \mathbf{k})$, closely related to the spectral function, can be deduced from this distribution. Near the Fermi level, for non-interacting electrons at low temperature, one would expect a sharp peak (in energy space) following the Fermi surface (in momentum space), and for real electrons the peak is broadened. The width of the peak determines the inverse lifetime, or scattering rate, of an electron at that momentum.

In the cuprates, the scattering rate around the Fermi surface observed by ARPES [32] can be interpreted as having two components [33] (see Fig. 2.4). First, there is an *isotropic* inelastic contribution with a linear temperature dependence, coming from electron-electron scattering in a marginal Fermi liquid. Second, there is an elastic *temperature-independent* contribution which is *anisotropic*. Measuring angles with respect to the k_x direction around the hole-like Fermi surface of the cuprates (centred at (π, π)), this anisotropic contribution peaks at angles $\theta = 0, \pi/2 \ldots$, and is smallest at $\theta = \pi/4, 3\pi/4 \ldots$; often this variation is modelled with a cosine, as shown in Fig. 2.4(b). The larger scattering rate in regions near $(\pi, 0)$ etc. means that the electrons there, having a shorter lifetime, are less well-defined, preempting the *pseudogap* regime where there are no low-energy excitations available to give rise to free particles — see Chapter 6 and Chapter 7.

In summary, our interpretation of this scattering rate can be written

$$\tau^{-1}(\theta, T) \sim \underbrace{A + BT}_{\tau_M^{-1}} + \tau_i^{-1} \cos^2 2\theta \, , \tag{2.4}$$

where the inverse lifetime τ_M^{-1} is the marginal Fermi liquid scattering rate, and the amplitude of the anisotropic contribution is τ_i^{-1}.

2.3 Transport theories

2.3.1 Conventional theory

In a conventional metal, transport properties are described well by a fairly straightforward theory. The *relaxation time approximation* is used, where quasiparticles, anywhere on the Fermi surface, decay toward equilibrium exponentially with a single lifetime τ

(a)   (b)
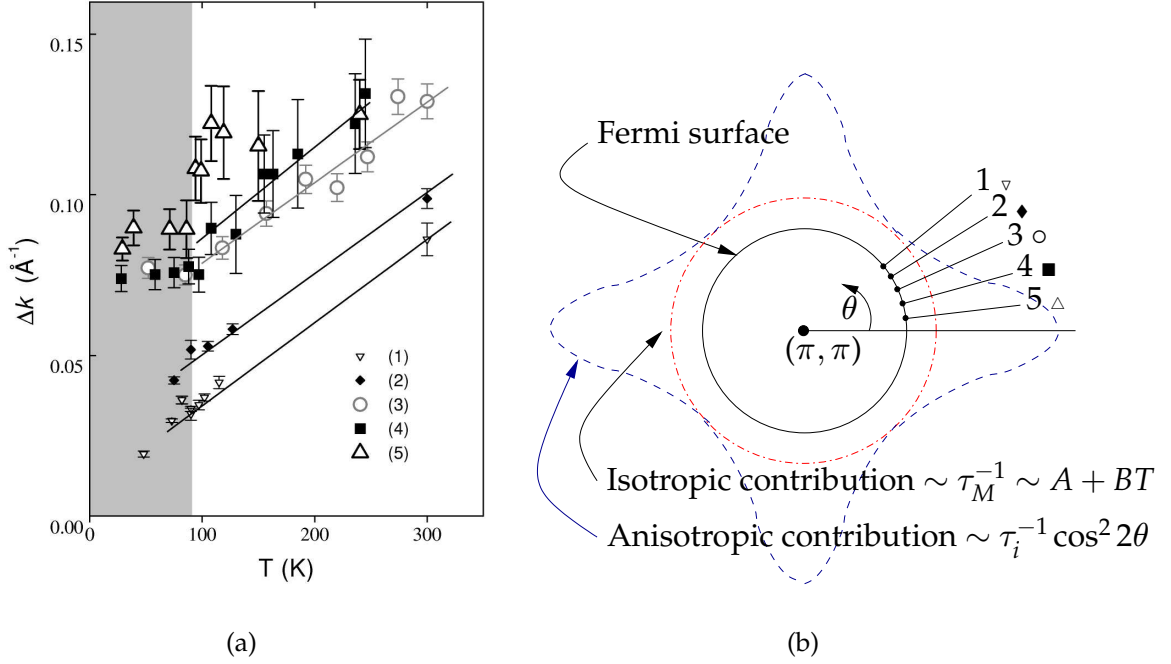
Figure 2.4: (a) Temperature and momentum dependence of momentum widths in $Bi_2Sr_2CaCu_2O_{8-\delta}$ measured by ARPES, taken from Valla *et al.* [32]. The temperature dependence has the same linear variation at different points on the Fermi surface (positions (1) to (5), corresponding to $\theta \sim \pi/4$ through $\theta \sim 0$ respectively), but there is an additional momentum-dependent, temperature-independent, scattering rate which is maximal at $\theta = 0$ (position (5)). (b) Schematic diagram of this variation of scattering rate; *c.f.* Eqn 2.4.

(see §2.4.2). For free electrons (Drude model) one can show that

$$
\begin{aligned}
\sigma^{xx} &\sim (ne^2\tau/m) & \rho &\sim \tau^{-1} \\
\sigma^{xy} &\sim (ne^2\tau/m)\,(\omega_c\tau) & \Rightarrow \qquad \cot\Theta_H &\sim \tau^{-1} \\
\Delta\sigma^{xx} &\sim -(ne^2\tau/m)\,(\omega_c\tau)^2 & \Delta\rho/\rho &\sim \tau^2
\end{aligned}
\tag{2.5}
$$

where n is the electron density, m is the effective mass of an electron, and the cyclotron frequency $\omega_c \equiv eB/m$. Temperature should only affect the scattering rate τ^{-1}, so ρ and $\cot\Theta_H$ are expected to have an identical temperature dependence, and the magnetoresistance is expected to behave as $\Delta\rho/\rho \sim \rho^{-2}$, which is Kohler's rule. The cuprates do not fit into this picture: $\rho \sim T$ whereas $\cot\Theta_H \sim T^2$, and Kohler's rule is violated as their magnetoresistance $\Delta\rho/\rho \sim T^{-4}$.

2.3.2   Two lifetime model

Anderson [7] proposed that in the high-T_c cuprates the forms in Eqn 2.5 should be altered to

$$\sigma^{xx} \sim \quad (ne^2\tau_{\mathrm{tr}}/m) \qquad\qquad\qquad\qquad \rho \sim \tau_{\mathrm{tr}}^{-1}$$

$$\sigma^{xy} \sim \quad (ne^2\tau_{\mathrm{tr}}/m)\,(\omega_c\tau_H) \qquad \Rightarrow \qquad \cot\Theta_H \sim \tau_H^{-1} \qquad\qquad (2.6)$$

$$\Delta\sigma^{xx} \sim \quad -(ne^2\tau_{\mathrm{tr}}/m)\,(\omega_c\tau_H)^2 \qquad\qquad \Delta\rho/\rho \sim \tau_H^2\,,$$

introducing two different scattering times: τ_{tr} for longitudinal transport, and τ_H for transverse Hall-like effects. If these scattering times have the different temperature dependences $\tau_{\mathrm{tr}}^{-1} \sim A + BT$ and $\tau_H^{-1} \sim C + DT^2$, the cuprate experimental results are reproduced correctly.

It has not proved easy to find models for the scattering of electrons which can reproduce this phenomenology. Many authors have focused on the possibility of anistropic scattering rates, beginning with the idea of "hot spots" on the Fermi surface at $(\pi, 0)$ etc. [34, 35, 36, 37], akin to the ARPES experiments above (see Chapter 6 and Chapter 7 again where a possible microscopic origin is discussed). Similar ideas include a varying lifetime around the Fermi surface [38], and an anisotropic scattering rate which saturates [39]. The simplicity of the Drude forms (Eqn 2.5) belies the complications which ensue when quantities become anisotropic. A conductivity must first be calculated by adding up the contributions from scattering rates in different places on the Fermi surface (see §2.4), which must be inverted as a whole to give the resistivity-like quantities: all momenta couple together, with the result that any effects are, if not muddled together, certainly nonintuitive.

Other proposals include a nearly-antiferromagnetic Fermi liquid with vertex corrections included [40], or even going beyond a Fermi liquid description inspired by the spinons and holons in 1D systems [41, 42]; one of the aims of this chapter is to gain intuition on whether a model that lies in a conventional Fermi liquid is capable of producing the Anderson phenomenology.

2.3.3   Small-angle scattering

The focus of this study will be a model that lies within Fermi liquid theory, but uses an unconventional form of the electron scattering rate including an anisotropic term with restricted momentum transfer. Abrahams *et al.* [33] proposed that the anisotropic contribution to the ARPES scattering rate (the τ_i^{-1} term in Eqn 2.4) could be ascribed to *small-angle scattering*. Varma and Abrahams [14] investigated a phenomenological model including such a term and calculated that the resulting Hall angle had the square of the temperature dependence of the resistivity, as required to match experiments on

the cuprates.

In a small-angle scattering event there is little change to the momentum of an electron, and intuitively such processes should make negligible difference to transport properties, but Varma and Abrahams claim that the combination with anisotropy creates an effective Lorentz force which changes sign every $\pi/4$ round the Fermi surface, and the resulting skewed distribution gives anomalous contibutions to the magnetotransport quantities. A possible physical origin of the small-angle scattering is dopant impurites lying out of the copper oxide plane, sufficiently far away that the momentum transfer is small. The $\cos^2 2\theta$ anisotropy (*c.f.* Eqn 2.4) could conceivably come from coupling to the copper $d(x^2 - y^2)$ orbital, or perhaps even a preview fluctuation of the instability to d-wave superconductivity at lower temperatures. These provide reassurance that there are credible physical mechanisms for the phenomenological model; at this stage we are not concerned further with them — only their consequences.

Small-angle scattering requires that we take account of not only where an electron has been scattered from (*scattering out*) but also where it scatters to (*scattering in*) — see Fig. 2.5. ARPES, which measures the lifetime of a momentum state, is blind to scattering in and so we are free to speculate on it. Quantitatively, the scattering rate $\tau^{-1}(\theta)$ can be written more fully as $\tau^{-1}(\theta, \theta')$, giving the rate of scattering from θ to θ' (note that these processes are elastic). Small-angle scattering processes exhibit a strong peak for θ close to θ', whereas conventional processes are insensitive to $\theta - \theta'$. At a point θ, ARPES observes the inverse lifetime of the state $\tau^{-1}(\theta) = \sum_{\theta'} \tau^{-1}(\theta, \theta')$. A possible realization of the full scattering rate is

$$\tau^{-1}(\theta, \theta') = \tau_M^{-1} + \tau_i^{-1}|\cos 2\theta||\cos 2\theta'|e^{\frac{-(\theta - \theta')^2}{2\theta_c^2}}/\theta_c \, , \tag{2.7}$$

where θ_c is the width of the small angle scattering (and note that the τ_i^{-1} of Eqn 2.4 is defined slightly differently). Fig. 2.5 shows a schematic visualization of the small-angle scattering process.

2.4 Calculations

2.4.1 Boltzmann transport theory

Boltzmann transport theory is a classical theory of transport in metals, and describes the electron liquid in terms of the distribution of electrons $f_\mathbf{k}$ in $\mathbf{k}$-space, and how this changes under an applied electric field $\mathbf{E}$, a magnetic field $\mathbf{B}$, and some combined scattering rate $C_\mathbf{k}$. The phenomenological scattering model described above will provide

PSfrag replacements
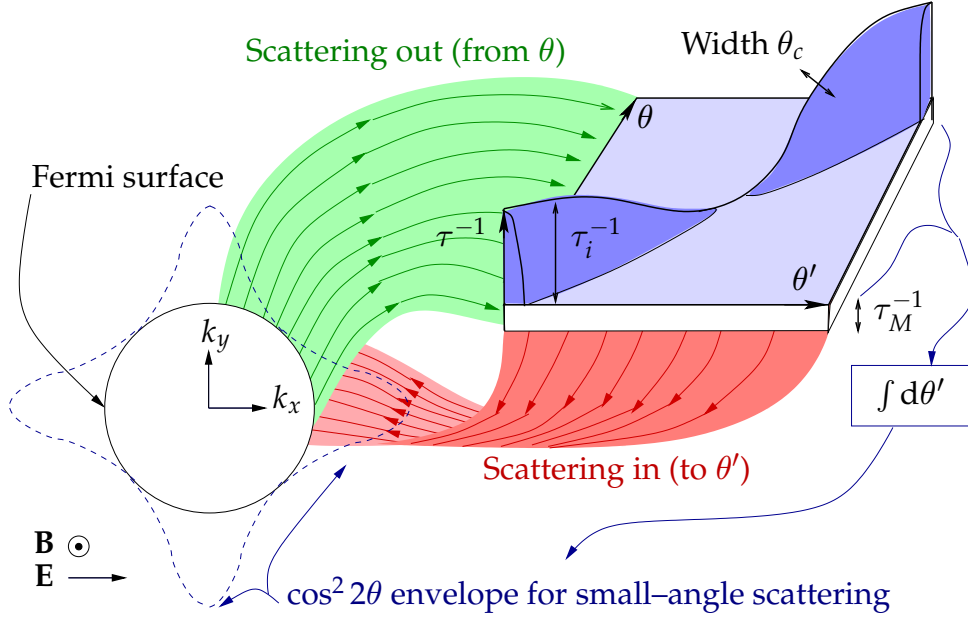
Figure 2.5: Schematic diagram of the small-angle scattering process. In general, each point on the Fermi surface loses electrons that are *scattered out*, and receives them when they are *scattered in*. For the small-angle scattering studied here, an individual electron has an even probability of being scattered (in) to anywhere else on the Fermi surface, *plus* an enhanced probability of being scattered back (in) to where it came (out) from; this probability varies around the Fermi surface and is zero in places. If all scattering-in angles are integrated over, the overall scattering-out rate, or lifetime, of a particular part of the Fermi surface must have the $\cos^2 2\theta$ envelope observed by ARPES.

the quantity $C_\mathbf{k}$, and from the change in distribution of electrons we will be able to calculate the conductivities σ^{xx}, σ^{xy} and $\Delta\sigma^{xx}$, from which the quantities in §2.2 can be derived.

In Appendix A I give a derivation of the linearized Boltzmann equation (Eqn A.1)

$$\mathbf{v_k} \times \mathbf{B} \cdot \frac{\partial g_\mathbf{k}}{\partial \mathbf{k}} - C_\mathbf{k} = \mathbf{E} \cdot \mathbf{v_k} \frac{\partial f_\mathbf{k}^0}{\partial \epsilon_\mathbf{k}} \tag{2.8}$$

where $g_\mathbf{k}$ is the departure from equilibrium such that $f_\mathbf{k} = f_\mathbf{k}^0 + g_\mathbf{k}$. $C_\mathbf{k}$ is the rate of change of occupation of the state at $\mathbf{k}$ due to scattering processes, combining *scattering in* to that $\mathbf{k}$-state and *scattering out* of that state. So we can write

$$C_\mathbf{k} \equiv \sum_{\mathbf{k}'} \Big[\underbrace{C_{\mathbf{k},\mathbf{k}'} g_{\mathbf{k}'}}_{\text{Scattering in}} - \underbrace{C_{\mathbf{k}',\mathbf{k}} g_\mathbf{k}}_{\text{Scattering out}} \Big] = \sum_{\mathbf{k}'} \Big[C_{\mathbf{k},\mathbf{k}'} g_{\mathbf{k}'} \Big] - g_\mathbf{k}/\tau(\mathbf{k}) \,, \tag{2.9}$$

where $C_{\mathbf{k},\mathbf{k}'}$ is the scattering rate from state $\mathbf{k}'$ to $\mathbf{k}$, and we have defined the *inverse lifetime* $\tau^{-1}(\mathbf{k})$ of a state as the combined scattering out rate $\sum_{\mathbf{k}'} C_{\mathbf{k}',\mathbf{k}}$. Hence, following

Kotliar *et al.* [43], we can write the Boltzmann equation in the form

$$\sum_{\mathbf{k'}} A_{\mathbf{k},\mathbf{k'}} g_{\mathbf{k'}} = \mathbf{E} \cdot \mathbf{v_k} \left(-\frac{\partial f_{\mathbf{k}}^0}{\partial \epsilon_{\mathbf{k}}} \right) , \tag{2.10}$$

defining the matrix A with elements

$$A_{\mathbf{k},\mathbf{k'}} \equiv \left(1/\tau(\mathbf{k}) + \mathbf{v_k} \times \mathbf{B} \cdot \nabla_{\mathbf{k}} \right) \delta(\mathbf{k} - \mathbf{k'}) - C_{\mathbf{k},\mathbf{k'}} . \tag{2.11}$$

To calculate the deviation from equilibrium $g_{\mathbf{k}}$, we need to invert the matrix A:

$$g_{\mathbf{k}} = A^{-1} \mathbf{E} \cdot \mathbf{v_k} \left(-\frac{\partial f_{\mathbf{k}}^0}{\partial \epsilon_{\mathbf{k}}} \right) ; \tag{2.12}$$

conductivities may be calculated directly from $g_{\mathbf{k}}$:

$$\mathbf{J} = 2 \sum_{\mathbf{k}} \mathbf{v_k} g(\mathbf{k}) \quad \Rightarrow \quad \sigma^{\mu\nu} = 2 \sum_{\mathbf{k},\mathbf{k'}} \delta(\epsilon_{\mathbf{k'}} - \epsilon_F) v_{\mathbf{k}}^{\mu} A_{\mathbf{kk'}}^{-1} v_{\mathbf{k'}}^{\nu} , \tag{2.13}$$

noting that $\left(-\partial f_{\mathbf{k}}^0 / \partial \epsilon_{\mathbf{k}} \right) \xrightarrow{T \to 0} \delta(\epsilon_{\mathbf{k}} - \epsilon_F)$, constraining all values of $\mathbf{k}$ under consideration to be on the Fermi surface, if $T \ll \epsilon_F$.

2.4.2   Jones–Zener expansion

Usually, the magnetic field $\mathbf{B}$ is small, and the matrix $A(\mathbf{k}, \mathbf{k'})$ can be inverted in powers of $\mathbf{B}$:

$$A^{-1} \simeq \underbrace{\mathcal{T}}_{A_0} - \underbrace{\mathcal{T}(\mathbf{v_k} \times \mathbf{B} \cdot \nabla_{\mathbf{k}})\mathcal{T}}_{A_1} + \underbrace{\mathcal{T}(\mathbf{v_k} \times \mathbf{B} \cdot \nabla_{\mathbf{k}})\mathcal{T}(\mathbf{v_k} \times \mathbf{B} \cdot \nabla_{\mathbf{k}})\mathcal{T}}_{A_2} + \ldots \tag{2.14}$$

with implicit matrix multiplication; $\mathcal{T}$ is defined by the condition

$$\mathcal{T}_{\mathbf{k},\mathbf{k'}} = \tau(\mathbf{k}) \left(\delta_{\mathbf{k},\mathbf{k'}} + \sum_{\mathbf{k''}} C_{\mathbf{k},\mathbf{k''}} \mathcal{T}_{\mathbf{k''},\mathbf{k'}} \right) . \tag{2.15}$$

The conductivities σ^{xx}, σ^{xy} and $\Delta\sigma^{xx}$ are generated by the terms at B^0, B^1 and B^2 respectively, and variables can be changed from (k_x, k_y) to $(\epsilon, \theta,)$ for a circular Fermi

surface:

$$\sigma^{xx} \propto \sum_{\mathbf{k},\mathbf{k}'} v_{\mathbf{k}}^x A_{0\mathbf{k},\mathbf{k}'} v_{\mathbf{k}'}^x \delta(\epsilon_{\mathbf{k}} - \epsilon_F) \qquad \propto \int \mathrm{d}\theta \, v_x(\theta)\hat{\tau}(\theta)v_x(\theta) \tag{2.16}$$

$$\sigma^{xy} \propto \sum_{\mathbf{k},\mathbf{k}'} v_{\mathbf{k}}^x A_{1\mathbf{k},\mathbf{k}'} v_{\mathbf{k}'}^y \delta(\epsilon_{\mathbf{k}} - \epsilon_F) \qquad \propto B \int \mathrm{d}\theta \, v_x(\theta)\hat{\tau}(\theta)\frac{\mathrm{d}}{\mathrm{d}\theta}\hat{\tau}(\theta)v_y(\theta) \tag{2.17}$$

$$\Delta\sigma^{xx} \propto \sum_{\mathbf{k},\mathbf{k}'} v_{\mathbf{k}}^x A_{2\mathbf{k},\mathbf{k}'} v_{\mathbf{k}'}^x \delta(\epsilon_{\mathbf{k}} - \epsilon_F) \qquad \propto B^2 \int \mathrm{d}\theta \, v_x(\theta)\hat{\tau}(\theta)\frac{\mathrm{d}}{\mathrm{d}\theta}\hat{\tau}(\theta)\frac{\mathrm{d}}{\mathrm{d}\theta}\hat{\tau}(\theta)v_x(\theta) \, . \tag{2.18}$$

The gradient $\nabla_{\mathbf{k}}$ has effectively become $\mathrm{d}/\mathrm{d}\theta$ under the change of variable (see later), and $\mathcal{T}$ can be written as a local operator $\hat{\tau}(\theta)$ (see Ref. [14] for more detail). Symmetry means that the three conductivities above are the only non-zero terms; and terms at higher orders in B will just add further contributions to the conductivities above. If the Fermi surface is not circular, very similar expressions can be derived (see later); θ becomes the path length s, and the density of states (or Jacobian) term $|v(s)|$ appears in various places.

In the relaxation time approximation, the second term of Eqn 2.15 is discarded, so the operator $\hat{\tau}$ becomes a normal function $\tau(\theta)$. Secondly, its momentum dependence is neglected, so in effect $\mathcal{T}(\mathbf{k},\mathbf{k}') \to \tau$. The dependences for σ^{xx}, σ^{xy} and $\Delta\sigma^{xx}$ thence become τ^1, τ^2 and τ^3 respectively, as summarized in Eqn 2.5.

For the model of Varma and Abrahams, $C_{\mathbf{k},\mathbf{k}'}$ takes the form of the phenomenological scattering rate proposition, such as that in Eqn 2.7, and we must solve Eqn 2.15 (in the θ basis). The original approach of Ref. [14] is to use θ_c as a perturbative parameter, and solve Eqn 2.15 iteratively; however, this route is flawed [21] — and in any case, to expect a perturbative correction to dominate one's results is manifestly inconsistent. Features of small angle scattering can be used to simplify the equations and produce analytic results [21]; we will compare with these results later.

Nevertheless, some insight can be gained from considering θ_c as a perturbative parameter. For the case of a circular Fermi surface,

$$\hat{\tau}(\theta) = \tau_M \left[1 + \frac{\theta_c^2 \tau_M}{\tau_i} \left(\cos^2 2\theta \frac{\partial^2}{\partial\theta^2} - 2\sin 4\theta \frac{\partial}{\partial\theta} \right) \right] \, , \tag{2.19}$$

which generates the expressions

$$\sigma^{xx} = \frac{ne^2}{m}\tau_M \left(1 - \frac{1}{2}\frac{\theta_c^2 \tau_M}{\tau_i}\right)$$

$$\sigma^{xy} = \frac{ne^2}{m}\omega_c \tau_M^2 \left(1 - \frac{\theta_c^2 \tau_M}{\tau_i}\right) \quad (2.20)$$

$$\Delta\sigma^{xx} = -\frac{ne^2}{m}\omega_c^2 \tau_M^3 \left(1 - \frac{3}{2}\frac{\theta_c^2 \tau_M}{\tau_i}\right).$$

for the conductivities. Since $\tau_M^{-1} \sim T$, there are apparently new temperature dependences at first order in θ_c^2. These are actually fallacious; for example, for the resistance $\rho = [\sigma^{xx}]^{-1}$, all orders in θ_c^2 must be resummed and a constant is added to the resistance — this is Matthiessen's rule.[1] However, any real effects of small angle scattering can be understood in terms of such an expansion in τ_M/τ_i, and we can postulate finitesimal corrections to the Drude forms:

$$\sigma^{xx} \sim \tau_M \left(\boxed{C_0^{xx}} - C_1^{xx}\frac{\tau_M}{\tau_i} + C_2^{xx}\frac{\tau_M^2}{\tau_i^2} + \dots\right), \quad (2.21)$$

$$\sigma^{xy} \sim \omega_c \tau_M^2 \left(C_0^{xy} - \boxed{C_1^{xy}}\frac{\tau_M}{\tau_i} + C_2^{xy}\frac{\tau_M^2}{\tau_i^2} + \dots\right), \quad (2.22)$$

$$\Delta\sigma^{xx} \sim -\omega_c^2 \tau_M^3 \left(C_0^{\Delta xx} - C_1^{\Delta xx}\frac{\tau_M}{\tau_i} + \boxed{C_2^{\Delta xx}}\frac{\tau_M^2}{\tau_i^2} \dots\right). \quad (2.23)$$

The observed transport properties are determined by the relative sizes of the $C_{\{0,1,2\}}^{\{xx,xy,\Delta xx\}}$ coefficients, and the circled terms are those that must dominate to match experiment. The resistivity $\rho = [\sigma^{xx}]^{-1}$ should be little affected by the anomalous terms and show the marginal Fermi liquid behaviour $\rho \sim \tau_M^{-1} \sim T$, so to match experiment $C_1^{xx} \ll C_0^{xx}$, etc. The Hall angle $\cot\Theta_H = \sigma^{xx}/\sigma^{xy}$, however, is observed to vary as $\cot\Theta_H \sim T^2 \sim \tau_M^{-2}$, so Eqn 2.22 must be dominated by C_1^{xy}. The magnetoresistance $\Delta\rho/\rho = -\Delta\sigma^{xx}/\sigma^{xx} - (\sigma^{xy}/\sigma^{xx})^2$ has an experimental dependence $\Delta\rho/\rho \sim T^{-4} \sim \tau_M^4$, which is apparently provided by $(\sigma^{xy}/\sigma^{xx})^2$. However, this term has the wrong sign, and so $\Delta\sigma^{xx}/\sigma^{xx}$ needs to have (negative) terms at τ_M^4 which dominate overall, and thence the next order coefficient $C_2^{\Delta xx}$ must be the largest.

To draw conclusions, we need to actually do some real calculations that effectively evaluate the sizes of the $C_{\{0,1,2\}}^{\{xx,xy,\Delta xx\}}$ coefficients, but the calculations must not rely on the expansions above. Next I shall detail our numerical approach (§2.4.3), which

---

[1]In fact, Matthiessen's rule does not hold for the case when the extra scattering has a different momentum dependence, as will be the case for our model.
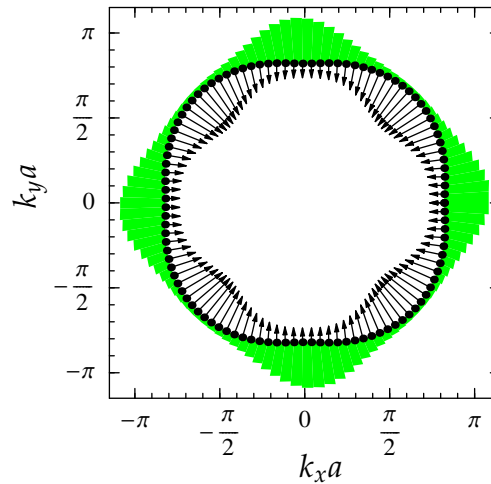
Figure 2.6: Fermi surface for the ARPES best-fit shape of Norman *et al.* [44], translated from its (π, π) centre. Discretization of the surface is illustrated by dots, although in practice several times as many points than shown are used (up to 1000). Fermi velocities at each point are indicated by arrows (length in arbitrary units); the scattering out rate $\tau^{-1}(\theta)$ is indicated by the shaded region (again in arbitrary units), and varies according to the model Eqn 2.7.

is entirely distinct from the perturbative analysis above, and then present its results (§2.4.4). In §2.5 I shall discuss these results within the context of the previous paragraph: is it possible for the small-angle scattering model to produce the right terms, large enough to match experimental observations?

2.4.3   Numerical method

Here I present a completely numerical solution of the Boltzmann equation for the small-angle scattering model. The input parameters will be first a dispersion $\epsilon_{\mathbf{k}}$ and chemical potential μ that together define a Fermi surface and Fermi velocities, and second a general scattering rate $\tau^{-1}(\theta, \theta')$ from a point on the Fermi surface at angle θ to one at θ'. An example of such a small angle scattering model is given in Eqn 2.7, but the calculations are not restricted to such a form.

To calculate the conductivities, we use Eqn 2.13, and change variables form (k_x, k_y) to (ϵ, s) where ϵ is the energy and s the distance round the Fermi surface. The ϵ sum in Eqn 2.13 vanishes with the $\delta(\epsilon - \epsilon_F)$, and there remains an s-sum constrained to the Fermi surface. The Jacobian can be shown to be $1/v(s)$ where $v = |\mathbf{v}(s)|$ is the Fermi speed. The Fermi surface is now discretized, giving n points separated by equal distances ds in $\mathbf{k}$ space. At each point i, the Fermi velocity $\mathbf{v}_i$ is obtained from the gradient of the dispersion $\epsilon_{\mathbf{k}}$; the scattering rate τ_{ij}^{-1} to any other point j is also required, and easily evaluated from the model $\tau^{-1}(\theta, \theta')$. Fig. 2.6 shows an example discretized Fermi surface with velocities and scattering rates.

A matrix A_{ij} (the A of Eqn 2.11) is constructed with with diagonal elements $A_{ii} =$

$\gamma_i - \tau_{ii}^{-1}/v_i$ and off-diagonal elements $A_{ij} = -\tau_{ij}^{-1}/v_j$, where $\gamma_i = \sum_j \tau_{ij}^{-1}/v_j$ is the total scattering-in to the point i (*c.f.* Eqn 2.9). To include the magnetic field, we note that $(\mathbf{v_k} \times \mathbf{B} \cdot \nabla_\mathbf{k}) \to Bv(s)\partial/\partial s$, becoming just a derivative with respect to s, so we can include $\mathbf{B}$ as additions $\pm B$ on the sub- and superdiagonals respectively. The size of B is arbitrary (as the Hall effect just scales with B and the magnetoresistance with B^2), but must be small enough that higher orders are not important, and in line with real experiments. We choose B such that $\cot \Theta_H \sim 10^2$ and the relative change in conductance with respect to $B = 0$ is small but observable, perhaps 10^{-3}.

Periodic boundary conditions are necessary, and we make sure that expression for τ_{ij}^{-1} is periodic with i and j, so there is scattering from $\theta = 2\pi - \delta$ to $\theta = 0 + \delta$, and that there are B elements in the corners of the matrix so that the first and last points are linked for the gradient operator. Finally, we multiply rows by $1/v_i$ to construct a symmetric matrix (A_{ij}/v_i), and Eqn 2.10 becomes

$$\sum_j \left(A_{ij}/v_i \right) g_j = \sum_j \left(\frac{\gamma_i}{v_i}\delta_{ij} - \frac{\tau_{ij}^{-1}}{v_i v_j} \right) g_j = v_i^x/v_i \qquad (2.24)$$

(v_i^x means the x-component of the Fermi velocity at the ith point round the Fermi surface). This is just a set of linear equations to solve for the displacements from equilibrium $\mathbf{g}$, from which we can obtain the conductivities

$$\sigma^{xx} = \sum_i g_i v_i^x/v_i \quad (B = 0) \ ; \qquad \sigma^{xy} = \sum_i g_i v_i^y/v_i \ ; \qquad \Delta\sigma^{xx} = \sigma^{xx} - \sigma^{xx}(B = 0) \quad (2.25)$$

(remembering the density of states Jacobian $1/v_i$). Unfortunately, the matrix (A_{ij}/v_i) has the nasty property that each of its rows and columns sum to zero: the matrix has zero determinant and is not invertible. Physically, this makes sense as particles are conserved — they must scatter to somewhere else on the Fermi surface. There are mathematical consequences; first that there is no solution unless the right hand side of the equation sums to zero also. v_i^x will satisfy this constraint because there is no net velocity without applied fields. Second, the problem is underspecified and there is no unique solution: if we add a number to every element of such that $g_i \to g_i + \zeta$, the result will still be a solution; we have not told the mathematics that g is a departure from equilibrium, so this also makes sense. In practice, fortunately, numerical linear equation solvers (see Appendix C) are able to produce a solution to the set of equations, which can be shifted $g_i \to g_i + \zeta$, choosing ζ to ensure $\sum_i g_i = 0$.

2.4.4   Results

Calculations have involved experimenting with many different dispersions and scattering rate functions, and exploring what the small angle scattering model is capable of producing. Fermi surfaces considered included the one illustrated in Fig. 2.8(a), the full range shown in Fig. 2.7, and the ARPES best-fit Fermi surface [44] (Fig. 2.6). A range of scattering rates were used, generally similar to Eqn 2.7, but extending to others such as the varying-θ_c model proposed by Varma and Abrahams [18]. In this section I will summarize our findings qualitatively, and in the following section (§2.4.5) I present quantitative results for a best-fit to the parametrization of Abrahams and Varma [21].

In general the **resistivity** is little affected by the introduction of small-angle scattering, and obeys a nearly linear-T law, persisting from the τ_M^{-1} of Eqn 2.4.

Similarly, the **Hall angle** generally maintains a nearly linear-T law from the τ_M^{-1} of Eqn 2.4, apart from one special case: when the Fermi surface is very close to *particle-hole symmetry*. Conventionally, the Hall coefficient changes sign when the Fermi surface goes from particle-like to hole-like, so there is a point in between when the Hall effect vanishes. In a simple tight-binding model this coincides with half-filling, as shown in Fig. 2.7(a), yielding a diamond-shaped Fermi surface — but this is pathological for transport calculations. Introducing a next-nearest-neighbour hopping term splits the particle-hole symmetry point away from half-filling, and now the Fermi surface that is particle-hole symmetric (for the Hall effect) consists of sections with with equal amounts of positive and negative curvature (see Fig. 2.7(b)).[2] The conventional Hall effect vanishes for such a Fermi surface; and when close to such a point, the temperature dependence of the Hall angle $\cot\Theta_H$ within the small angle scattering model can become quadratic $\sim T^2$, as shown in Fig. 2.8(b).

For the **magnetoresistance**, I was unable to find a set of parameters where there was any significant deviation from a $\Delta\rho/\rho \sim T^{-2}$ law, regardless of whether the Fermi surface is near the particle-hole symmetric point where the Hall angle temperature exponent changes. Comparing to the resistivity, which has the marginal Fermi liquid temperature dependence $\rho \sim T$, the magnetoresistance behaves as $\Delta\rho/\rho \sim \rho^{-2}$. This is exactly what one would expect from the Drude picture (Eqn 2.5): Kohler's rule is well obeyed, in contradiction with experimental measurements on the cuprates.

---

[2]Note that shape alone does not determine particle-hole symmetry as the variation in Fermi speed is also significant.
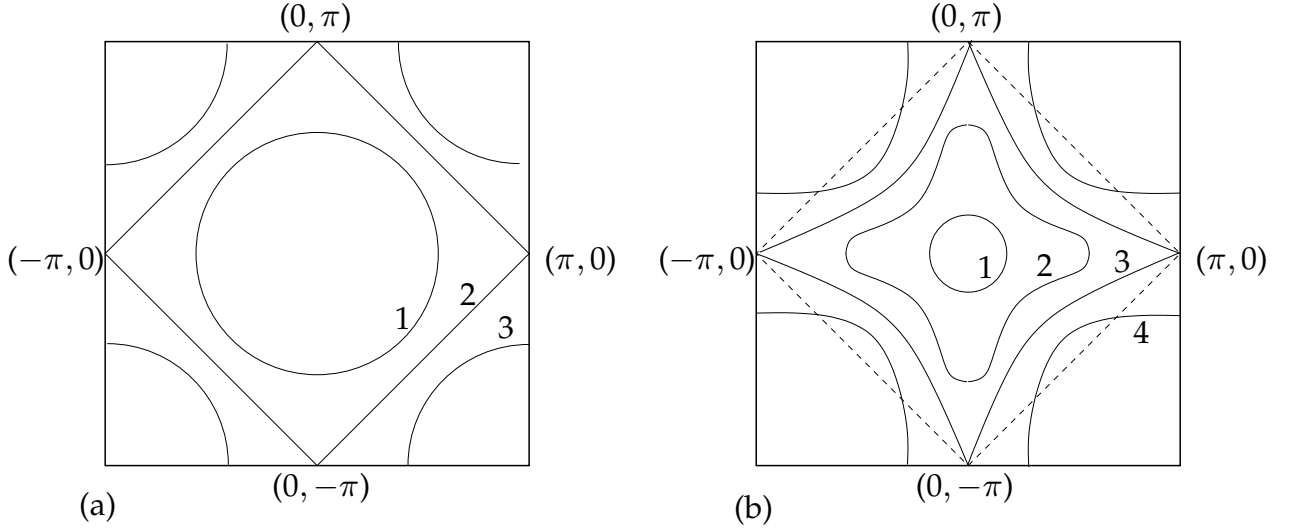
Figure 2.7: Schematic diagram of the evolution of 2D Fermi surfaces from particle-like to hole-like. (a) A simple tight-binding model evolves from a particle-like circle (1) to a hole-like circle (3) via a diamond (2) at half-filling. (b) Introduction of a t' next-nearest-neighbour term allows the Fermi surface to become particle-hole symmetric (in terms of the Hall effect) before half-filling (2), and becomes hole-like by curvature (3) before enclosing (π, π) (4). The ARPES-observed Fermi surface feature in the cuprates [44] is not apparently particle-hole symmetric, but slightly square like (4).
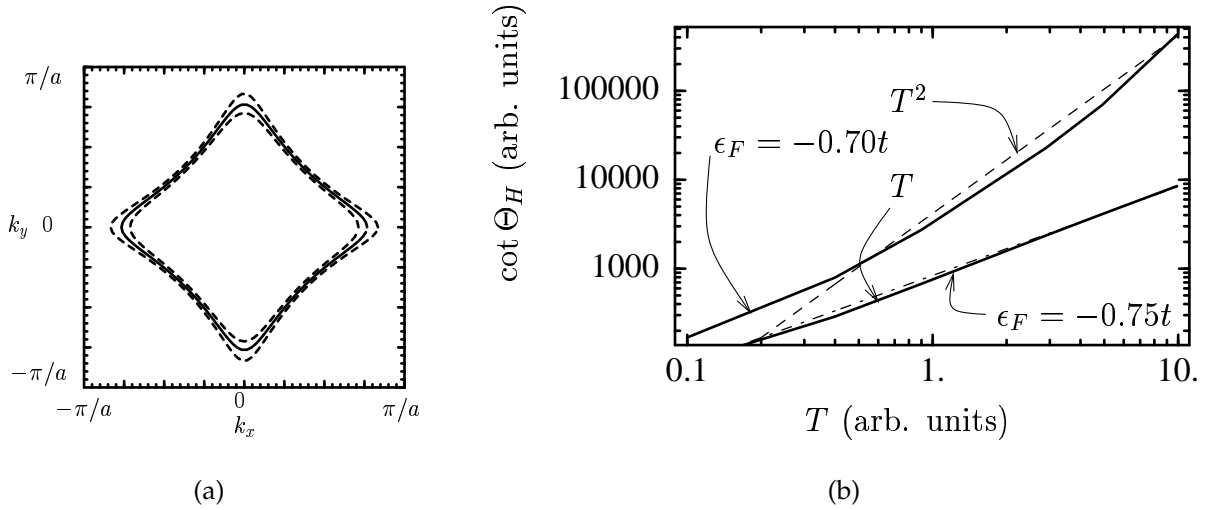
Figure 2.8: (a) Three similar Fermi surfaces for the dispersion $\epsilon_{\mathbf{k}} = -(\cos k_x + \cos k_y + 0.5966 \cos k_x \cos k_y)$; the solid line traces a particle-hole symmetric Fermi surface ($\epsilon_F = -0.70t$). (b) Log-log graph of $\cot\Theta_H$ against temperature T. A T^2 law (dashed line) is possible for the particle-hole symmetric Fermi surface shown in (a) but on altering the Fermi level slightly, the linear-T law (dot-dashed line) quickly returns ($\epsilon_F = -0.75t$). Parameters used: $\theta_c \sim 0.02$, $\tau_i^{-1} \sim 10$, $\tau_M^{-1} = 0.1 + T$; graphs reproduced from Ref. [15].

28

2.4.5   Example calculation

In this section, I shall provide a concrete example which fits the qualitative picture outlined in the previous section. Abrahams and Varma perform a set of calculations in Ref. [21], demonstrating that the Hall angle can exhibit the T^2 dependence observed experimentally, but they do not calculate the magnetoresistance. I shall present results of numerical calculations (as §2.4.3) for the resistance, Hall angle and magnetoresistance, using a set of parameters reverse-engineered to match those of Abrahams and Varma. The first of these parameters is the dispersion

$$\epsilon_{\mathbf{k}} = -0.25(\cos k_x + \cos k_y) - 0.03(\cos 2k_x + \cos 2k_y) - 0.09(\cos k_x \cos k_y) , \quad (2.26)$$

used with a Fermi level of $\epsilon_F = -0.19$ (units arbitary) to give the Fermi surface shown in Fig. 2.9(a). A scattering rate

$$\tau^{-1}(\theta, \theta') = AT + B(1 - (\theta - \theta')^2/\theta_c^2) \quad (2.27)$$

is used, relying upon the density of states to provide the anisotropy (as Abrahams and Varma do [21]). Matching to ARPES observations, A is chosen to give a gradient $\tau_M^{-1} = 0.015(T/100K)$eV, and B such that $\tau_i^{-1} = 0.24$eV at $\theta = \pi/8$. Finally, I choose the width of the small-angle scattering $\theta_c = 0.18$.

These choices are made to ensure the calculations are consistent with experimental quantities. The residual resistance ratio from experiment is $\rho(100K)/\rho(0K) \sim 8$; calculating resistances at 200K and 100K and extrapolating from these down to 0K gives a comparable ratio of 7.77 for the parameters detailed above. The anisotropy in the scattering rate near 0K is experimentally measured as $\tau_i^{-1}(0)/\tau_i^{-1}(\pi/4) = 4.5$, and my parameters result in a value of 4.27 (see Fig. 2.9(b), bottom, which shows the total scattering rate τ^{-1} as a function of θ at 100K). Fig. 2.9(b), top, shows that my Fermi velocity component $v_y(\theta)$ is a good match to the form used by Abrahams and Varma. Finally, it should be noted that the Fermi surface required to match Abrahams and Varma's calculations is quite different from that observed by ARPES (Fig. 2.6); Abrahams and Varma do not themselves use a Fermi surface directly.

Fig. 2.10 shows the results from conductivity calculations with the above parameters. The resistance in Fig. 2.10(a) exhibits a linear-T law, as expected. The Hall angle, plotted against T^2 in Fig. 2.10(b), achieves a reasonable fit to a T^2 law, in good agreement with the graphs in Ref. [21] — the model is sufficiently close to the particle-hole symmetry point discussed in §2.4.4. So far, experiment can be matched by the small angle scattering model, but for the magnetoresistance we find that Varma and Abra-
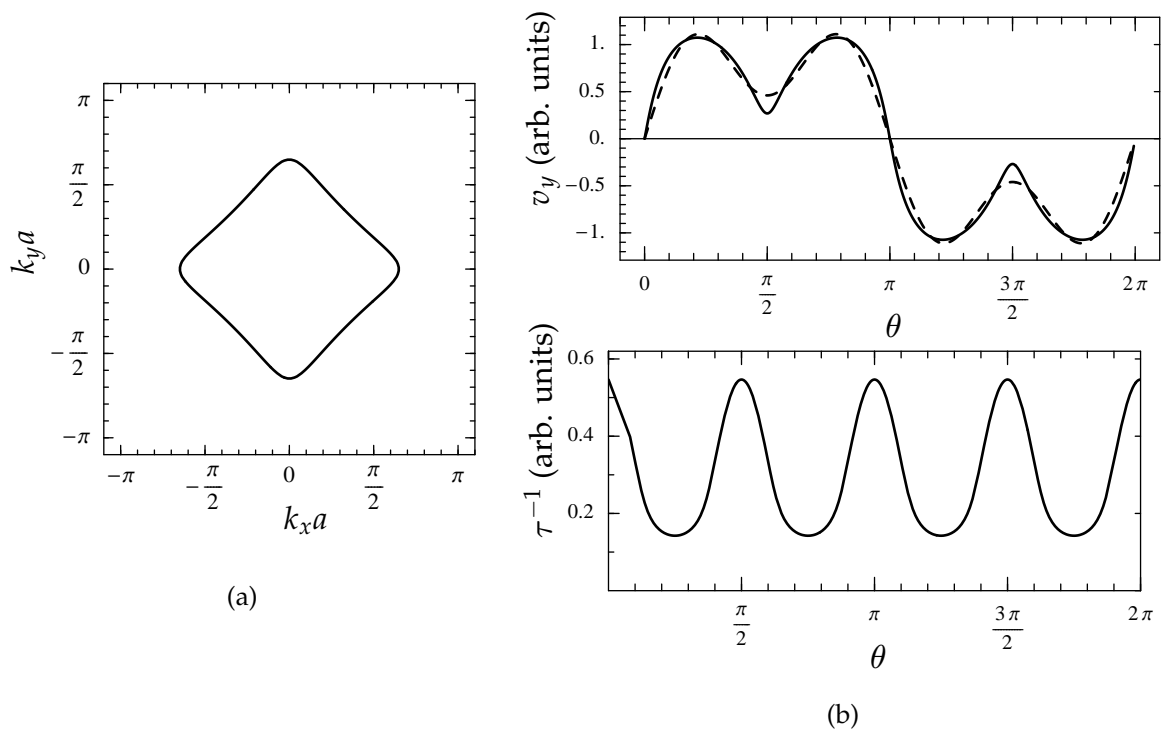
Figure 2.9: Illustration of properties of a small-angle scattering model with parameters matching that of Varma and Abrahams [21]. (a) Fermi surface, according to Eqn 2.26 with $\epsilon_F = -0.19$ (translated from real centre at (π, π)) (b) Top: Fermi velocity component v_y around the Fermi surface (solid line), compared with $\sin\theta - 0.54\sin 3\theta$ used in Ref. [21] (dashed line). Bottom: Anisotropic scattering rate $\tau^{-1}(\theta)$ at 100K.

(a) Resistance   (b) Hall angle   (c) Magnetoresistance
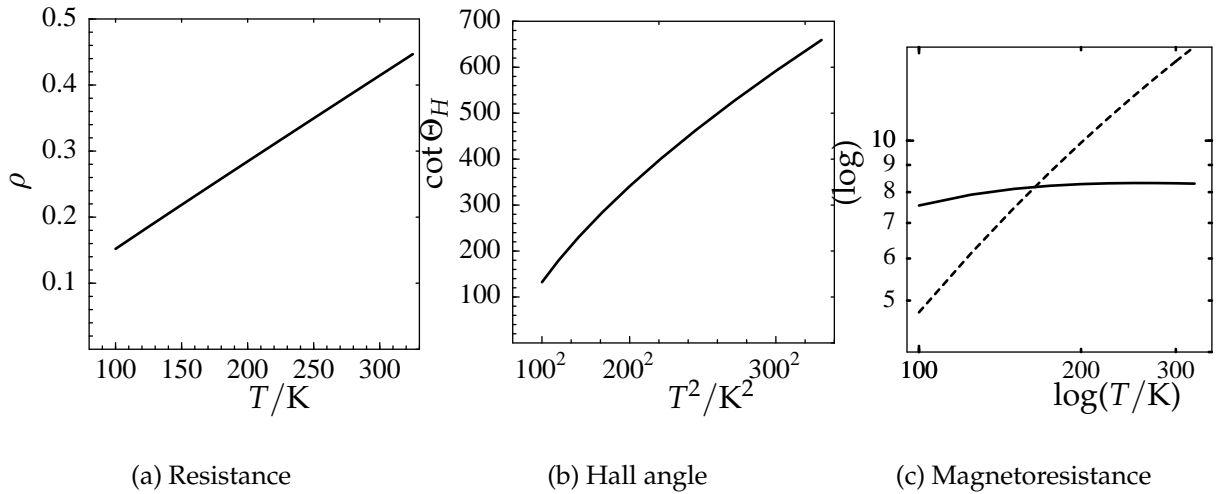
Figure 2.10: Graphs of the results of calculations with parameters matching the model of Varma and Abrahams [21]; other parameters in fact give very similar results sufficiently near particle-hole symmetry. The vertical axes have arbitrary units. (a) The resistance obeys a good linear-T law. (b) The Hall angle is acceptably close to having a T^2 dependence. (c) Log-log graph of the magnetoresistance. $(\Delta\rho/\rho)\rho^2$ (solid line) does not change significantly with temperature — Kohler's rule is obeyed, unlike the cuprates. $(\Delta\rho/\rho)\cot^2\Theta_H$ (dashed line) on the other hand does vary with temperature, whereas this quantity is thought to be T-independent in the cuprates (a "modified Kohler's rule").

hams' model produces a resistance which always obeys Kohler's rule (Fig. 2.10(c)), in conflict with experiments on the cuprates. In the next section I shall discuss our findings and place them within the analytical framework described in §2.4.2.

2.5   Discussion

We can understand our results in terms of the series expansion proposed in Eqn 2.21, Eqn 2.22 and Eqn 2.23: in effect, small-angle scattering processes generate extra terms at higher orders in the marginal Fermi liquid scattering rate τ_M^{-1}, that lead to new temperature dependences. If these new terms dominate, the temperature dependences of transport properties may be anomalous. The numerical calculations of the previous section have established where this is possible, and I shall compare my findings with those of Abrahams and Varma [21]. First, for the resistivity, we are in agreement with Abrahams and Varma that small-angle scattering has little effect, and the original linear-T term always dominates.

2.5.1   Hall angle

For the Hall angle, however, to reproduce the experimentally observed T^2 dependence it is necessary that the conventional term is small and that Eqn 2.22 is dominated by

31

the new term at first order (circled). We find that the only circumstance in which this can happen is when the Fermi surface is tuned to a particle-hole symmetric one where the conventional term vanishes. Abrahams and Varma [21] claim the new term can be significantly larger than the conventional term, enough to dominate. In fact their calculations lie very close to particle-hole symmetry: their Fermi surface is characterized with a parameter ρ, which they choose to be $\rho = 0.54$; particle-hole symmetry occurs at $\rho = 1/\sqrt{3} \sim 0.577$.

Furthermore, our calculations show that deviations from particle-hole symmetry quickly produce a large variation in the Hall angle temperature exponent, in contrast to the experimental situation where changes with doping are slight [28, 45]. However, we have assumed a naïve rigid band model, and there may be correlation effects that pin the Fermi surface to exact particle hole symmetry [46], so this sensitivity does not preclude this model. Hence we consider the magnetoresistance.

2.5.2   Magnetoresistance

I was unable to find a set of parameters for which our numerical calculations for the magnetoresistance could match experiment. The temperature dependence of the magnetoresistance always varied roughly as T^{-2} (the Drude-like inverse square of the linear-T dependence of the resistivity), in contrast to the experimentally observed T^{-4}. Whilst the exact law observed experimentally is still uncertain, Kohler's rule is certainly broken, and my calculations found no significant violations of Kohler's rule from a small-angle scattering model.

Varma and Abrahams never calculate the magnetoresistance directly, but instead extrapolate from the Hall angle that $\Delta\rho/\rho \sim \cot^{-2}\Theta_H$, which would give the experimentally observed temperature dependence. Varma and Abrahams cite the Ong construction [47] for this conclusion, but this is not valid for the types of scattering rate under consideration. Eqn 2.3 and Eqn 2.2 show that $\Delta\rho/\rho = -\Delta\sigma^{xx}/\sigma^{xx} - \cot^{-2}\Theta_H$; if the second term dominates, the magnetoresistance would have the wrong sign, so the significant contributions must come from $\Delta\sigma^{xx}$. To match the experimental T^{-4} dependence, Eqn 2.23 must be dominated by the *second* order term (circled), which is one higher than that for the Hall angle. Both the zeroth and first order terms need to be insignificant in comparison to the second order term; and we can never win in a way analagous to the Hall angle, and have the lower order terms vanish for a special case, as it can be shown analytically that the zeroth order term is *positive definite*.

So, although the small-angle scattering model can reproduce the temperature dependence of the experimentally observed Hall angle for a specially *tuned* Fermi surface,

the temperature dependence of the magnetoresistance does not match experiment and no further tuning of the Fermi surface can help.

2.6 Summary

Varma and Abrahams proposed a phenomenological transport model for the cuprates, that they argue can account for the anomalous temperature dependences of in-plane magnetotransport properties. This is an anisotropic scattering model, where scattering rates are large in certain directions as observed by ARPES. These anisotropic processes are allocated to small-angle scattering, where the electrons are highly likely to be scattered to the same direction they were originally moving in. Intuitively, it seems unlikely that these processes can have dramatic effects, and indeed this is generally the case.

Our work (which has been published [15]), has involved studying Varma and Abrahams' small-angle scattering model by means of a numerical solution to the Boltzmann transport equation. Given a linear-T resistivity, the anomalous T^2 temperature dependence of the Hall angle observed in the cuprates can be reproduced by the small-angle scattering model, but only for a specially tuned Fermi surface — near particle-hole symmetry where there is no conventional Hall effect. However, the magnetoresistance produced by the model is always conventional, and never breaks Kohler's rule, whereas experiments on the cuprates demonstrate an unambiguous violation. Varma and Abrahams did not calculate the magnetoresistance directly, and a major conclusion of the work presented here is the importance of the magnetoresistance as a probe to distinguish between transport theories.

Interestingly, the conclusion of Varma and Abrahams that the Hall scattering rate τ_H^{-1} originates from the square of the resistivity scattering rate τ_{tr}^{-1} fits in with recent experiments, even though we have shown here that it cannot be explained by small-angle scattering. Woods *et al.* [48] show a relationship between ρ and $\cot \Theta_H$ from experiments irradiating $Nd_{2-x}Ce_xCuO_4$. Optical conductivity or AC Hall effect measurements do not see the expected Lorentzian shape, but their observations are instead consistent with the normal scattering rate (together with a frequency term) entering squared [49, 50]. These experiments are believed to be crucial for progressing our understanding of transport in the cuprates.

Classical Boltzmann transport theory can only produce additive corrections to conductivities, and cannot naturally produce the multiplicative forms proposed by Anderson. There are many strange features of the electron liquid in the cuprates in the normal state near optimal doping, and it seems likely that the explanation for the anomalous

transport properties does not lie within the single electron-like quasiparticle picture. Understanding the properties of this non-Fermi liquid remains a key to deciphering the unconventional normal-state properties of the cuprates, and even their supercond- uctivity. The remainder of this thesis is devoted to the investigation of a microscopic model which leads to insight into the detailed behaviour of the quasiparticles in such a strongly correlated fluid, and provides hints as to the origin of the anisotropic behav- iour which underlies the models studied within this chapter.

Chapter 3

DYNAMICAL MEAN FIELD THEORY

Rhythm, said Stephen, is the first formal esthetic relation of part to part in any esthetic whole or of an esthetic whole to its part of parts or of any part to the esthetic whole of which it is a part.

JAMES JOYCE
A Portrait of the Artist as a Young Man [51]

3.1 Introduction

Over the last decade, understanding of the strongly correlated metallic state has progressed significantly due to Dynamical Mean-Field Theory (DMFT) [52]. Materials which lie near the Mott metal-insulator transition, such as some transition metal oxides, exhibit a range of peculiar phenomena which have eluded understanding. Theorists have struggled to solve microscopic models for these materials, such as the Hubbard model, and DMFT provides a well-founded, successful approximation within which a many-body interacting system can be investigated in its entirety.

The difficulty of studying strongly correlated systems is that the electrons are intermediate between the well-understood limits of localized and itinerant nature. Perturbation theory starting from either limit generally fails because there is no small parameter; a wide range of energy scales is important. DMFT, in effect, solves a compromise situation where electrons are localized over short timescales, but itinerant over long timescales. It is inherently non-perturbative, and can easily be shown to be exact in both the non-interacting (itinerant) limit and in the atomic (localized) limit (see §3.3). In §3.5 I shall mention some of problems DMFT has successfully tackled, particularly focusing upon the Mott metal-insulator transition.

In DMFT, local dynamics are recreated fully on a single site of the crystal lattice, which is coupled to a self-consistent "bath" representing the rest of the lattice. This description was first derived from the limit of infinite dimensions [53] (see §3.3.2), where such a representation is exact. In lower numbers of dimensions, it is an approximation. Any model of a strongly correlated system must make drastic approximations for solvability, and often in their results it is hard to distinguish real physics from artifacts of the model. However, for DMFT, not only do we know precisely what approximation is being made, but we know also that the limit of high dimensions may have physical relevance. For example, if DMFT does not reproduce physical reality and there is a phase transition lying between three and infinite dimensions, we could ask where it occurs, and whether it is accessible in materials a with large coordination number.

I shall now give a qualitative description of the DMFT procedure; a more detailed explanation is given in §3.2. Concentrating upon a single site in the crystal lattice, there are 4 possible local states on this site: $|0\rangle$, $|\uparrow\rangle$, $|\downarrow\rangle$, $|\uparrow\downarrow\rangle$. Electrons can move on and off the site, and the effect of the rest of the lattice is encoded in a *Green's function* which gives the probability[1] of an electron leaving any of these states, and then coming back to one of them after a given time. As a mean-field approximation, we imagine every site to be identical, and each has the same Green's function. Such a Green's function

---

[1]Strictly, the accumulated quantum mechanical phase.

36

must be *self-consistent*: fluctuations from one site must correspond in some way with those of surrounding sites. The construction of self-consistency conditions for local Green's functions forms the core of DMFT.

Returning to the four states mentioned above, if the electrons can be considered independent (non-interacting), the states are indistinguishable and we know the correct mean-field Green's function for the single site, and also know exactly the Green's function solution for the whole lattice. We wish to add a Coulomb repulsion, and do this by energetically penalizing the last state $| \uparrow\downarrow \rangle$ because it has two electrons on the site. DMFT works by comparing Green's functions for just the single site with and without this repulsion, and uses the difference to estimate how the non-interacting solution for the whole lattice should be changed when interactions are present everywhere. It is a key assumption of DMFT that the effect of interactions is the same everywhere across the whole system (quantitatively, a local *self-energy*), and this is where the approximation of DMFT is made.

Self-consistency is achieved by averaging all the sites in this constructed interacting system, and checking that the average site is identical to the single site we started with.[2] We had to start from an arbitrary guess for the single-site Green's function, and this guess must be adjusted until it is self-consistent. The physics we investigate is that of the resulting constructed self-consistent interacting system.

Mathematically, we need to choose a representation for the completely arbitrary single site Green's function, and we do this by imagining there to be a "bath" surrounding the single site, providing a spectrum of excitations for the system to explore. This bath can be represented in many different ways, providing different manifestations of DMFT. The most important representation is that of an *impurity model* where the bath consists of (non-interacting) sites connected to the original, impurity, site. Many of the techniques developed in the past for studying impurity models [54] can be used within DMFT (see §3.3.3).

A down-side of DMFT is that the bath needs an infinite number of degrees of freedom to represent the Green's function exactly; an impurity model would have to have an infinite number of sites. Clearly, such a system is not in practice solvable on a computer, and so further approximations have to be made. There are a variety of techniques researchers have used, and I shall discuss some in §3.4. Chapter 4 describes in detail the "two-site" approach which will be my choice of technique.

---

[2]It is not the same in general, because the "averaging" procedure is unavoidably different from the initial procedure for spreading the influence of the interactions across the lattice.

3.2　The pure DMFT procedure

There are many ways of understanding or deriving DMFT and its self-consistency equations, and in this section I shall derive the self-consistency equations in a way similar to the "effective medium" description in Ref. [52], which emphasizes DMFT's relationship as a dynamical extension of Hartree–Fock mean-field theory. The outcome is the same as a formal expansion in the limit of a large number of dimensions (see §3.3.2).

Let us focus on a single site of the Hubbard model (Eqn 1.1). Later we will assume that all sites are identical. We nominally integrate out all the other sites in the lattice, leaving an effective action for the single site. The Hamiltonian contains an on-site Coulomb repulsion U, which clearly must be retained; but the hopping terms t_{ij} no longer appear explicitly, but are captured in a Green's function, and will only appear directly in self-consistency conditions. In the coherent state path integral formalism [55], the effective action for our single site is:

$$S_{\text{eff}} = -\int_0^\beta d\tau \int_0^\beta d\tau' \, c_\sigma^\dagger(\tau) \mathscr{G}_0^{-1}(\tau - \tau') c_\sigma(\tau') + U \int_0^\beta d\tau \, c_\uparrow^\dagger(\tau) c_\uparrow(\tau) c_\downarrow^\dagger(\tau) c_\downarrow(\tau). \quad (3.1)$$

The function $\mathscr{G}_0(\tau - \tau')$ (spin-less for simplicity) completely encapsulates the dynamics of electrons leaving the site at imaginary time τ' and returning at an imaginary time τ'. We allow an electron to pick up an arbitrary quantum mechanical phase in the intervening time. The Hamiltonian was not Gaussian, so we cannot in practice integrate out all the other sites in the lattice, and we do not know the function $\mathscr{G}_0$ *a priori*. However, fluctuations according to this function will be to neighbouring sites, that we are reckoning to be the same as the original site, and this allows the construction of self-consistency conditions: $\mathscr{G}_0$ can be constrained.

Let us suppose that we can exactly represent the effects of introducing a U term to some arbitrary $\mathscr{G}_0$, and calculate the many-particle Green's function

$$G_{\text{local}}(\tau - \tau') \equiv -\langle Tc(\tau) c^\dagger(\tau')\rangle_{S_{\text{eff}}} . \quad (3.2)$$

G_{local} is in effect an interacting Green's function originated from the "non-interacting" Green's function $\mathscr{G}_0$, and so we can write down a Dyson's equation [56], defining a *self-energy* Σ_{local},[3] in Fourier-transformed Matsubara-frequency space:

$$G_{\text{local}}^{-1}(i\omega_n) = \mathscr{G}_0^{-1}(i\omega_n) - \Sigma_{\text{local}}(i\omega_n) . \quad (3.3)$$

---

[3]If one works diagrammatically, it turns out that the effect of interactions can be factored out, and separated from the non-interacting Green's function as the self-energy.

We now make use of the DMFT *ansatz* that the self-energy is assumed to be spatially homogeneous, but retains a frequency dependence: the true self-energy $\Sigma(i, i\omega_n)$ (or Fourier-transformed to $\Sigma(\mathbf{k}, i\omega_n)$) becomes $\Sigma_{local}(i\omega_n)$. So, we can construct a trial interacting Green's function G_{latt} for the extended lattice by combining the non-interacting lattice Green's function,

$$G_{0,latt}^{-1}(\mathbf{k}, i\omega_n) = i\omega_n + \mu - \epsilon_{\mathbf{k}} , \tag{3.4}$$

with the local self-energy $\Sigma_{local}(i\omega_n)$, using a second Dyson's equation:

$$G_{latt}^{-1}(\mathbf{k}, i\omega_n) = G_{0,latt}^{-1}(\mathbf{k}, i\omega_n) - \Sigma_{local}(i\omega_n)$$
$$= i\omega_n + \mu - \epsilon_{\mathbf{k}} - \Sigma_{local}(i\omega_n) . \tag{3.5}$$

G_{latt} is a trial function because $\mathscr{G}_0$ was arbitrary, and we need to formulate a self-consistency condition to constrain it. To do this, we need to know what is going on locally, so we find the on-site component of G_{latt}, *i.e.* at $\mathbf{R} = 0$, as a Fourier transform: $G_{latt,ii}(i\omega_n) = \sum_{\mathbf{k}} G_{latt}(\mathbf{k}, i\omega_n)$. The DMFT self-consistency requirement is that this local Green's function is the same as the interacting Green's function of the local effective action:

$$G_{local}(i\omega_n) \doteq \sum_{\mathbf{k}} G_{latt}(\mathbf{k}, i\omega_n) , \tag{3.6}$$

where the $\mathbf{k}$-sum is normalized, and I have used the symbol $\doteq$ to denote that the quantities should be made self-consistent. This is a functional condition and sufficient to constrain the function $\mathscr{G}_0(i\omega_n)$, arbitrary to start with. $\mathscr{G}_0(i\omega_n)$ should be iteratively adjusted until the Green's functions in Eqn 3.6 are matched. The condition can be rewritten without the self-energy explicitly present, to give a more succinct self-consistency condition for $\mathscr{G}_0$ in terms of the Green's function resulting from the effective action, G_{local}:

$$G_{local}(i\omega_n) \doteq \sum_{\mathbf{k}} \frac{1}{i\omega_n + \mu - \epsilon_{\mathbf{k}} - \Sigma_{local}(i\omega_n)}$$
$$= \sum_{\mathbf{k}} \frac{1}{i\omega_n + \mu - \epsilon_{\mathbf{k}} - (\mathscr{G}_0^{-1}(i\omega_n) - G_{local}^{-1}(i\omega_n))}, \tag{3.7}$$

(from Eqn 3.6 and Eqn 3.5). Dynamical Mean-Field Theory can be summarized by Eqn 3.7, Eqn 3.1 and Eqn 3.2 together. Fig. 3.1 shows the self-consistency procedure in the form of a flow chart. When self-consistency has been achieved, the lattice Green's function with the local self-energy, $G_{latt}(\mathbf{k}, i\omega_n)$ is the physically meaningful correlation function, and the output from DMFT by which the solution will be characterized.

So, to summarize, we constructed an effective single-site action with an arbitrary
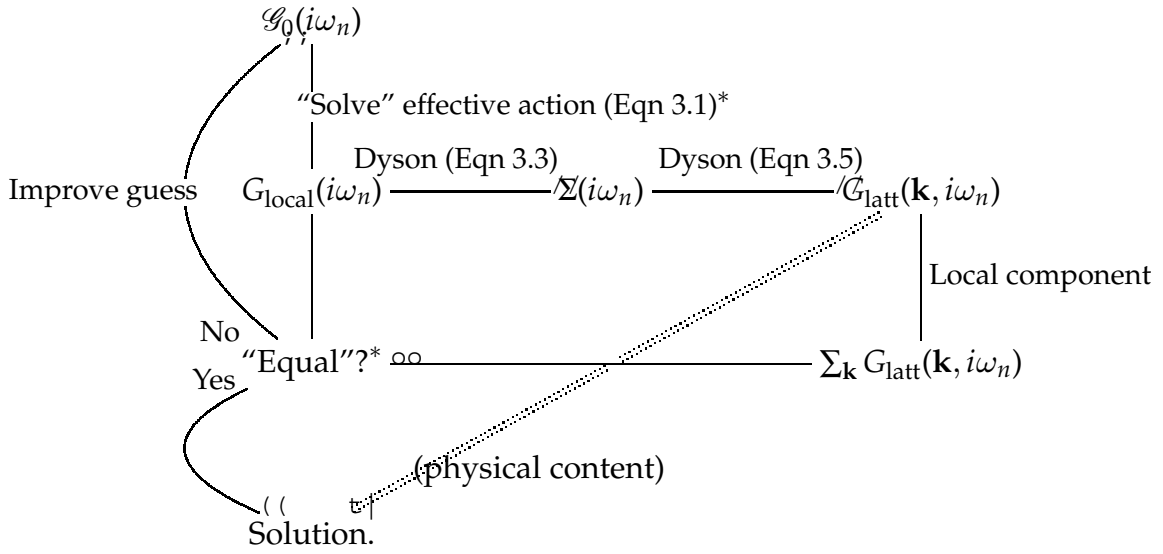
Figure 3.1: Flow chart showing the pure dynamical mean-field theory self-consistency procedure. The stages indicated with an asterisk cannot be implemented exactly and must be approximated.

dynamical field representing fluctuations of electrons away from that site. Solving this effective action yields a frequency-dependent self-energy which is combined— uniformly in space— with the non-interacting Green's function for the extended lattice, to give a trial interacting Green's function for the extended lattice. Finally, the scheme must be self-consistent, and we achieve this by requiring that the local Green's function of the extended lattice (containing the local self-energy) is the same as the interacting Green's function for the single site, and this constrains the initial dynamical field.

3.3 Discussion

This section contains elaboration on some elements of the previous section. I shall develop some intuition about DMFT (§3.3.1), describe the the more rigorous formulation of DMFT as an infinite dimensional limit (§3.3.2), and discuss the equivalence of the effective action with an impurity model (§3.3.3), a mapping which underlies several approaches to solving the DMFT equations.

Dynamical field   Often the picture of DMFT in terms of the Green's function $\mathscr{G}_0$ is best replaced by describing the arbitrary adjustable part of the local action as a dynamical field $\Delta(i\omega_n)$, with the relationship $\mathscr{G}_0^{-1}(i\omega_n) = i\omega_n + \mu - \Delta(i\omega_n)$. $\Delta(i\omega_n)$ encapsulates the ability of the local model to represent fluctuations, and appears in later equations, such as (for Eqn 3.3):

$$G_{\text{local}}^{-1}(i\omega_n) = i\omega_n + \mu - \Delta(i\omega_n) - \Sigma_{\text{local}}(i\omega_n) \ . \tag{3.8}$$

DMFT can represent the atomic limit $t_{ij} = 0$ exactly, as it corresponds to $\Delta(i\omega_n) = 0$, where sites are completely decoupled. Conversely, the non-interacting limit $U = 0$ can be trivially represented within DMFT by setting $\Sigma_{\text{local}}(\omega) = 0$.

Spin   All the Green's functions described above had a spin index which was omitted for notational simplicity. The self-consistent procedure should be carried out separately for each spin, and the two spins are coupled together only at the stage of solving the local action, via the Hubbard U term.

Frequencies   In later chapters I shall be only concerned with zero temperature properties, and shall therefore use the analytic continuation from Matsubara frequencies to real frequency: $i\omega_n \to \omega - i\delta$. In some calculations, it will be necessary to retain a small δ, but in general I shall omit it from equations. I shall also drop the "local" subscript from $\Sigma_{\text{local}}(\omega)$ as there is only one self-energy.

3.3.1   Intuition

Examining Eqn 3.7, we may deduce that the DMFT interacting lattice Green's function $G_{\text{latt}}(\omega)$ can be written rather simply in terms of the local non-interacting lattice Green's function $G_{0,\text{latt,local}}(\omega)$:

$$G_{\text{latt}}(\omega) = G_{0,\text{latt,local}}(\omega - \Sigma_\sigma(\omega)) , \quad \text{where} \quad G_{0,\text{latt,local}}(\omega) = \sum_{\mathbf{k}} \left[\omega + \mu - \epsilon_{\mathbf{k}}\right]^{-1} ; \quad (3.9)$$

we have effectively made the transformation $\omega \to \omega - \Sigma(\omega)$. Without the mean-field approximation, we would have $\Sigma(\mathbf{k}, \omega)$ and the transformation would not be possible. This gives some insight into the reduction DMFT has made and what is going on within its approximation. If Σ fluctuates significantly, the effective ω will pass back and forward through the non-interacting band, therefore making several new bands; it is these that form the Hubbard bands, for example.

We can rewrite the sum in Eqn 3.7 as an integral, with the non-interacting lattice Green's function written in terms of the non-interacting density of states $\rho_0(\omega)$:

$$G_{\text{lat}}(\omega) = \int_{-\infty}^{+\infty} \frac{\rho_0(\epsilon) \mathrm{d}\epsilon}{\omega + \mu - \epsilon - \Sigma_\sigma(\omega)} \tag{3.10}$$

(using the definition $\rho_0(\epsilon) \equiv \frac{1}{N} \sum_{\mathbf{k}} \delta(\epsilon - \epsilon_{\mathbf{k}})$). This identity demonstrates that the only information that DMFT knows about the lattice is its non-interacting density of states. It turns out that conventional DMFT is generally insensitive to the lattice type, apart

from special cases [57].

Hartree mean-field theory may be regarded as the static limit of dynamical mean-field theory: it allows a self-energy that is not frequency-dependent, typically $\Sigma = Un$, where n is the band filling, and momentum-dependent quantities can be included more easily than in DMFT. The inclusion of fluctuations is crucial, however; for example, the Stoner criterion for magnetism that Hartree mean-field theory predicts is wrong, vastly overestimating the region of stability for magnetic order when compared with DMFT (see §4.4 and Chapter 6).

3.3.2   Infinite dimensions

Although the preceding section (§3.2) presents DMFT as simply a local mean-field approximation scheme, the theory results from an entirely controlled series expansion in $1/d$, for spatial dimension d. DMFT is exact in infinite dimensions, and in fact the local effective action above (Eqn 3.1) can be derived rigorously in this limit: non-local corrections can be shown to appear only at a higher orders in $1/d$. Ref. [52] gives a detailed description of rigorous derivations of the DMFT equations; for example, from a "cavity" approach, analogous to the Weiss theory of magnetism. It also shows how perturbation theory is local in infinite dimensions, giving a formal expansion in $1/d$.

The infinite dimensional limit can be understood quite simply, in fact. As the dimensionality d is increased, the electron has many possible directions to go in, and the probability of it returning to its starting site becomes vanishingly small, so the problem can be formulated locally. Quantitatively, it is necessary to scale the hopping $t \sim 1/\sqrt{d}$ so that the kinetic energy in the Hamiltonian has the same effective magnitude with respect to the potential energy, otherwise t would completely dominate over U. Non-local contributions to the action contain more hopping terms and thus vanish in the limit $d \to \infty$.

Although it might appear that the infinite-dimensional limit is unphysical, it is nevertheless a completely controlled approximation; unlike many other approaches to strongly correlated systems, the exact assumptions are of the theory are known, and sum rules etc. are likely to be obeyed. If results show features of the approximation and not of the real physical system, this is still interesting, because it means that physics in infinite dimensions is different; questions can be asked such as where the transition might be. Since many crystals have coordination numbers as high as twelve, perhaps the effective value of $1/d$ is quite small and such a transition may be practically accessible.

DMFT can be extended to finite dimensions by including terms of order $1/d$ etc.,

and formally this produces a coupled pair of self-consistency schemes. [58, 52] The focus of this thesis, however, will be on "cluster" DMFT (see Chapter 5), which is in effect also a finite dimensional extension, without constituting a formal expansion in $1/d$; instead it allows lattice geometry to play a rôle.

3.3.3   Impurity models

Dynamical mean-field theory is often studied through an *impurity model*, and such a representation will underlie several approaches to solving the DMFT equations presented later. An impurity model is one possible realization of the effective action in Eqn 3.1, which we hope to use to calculate the exact local interacting Green's function. Let us consider a Anderson impurity model with a Hamiltonian

$$\mathcal{H} = \sum_{i\sigma} \epsilon_i a_{i\sigma}^\dagger a_{i\sigma} + \sum_{i\sigma} V_i(a_{i\sigma}^\dagger c_\sigma + c_\sigma^\dagger a_{i\sigma}) - \mu \sum_\sigma c_\sigma^\dagger c_\sigma + U c_\uparrow^\dagger c_\uparrow c_\downarrow^\dagger c_\downarrow \qquad (3.11)$$

(see also Eqn 5.14 in §5.3). An impurity site (with creation operator $c_\sigma^\dagger$) has a Hubbard double-occupancy penalty U and is connected to a set of bath sites (with creation operators $a_{i\sigma}^\dagger$, with i labelling the sites). The energy levels ϵ_i and couplings V_i for each site parametrize the dynamical field and are to be constrained by self-consistency conditions. The label i is abstract and unconnected with the extended lattice index: the bath sites are there to model separately the dynamics of an electron moving off the impurity site. If these bath sites are integrated out, the action is identical to Eqn 3.1 with

$$\mathcal{G}_0^{-1}(i\omega_n) = i\omega_n + \mu - \sum_i \frac{V_i^2}{i\omega_n - \epsilon_i} \ . \qquad (3.12)$$

So for an impurity model, the dynamical field $\Delta(i\omega_n) = \sum_i \frac{V_i^2}{i\omega_n - \epsilon_i}$. If there are an infinite number of sites, one can choose a set of poles and residues $\{\epsilon_i, V_i\}$ to reproduce any Green's function and hence the mapping from DMFT to an impurity model is exact. However, when infinitely sized the impurity model is clearly impossible to solve computationally; the exact single-site action remains intractable. Some approximation must be made, such as truncating to a finite-sized bath (see §3.4.2).

   An advantage of the impurity model mapping is that the Anderson impurity model has been studied extensively in the past [54]. Although general understanding of the physics of the Anderson model is not directly useful since DMFT requires a complete solution of an arbitrary model, there are several techniques for the Anderson impurity model which can be adapted for DMFT, such as the numerical renormalization group method (see §3.4.2).

3.4   Methods of solution

Unfortunately, the pure DMFT procedure as described in §3.2 cannot be achieved exactly in practice, for two separate stages. First, solving the local effective action for the local Green's function (Eqn 3.1, Eqn 3.2) remains intractable; whilst we have reduced the complexity of the Hubbard Hamiltonian to a single site, it still has an infinite number of degrees of freedom that parametrize the whole function $\mathscr{G}_0(i\omega_n)$. Further approximations have to be made (in addition to the DMFT assumption of local self-energy), and there are a variety of possibilities which I shall discuss below.

Second, the self-consistency condition (Eqn 3.6 or Eqn 3.7) involves matching two *functions*, giving an infinite number of degrees of freedom to be compared. With an approximated effective action however, there are a finite number of adjustable parameters, and the Green's functions cannot now be made exactly the same. To match them, there is a choice to be made of a sensible set of criteria, generally equal in number to the degrees of freedom of the effective action, and also how to optimally improve the (initially arbitrary) function $\mathscr{G}_0(i\omega_n)$ for the next iteration. If one chooses to work on the Bethe lattice (see Appendix B), the **k**-sum in Eqn 3.7 can be carried out analytically and the equation rearranged to give a new $\mathscr{G}_0$ explicitly: $\mathscr{G}_0^{-1}(i\omega_n) = i\omega_n + \mu - t^2 G_{\text{local}}(i\omega_n)$ (Eqn B.11). There will still remain the problem of choosing the parameters of the approximate effective action to best represent this function, though.

The following sections contain descriptions of two major classes of approximation scheme for the solution of the DMFT self-consistency equations. Quantum Monte Carlo is probably the most widely used; Exact Diagonalization can be used as part of many schemes, and indeed underlies the technique I shall ultimately use. There are many other techniques which have been applied to tackle the DMFT equations [52] (for example, Iterated Perturbation Theory [59] which extrapolates between the small and large U limits) but I shall not describe them further here.

3.4.1   Quantum Monte Carlo

Quantum Monte Carlo (QMC) is probably the most commonly used method for solution of the DMFT equations. The scheme was developed independently by Jarrell [60], Rozenberg, Zhang and Kotliar [61], and Georges and Krauth [62], based upon the work of Hirsch and Fye on impurity models [63]. To calculate G from $\mathscr{G}_0$ using the action S_{eff}, first imaginary time is discretized, turning the integrals into sums. Secondly, the quartic term is decoupled with a Hubbard–Stratonovich transformation, introducing an auxiliary field consisting of Ising-like spins $s_i \in \{+1, -1\}$. Solving the effective action for the interaction Green's function has now reduced to summing over all possible

sets $\{s_i\}$, and this is done in practice by Monte Carlo sampling. The Bethe lattice can provide the self-consistent link back to $\mathcal{G}_0$ (Eqn B.11).

The technique has many successes and has a great deal of flexibility for dealing with more complex Hamiltonians. However, there are disadvantages which make it unsuitable for our purposes. First, low temperatures are difficult to access, since τ is discretized and low temperatures correspond to more time slices. Second, physical and experimentally significant quantities are real frequency functions (the density of states and spectral function); QMC only produces $G(i\omega_n)$, which needs to be analytically continued. This process is not well-defined since the functions are not complete, and difficult in practice. It is possible via maximum entropy methods for example; some authors resort to extrapolating results from the first two Matsubara frequencies [64].

3.4.2   Exact diagonalization

The exact diagonalization technique (ED) [65, 66] is based upon the representation of the effective action by an impurity model (§3.3.3) with a *finite* number of sites. This approximate Hamiltonian can only reproduce limited forms of $\mathcal{G}_0$, but it can be diagonalized exactly if there are not too many sites: the Hamiltonian is rewritten as a matrix connecting different *many-particle* states, and all its eigenvalues and eigenvectors found. From these, we can construct the interacting Green's function by means of the Lehmann representation [56, 52]:

$$G(i\omega_n) = \langle Tc_0^\dagger c_0 \rangle = \frac{1}{\mathcal{Z}} \sum_{i,j} \left| \langle j | c_0^\dagger | i \rangle \right|^2 \frac{e^{-\beta E_j} + e^{-\beta E_i}}{E_i - E_j - i\omega_n} \, , \qquad (3.13)$$

where i and j are eigenstates with energies E_i, E_j, and $\mathcal{Z}$ the appropriate partition function. The simplest way of implementing the self-consistency condition (Eqn 3.6) is to work on the Bethe lattice and construct a new $\mathcal{G}_0$ as Eqn B.11 (automatically satisfying Eqn 3.7), and then somehow find the best set $\{\epsilon_i, V_i\}$ of bath parameters to represent this function in the impurity model (Eqn 3.12).

This method has proved successful, and does not suffer from some of the problems of QMC: zero temperature is easy, and there is no problem with calculating densities of states and other spectral quantities as Eqn 3.13, being analytic in $i\omega_n$, can be directly analytically continued. However, the computational difficulty of diagonalizing the impurity model Hamiltonian increases exponentially with its size; ~ 12 sites is the limit (fewer at finitesimal temperature). This lack of resolution leads to difficulty in accurately representing a new $\mathcal{G}_0$; typically, this is done blindly with a conjugate gradient algorithm, and when the functions have such different shapes, it cannot be reliable.

An alternative way to truncate the Hilbert space of the Hamiltonian is only to keep states that lie low in energy, and iterate; such an idea underlies the Numerical Renormalization Group (NRG) technique [67, 68], using procedures first developed for the Anderson impurity model.

A better-justified method is to give up hope of matching the Green's functions point-by-point, and carefully construct a set of physically-motivated criteria, each corresponding to a degree of freedom of the impurity model. These criteria are quantities that one should ensure are the same for both the local impurity and lattice Green's functions; for example, the electron filling. The simplest such method is Potthoff's "two-site" DMFT [69] in which the impurity model has just a single bath site. This technique has been surprisingly successful; I shall discuss it in Chapter 4 and the rest of this thesis will be based on it.

3.5   Some applications of DMFT

Dynamical mean-field theory has been applied to a huge number of different systems. Its most important success is understanding the Mott transition, and I shall describe this in detail below (§3.5.1). In the study of magnetism, DMFT has shown how the conventional Stoner picture significantly overestimates the extent of magnetism: order is destroyed by fluctuations [70]. Wahle *et al.* showed how a Heisenberg exchange interaction can stabilise ferromagnetic order within the Hubbard model [71], and the Curie-Weiss law can be derived within dynamical mean-field theory [72]. Other studies of magnetism include Refs. [73, 74, 75], and magnetic ordering will be studied later in this thesis (see §4.4 and §6.3.1).

Density functional theory has been a successful tool for modelling the fine details of real materials. It has generally depended on the rather crude assumptions of the Local Density Approximation (LDA) and its variants, but it has been possible to marry in the abilities of DMFT to deal rather well with strong correlations (*e.g.* in materials such as correlated oxides) with considerable success [76, 77]. Specific examples include the *ab initio* calculation of key features of the phase diagram of plutonium [78], and studies of finite-temperature magnetism in iron and nickel [79].

3.5.1   Mott transition

The Mott transition is a metal-insulator transition caused by correlations between electrons. A conventional insulating material has a band which is completely full, and there is an energy gap above it greater than T, so few free carriers can be excited and

conduction is difficult. In a Mott insulator, however, the repulsive interaction U between electrons causes a gap of order U to form in the *middle* of a band, and materials which should apparently be metals turn out to insulate (for example, NiO [80]).

Although the Mott insulating state itself is well-understood, its relationship to the phases surrounding it remains controversial: how might the transition from a metal take place, with changing doping levels or changing effective interaction strength? The Hubbard model (Eqn 1.1) often provides a theoretical starting point; its input parameters (at zero temperature) are the electron filling (or doping level) n and an interaction strength U, forming a (U, n) phase diagram within which such a Mott transition can be investigated. Phase transitions caused by correlations are exceedingly sensitive, and in a Mott transition, the resistivity of a material can change by many orders of magnitude with a tiny change to a control parameter. In practice, the transition is often complicated by other effects such as orbital ordering; for example, V_2O_3 (the onetime generic Mott insulator) is plagued by many subtle effects — although recently, doping this compound with chromium has yielded clearer phases [81].

Historically, there have been three apparently conflicting views of the Mott transition at half-filling ($n = 1$) for increasing interaction strength U. First was the picture of **Hubbard** [82], who described a metallic band splitting into two bands, the upper band corresponding to doubly-occupied sites. The bands are an energy U apart, and when U reaches a certain value they will leave a gap between them, and at half-filling the material will therefore be an insulator. Whilst the concept of double-occupation is local and does not naturally fall into a metallic picture, the general idea of Hubbard bands have stood up to scrutiny, as we shall see later. There is also clear experimental evidence for Hubbard bands; for example, Fujimori *et al.* [83] observed well-formed lower Hubbard bands via photoemission spectroscopy of d^1 oxides (and see also Fig. 7.13(a)).

The second view approaches the transition from the opposite limit, the metallic state. **Brinkman and Rice** [84] described how the metallic quasiparticle becomes gradually more impeded by correlations and its effective mass thus increases, and the bandwidth decreases; when the mass becomes infinite, the material is an insulator.

It is difficult to see how to reconcile these views, but DMFT calculations provided the answer: Fig. 3.2 shows the characteristic *three peak* structure [85] that emerges (see also Fig. 4.4). There is a narrow central quasiparticle band, together with two incoherent Mott–Hubbard bands centred at $\pm U$. When the interaction strength U is small there is just a single non-interacting band, and as U increases, the upper and lower Hubbard bands split off, as in the Hubbard picture. However, unlike the Hubbard picture, a portion of the central peak remains, and the system is still metallic. Upon increasing U further, the central peak becomes narrower, and thus heavier, as in the Brinkman–Rice
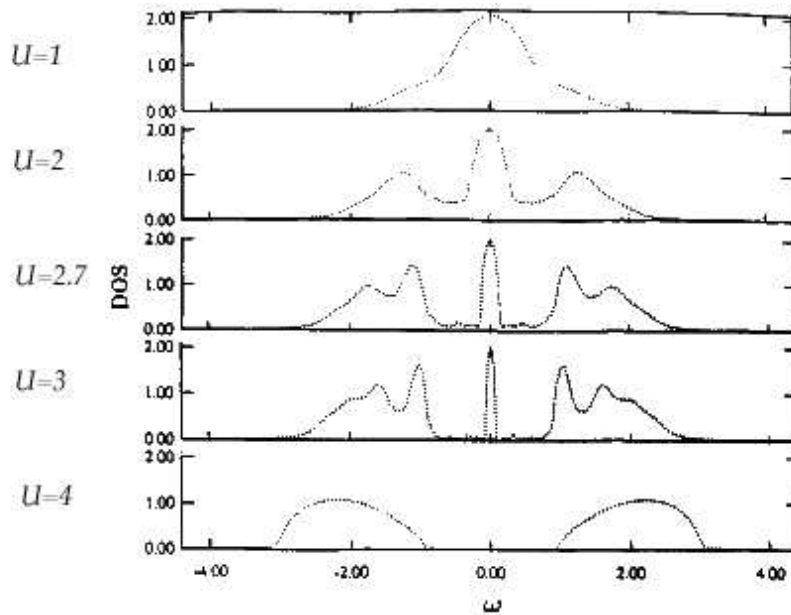
Figure 3.2: Density of states calculated by the iterated perturbation theory approach to DMFT, for various values of U (in units of $2t$), Fig. 3 of Ref. [59]. The spectrum has a three peak structure, consisting of the upper and lower Hubbard bands and a central quasiparticle peak, which gradually gets narrower. This vanishes at the transition, whereupon the material becomes insulating.

picture. Finally, it becomes delta-function-like and suddenly vanishes, leaving the two band Mott–Hubbard insulating picture remaining; at this point the system has become an insulator. The three peak structure can be interpreted in the time domain also: on long time scales (small energies) the electron is itinerant (central quasiparticle peak), but on short time scales (large energies), it is localized (Hubbard bands). The simultaneous observation of features at both large and small energy scales is only possible in a non-perturbative approach like DMFT.

Properties of the narrow quasiparticle peak agree with experiments on V_2O_3 [86] and $NiS_{2-x}Se_x$ [87], and DMFT predictions for the nature of the Mott phase transition have also been verified in V_2O_3 [81, 88]. Questions about the Mott transition still remain unresolved [89, 90, 91]; for example, some calculations show a coexistence region $U_{c1} < U < U_{c2}$. The two critical points correspond to the point when a gap initially forms (U_{c1}), and secondly when the central quasiparticle peak vanishes (U_{c2}); if the transition is approached from high U, the insulating solution persists down to U_{c1}, but from low U the metallic solution persists up to $U_{c2} > U_{c1}$. The hysteretic behaviour in experiments on V_2O_3 [81, 88] appears to verify this finding.

The third mechanism for a metal-insulator transition, due to **Slater** [92], is the appearance of antiferromagnetism, which could destroy the picture presented so far. At half-filling on an unfrustrated bipartite lattice, the Fermi surface is perfectly nested, *i.e.* there is a wave-vector $\mathbf{q}$ such that $\epsilon_{\mathbf{k}} = \epsilon_{\mathbf{k+q}}$. This means that there is an infinite

susceptibility to ordering at this wave-vector, and an infinitesimal interaction strength will cause ordering; a square lattice will go spontaneously antiferromagnetic. Each quasiparticle at $\mathbf{k}$ will hybridize with the one at $\mathbf{k} + \mathbf{q}$, generating a gap at the Fermi level, turning the metal into an insulator. The Slater antiferromagnetic insulator has a lower energy than the paramagnetic states described above, making the results of those calculations questionable as they do not concern the real ground state. Experimentally, as temperature is reduced, the antiferromagnetism will set in before any sign of the Mott physics described above. At present, this issue is not satisfactorily resolved by DMFT, but there has been progress.

At a first glance, conventional DMFT cannot deal with antiferromagnetism because of its local single site picture, but a crude representation may be made by mapping to the opposite spin on neighbouring sites in the self-consistency condition [93]; §4.4.2 contains such a calculation. However, effects of the geometry of the crystal lattice such as frustration are essential for understanding the interplay of antiferromagnetism and the metal-insulator transition, and to include such features a "cluster" approach to DMFT is necessary (see Chapter 5). Parcollet *et al.* [64] used a cluster DMFT approach on a model where the magnetism was frustrated by a next-nearest neighbour hopping, and concluded that the broad conclusions of the paramagnetic studies remain valid. However, features of the physics of the Mott transition and the unfrustrated Hubbard model off half-filling remain controversial, and the subject of scrutiny in the literature. A large portion of this thesis will be devoted to the development of a cluster DMFT method which is sufficiently computationally cheap to be able to access the entire phase diagram of the 2D Hubbard model with complete spectral information. The hope is that such a survey will begin to answer some of questions emerging from above, such as how the Mott transition might happen in the presence of antiferromagnetism (see §6.3.2 and §7.4).

3.6 Summary

A detailed description of dynamical mean-field theory has been given in this chapter. DMFT is a mean-field theory that includes the dynamics of the electrons via a self-consistency scheme. The theory is formulated in terms of two different Green's functions, one for an effective impurity model and one for the extended lattice, which share the same local self-energy. Self-consistency ensures that the on-site projections of the two Green's functions match each other. DMFT is exact in the limit of infinite coordination number, which gives the theory a rigorous basis; it has proved a versatile technique that had many successes in improving our understanding of strongly corre-

lated systems. The most notable is the three-peak picture of the Mott metal-insulator transition, synthesizing the pictures of Mott–Hubbard and Brinkman–Rice. DMFT is constantly being developed and remains at the forefront of current research.

Approximations are required to solve the interacting local problem at the core of DMFT. §3.4 described a few of the many possible approximations; it is crucial to choose a method of solution that is appropriate to the phenomena that one would like to investigate. In this thesis I am going to focus on a minimal "two-site" representation of the local problem (described in Chapter 4), so that the entire phase diagram of the 2D Hubbard model can be studied in detail on a normal computer. Calculational effort can redirected into extending DMFT to a cluster formulation (Chapter 5) so that a weak momentum-dependence can be included in the DMFT equations; questions such as the interplay of antiferromagnetism with the Mott transition are now possible subjects of investigation.

Chapter 4

TWO-SITE DMFT

"Well, if you knows of a better 'ole, go to it."

BRUCE BAIRNSFATHER[94]

51

4.1 Introduction

The previous chapter contained a description of dynamical mean-field theory (DMFT), an approach to strongly correlated electrons systems based upon a rigorous infinite-dimensional limit. To use DMFT in practice, some kind of approximation to its self-consistency equations is required, for which there is considerable flexibility. In this chapter I introduce what is probably the minimal possible implementation of DMFT, named "two-site" DMFT by Potthoff [69]. A rather drastic approximation is involved, but the results of two-site DMFT are surprisingly successful and can reproduce much of the physics of the Mott transition. It is proposed mainly as a kernel for extended versions of DMFT.

DMFT maps the interacting electron system onto a local model, that contains a set of "bath" states coupled to an impurity, and the bath is constrained self-consistently. In two-site DMFT, this bath is truncated to a *single site*, so the impurity model consists of just two sites. A straight Hubbard model with two sites allows the deduction of a surprising amount of Mott physics [95]; two-site DMFT adds the capabilities of DMFT self-consistency, and a remarkably good picture of the behaviour of interacting electrons emerges, with very little computational effort. The model succeeds because of its simplicity: a two-site model can be tackled analytically, and physical ideas can be used to motivate the self-consistency conditions, unlike conventional DMFT. The band filling and the shape of the quasiparticle peak in the density of states are the specific physical quantities examined in two-site DMFT.

The idea of reducing DMFT to the minimal two-site representation was investigated by initial workers in the field [96], but the first full published results were by Potthoff [69]. He showed that two-site DMFT produces a reasonable description of the Mott transition in comparison to much more sophisticated DMFT techniques (see §4.3.3). Satisfactory results are found for other properties of the Fermi liquid, the Luttinger sum rule, and thermodynamic consistency [69].

Philosophically, two-site DMFT can be regarded as the first step towards a DMFT implementation with more degrees of freedom, each corresponding to one of a larger set of physically-justified self-consistency conditions. DMFT with just a single degree of freedom becomes Hartree–Fock mean-field theory, where the single parameter used to self-consistently constrain the bath is the band filling, n: clearly an essential characteristic for a sane mean-field theory. In two-site DMFT a second degree of freedom is introduced, meaning that dynamics can be represented in a minimal, yet self-consistent, way. Properties of the quasiparticle peak, an essential parameter for the evolution of a Fermi liquid, may now be taken into consideration; and the result

is the appearance of a Mott transition. One could imagine building up a succession of more sophisticated such characteristics to examine, and reaching the complexity of other approaches to DMFT, but well-motivated physically instead of relying upon rather blind direct matching of Green's functions, used in typical exact diagonalization approaches (§3.4.2).

The next section (§4.2) contains a detailed derivation of the two-site DMFT self-consistency conditions, along the lines of Potthoff's paper [69]. We shall work only at absolute zero ($T = 0$); whilst finitesimal temperatures are possible to formulate within two-site DMFT, it is less likely to be reliable as more detailed, flexible spectra would be required. The practicalities for the implementation of the two-site DMFT self-consistency conditions and the calculation of all the necessary quantities are described in §4.3. I discuss the details of its paramagnetic solution in §4.3.3, verifying Potthoff's results. We wish to investigate the magnetic phase diagram of the Hubbard model; two-site DMFT can easily be extended to cover ferromagnetism (§4.4), and antiferromagnetism can also be represented, as I show in §4.4.1.

Whilst bare two-site DMFT does produce a credible phase diagram, it exhibits signatures of a struggle with the tiny phase space available (§4.4.2). However, our intention for two-site DMFT was not that it should stand alone, but should make up a reliable kernel for extensions to DMFT, as I shall discuss at the end of this chapter (§4.5). In Chapter 5 I will describe how to use two-site DMFT within one possible such extension: cluster DMFT.

4.2 Potthoff's "two-site" DMFT

This section contains an exposition of two-site DMFT as proposed by Potthoff [69]; I shall make frequent reference back to the conventional DMFT procedure as described in §3.2. The basis of two-site DMFT is the exact diagonalization technique (§3.4.2), with an impurity model consisting of two sites only — the bath is drastically simplified to just a single site. The first problem of DMFT mentioned in §3.4, dealing with the interacting effective action, is thus easily solved since the two-site model is easily diagonalized. DMFT self-consistency conditions for this model are derived below; the model has two degrees of freedom (per spin), and thus we require two conditions to constrain them (the second problematic stage mentioned in §3.4), which will be provided by band filling and properties of the quasiparticle at the Fermi level.

Let us start with the impurity model that will realize the effective action (Eqn 3.1).

The Hamiltonian (*c.f.* Eqn 3.11) is

$$\mathcal{H} = \sum_\sigma \epsilon_{c\sigma} \hat{a}_\sigma^\dagger \hat{a}_\sigma + \sum_\sigma V_\sigma(\hat{a}_\sigma^\dagger \hat{c}_\sigma + \hat{c}_\sigma^\dagger \hat{a}_\sigma) - \mu \sum_\sigma \hat{c}_\sigma^\dagger \hat{c}_\sigma + U\hat{c}_\uparrow^\dagger \hat{c}_\uparrow \hat{c}_\downarrow^\dagger \hat{c}_\downarrow \, , \tag{4.1}$$

where the impurity has creation operator $c^\dagger$ and the bath site $a^\dagger$, and we have included spin dependence explicitly. V_σ controls the hopping amplitude, or hybridization, between the two sites, and $\epsilon_{c\sigma}$ controls the balance of electrons on the two sites. Diagonalizing the non-interacting ($U = 0$) model gives the Green's function for spin-σ electrons on the impurity site ($c^\dagger$):

$$\mathcal{G}_\sigma^{-1}(\omega) = \omega + \mu - \frac{V_\sigma^2}{\omega - \epsilon_{c\sigma}}; \quad \text{so} \quad \Delta_\sigma(\omega) = \frac{V_\sigma^2}{\omega - \epsilon_{c\sigma}} \tag{4.2}$$

(*c.f.* Eqn 3.12 and also §3.3). The parameters $\{\epsilon_{c\sigma}, V_\sigma\}$ thus completely characterize $\mathcal{G}$; our self-consistency loop is begun with $\{\epsilon_{c\sigma}, V_\sigma\}$ set to arbitrary values, which will be changed at the end of the loop according to the self-consistency conditions.

The interacting Hamiltonian (Eqn 4.1, $U > 0$) is exactly diagonalized with respect to the many-particle basis of 16 states. Using the Lehmann decomposition (Eqn 3.13, see also Eqn 4.13), the interacting impurity Green's function $G_{\text{imp},\sigma}(\omega)$ is calculated, and the local self-energy can be extracted (using Dyson's equation, *c.f.* Eqn 3.3):

$$\Sigma_\sigma(\omega) = \omega + \mu - \frac{V_\sigma^2}{\omega - \epsilon_{c\sigma}} - G_{\text{imp},\sigma}^{-1}(\omega) \, . \tag{4.3}$$

We can now construct the lattice Green's function by introducing this self-energy to the non-interacting lattice Green's function, exactly as Eqn 3.5. Finally, for self-consistency, we want to match the local Green's function of the extending lattice with the local impurity Green's function (Eqn 3.6), *i.e.*

$$G_{\text{imp},\sigma}(\omega) \doteq G_{\text{lat},\sigma}(\omega) = \sum_{\mathbf{k}} \frac{1}{\omega + \mu - \epsilon_{\mathbf{k}} - \Sigma_\sigma(\omega)} \, . \tag{4.4}$$

We must now decide how to implement this self-consistency condition; clearly, it is not possible to exactly match the two functions using only two variables. The key to two-site DMFT's success is Potthoff's choice of physically motivated conditions to compare the functions by [69].

The first is that their electron fillings are the same, *i.e.*

$$n_{\text{imp},\sigma} \equiv \langle c_\sigma^\dagger c_\sigma \rangle \doteq n_{\text{lat},\sigma} \equiv -\frac{1}{\pi} \int_{-\infty}^0 d\omega \lim_{\omega \to \omega - i\delta} \text{Im} \, G_{\text{lat},\sigma}(\omega) \, , \tag{4.5}$$
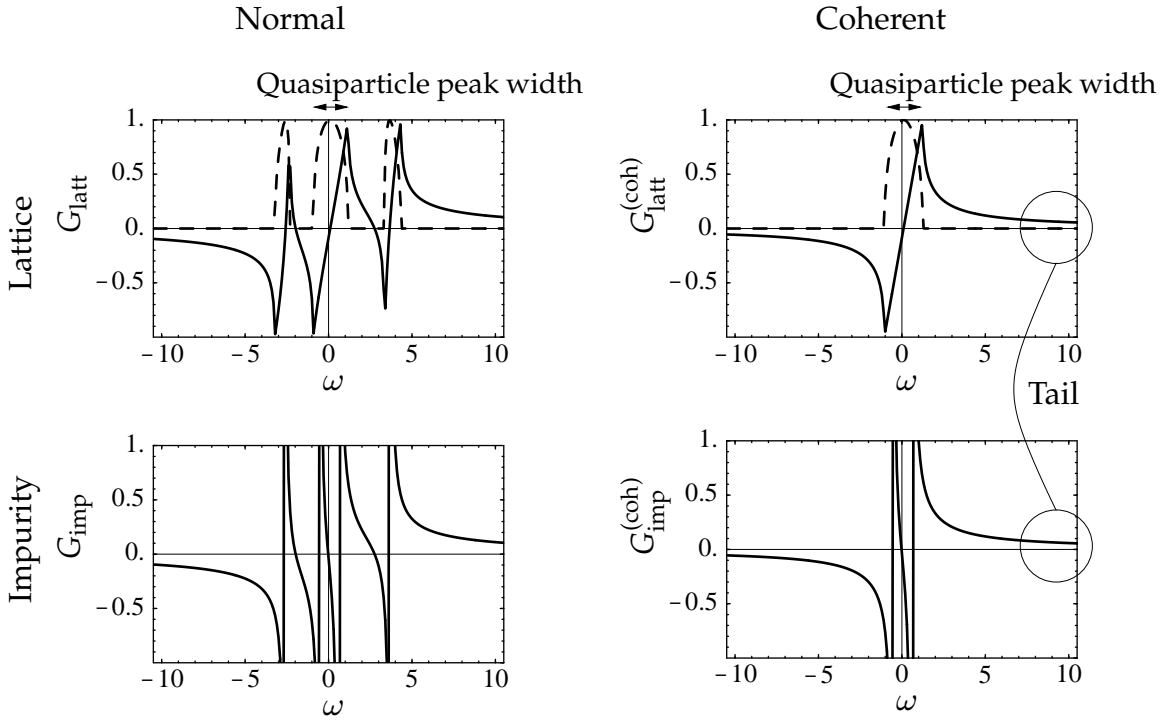
Figure 4.1: Self-consistent Green's functions for two-site DMFT at $U = 4.1t, n = 0.9$ on the Bethe lattice. The solid lines are the real parts, and the dashed lines the imaginary parts (for the impurity Green's functions these are δ-functions and not shown). The impurity and lattice Green's functions have the same filling; additionally, the coherent part of the functions have the same high frequency tails (indicated at right), which sets the width of the quasiparticle peak (indicated on top).

where $n_{\text{imp},\sigma}$ is the number of electrons on the impurity site, for the ground state of the impurity model Hamiltonian. Whilst such an essential quantity must clearly be matched for the self-consistency to be physically sensible, a more formal argument is possible by comparison of the two Green's functions at high frequency ω [69]. In this limit, the self-energy of the impurity model can be calculated by perturbation theory: $\Sigma_\sigma(\omega) = U n_{\text{imp}\bar{\sigma}} + U^2 n_{\text{imp}\bar{\sigma}}(1 - n_{\text{imp}\bar{\sigma}})/\omega + O(1/\omega^2)$, where n is the *impurity* site filling (under the unperturbed Hamiltonian). Conversely, calculating $\Sigma_\sigma(\omega)$ for the Hubbard model (on the extended lattice) yields an identical expression, but in terms of the *lattice* local filling n_{latt} instead of n_{imp}. In DMFT, we are transferring the impurity self-energy unchanged to the lattice, and so for these high-energy expansions to be the same, it is necessary that the impurity and lattice fillings are the same. Furthermore, the high energy form of the lattice Green's function with the above impurity self-energy to is identical to the exact high-energy expansion found by calculating moments of the interacting density of states [97].

The second self-consistency condition is more subtle, and involves comparing features of the quasiparticle peak at the Fermi level (see Fig. 4.1). In order to separate the quasiparticle peak from the rest of the function, we focus on the low frequency behaviour of the self-energy, and write it as $\Sigma_\sigma(\omega) = a_\sigma + b_\sigma \omega + O(\omega^2)$. This will characterize

55

a normal but renormalized quasiparticle, with a *quasiparticle residue z* defined:

$$z_\sigma = \left(1 - \frac{d\Sigma_{\text{local},\sigma}}{d\omega}(0)\right)^{-1} = \frac{1}{(1 - b_\sigma)}\,. \qquad (4.6)$$

We can construct *coherent* impurity and lattice Green's functions, by combining the non-interacting Green's function with the low frequency self-energy $(a_\sigma + b_\sigma \omega)$ in place of the full $\Sigma_\sigma(\omega)$ in a Dyson's equation. These are called coherent because the effect of such a self-energy is merely to renormalize the width, height and position of the poles of the non-interacting Green's function:

$$G^{(\text{coh})}_{\text{latt},\sigma}(\mathbf{k},\omega) = \frac{1}{\omega + \mu - \epsilon_{\mathbf{k}} - a_\sigma - b_\sigma \omega} = \frac{z_\sigma}{\omega - z_\sigma\left[\epsilon_{\mathbf{k}} - \mu + a_\sigma\right]} \qquad (4.7)$$

$$G^{(\text{coh})}_{\text{imp},\sigma}(\omega) = \frac{1}{\omega + \mu - \Delta_\sigma(\omega) - a_\sigma - b_\sigma \omega} = \frac{z_\sigma}{\omega - z_\sigma\left[\Delta_\sigma(\omega) - \mu + a_\sigma\right]} \qquad (4.8)$$

(recall that $\Delta_\sigma(\omega) = V_\sigma^2/(\omega - \epsilon_{c\sigma})$ for the two-site impurity model, see Eqn 4.2). The quasiparticle residue z_σ indicates how much of the original non-interacting quasiparticle is left now there are interactions (*c.f.* Fermi liquid theory, §1.1).

The coherent Green's functions encapsulate properties of the zero energy quasiparticle peak, and we characterize the peak by its high-energy tails; keeping only the coherent part of the self-energy causes the peak to become isolated from the result of the spectrum. To examine the tails of the Green's functions, we expand their coherent forms at high frequency ω, and compare the lattice and impurity cases analytically to derive a self-consistency condition. Fig. 4.1 shows some typical impurity and lattice Green's functions in their normal and coherent forms, at self-consistency. So, for the lattice Green's function

$$G^{(\text{coh})}_{\text{latt},\sigma}(\mathbf{k},\omega) = \frac{z_\sigma}{\omega}\left[1 + \frac{z_\sigma(\mu - a_\sigma - \epsilon_{\mathbf{k}})}{\omega}\right]^{-1}$$

$$\simeq \frac{z_\sigma}{\omega} - \frac{z_\sigma^2}{\omega^2}(\mu - a_\sigma - \epsilon_{\mathbf{k}}) + \frac{z_\sigma^3}{\omega^3}(\mu - a_\sigma - \epsilon_{\mathbf{k}})^2 + O(1/\omega^4)\,, \qquad (4.9)$$

and for the impurity Green's function

$$G^{(\text{coh})}_{\text{imp},\sigma}(\omega) \simeq \frac{z_\sigma}{\omega}\left[1 + \frac{z_\sigma(\mu - a_\sigma)}{\omega} + \frac{z_\sigma V_\sigma^2}{\omega^2} + O(1/\omega^3)\right]^{-1}$$

$$\simeq \frac{z_\sigma}{\omega} - \frac{z_\sigma^2}{\omega^2}(\mu - a_\sigma) + \frac{z_\sigma^2}{\omega^3}\left[V_\sigma^2 + z_\sigma(\mu - a_\sigma)^2\right] + O(1/\omega^4)\,. \qquad (4.10)$$

Comparing order-by-order in $1/\omega$ up to $O(1/\omega^4)$ in Eqn 4.4, they match if:

$$\sum_{\mathbf{k}} \epsilon_{\mathbf{k}} = 0 \quad \text{and} \quad V_\sigma^2 = z_\sigma \sum_{\mathbf{k}} \epsilon_{\mathbf{k}}^2 \ . \tag{4.11}$$

The non-interacting dispersion can always be shifted such that the first condition is true, and the second provides our other two-site DMFT self-consistency condition. It constrains the couplings V_σ in terms of the quasiparticle residues z_σ, which are calculated from the local self-energy of the impurity model (Eqn 4.6), and a lattice-dependent prefactor equal to the second moment of the non-interacting density of states. On the Bethe lattice, $\sum_{\mathbf{k}} \epsilon_{\mathbf{k}}^2 = t^2$ (see Eqn B.9).

To summarize, the four self-consistency equations for two-site dynamical mean-field theory are:

$$\begin{aligned} n_{\text{imp},\sigma} &= n_{\text{lat},\sigma} \\ V_\sigma^2 &= z_\sigma \sum_{\mathbf{k}} \epsilon_{\mathbf{k}}^2 \ . \end{aligned} \tag{4.12}$$

The self-consistency procedure is illustrated as a flowchart in Fig. 4.2; the bath parameters of the two-site DMFT effective impurity model are constrained by matching the on-site lattice and impurity Green's functions using the electron filling and the weight, centre of gravity and variance of the coherent quasiparticle peak. In the next section (§4.3) I will describe how these self-consistency conditions can be implemented in practice.

4.3   Method

In this section I shall discuss the implementation of the two-site DMFT self-consistency procedure described in the previous section. First, given the impurity parameters $\{\epsilon_{c\sigma}, V_\sigma\}$, we need to calculate the impurity and lattice fillings ($n_{\text{imp},\sigma}$, $n_{\text{latt},\sigma}$) and the quasiparticle weight z_σ. Second, we need a method for adjusting the input parameters $\{\epsilon_{c\sigma}, V_\sigma\}$ to satisfy the self-consistency equations (Eqn 4.12). We wish to consider a given total electron filling n_{Aim}, so the chemical potential μ becomes an additional input parameter constrained by the extra self-consistency equation $\sum_\sigma n_{\text{latt},\sigma} \doteq n_{\text{Aim}}$.

4.3.1   Calculations

The first stage is to construct the impurity Hamiltonian (Eqn 4.1) as a matrix connecting the $2^4 = 16$ possible many-electron states. It can be separated into sectors $\{n_\uparrow, n_\downarrow\}$ with
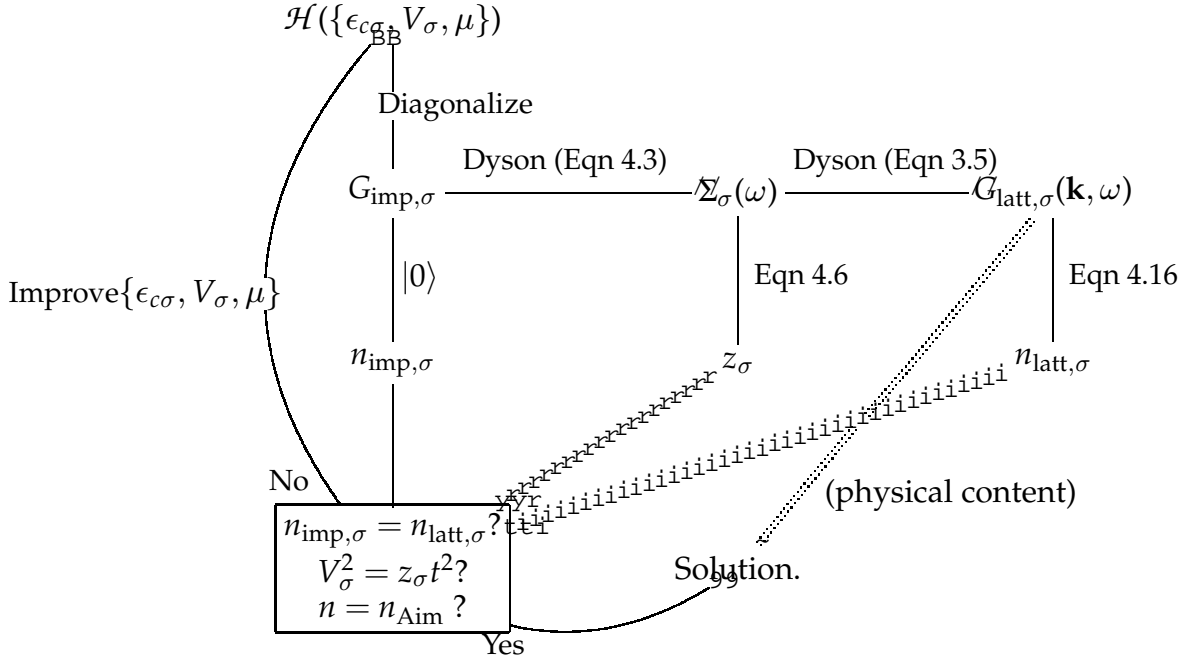
Figure 4.2: Flow chart showing the two-site dynamical mean-field theory self-consistency procedure.

the same number of electrons, which are disconnected since the Hamiltonian conserves particles.[1] A numerical diagonalization (see Appendix C) gives a set of eigenvalues and eigenvectors, from which the ground state can be identified. The impurity filling $n_{\mathrm{imp},\sigma} = \langle 0|c_\sigma^\dagger c_\sigma|0\rangle$ is calculated easily from the eigenvectors.

The overlap between the ground state, and each excited state that has an electron added or removed, is used to calculate the zero temperature Green's function on the impurity site, by means of the Lehmann representation (*c.f.* Eqn 3.13):

$$G_{\mathrm{imp},\sigma}(\omega) = \sum_i \frac{\left|\langle 0|c_\sigma^\dagger|i\rangle\right|^2}{\omega - (E_0 - E_i)} + \frac{\left|\langle i|c_\sigma^\dagger|0\rangle\right|^2}{\omega - (E_i - E_0)} , \tag{4.13}$$

where the sum is over all eigenstates i, which can be written $G_{\mathrm{imp},\sigma}(\omega) = \sum_i a_{i\sigma}/(\omega - b_{i\sigma})$ in terms of a set of residues and poles $\{a_{i\sigma}, b_{i\sigma}\}$. We can now calculate the local self-energy defined in Eqn 4.3 at any ω, given $\{a_{i\sigma}, b_{i\sigma}\}$:

$$\Sigma_\sigma(\omega) = \omega + \mu - \frac{V_\sigma^2}{\omega - \epsilon_{c\sigma}} - \left(\sum_i \frac{a_{i\sigma}}{\omega - b_{i\sigma}}\right)^{-1} ; \tag{4.14}$$

---

[1]This is in practice unnecessary for such a small matrix, but will become necessary for later calculations.

and hence also the quasiparticle weight (Eqn 4.6):

$$z_\sigma^{-1} = \frac{\sum_i a_{i\sigma}/b_{i\sigma}^2}{\left(\sum_i a_{i\sigma}/b_{i\sigma}\right)^2} - \frac{V_\sigma^2}{\epsilon_c^2} \; . \tag{4.15}$$

The final quantity is the lattice filling $n_{\text{latt},\sigma}$, which is the most time consuming quantity to evaluate, as a numerical integration is required. From Eqn 4.4 and Eqn 4.5 we have

$$n_{\text{lat},\sigma} = -\frac{1}{\pi} \int_{-\infty}^{0} d\omega \operatorname*{Im}_{\omega \to \omega - i\delta} \sum_{\mathbf{k}} \frac{1}{\omega + \mu - \epsilon_{\mathbf{k}} - \Sigma_\sigma(\omega)} \; . \tag{4.16}$$

If the local Green's function or density of states is known analytically, we can use the form given in Eqn 3.10:

$$n_{\text{lat},\sigma} = -\frac{1}{\pi} \int_{-\infty}^{0} d\omega \operatorname*{Im}_{\omega \to \omega - i\delta} G_0(\omega + \mu - \Sigma_\sigma(\omega)) = -\frac{1}{\pi} \int_{-\infty}^{0} d\omega \rho_0(\omega + \mu - \Sigma_\sigma(\omega)) \;, \tag{4.17}$$

where G_0 (ρ_0) is the non-interacting local Green's function (density of states) for the lattice under consideration. For the Bethe lattice (see §B.1, Eqn B.7)

$$n_{\text{lat},\sigma} = \frac{1}{2t^2\pi} \int_{-\infty}^{0} d\omega \begin{cases} 0 & \text{if} \quad |\omega + \mu - \Sigma_\sigma(\omega)| > 2t \\ \sqrt{(\omega + \mu - \Sigma_\sigma(\omega))^2 - 4t^2} & \text{if} \quad |\omega + \mu - \Sigma_\sigma(\omega)| < 2t \end{cases} \; . \tag{4.18}$$

The integration must be carried out numerically (see Appendix C) since the algebraic form of $\Sigma_\sigma(\omega)$ (see Eqn 4.14) is rather unwieldy.

4.3.2 Self-consistency

We can now calculate all quantities we need, given the input parameters $\{\epsilon_{c\sigma}, V_\sigma, \mu\}$, and we now need to decide how these should be adjusted to achieve self-consistency (Eqn 4.12). Consider the highly non-linear function $\mathbf{F}$ which evaluates the vector distance from self-consistency:

$$\mathbf{F} \begin{pmatrix} \epsilon_{c\uparrow} \\ \epsilon_{c\downarrow} \\ V_\uparrow \\ V_\downarrow \\ \mu \end{pmatrix} = \begin{pmatrix} n_{\text{imp},\uparrow} - n_{\text{latt},\uparrow} \\ n_{\text{imp},\downarrow} - n_{\text{latt},\downarrow} \\ V_\uparrow^2 - z_\uparrow t^2 \\ V_\downarrow^2 - z_\downarrow t^2 \\ n_{\text{latt},\uparrow} + n_{\text{latt},\downarrow} - n_{\text{Aim}} \end{pmatrix} \tag{4.19}$$

(for the Bethe lattice); we wish to solve the equation $\mathbf{F}(\mathbf{x}) = \mathbf{0}$. The problem is multi-dimensional root-finding, for which I chose to use the Broyden method, the optimal variant of Newton's method for problems with a computationally expensive evaluation of $\mathbf{F}$ and an unavailable gradient $\nabla \mathbf{F}$ (see §C.1 for further discussion). If successful, root-finding yields a set $\mathbf{x} = \{\epsilon_{c\sigma}, V_\sigma, \mu\}$ of self-consistent input parameters. There is no reason why these should be unique, and indeed multiple solutions for a given (U, n) pair certainly occur (a simple example is coexistence of ferromagnetic and paramagnetic solutions; see §4.4), and the ground state must be identified by comparing the *energies* of the solutions.

Dynamical mean-field theory describes a truly interacting many-body system, and the energy of such a system is not trivial to calculate. For a non-interacting system we may calculate the energy as a quantity similar to $\int_{-\infty}^0 \mathrm{d}\omega\,\omega\rho(\omega)$, but when interactions are present the density of states is specific to a given electron filling. We must imagine summing the energy — the chemical potential — of adding each electron cumulatively to the system. Each time the density of states as a whole will change due to the influences of this extra electron. This does not lead to a practical means of calculating the energy, because we have to find self-consistent solutions for specific values of the filling, n.

There is an alternative method for calculating the ground state energy, however. Whilst the two-body Hubbard interaction prohibits direct calculation of the energy as $\langle \mathcal{H} \rangle$, we can proceed by dividing the Hamiltonian into its kinetic energy $\langle \epsilon_{\mathbf{k}} \rangle$ and potential energy parts. The former is directly calculable, and the latter can be deduced by virtue of its relationship with the full Hamiltonian [98, 99]. The result for the total energy is

$$E = -\frac{1}{\pi} \int_{-\infty}^0 \mathrm{d}\omega \lim_{\omega \to \omega - i\delta} \sum_{\mathbf{k},\sigma} \left[\epsilon_{\mathbf{k}} + \tfrac{1}{2}\Sigma_\sigma(\omega) \right] G_{\mathrm{lat},\sigma}(\mathbf{k}, \omega) \tag{4.20}$$

$$= \sum_\sigma \int_{-\infty}^0 \mathrm{d}\omega \left[\omega + \mu - \tfrac{1}{2}\Sigma_\sigma(\omega) \right] \rho_0(\omega + \mu - \Sigma_\sigma(\omega)) , \tag{4.21}$$

where ρ_0 is the non-interacting local density of states (*c.f.* Eqn 4.17, Eqn 4.16 and Eqn 3.10). This expression coincides with Eqns (36,37) of Ref. [69]. In summary, the energy of a solution can be calculated merely by means of a further numerical integration akin to the lattice filling; the ease of this calculation is a further advantage of two-site DMFT.

As a final note, we wish to explore the two-dimensional (U, n) phase diagram, and this can be achieved efficiently by "seeding" the self-consistency loop with parameters corresponding to previously calculated neighbouring points.

4.3.3   Results for the paramagnetic phase

In this section I shall outline results for the *paramagnetic* solution of the two-site DMFT equations on the Bethe lattice (bandwidth $4t$), wherein all quantities are constrained to be identical for $\sigma = \uparrow$ and $\sigma = \downarrow$.

At **half-filling**, the numerics become pathological, but progress can be made analytically. Apart from the sectors which contain two electrons out of the maximum four, the Hamiltonian matrix is only 2×2 and can be diagonalized analytically. At half-filling the system should be particle-hole symmetric, which must also be true for the impurity model; and the energy of the eigenstate with n electrons is the same as the eigenstate with $4 - n$ electrons. Comparing $n = 0$ and $n = 4$ yields $\mu = (U + \epsilon_{c\uparrow} + \epsilon_{c\downarrow})/2$, and comparing $n = 1$ and $n = 3$ gives two possibilities: either $\epsilon_{c\uparrow} = \epsilon_{c\downarrow} = 0$ (and V_σ unconstrained), or $\epsilon_{c\uparrow} = -\epsilon_{c\downarrow}$ and $V_\uparrow = \pm V_\downarrow$. Solving the first case for self-consistency with $V_\uparrow = V_\downarrow$ gives the key result

$$
z_\sigma = \begin{cases} 1 - (U/6t)^2 & \text{if} \quad U < 6t \\ 0 & \text{if} \quad U > 6t \, . \end{cases} \tag{4.22}
$$

This demonstrates the Mott transition: the quasiparticle residue falls off as the interaction strength is increased, and the system becomes an insulator at $U_c = 6t$ (compared to a bandwidth of $4t$). The parabolic form is the same as the Gutzwiller variational approach [84]. The critical value $U_c = 6t$ compares reasonably well with the Brinkman-Rice result of $U_c = 6.79t$; there is better agreement with ED and NRG DMFT calculations (see Fig. 1 of Ref. [69]).

Using the full numerical two-site DMFT calculations to investigate off half-filling gives results for the quasiparticle residue z as shown in Fig. 4.3: there is no Mott transition, as z no longer suddenly becomes exactly zero but falls off increasingly gently further away from half-filling.

Returning to the half-filling case, Fig. 4.4 shows how the density of states within two-site DMFT evolves with U. The classic three-peak structure of more sophisticated DMFT approaches (§3.5.1) is captured neatly: as U increases the Hubbard bands form and move apart, and the central quasiparticle becomes heavier until the peak suddenly vanishes at the Mott transition. Off half-filling the density of states retains the three peak form, but increasing amounts of weight fall in the central band. Fig. 3 of Ref. [69] shows some examples, which coincide with my calculations.
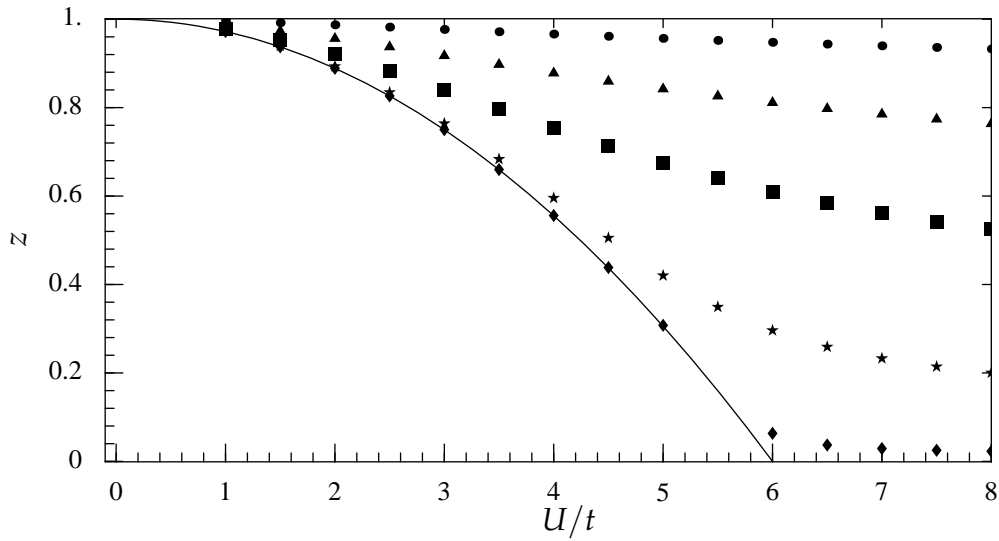
Figure 4.3: Quasiparticle residue z as a function of U for various values of the electron filling. Solid line: analytic form at $n = 1$ (half-filling) $z = 1 - (U/6t)^2$; the other data points $\blacklozenge, \bigstar, \blacksquare, \blacktriangle, \bullet$ correspond to $n = 0.99, 0.9, 0.7, 0.5, 0.25$ respectively.
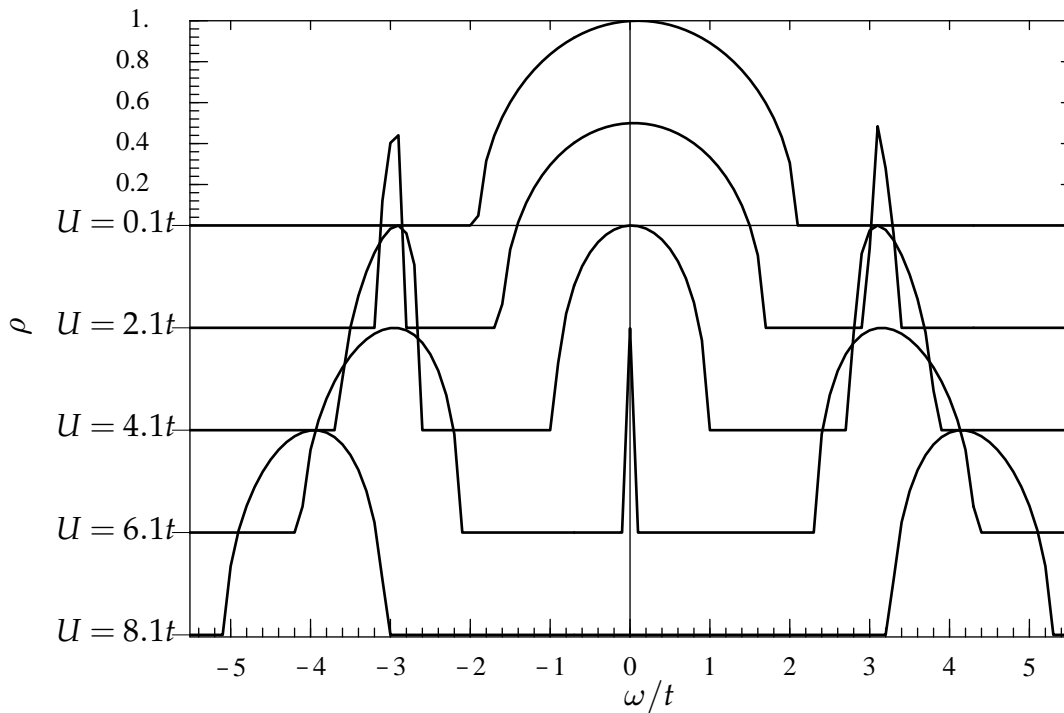
Figure 4.4: Density of states for two-site DMFT on the Bethe lattice at $U = \{0.1t, 2.1t, 4.1t, 6.1t, 8.1t\}$ very near to half-filling. The pictures of Mott–Hubbard and Brinkman–Rice are both captured by two-site DMFT; Hubbard bands can be seen coexisting with an increasingly heavy central quasiparticle which vanishes at higher U: the Mott transition.

4.4 Ferromagnetic and antiferromagnetic phases

To allow for the possibility of magnetism, quantities should be permitted to differ depending on the spin σ, and if the spin symmetry remains broken in the self-consistent solution, the state is *ferromagnetic*: each site in the real lattice would have identical magnetic properties. The two-site DMFT equations as formulated above can produce such solutions.

4.4.1 Representing antiferromagnetism

We also wish to allow for the possibility of *antiferromagnetism*, where the magnetic properties of each site alternates: on a *bipartite lattice* each lattice site can be labelled A or B, and A sites are only connected to B sites. A $\uparrow$ spin on an A site has identical properties to a $\downarrow$ on a B site, which means that we can derive a new set of self-consistency equations for DMFT, such that an $\uparrow$ spin fluctuates so that surrounding sites see it as a $\downarrow$ spin, and vice versa [93].

We begin the derivation of antiferromagnetic self-consistency equations for DMFT by dividing the kinetic energy part of the Hamiltonian into sublattices:

$$\mathcal{H}_0^{\mathrm{AFM}} = \sum_{\mathbf{k}} \epsilon_{\mathbf{k}} \hat{c}_{\mathbf{k}}^\dagger \hat{c}_{\mathbf{k}} = \tfrac{1}{2} \sum_{\mathbf{k}} \epsilon_{\mathbf{k}} \left[\hat{c}_{A\mathbf{k}}^\dagger \hat{c}_{B\mathbf{k}} + \hat{c}_{B\mathbf{k}}^\dagger \hat{c}_{A\mathbf{k}} \right] , \tag{4.23}$$

which leads to a matrix lattice Green's function

$$\mathsf{G}_{0,\mathrm{latt},\sigma}^{\mathrm{AFM}}{}^{-1}(\mathbf{k}, \omega) = \tfrac{1}{2} \begin{pmatrix} \omega + \mu & -\epsilon_{\mathbf{k}} \\ -\epsilon_{\mathbf{k}} & \omega + \mu \end{pmatrix} , \tag{4.24}$$

where the sublattice is the matrix index. Matrices within DMFT are discussed in detail within the context of cluster DMFT (Chapter 5); this section will just contain a brief summary of results, which will be superseded. The self-energies calculated from the impurity model can be introduced to the diagonals of the Green's functions, giving:

$$G_{\mathrm{latt},\sigma}^{\mathrm{AFM}}(\mathbf{k}, \omega) = \frac{\omega + \mu - \Sigma_{\bar{\sigma}}}{(\omega + \mu - \Sigma_{\sigma})(\omega + \mu - \Sigma_{\bar{\sigma}}) - \epsilon_{\mathbf{k}}^2} \tag{4.25}$$

where I have used the label σ represents $A \uparrow \equiv B \downarrow$ and $\bar{\sigma}$ represents $A \downarrow \equiv B \uparrow$. This function should be used in Eqn 4.5 to calculate the lattice filling for the antiferromagnetic case. When the local density of states is known we can evaluate the $\mathbf{k}$-sum and

write (*c.f.* Eqn 4.17):

$$n_{\text{latt},\sigma}^{\text{AFM}} = \int_{-\infty}^{0} \mathrm{d}\omega \sqrt{\left|\frac{\omega + \mu - \Sigma_{\bar{\sigma}}}{\omega + \mu - \Sigma_{\sigma}}\right|} \rho_0 \left(\sqrt{|(\omega + \mu - \Sigma_{\sigma})(\omega + \mu - \Sigma_{\bar{\sigma}})|} \right) ; \qquad (4.26)$$

regions where $(\omega + \mu - \Sigma_\sigma)(\omega + \mu - \Sigma_{\bar{\sigma}}) < 0$ are excluded, noting the structure of the Green's function in the complex plane (see §B.1). A direct treatment of antiferromagnetism on the Bethe lattice yields an identical result (see §B.3). Finally, for the second self-consistency condition involving the quasiparticle peak, we expand the coherent part of the antiferromagnetic lattice Green's function as per Eqn 4.9, giving the condition

$$V_\sigma^2 \doteq z_{\bar{\sigma}} \sum_{\mathbf{k}} \epsilon_{\mathbf{k}}^2 . \qquad (4.27)$$

The only difference from Eqn 4.12 is that opposite spin species are matched, as one might expect intuitively.

4.4.2   Results

Simple ferromagnetism

Ferromagnetism emerges for $U > 4t$, and at half filling this critical value can be derived analytically similarly to §4.3.3. As U increases, it extends away from half-filling as shown in Fig. 4.5, reaching for example $n \sim 0.8$ at $U = 8t$; this is a very much smaller extent than the Stoner criterion predicts. There are two different ferromagnetic solutions, with different magnetizations (as shown in Fig. 4.6); one is fully polarized.[2] Nowhere on the phase diagram do either of the ferromagnetic solutions have a lower energy than the paramagnetic solution.

A mean-field Heisenberg term $-F\langle m\rangle \hat{m}/2 + F\langle m\rangle^2/4$ can be introduced to the Hamiltonian to stabilize itinerant ferromagnetism.[3] The energy of the saturated ferromagnetic solution can be decreased sufficiently that it becomes the ground state, and a phase diagram in excellent agreement with the more sophisticated DMFT approach of Vollhardt and coworkers (Fig. 2 of Ref. [71]) was found.

Simple antiferromagnetism

There are two antiferromagnetic solutions, which are energetically favoured over the paramagnet for some regions of the phase diagram, as shown in Fig. 4.5. First, by

---

[2]This saturated solution was hard to pin down because it is one of a large subspace of identical solutions.

[3]$\langle m\rangle$ was introduced as an extra free parameter with a self-consistency condition $\langle m\rangle \doteq n_\uparrow - n_\downarrow$.
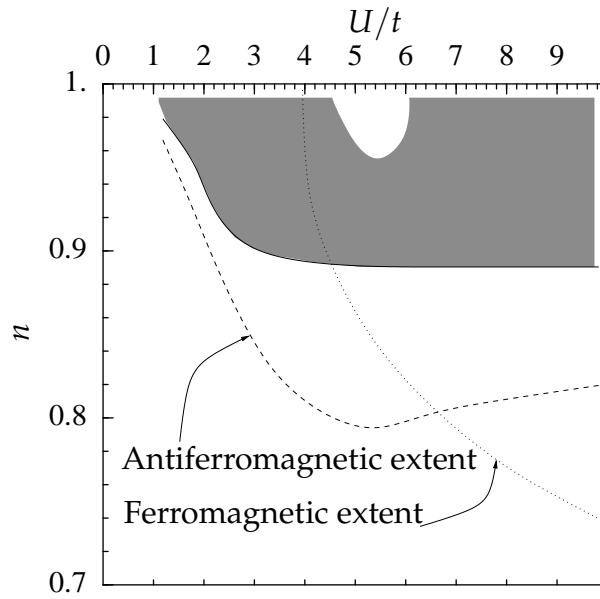
Figure 4.5: Phase diagram for the simple antiferromagnetic and ferromagnetic phases within two-site DMFT on the Bethe lattice (bandwidth $4t$). The dashed (dotted) line shows the extent of the antiferromagnetic (ferromagnetic) phases, although they are not necessarily energetically favoured within these regions; the shaded region indicates where there is an antiferromagnetic ground state (apart from the hole, which is discussed in the text). Very close to half-filling ($n = 1$), the ground state is antiferromagnetic for all U.

(a) $U = 7.5t$ (b) $n = 1$
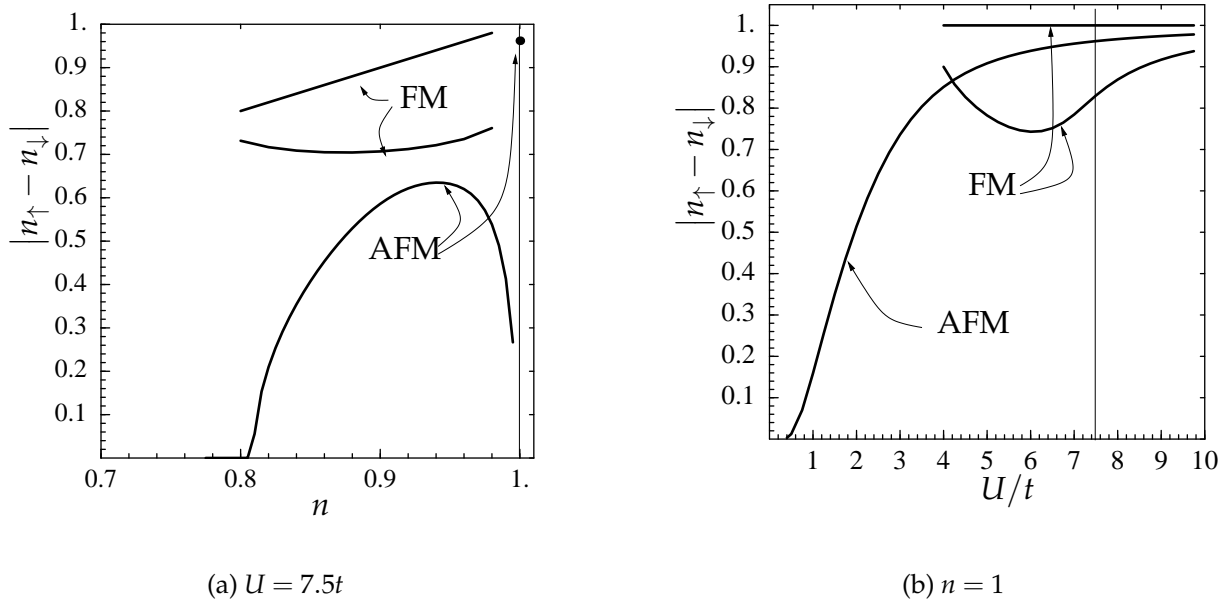
Figure 4.6: Cross-sections of the variation of magnetization with n and U, for the simple magnetic solutions of two-site DMFT on the Bethe lattice (bandwidth $4t$). Two ferromagnetic (FM) phases, one of which is saturated, are shown, although these are never energetically favoured. There are two antiferromagnetic (AFM) solutions, one of which is constrained to very near half-filling, and for these the *sublattice* magnetization is shown. (a) Variation with filling n at $U = 7.5t$. Antiferromagnetism at half-filling is indicated by a •. Paramagnetism becomes favoured over antiferromagnetism for $n \lesssim 0.885$. (b) Variation with interaction strength U at half-filling ($n = 1$). Antiferromagnetism is energetically favoured everywhere.

65
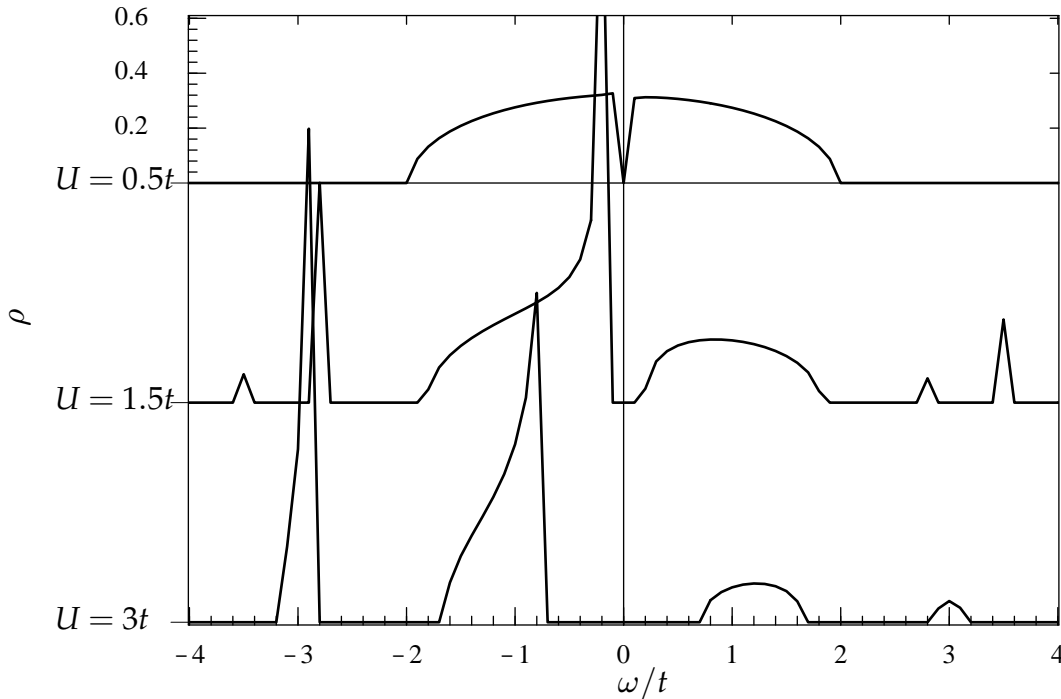
Figure 4.7: Sublattice-resolved densities of states for simple antiferromagnetic solutions to two-site DMFT on the Bethe lattice (bandwidth $4t$) for $U = \{0.5t, 1.5t, 3t\}$ at half-filling. A Slater gap is formed immediately U becomes finitesimal. The densities of states for the other sublattice are identical but reflected such that $\omega \to -\omega$.

predefining μ as in §4.3.3, a solution can be found at exactly half-filling; there is also a very similar state slightly off half-filling, extending at most to $n \sim 0.995$ at $U \sim 5t$ (not shown in Fig. 4.5). The state is an insulating Slater antiferromagnet for any finitesimal $U > 0$, and Fig. 4.6(b) shows its Hartree-like magnetization curve; its density of states is plotted for various values of U in Fig. 4.7.

A second, metallic, antiferromagnetic state exists which has a maximum extent off half-filling of $n = 0.8$ at $U = 5.5t$, and thereafter recedes (see Fig. 4.5). Its magnetization as a function of U and n is shown in Fig. 4.8; the magnetization drops to zero again near half-filling for interaction strengths above the Mott transition ($U = 6t$), which perhaps indicates how a metallic solution is becoming unfavourable near to the half-filling insulating state. The quasiparticle weight falls off similarly to the paramagnetic state shown in Fig. 4.3. Looking at this transition as U increases close to half-filling, there is a cusp in the magnetization (see inset of Fig. 4.8) where there no solutions could be found (the hole in Fig. 4.5). In this region, there is behaviour reminiscent of the Falicov–Kimball model, where one spin species is localized and the other itinerant: $|z_\uparrow - z_\downarrow|$ exhibits a large peak here.
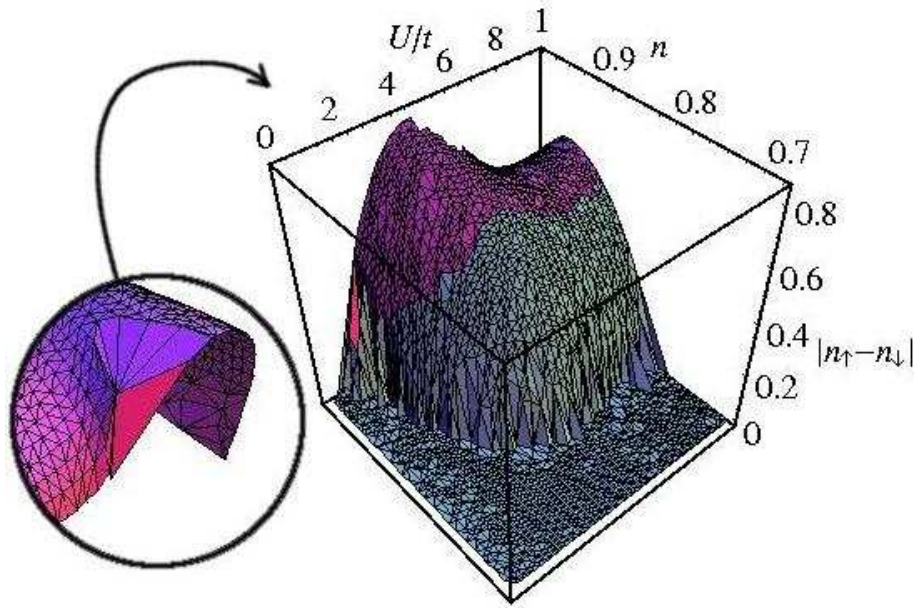
Figure 4.8: Magnetization of the simple antiferromagnetic solution to two-site DMFT on the Bethe lattice (bandwidth $4t$) as a function of interaction strength U and filling n. The phase is energetically favoured nearer to half-filling (darker shading), but there is a hole (inset) near the Mott transition ($U = 6t$) where solutions cannot be found.

Degenerate eigenstates

Yet, it turns out that there is a further set of solutions (with all three types of order) that are generally lower in energy than the previous ones; they come from impurity models with *degenerate* ground states — with different numbers of electrons. For such phases, we use a thermodynamic average of the two states of the impurity model which are lowest in energy. The relative weight of the two states, $0 \leq \alpha \leq 1$, is a new parameter, with the matching self-consistency condition that the two states really are degenerate. If they are degenerate, any linear combination is a valid ground state (and off self-consistency the state is unphysical in any case).

In total there are eleven distinct phases within magnetic two-site DMFT, including both the "degenerate" solutions and those described previously; Fig. 4.9 shows a schematic phase diagram. A region where ferromagnetism is favoured has now emerged; its extent is within the boundary $n > 0.71$ found by the authors of Ref. [100]. The ferromagnetic magnetization increases roughly linearly from zero towards half-filling and does not change significantly with U. All the ground state phases still exhibit the quasiparticle weight decreases similar to Fig. 4.3, characterizing the Mott transition.

The degeneracy is indicative that the limit of unenhanced two-site DMFT has been reached, and I shall not discuss the properties of these phases in further detail as they will be superseded by results in later chapters.
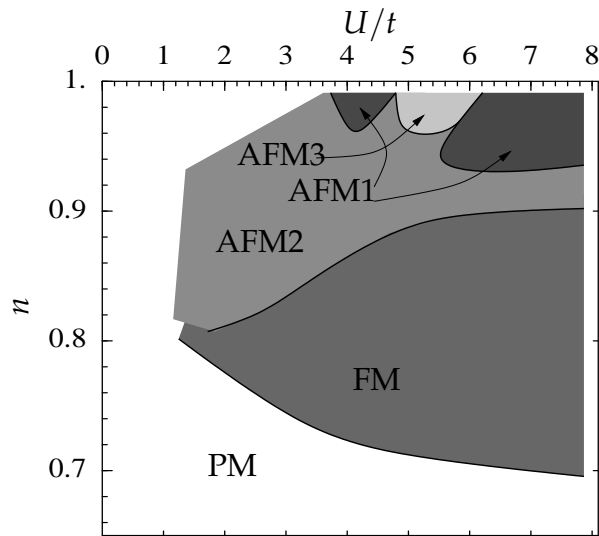
PSfrag replacements

Figure 4.9: Phase diagram for the antiferromagnetic (AFM) and ferromagnetic (FM) phases within two-site DMFT on the Bethe lattice (bandwidth $4t$), including those from impurity models with degenerate ground states (AFM2, AFM3 and FM). The paramagnetic phase (PM) and the AFM1 phase are the "simple" (non-degenerate) phases of Fig. 4.5. At lower n than shown, there is a region where the ground state phase becomes an antiferromagnet with a tiny moment. At high U, the phase boundaries continue horizontally at roughly the same fillings.

4.5 Summary

In this chapter I have described a minimal representation of DMFT where a single bath site provides the spectrum of excitations for the mean-field model to explore. This approach is remarkably successful: for example, the broad features of the Mott transition can be reproduced (see §4.3.3 and Ref. [69]). I have extended two-site DMFT to encompass ferro- and antiferromagnetic phases, which produces a reasonable phase diagram and predicts a much smaller extent of magnetism than static Hartree mean-field theory, a result in agreement with more sophisticated DMFT studies.

I have restricted my description of the phases to a brief survey, since they form an initial test of two-site DMFT, and the results will be superseded by the more sophisticated results in later chapters. The final phase diagram in Fig. 4.9 is not entirely satisfactory; the degenerate states are symptomatic of the struggle to represent the necessary physics within the restrictions of the two-site impurity model, and the self-consistency only manages to succeed by combining together the physics of two different impurity states by making them degenerate. The results of this chapter serve only to justify two-site DMFT as a good, quickly calculable kernel for extensions to DMFT; it is a method with frugal computation requirements that, despite its crudeness, can produce pictures of interacting systems that in general have only been possible with far more sophisticated approaches.

When further degrees of freedom are added to the two-site DMFT model, the prob-

lems caused by its simplicity will reduce. The most obvious way of extending two-site DMFT would be the addition of further bath sites to the impurity model to represent the dynamics of non-local electrons more accurately. Suitable extra physically-relevant self-consistency conditions should then be devised to constrain the bath parameters, in contrast to the conventional exact diagonalization approach to DMFT where self-consistency is implemented rather blindly. Extending the coherent Green's functions (Eqn 4.7 and Eqn 4.8) to include further terms is one possibility for deriving such self-consistency conditions; and whilst including a ω^2 term to the reduced self-energy is pathological, terms such as ω^{-1} etc. would be possible. More generally, the whole self-energy can be used as a variational functional, as discussed in a further paper of Potthoff [101]. An alternative to such a mathematical approach is to take advantage of specific emergent spectral features, inspired by physical intuition.

However, instead of following the conventional DMFT route of representing the interacting sea faithfully, we can channel our spare computational resources into different areas, and let dynamics be captured minimally. For example, we could include multiple orbitals or bands, to model real materials where band degeneracy causes interesting physics. One fruitful subject of study would be ruthenate compounds, which exhibit fascinating behaviour indicative of strong electronic correlations, such as unconventional superconductivity in Sr_2RuO_4 [102] and metamagnetic quantum criticality in $Sr_3Ru_2O_7$ [11]. The evolution of magnetism across the strontium/calcium ruthenate series, $Sr_{n+2-x}Ca_xRu_{n+1}O_{3n+4}$, is counter-intuitive, and DMFT would be an ideal tool for investigating whether this is due to the influence of local physics on a good Fermi liquid (Sr_2RuO_4). Koga *et al.* [103] used a method based on two-site DMFT to study orbital-selective Mott transitions in the $Ca_{2-x}Sr_xRuO_4$ compounds, further evidence of the efficacy of two-site DMFT.

However, prior to tackling such materials, we want to be sure of modelling magnetism accurately, mindful of the pitfalls of studying paramagnetic phases where there is lower-energy antiferromagnetism present [64]. A cluster formulation provides a more satisfactory approach to antiferromagnetism than the single impurity site approach of this chapter. The rest of this thesis will focus upon *cluster DMFT* (described in Chapter 5), where the impurity model consists of a cluster of impurity sites each connected to a bath representing off-cluster dynamics; I shall use two-site DMFT as the impurity solver, so each bath is reduced to a single site. The computational effort saved by the minimal two-site implementation of the DMFT self-consistency means that the phase diagram of the 2D Hubbard model can be comprehensively explored under a cluster model, in contrast to conventional DMFT where the huge computational requirements limit investigation to just a few points in parameter space.

Chapter 5

CLUSTER DMFT

HAMLET: Do you see yonder cloud that's
almost in shape of a camel?
LORD POLONIUS: By the mass, and 'tis like a
camel, indeed.
HAMLET: Methinks it is like a weasel.
LORD POLONIUS: It is backed like a weasel.
HAMLET: Or like a whale?
LORD POLONIUS: Very like a whale.

WILLIAM SHAKESPEARE
Hamlet [104]

5.1 Introduction

Conventional DMFT is formulated by isolating a single site from the crystal lattice, and representing the interaction of that site with the rest of the system with a self-consistent bath. If a cluster of sites is extracted from the lattice instead of the single site, and embedded in a self-consistent medium (see Fig. 5.1), we have *cluster DMFT*. The geometry of neighbouring sites can be included in the theory, and the DMFT equations now have some momentum dependence. In practical terms, different types of magnetic order can be investigated consistently, and there is now possibility of anisotropy in the Brillouin zone; this is invisible to conventional DMFT and turns out to be very important. After describing in detail how exactly I shall interpret cluster DMFT (§5.2), I shall eventually focus upon the combination of two-site DMFT (Chapter 4) with cluster DMFT, described in §5.3.

Conventional DMFT distinguishes between different crystal lattices only by means of their densities of states (*c.f.* Eqn 3.10), and is thus fairly insensitive to lattice intricacies [52]. Antiferromagnetism on a bipartite lattice can be dealt with crudely within conventional DMFT by imagining electrons to change spin orientation as they hop between identical sites, as in reality alternate sites have opposite spin properties. A reasonable magnetic phase diagram can be produced with this method (as described in §4.4.2 for two-site DMFT); and it is even possible to see consequences of frustration.[1] In general, however, conventional DMFT is not an ideal theory for studying magnetism; phenomena such as frustration are highly dependent on the local geometrical environment. Furthermore, the momentum dependence of any quantity calculated within conventional dynamical mean-field theory cannot vary from that of the non-interacting dispersion (*c.f.* Eqn 3.5, Eqn 3.9), and it is known experimentally that significant momentum anisotropy can emerge, for example from photoemission studies of the cuprates. So, to capture fully the dynamical effects of inter-site correlations, and resolve features in momentum space, a cluster DMFT approach is necessary.

There are several different formulations of cluster DMFT, and indeed its derivation is fundamentally ambiguous — I shall discuss possible approaches in §5.1.1. DMFT is exact in infinite dimensions, and cluster DMFT can be formulated to provide rigorous finite dimensional corrections, at $O(1/d)$, to DMFT. Whilst the cluster approach considered in this thesis (described in detail in §5.2) is not such a well-defined extension of DMFT, it will improve upon conventional DMFT as it is a step towards the limit of infinite cluster size, where cluster DMFT is clearly exact. Here the self-consistency condi-

---

[1]*c.f.* Santoro *et al.* [57], who studied the infinite-dimensional diamond lattice, which is bipartite but not nested.

tions will have become an insignificant, albeit sophisticated, boundary condition. For small clusters, the momentum dependence of quantities will be weak, and the possible Fermi surface shapes highly constrained — but improved from conventional DMFT which is restricted to shapes resulting from the non-interacting dispersion only. As the cluster size increases, higher Fourier modes become available to characterize the dispersion, and the representation of the Fermi surface can become more accurate.

Naturally, having to solve a cluster significantly increases computational requirements, due to the vast increase in Hilbert space size. The focus of this thesis will be the use of a minimal DMFT kernel (two-site DMFT as described in Chapter 4) to solve the DMFT equations emerging from the cluster problem; such an approach enables a complete survey of the phase diagram of the 2D Hubbard model. In §5.3 I shall describe how to formulate two-site cluster DMFT for an arbitrary cluster (within the cluster DMFT approach of §5.2), and in the succeeding sections I will derive equations for the specific cases of a 2×1 site "pair-cluster" (§5.3.1) and then a 2×2 site "quad-cluster" (§5.3.1). The final two chapters (Chapter 6 and Chapter 7) contain a complete description of the results of these calculations.

5.1.1   Approaches to cluster DMFT

There is no unique generalization of DMFT to cluster DMFT [105]. Different schemes will arise for the cluster formulation depending upon what one takes the fundamental ansatz behind DMFT to be — for example, whether it is a formal infinite dimensional limit, or as a mean-field theory with dynamics included through an effective medium.

If one regards DMFT as a strict infinite dimensional limit, a cluster DMFT can be derived formally by expanding to $O(1/d)$ [58, 52]. Perturbation theory is local in infinite dimensions [53, 52] and the original DMFT equations can be derived from a Luttinger–Ward functional restricted to local Green's functions. Allowing in addition nearest-neighbour Green's functions produces a cluster-like scheme, requiring the simultaneous solution of two impurity models, coupled via self-consistency conditions. However, this scheme has been shown to be non-causal [105], and the lattice geometry does not enter the equations, as the coordination number $z < \infty$ is the only new parameter.

The Dynamical Cluster Approximation (DCA) [106, 107] involves dividing the Brillouin zone into a number of cells N_c, and in effect a separate instance of conventional DMFT is set up for each cell, centred at $\mathbf{K}$. The DMFT self-consistency condition
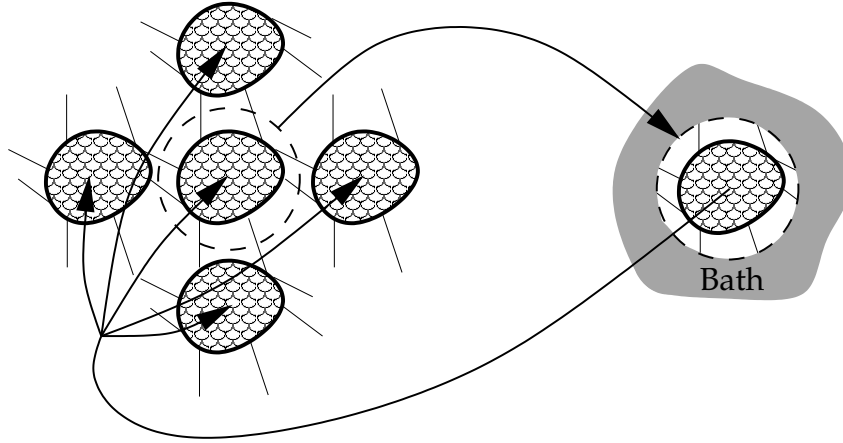
PSfrag replacements

Figure 5.1: In the cluster DMFT procedure, a small cluster is identified and isolated from the rest of the lattice. A bath is connected to the cluster to represent the dynamics of electrons hopping to neighbouring clusters. To reconstruct the extended system, the cluster is re-embedded in the lattice, and bath adjusted to ensure it is self-consistent with this embedding.

(Eqn 3.7) turns into N_c equations

$$G_{\text{local}}(\mathbf{K}, i\omega_n) = \sum_{\mathbf{k}} \frac{1}{i\omega_n + \mu - \epsilon_{\mathbf{K}+\mathbf{k}} - \Sigma_{\text{local}}(\mathbf{K}, i\omega_n)} \ , \qquad (5.1)$$

where $\mathbf{k}$ is labelling the momenta within a single cell. Each cell explores a different part of the dispersion relation $\epsilon_{\mathbf{k}}$, and so the result is slightly lattice-dependent. The DCA can also be formulated in real space [105], and it can be shown to be causal.

In contrast to dividing up momentum space, we can divide real space into clusters, and this provides the most natural way of approaching phenomena such as antiferromagnetism. A real space cluster is the basis of Cellular Dynamical Mean Field Theory (CDMFT) [108, 109, 110], and self-consistency conditions can be constructed on consideration of its links to surrounding clusters. My approach to cluster DMFT, which I shall derive carefully in the next section (§5.2), is closely related to CDMFT.

5.2   My cluster DMFT formulation

The broad outline of the cluster DMFT procedure is illustrated in Fig. 5.1. We begin by dividing our interacting Hamiltonian (perhaps the Hubbard model, Eqn 1.1) into clusters, each with N_c sites. For each cluster, at a *superlattice* position labelled $\mathbf{R}$, there will be terms solely contained in that cluster (the Hubbard repulsion U and hopping between cluster sites), which I shall collect into $\mathcal{H}_{\mathbf{R}}$. Secondly, there are terms that interlink clusters, which I shall collect into $\mathcal{H}_{\mathbf{R}}^{\Delta}$, being careful with counting and keep-

ing daggered terms within their own cluster. So, the total Hamiltonian is

$$\mathcal{H} = \sum_{\mathbf{R}} \left[\mathcal{H}_{\mathbf{R}} + \mathcal{H}_{\mathbf{R}}^{\Delta} \right] = \sum_{\mathbf{R}} \left[\mathcal{H}_{\mathbf{R}} + \sum_{\Delta \mathbf{R}} \mathcal{H}_{\mathbf{R},\mathbf{R}+\Delta\mathbf{R}}^{\Delta} \right] , \tag{5.2}$$

showing how the part $\mathcal{H}_{\mathbf{R}}^{\Delta}$ which interlinks clusters can be further dissected, according to which neighbouring cluster (at position $\mathbf{R} + \Delta\mathbf{R}$) is involved. Similarly to conventional DMFT, we focus on a single cluster, and imagine integrating out all sites which do not belong to that cluster. This will leave an effective action (*c.f.* Eqn 3.1 for conventional DMFT) of the form:

$$S_{\text{eff}} = - \int_0^{\beta} d\tau \int_0^{\beta} d\tau' \sum_{i,j} c_{i\sigma}^{\dagger}(\tau) \mathcal{G}_{0,ij}^{-1}(\tau - \tau') c_{j\sigma}(\tau') + U \int_0^{\beta} d\tau \sum_i c_{i\uparrow}^{\dagger}(\tau) c_{i\uparrow}(\tau) c_{i\downarrow}^{\dagger}(\tau) c_{i\downarrow}(\tau) , \tag{5.3}$$

where i, j label positions within the cluster, and $\mathcal{G}_0$ has become a matrix, between pairs of sites in the cluster. The Green's function $\mathcal{G}_{0,ij}$ represents the dynamics of electrons leaving the cluster from site j and returning to site i after picking up an arbitrary quantum mechanical phase; a realization of the action must enable each element of the matrix $\mathcal{G}_0$ to represent an arbitrary function. Supposing we can solve this action, we can calculate the interacting Green's function for this action (*c.f.* Eqn 3.2), which will also be a matrix

$$G_{\text{local},ij}(\tau - \tau') \equiv - \langle T c(\tau)_i c^{\dagger}(\tau')_j \rangle_{S_{\text{eff}}} , \tag{5.4}$$

and extract a matrix self-energy for the cluster (*c.f.* Eqn 3.3):

$$\mathsf{G}_{\text{local}}^{-1}(i\omega_n) = \mathcal{G}_0^{-1}(i\omega_n) - \Sigma_{\text{local}}(i\omega_n) . \tag{5.5}$$

Next, we wish to embed this self-energy in the lattice. To do this, we have to know the non-interacting Green's function as a matrix within the cluster basis. Let us start from Eqn 5.2 with no interactions ($U = 0$), and define a Fourier transform for the cluster superlattice of positions $\mathbf{R}$ which will have $\mathbf{k}$ vectors in some geometry-dependent *Reduced Brillouin Zone (RBZ)*

$$\begin{aligned} c_{\mathbf{R},i}^{\dagger} &= \frac{1}{\sqrt{N}} \sum_{\mathbf{k} \in \text{RBZ}} e^{i\mathbf{k}.\mathbf{R}} c_{\mathbf{k},i}^{\dagger} \\ c_{\mathbf{k},i}^{\dagger} &= \frac{1}{\sqrt{N}} \sum_{\mathbf{R} \in \text{superlattice}} e^{-i\mathbf{k}.\mathbf{R}} c_{\mathbf{R},i}^{\dagger} . \end{aligned} \tag{5.6}$$

Operators are defined specific to each site at position i within the cluster, but with a superlattice momentum $\mathbf{k}$, transformed from the independent position $\mathbf{R}$ of the cluster

as a whole. The Hamiltonian becomes

$$\mathcal{H}_0 = \sum_{\mathbf{k}} \hat{\mathbf{c}}_{\mathbf{k}}^{\dagger} \cdot \left[\mathsf{H} + \sum_{\Delta \mathbf{R}} e^{i\mathbf{k}\cdot\Delta\mathbf{R}} \mathsf{H}^{\Delta} \right] \cdot \hat{\mathbf{c}}_{\mathbf{k}} = \sum_{\mathbf{k}} \hat{\mathbf{c}}_{\mathbf{k}}^{\dagger} \cdot \mathsf{H}_0(\mathbf{k}) \cdot \hat{\mathbf{c}}_{\mathbf{k}} \tag{5.7}$$

where $\hat{\mathbf{c}}_{\mathbf{k}}$ is a vector consisting of the operators for each cluster site. H and H^{Δ} are matrices with respect to the index of a site within the cluster: H is hopping contained within the cluster, and H_{ij}^{Δ} is the hopping element from site i of the cluster at $\mathbf{R}$ to site j of the cluster at $\mathbf{R} + \Delta\mathbf{R}$ (for an example, see Eqn 5.25 and Eqn 5.26). The end result is a non-interacting Hamiltonian matrix $\mathsf{H}_0(\mathbf{k})$ for the cluster, from which we know the non-interacting Green's function matrix (*c.f.* Eqn 3.4):

$$\mathsf{G}_{0,\mathrm{latt}}^{-1}(\mathbf{k}, i\omega_n) = (i\omega_n + \mu)\mathsf{I} - \mathsf{H}_0(\mathbf{k}) , \tag{5.8}$$

and can insert the self-energy matrix (*c.f.* Eqn 3.5):

$$\mathsf{G}_{\mathrm{latt}}^{-1}(\mathbf{k}, i\omega_n) = \mathsf{G}_{0,\mathrm{latt}}^{-1}(\mathbf{k}, i\omega_n) - \Sigma_{\mathrm{local}}(i\omega_n) . \tag{5.9}$$

One of the ambiguities of cluster DMFT is how the local cluster self-energy should be combined with the lattice Green's function; here we are choosing to do it element-by-element in the matrix, and this is particular to the cluster DMFT scheme. There are alternative possibilities; one example is that used in "PCDMFT" [105], where the real space self-energy Σ_{ij} between two lattice sites is estimated by averaging hops that are equivalent to ij within the cluster, and the result Fourier transformed.

Finally, the dynamical field matrix in $\mathscr{G}_0$ in the initial action is constrained, by comparing the local lattice Green's function with the interacting Green's function of the effective action. These matrices are matched element-by-element, giving an identical expression to Eqn 3.6:

$$\mathsf{G}_{\mathrm{local}}(i\omega_n) \doteq \sum_{\mathbf{k}} \mathsf{G}_{\mathrm{latt}}(\mathbf{k}, i\omega_n) . \tag{5.10}$$

Similarly to above, comparing the Green's function matrices element-by-element is a choice, and our cluster DMFT scheme is now specified, by these two choices (Eqn 5.9 and Eqn 5.10). The DCA self-consistency conditions, for example, differ from our approach as patches of momentum space are compared instead of matrix elements with respect to the spatial cluster in our case.

As with the original DMFT procedure, everything above should be duplicated for the two spin species, which are coupled only by the electron-electron interaction in the effective action.

5.2.1   Extracting physical properties

In conventional DMFT, the constructed lattice Green's function $G_{latt}(\mathbf{k}, i\omega_n)$ is clearly the real physical correlation function. In cluster DMFT, we have a matrix lattice Green's function $G_{latt}(\mathbf{k}, i\omega_n)$, and the operators for a specific cluster site are not physical quantities, so some manipulation is required to extract physical properties. Diagonalizing the non-interacting Hamiltonian $H_0(\mathbf{k})$ gives a set of N_c eigenstates corresponding to N_c bands in the first reduced Brillouin zone (RBZ). The interacting Green's function can be transformed likewise, and each eigenstate produces a Green's function which characterizes the quasiparticles in that band.

More explicitly, let us suppose J is the matrix of normalized eigenvectors of $H_0(\mathbf{k})$, such that $H_0 = JDJ^\dagger$ where D is a diagonal matrix with eigenvalues on its diagonal (*c.f.* Eqn 5.27, Eqn 5.37 and Eqn 5.38 for specific examples). I shall term this basis of eigenstate bands the *quasiparticle basis*. To calculate the quantity represented by the matrix O within the quasiparticle basis, the trace in Eqn 1.2 can be transformed into the cluster index basis, giving

$$
\begin{aligned}
\text{tr } O[(\omega + \mu)I - D]^{-1} &= \text{tr } JOJ^\dagger J[(\omega + \mu)I - D]^{-1}J^\dagger \\
&= \text{tr } JOJ^\dagger[(\omega + \mu)I - H_0]^{-1} \\
&= \text{tr } JOJ^\dagger G_{latt} \, ,
\end{aligned} \tag{5.11}
$$

where in the last line the non-interacting Green's function (in the cluster basis) can be recognized and is replaced with the interacting Green's function. Using matrices O with just a single non-zero element on its diagonal gives results corresponding to a single quasiparticle band, and we can calculate the momentum-dependent Green's function $G_{qp}(\omega, \mathbf{k})$ whose imaginary part gives us the full spectral function. Specific examples can be seen in Eqn 5.35 and Eqn 5.45.

If the cluster's symmetry is completely broken in an otherwise non-interacting system, the real quasiparticles of the system will live in the bands of eigenstates described above. For example, on the two sublattices of the 2D square lattice, the quasiparticles at $\mathbf{k}$ are superpositions of the original particles at $\mathbf{k}$ and $\mathbf{k} + (\pi/2a, \pi/2a)$, and both bands only extend to the edges of the first RBZ diamond of Fig. 5.2(b) (p81); expressions outside this region will be umklapped, to reproduce its features periodically. I shall often represent such a system with an extended zone scheme, where (in this case) the second band is drawn in the second RBZ, the remaining half of the original Brillouin zone.

The energy calculation for conventional DMFT (described in §4.3 for the case of two-site DMFT) can easily be extended to cluster DMFT. All quantities in Eqn 4.20 become matrices, and we need to take the trace and then integrate over ω (as in Eqn 1.2).

The non-interacting (or kinetic) energy part $\epsilon_\mathbf{k}$ is simply H_0; the final expression is [98, 99]:

$$E = -\frac{1}{\pi} \int_{-\infty}^{0} d\omega \lim_{\omega \to \omega - i\delta} \sum_{\mathbf{k},\sigma} \mathrm{tr} \left[\left(\mathsf{H}_0(\omega, \mathbf{k}) + \tfrac{1}{2}\Sigma(\omega) \right) \cdot \mathsf{G}_{\mathrm{lat}}(\omega, \mathbf{k}) \right] . \tag{5.12}$$

5.3   Two-site cluster DMFT

In this section I will describe the extension of the two-site DMFT self-consistency procedure (§4.2) as a cluster scheme, according to the formulation in §5.2. The form of the impurity model Hamiltonian is the same as as the non-cluster equivalent (Eqn 4.1):

$$\mathcal{H} = \mathcal{H}_{0,\mathrm{bath}} + \mathcal{H}_{0,\mathrm{imp}\leftrightarrow\mathrm{bath}} + \mathcal{H}_{0,\mathrm{imp}} + \mathcal{H}_{U,\mathrm{imp}} , \tag{5.13}$$

there is a bath connected to an impurity part, that has Hubbard U interactions. $\mathcal{H}_{0,\mathrm{imp}}$ consists of just $-\mu$ and $-t$ terms, and together with $\mathcal{H}_{U,\mathrm{imp}}$ should exactly reproduce the original lattice Hamiltonian for the isolated cluster sites only. As usual, this Hamiltonian should be exactly-diagonalized, and the interacting impurity Green's function $\mathsf{G}_{\mathrm{local}}(\omega)$ calculated according to Eqn 5.4. This Green's function will be a matrix with respect to cluster sites, with elements corresponding to particle excitations within the impurity sector; from the ground state, an electron may be annihilated from one cluster site and recreated at another.

To extract the self energy, we first need the non-interacting impurity Green's function matrix for the cluster, to use in Dyson's equation together with the interacting function. Writing the non-interacting Hamiltonian as a matrix with respect to the impurity or bath sites, gives

$$\mathcal{H}_0 = \begin{pmatrix} \hat{\mathbf{c}}^\dagger & \hat{\mathbf{a}}^\dagger \end{pmatrix} \begin{pmatrix} \mathsf{H}_{0,\mathrm{imp}} & \mathsf{V} \\ \mathsf{V}^\dagger & \epsilon \end{pmatrix} \begin{pmatrix} \hat{\mathbf{c}} \\ \hat{\mathbf{a}} \end{pmatrix} \tag{5.14}$$

where $\hat{\mathbf{c}}$ and $\hat{\mathbf{a}}$ are vectors of impurity and bath operators respectively. $\mathcal{H}_{0,\mathrm{imp}}$ is made up from the $\mathsf{H}_{0\mathrm{imp}}$ submatrix, the non-interacting original tight-binding Hamiltonian for the cluster; $\mathcal{H}_{0,\mathrm{imp}\leftrightarrow\mathrm{bath}}$ is made up from the V_{ij}, the hopping from impurity site i to bath site j; and $\mathcal{H}_{0,\mathrm{bath}}$ is made up from ϵ, the on-site bath site energies and possible hoppings between bath sites.

At the moment, this formulation is completely general, and not specific to two-site DMFT; for example, if V is a $1 \times N$ vector, the Hamiltonian represents a single impurity site connected to a chain of bath sites, and would work for the conventional exact diagonalization procedure (§3.4.2). For two-site DMFT, we generally choose an

equal number of bath sites as impurity sites, making V square.[2] This truncation to a minimal bath is the drastic approximation of two-site cluster DMFT; V needs an infinite length to be able to reproduce a completely arbitrary matrix of functions $\mathscr{G}_0(\omega)$.

V need not be hermitian, as there is no reason why the hopping from impurity site i to bath site j is the same as that from impurity site j to bath site i; the hermiticity of the Hamiltonian is provided by $V^\dagger$. If each submatrix of Eqn 5.14 is 1×1, we recover the original two-site DMFT impurity Hamiltonian, Eqn 4.1.

We wish to integrate out the bath sites; this means inverting the matrix $\omega I - H_0$, throwing away all impurity-connected parts, and reinverting the remaining impurity-part submatrix. In fact, the quantity we shall need is $G_{0,\text{imp}}^{-1}$ so the last reinversion stage is unnecessary. So, writing:

$$\begin{pmatrix} \omega I - H_{0\text{imp}} & -V_0 \\ -V_0^\dagger & \omega I - \epsilon \end{pmatrix}^{-1} = \begin{pmatrix} G_{0,\text{imp}} & X \\ X^\dagger & Y \end{pmatrix} , \tag{5.15}$$

gives the equations

$$I = \omega G_{0,\text{imp}} - H_{0,\text{imp}} G_{0,\text{imp}} - V_0 X^\dagger \tag{5.16}$$

$$0 = \omega X^\dagger - V_0^\dagger G_{0,\text{imp}} - \epsilon X^\dagger , \tag{5.17}$$

and eliminating $X^\dagger$ yields

$$G_{0,\text{imp}}^{-1} = \omega I - H_{0,\text{imp}} - V(\omega I - \epsilon)^{-1} V^\dagger . \tag{5.18}$$

Without loss of generality, we can choose ϵ to be diagonal; if it is not, we can diagonalize it and Eqn 5.18 shows that the matrix of eigenvectors would merely premultiply V, which was arbitrary in the first place. This remains true when interactions are reintroduced, as we can integrate out the bath sites even if the impurity Hamiltonian is non-Gaussian. With a diagonal ϵ, Eqn 5.18 is rather simple, and it is clear that the non-cluster two-site formula Eqn 4.2 is recovered when the quantities are not matrices.

We can now extract the cluster self-energy matrix (*c.f.* Eqn 5.5 and Eqn 4.3 previously): $\Sigma_{\text{local}}(\omega) = G_{0,\text{imp}}^{-1}(i\omega_n) - G_{\text{local}}^{-1}(\omega)$ and construct the lattice Green's function according to Eqn 5.9, using the non-interacting cluster-specific lattice Green's function.

Let us now derive the self-consistency conditions for matching the impurity and lattice matrix Green's functions, *i.e.* the two-site versions of Eqn 5.10. Firstly, we match

---

[2]This is not true if the cluster is large enough to have "internal" sites, *i.e.* not on its boundary. These impurity sites should not have any bath sites attached to them as their environment should be the same as the original Hamiltonian, and V will no longer be square.

the lattice and impurity fillings for each cluster site n_i, which is just a matter of calculating the quantities in Eqn 4.5 for each cluster site separately. This gives N_c self-consistency conditions, where N_c is the number of sites in the cluster.

For the second condition, we wish to characterize quasiparticles by considering the self-energy at low energy. So we find matrices Σ_0 and Σ_1 such that $\Sigma(\omega) = \Sigma_0 + \omega\Sigma_1 + O(\omega^2)$, and define the *quasiparticle residue matrix* Z (*c.f.* Eqn 4.6) as:

$$\mathsf{Z} = \left(\mathsf{I} - \frac{d\Sigma_{\text{local}}}{d\omega}(0)\right)^{-1} = (\mathsf{I} - \Sigma_1)^{-1} . \tag{5.19}$$

Analogously to Eqn 4.7 and Eqn 4.8 we can define coherent lattice and impurity matrix Green's functions

$$
\begin{aligned}
\mathsf{G}_{\text{latt}}^{(\text{coh})}(\mathbf{k}, \omega) &= \left[\omega\mathsf{I} - \mathsf{H}_0(\mathbf{k}) - \Sigma_0 - \omega\Sigma_1\right]^{-1} \\
&= \left[\omega\mathsf{I} - \mathsf{Z}(\mathsf{H}_0(\mathbf{k}) + \Sigma_0)\right]^{-1}\mathsf{Z} \tag{5.20}
\end{aligned}
$$

$$
\begin{aligned}
\mathsf{G}_{\text{imp}}^{(\text{coh})}(\omega) &= \left[\omega\mathsf{I} - \mathsf{H}_{0,\text{imp}} - \mathsf{V}(\omega\mathsf{I} - \epsilon)^{-1}\mathsf{V}^\dagger - \Sigma_0 - \omega\Sigma_1\right]^{-1} \\
&= \left[\omega\mathsf{I} - \mathsf{Z}(\mathsf{H}_{0,\text{imp}} + \mathsf{V}(\omega\mathsf{I} - \epsilon)^{-1}\mathsf{V}^\dagger + \Sigma_0)\right]^{-1}\mathsf{Z} , \tag{5.21}
\end{aligned}
$$

where the definition of G_{latt} has come from Eqn 5.8, and that of G_{imp} from Eqn 5.18. Expanding these at high frequency analogously to Eqn 4.9 and Eqn 4.10 gives for the lattice Green's function

$$
\begin{aligned}
\mathsf{G}_{\text{latt}}^{(\text{coh})}(\mathbf{k}, \omega) &= \frac{1}{\omega}\left[1 - \frac{\mathsf{Z}\left[\Sigma_0 + \mathsf{H}_0(\mathbf{k})\right]}{\omega}\right]^{-1}\mathsf{Z} \\
&\simeq \frac{\mathsf{Z}}{\omega} + \frac{\mathsf{Z}\left[\Sigma_0 + \mathsf{H}_0(\mathbf{k})\right]\mathsf{Z}}{\omega^2} + \frac{\mathsf{Z}\left[\Sigma_0 + \mathsf{H}_0(\mathbf{k})\right]\mathsf{Z}\left[\Sigma_0 + \mathsf{H}_0(\mathbf{k})\right]\mathsf{Z}}{\omega^3} + O(1/\omega^4) ,
\end{aligned}
$$

and for the impurity Green's function

$$
\begin{aligned}
\mathsf{G}_{\text{imp}}^{(\text{coh})}(\omega) &\simeq \frac{1}{\omega}\left[1 - \frac{\mathsf{Z}\left[\Sigma_0 + \mathsf{H}_{0,\text{imp}}\right]}{\omega} - \frac{\mathsf{Z}\mathsf{V}\mathsf{V}^\dagger}{\omega^2} + O(1/\omega^3)\right]^{-1}\mathsf{Z} \\
&\simeq \frac{\mathsf{Z}}{\omega} + \frac{\mathsf{Z}\left[\Sigma_0 + \mathsf{H}_{0,\text{imp}}\right]\mathsf{Z}}{\omega^2} + \frac{\mathsf{Z}\left\{\mathsf{V}\mathsf{V}^\dagger + \left[\Sigma_0 + \mathsf{H}_{0,\text{imp}}\right]\mathsf{Z}\left[\Sigma_0 + \mathsf{H}_{0,\text{imp}}\right]\right\}\mathsf{Z}}{\omega^3} + O(1/\omega^4) .
\end{aligned}
$$

We now compare the Green's functions order-by-order in $1/\omega$. At $O(1/\omega)$ they clearly match, and at $O(1/\omega^2)$ they match as long as:

$$\sum_{\mathbf{k}}\left[\mathsf{H}_0(\mathbf{k}) - \mathsf{H}_{0,\text{imp}}\right] = 0 . \tag{5.22}$$

Consulting Eqn 5.7 (where $H_0(\mathbf{k})$ is defined), $e^{i\mathbf{k}\cdot\Delta\mathbf{R}}$ generally averages to zero, so H^Δ disappears and we are left with just H, which is just the hopping elements within the cluster, and the same as $H_{0,\mathrm{imp}}$. If $e^{i\mathbf{k}\cdot\Delta\mathbf{R}}$ does not average to zero, the energy origin of the lattice dispersion can be shifted.

If Eqn 5.22 is thus satisfied, then the Green's functions match at the next order, $O(1/\omega^3)$, if:

$$\sum_{\mathbf{k}} \left[H_0(\mathbf{k})ZH_0(\mathbf{k}) - H_{0,\mathrm{imp}}ZH_{0,\mathrm{imp}} - VV^\dagger \right] = 0 . \tag{5.23}$$

This provides the second self-consistency equation for cluster two-site DMFT. It is a matrix equation for hermitian matrices, so provides N_c^2 real self-consistency conditions if quantities are complex. The self-consistency condition for non-cluster two-site DMFT (Eqn 4.12) is reproduced if $H_0(\mathbf{k}) \to -\mu - \epsilon_{\mathbf{k}}$, $H_{0,\mathrm{imp}} \to -\mu$, and $V \to V$.

An important question is whether the number of self-consistency conditions is the same as the number of variables. Counting complex numbers as two degrees of freedom, $2N_c^2$ elements of V plus N_c elements of ϵ gives a total of $2N_c^2 + N_c$ variables. But we only found $N_c^2 + N_c$ self-consistency conditions, so there are more variables than can be constrained. Some can be eliminated due to gauge symmetry of the impurity Hamiltonian — the phase of the bath sites can be rotated arbitrarily — but in general there remain too many. We have to make a choice of which variables to keep, and apply some further constraints to our impurity models. This is not a problem as two-site DMFT has already made a somewhat arbitrary choice of degrees of freedom; we are after the simplest possible model in any case, and flexibility in choosing a sensible small set of parameters is an advantage.

In this section, I have again completely ignored spin indices for clarity. Every quantity can be duplicated for $\sigma = \uparrow$ and $\sigma = \downarrow$, and the two spins are only coupled in the exact diagonalization of the impurity Hamiltonian, via the Hubbard U interaction terms.

5.3.1 Pair-cluster (2×1)

This section contains a derivation of the cluster two-site DMFT equations for a cluster consisting of just a pair of sites, a specific instance of the formalism described above (§5.3). I shall only include nearest-neighbour hopping, and work on a 2D square lattice, which is bipartite; every site is a member of one of the two sublattices, and connected only to sites in the other sublattice. Figure 5.2(a) illustrates how the square lattice is divided into pair-clusters. The two cluster sites will represent the two sublattices, and when their spin content is different, the system will have an antiferromagnetic moment. The tight-binding non-interacting Hamiltonian can be divided into clusters
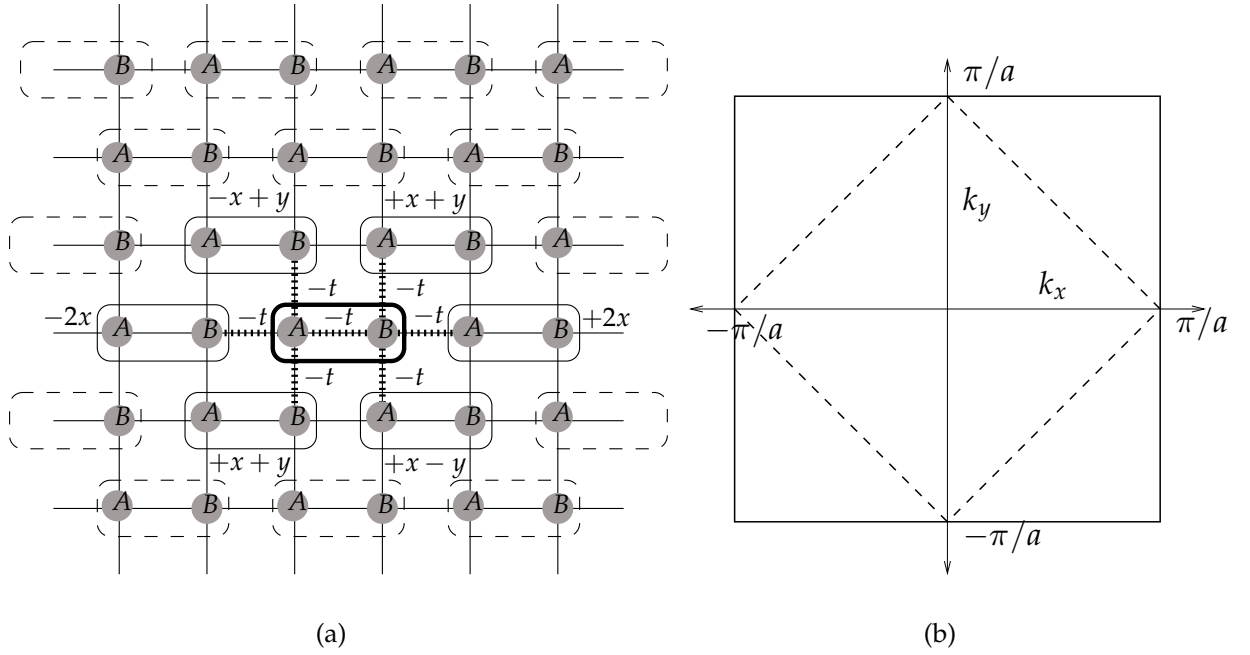
(a)   (b)

Figure 5.2: (a) Division of the 2D square lattice in to clusters consisting of a pair of sites. Each cluster has six neighbouring clusters, at displacements of $(\pm a, \pm a)$ and $(\pm 2a, 0)$, and all hoppings connect a site to the opposite sublattice. (b) All quantities in the Fourier-transformed pair-cluster model have momenta which live in the first reduced Brillouin zone, a diamond shape shown with a dashed line. The second reduced Brillouin zone makes up the rest of the original square.

as Eqn 5.2, and written

$$
\begin{aligned}
\mathcal{H} = -t \sum_{\mathbf{R}} & c^{\dagger}_{\mathbf{R},A} c_{\mathbf{R},B} + c^{\dagger}_{\mathbf{R},B} c_{\mathbf{R},A} \\
& + c^{\dagger}_{\mathbf{R},A} c_{\mathbf{R}+(-2a,0),B} + c^{\dagger}_{\mathbf{R},A} c_{\mathbf{R}+(-a,a),B} + c^{\dagger}_{\mathbf{R},A} c_{\mathbf{R}+(-a,a),B} \\
& + c^{\dagger}_{\mathbf{R},B} c_{\mathbf{R}+(2a,0),A} + c^{\dagger}_{\mathbf{R},B} c_{\mathbf{R}+(a,a),A} + c^{\dagger}_{\mathbf{R},B} c_{\mathbf{R}+(a,a),A} ,
\end{aligned}
\tag{5.24}
$$

where A and B represent the two sites within the cluster, and the superlattice position $\mathbf{R} = n(2a, 0) + m(a, a)$ is the position of the cluster as a whole. Daggered operators are kept in their own cluster: the hermitian conjugates to the last few terms appear in other clusters. Defining a Fourier transform according to Eqn 5.6 gives a reduced Brillouin zone (RBZ) consisting of a diamond shape (see Fig. 5.2(b)), and the Hamiltonian becomes

$$
\begin{aligned}
\mathcal{H} = -t \frac{1}{N} \sum_{\mathbf{R},\mathbf{k},\mathbf{k}'(\text{RBZ})} & e^{i(\mathbf{k}'-\mathbf{k}).\mathbf{R}} c^{\dagger}_{\mathbf{k}',A} c_{\mathbf{k},B} \left[1 + e^{+i2k_xa} + e^{+ik_xa+ik_ya} + e^{+ik_xa-ik_ya} \right] \\
& + c^{\dagger}_{\mathbf{k}',B} c_{\mathbf{k},A} \left[1 + e^{-i2k_xa} + e^{-ik_xa+ik_ya} + e^{-ik_xa-ik_ya} \right] .
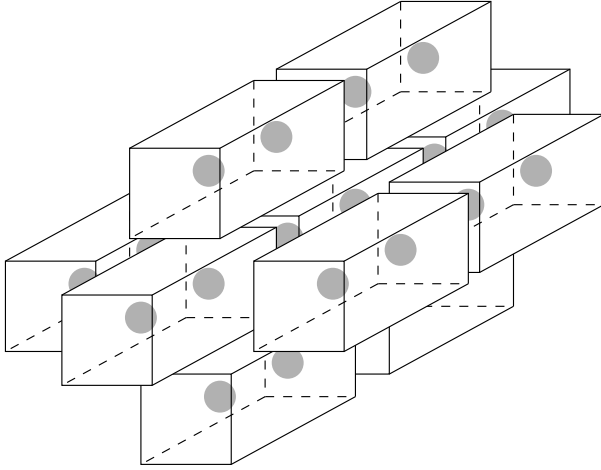\end{aligned}
\tag{5.25}
$$

81

Figure 5.3: An illustration of the pair-cluster scheme extended to three dimensions, showing a a cluster and its ten nearest neighbours. No calculations were done using this scheme; it is shown merely to illustrate the ease of extending the pair-cluster scheme to higher dimensions.
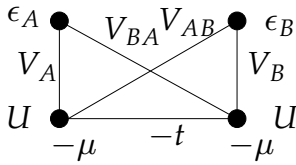

Figure 5.4: Impurity model used for pair-cluster two-site DMFT (*c.f.* Eqn 5.28). There is an impurity site (with a Hubbard U interaction) representing each sublattice A and B, connected together with a $-t$ hopping element from the original lattice; each is connected by various couplings $V_{...}$ to two bath sites with energies $\epsilon_{...}$.

Carrying out the **R** sum gives $N\delta(\mathbf{k}' - \mathbf{k})$, and hence

$$\mathcal{H} = \sum_{\mathbf{k} \in \text{RBZ}} \begin{pmatrix} c_{\mathbf{k},A}^\dagger & c_{\mathbf{k},B}^\dagger \end{pmatrix} \begin{pmatrix} 0 & e^{ik_x a}\epsilon_{\mathbf{k}} \\ e^{-ik_x a}\epsilon_{\mathbf{k}} & 0 \end{pmatrix} \begin{pmatrix} c_{\mathbf{k},A} \\ c_{\mathbf{k},B} \end{pmatrix}, \qquad (5.26)$$

defining the matrix $\mathsf{H}_0(\mathbf{k})$ of Eqn 5.7, where the 2D square lattice dispersion $\epsilon_{\mathbf{k}} = -2t(\cos k_x a + \cos k_y a)$. The Hamiltonian in Eqn 5.26 is valid for an arbitrary number of dimensions, since we can replace the k_y terms with a sum over further dimensions, and these terms will be recollected in $\epsilon_{\mathbf{k}}$; x remains special as the cluster is aligned along this direction. Figure 5.3 shows a representation of a 3D pair-cluster scheme.

To find the true quasiparticles when the cluster symmetry is broken (*c.f.* §5.2.1), we diagonalize this Hamiltonian to give $\mathsf{H}_0(\mathbf{k}) = \mathsf{J}\mathsf{D}\mathsf{J}^\dagger$, where

$$\mathsf{J} = \frac{1}{\sqrt{2}} \begin{pmatrix} 1 & 1 \\ e^{-ik_x a}\text{sgn}\epsilon_{\mathbf{k}} & -e^{-ik_x a}\text{sgn}\epsilon_{\mathbf{k}} \end{pmatrix} \quad \text{and} \quad \mathsf{D} = \begin{pmatrix} |\epsilon_{\mathbf{k}}| & 0 \\ 0 & -|\epsilon_{\mathbf{k}}| \end{pmatrix}. \qquad (5.27)$$

As expected, each eigenstate is identical in the first and second RBZs, and in a single RBZ, both eigenstates together can recreate the complete original dispersion. The second band of quasiparticles is just the upper half of the original dispersion (*i.e.* where $\epsilon_{\mathbf{k}} > 0$). We will use the matrix J to transform between the cluster site (sublattice) operators to bands of real quasiparticles, as described in §5.2.1.

Let us proceed onto the two-site DMFT procedure, and apply §5.3 to the pair-cluster. Each impurity site of the cluster has a bath site attached, and hopping is al-

lowed from either impurity site to either bath site. This impurity model is shown in Fig. 5.4, and its Hamiltonian, divided into submatrices for impurity and bath sites (as Eqn 5.14), is

$$
\mathcal{H} = \sum_\sigma \hat{\mathbf{C}}_\sigma^\dagger
\begin{pmatrix}
0 & -t & V_{A,\sigma} & V_{AB,\sigma} \\
-t & 0 & V_{BA,\sigma} & V_{B,\sigma} \\
V_{A,\sigma}^* & V_{BA,\sigma}^* & \epsilon_{A,\sigma} & 0 \\
V_{AB,\sigma}^* & V_B^* & 0 & \epsilon_{B,\sigma}
\end{pmatrix}
\hat{\mathbf{C}}_\sigma + U \hat{c}_{A\uparrow}^\dagger \hat{c}_{A\uparrow} \hat{c}_{A\downarrow}^\dagger \hat{c}_{A\downarrow} + U \hat{c}_{B\uparrow}^\dagger \hat{c}_{B\uparrow} \hat{c}_{B\downarrow}^\dagger \hat{c}_{B\downarrow} ,
$$

(5.28)

where $\hat{\mathbf{C}}_\sigma^\dagger = \begin{pmatrix} \hat{c}_{A,\sigma}^\dagger & \hat{c}_{B,\sigma}^\dagger & \hat{a}_{A,\sigma}^\dagger & \hat{a}_{B,\sigma}^\dagger \end{pmatrix}$ — recall that impurity sites correspond to $\hat{c}^\dagger$ and bath sites $\hat{a}^\dagger$. As ever, we exactly-diagonalize this many-particle Hamiltonian, and extract a matrix self-energy which is inserted into the lattice Green's function. In matrix form, the impurity Green's function is

$$
\mathsf{G}_{\text{imp}}^{-1}(\omega) =
\begin{pmatrix}
\omega + \mu - \frac{|V_A|^2}{\omega - \epsilon_A} - \frac{|V_{BA}|^2}{\omega - \epsilon_B} - \Sigma_{AA}(\omega) & t - \frac{V_A V_{AB}^*}{\omega - \epsilon_A} - \frac{V_B^* V_{BA}}{\omega - \epsilon_B} - \Sigma_{AB}(\omega) \\
t - \frac{V_A^* V_{AB}}{\omega - \epsilon_A} - \frac{V_B V_{BA}^*}{\omega - \epsilon_B} - \Sigma_{AB}^*(\omega) & \omega + \mu - \frac{|V_{AB}|^2}{\omega - \epsilon_A} - \frac{|V_B|^2}{\omega - \epsilon_B} - \Sigma_{BB}(\omega)
\end{pmatrix}
$$

(5.29)

(using Eqn 5.18), and the lattice Green's function is

$$
\mathsf{G}_{\text{latt}}^{-1}(\mathbf{k}, \omega) =
\begin{pmatrix}
\omega + \mu - \Sigma_{AA}(\omega) & -e^{ik_x a} \epsilon_{\mathbf{k}} - \Sigma_{AB}(\omega) \\
-e^{-ik_x a} \epsilon_{\mathbf{k}} - \Sigma_{AB}^*(\omega) & \omega + \mu - \Sigma_{BB}(\omega)
\end{pmatrix} ,
$$

(5.30)

where I have dropped spin indices for clarity. These two Green's functions should be matched for self-consistency (Eqn 5.10). Within the two-site cluster DMFT scheme (§5.2), this requirement is implemented first by the condition that electron fillings for the impurity and lattice are the same. The impurity fillings can be calculated from the ground state of the exact diagonalized Hamiltonian

$$
n_{\text{imp},A,\sigma} = \langle 0 | \hat{c}_{A\sigma}^\dagger \hat{c}_{A\sigma} | 0 \rangle ; \qquad n_{\text{imp},B,\sigma} = \langle 0 | \hat{c}_{B\sigma}^\dagger \hat{c}_{B\sigma} | 0 \rangle ,
$$

(5.31)

and for the lattice fillings we can use Eqn 1.2; both O and G become matrices in the cluster index basis. For the case of the A sublattice, we have

$$
\begin{aligned}
n_{\text{lat},A} &= \frac{1}{\pi} \int_{-\infty}^{0} d\omega \, \text{Im} \sum_{\mathbf{k}} \text{tr} \begin{pmatrix} 1 & 0 \\ 0 & 0 \end{pmatrix} \begin{pmatrix} \omega + \mu - \Sigma_{AA}(\omega) & e^{ik_x a} \epsilon_{\mathbf{k}} - \Sigma_{AB}(\omega) \\ -e^{-ik_x a} \epsilon_{\mathbf{k}} - \Sigma_{AB}^*(\omega) & \omega + \mu - \Sigma_{BB}(\omega) \end{pmatrix}^{-1} \\
&= \frac{1}{\pi} \int_{-\infty}^{0} d\omega \, \text{Im} \sum_{\mathbf{k}} \frac{\omega + \mu - \Sigma_{BB}}{(\omega + \mu - \Sigma_{AA})(\omega + \mu - \Sigma_{BB}) - |\Sigma_{AB}|^2 - 2\text{Re}[\Sigma_{AB} \epsilon_{\mathbf{k}} e^{-ik_x a}] - \epsilon_{\mathbf{k}}^2} ,
\end{aligned}
$$

(5.32)

where I have again dropped the spin-dependence, and have shown neither the ω dep-

endence of the self-energies nor the analytic continuation explicitly. The second self-consistency condition, Eqn 5.23, gives:

$$\begin{pmatrix} 3t^2 Z_B - |V_A|^2 - |V_{BA}|^2 & V_A V_{AB}^* + V_B^* V_{BA} \\ V_A^* V_{AB} + V_B V_{BA}^* & 3t^2 Z_A - |V_B|^2 - |V_{AB}|^2 \end{pmatrix} \doteq 0 \tag{5.33}$$

where we have carried out the **k**-sums, and Z_A and Z_B are the diagonal elements of the quasiparticle residue matrix Z, calculated from the derivatives of the self-energy matrix $\mathbf{\Sigma}$ at $\omega = 0$ (Eqn 5.19).

As discussed in the previous section, two-site cluster DMFT will be underspecified in general, as there will be more parameters than self-consistency conditions. For the pair-cluster, after choosing V_A, V_B to be real (using gauge symmetry), there are 8 input parameters left (ϵ_A, ϵ_B, V_A, V_B, V_{AB}, V_{BA}, V_{AB}^*, V_{BA}^*) and 6 matching conditions (n_A, n_B, plus the four matrix elements of Eqn 5.33), doubled if spin is included. Continuing our philosophy of adopting the minimal possible implementation of DMFT, so that it may be solved quickly for a wide range of parameters, we choose to take all the cross-hoppings (V_{AB}, V_{BA}, V_{AB}^*, V_{BA}^*) as zero, which leaves four variables and four equations. The off-diagonal elements of Eqn 5.33 are satisfied, and the remainder simplify to

$$3t^2 Z_B \doteq V_A^2$$
$$3t^2 Z_A \doteq V_B^2 . \tag{5.34}$$

The equality of impurity and lattice fillings on each cluster site, together with Eqn 5.34 — all duplicated for the two spin species — provide eight self-consistency conditions for two-site pair-cluster DMFT. The resulting self-consistent solutions will be presented in Chapter 6.

After self-consistency is achieved, we need to calculate further quantities. To compare different phases, the energy of a solution is required, and this is given by Eqn 5.12, using Eqn 5.26 for $\mathsf{H}_0(\mathbf{k})$ and Eqn 5.30 (inverted) for $\mathsf{G}_{\text{latt}}(\mathbf{k}, \omega)$. To determine the spectral weight for a real quasiparticle (in a non-interacting-eigenstate band, rather than in the cluster basis), we can use Eqn 5.11. The quantity $\mathsf{J}0\mathsf{J}^\dagger$ in Eqn 5.11 becomes $\begin{pmatrix} 1 & e^{ik_x a} \\ e^{-ik_x a} & 1 \end{pmatrix}$, giving

$$G(\mathbf{k}, \omega) = \frac{\omega + \mu - \left[\Sigma_A(\omega) + \Sigma_B(\omega)\right]/2 + \epsilon_\mathbf{k} + \Sigma_{AB}(\omega) \cos k_x a}{\left[\omega + \mu - \Sigma_A(\omega)\right]\left[\omega + \mu - \Sigma_B(\omega)\right] - \Sigma_{AB}^2(\omega) - 2\Sigma_{AB}(\omega)\epsilon_\mathbf{k} \cos k_x a - \epsilon_\mathbf{k}^2} , \tag{5.35}$$

for the minimal model where $\Sigma_{AB}(\omega)$ must be real. Evaluating $G(\mathbf{k}, \omega)$ in the second

RBZ gives the second band of quasiparticles.

Eqn 5.35 can be compared with the lattice Green's function used for the study of antiferromagnetism from a single site, Eqn 4.25. Concentrating on the denominators,[3] the form is the same except Σ_{AB} was neglected previously: this self-energy term encapsulates correlations between the sites and its presence will prove to be important. Eqn 5.35 also demonstrates the limited **k**-dependence in an approach involving a small cluster: Fermi surface can only be some combination of the shape provided by the non-interacting dispersion $\epsilon_{\mathbf{k}}$ and a lemon shape corresponding to $\epsilon_{\mathbf{k}} \cos k_x a$. The coefficients of these terms are ω-dependent (from the local self-energies), and the DMFT self-consistency will adjust where in energy each term has an influence — most importantly at $\omega = 0$ where the Fermi surface is formed.

5.3.2 Quad-cluster (2×2)

Whilst the 2×1 cluster produced many interesting results (see Chapter 6), there are artifacts due to the cluster breaking the x-y symmetry of the lattice. Extending to a 2×2 cluster removes this problem, and also means that more Fermi surfaces shapes (such as those with tetragonal symmetry) can be supported. In this section I shall describe the cluster basis and two-site DMFT equations for such a "quad-cluster," providing a second instantiation of the general quantities derived in §5.2 and §5.3.

As previously, the lattice is divided into clusters (illustrated in Fig. 5.5), and the non-interacting lattice Hamiltonian becomes

$$
H_0(\mathbf{k}) = \begin{pmatrix}
0 & -2te^{ik_x a}\cos k_x a & 0 & -2te^{ik_y a}\cos k_y a \\
-2te^{-ik_x a}\cos k_x a & 0 & -2te^{ik_y a}\cos k_y a & 0 \\
0 & -2te^{-ik_y a}\cos k_y a & 0 & -2te^{-ik_x a}\cos k_x a \\
-2te^{-ik_y a}\cos k_y a & 0 & -2te^{ik_x a}\cos k_x a & 0
\end{pmatrix}, \quad (5.36)
$$

as a matrix with respect to cluster sites. Diagonalization is straightforward and gives four eigenvalues

$$
\begin{pmatrix}
+2t(-\cos k_x a - \cos k_y a) \\
+2t(+\cos k_x a + \cos k_y a) \\
+2t(+\cos k_x a - \cos k_y a) \\
+2t(-\cos k_x a + \cos k_y a)
\end{pmatrix}, \quad (5.37)
$$

---

[3]We should really be comparing with Eqn 4.25 transformed to the quasiparticle basis; this is why there are differences in the numerator.

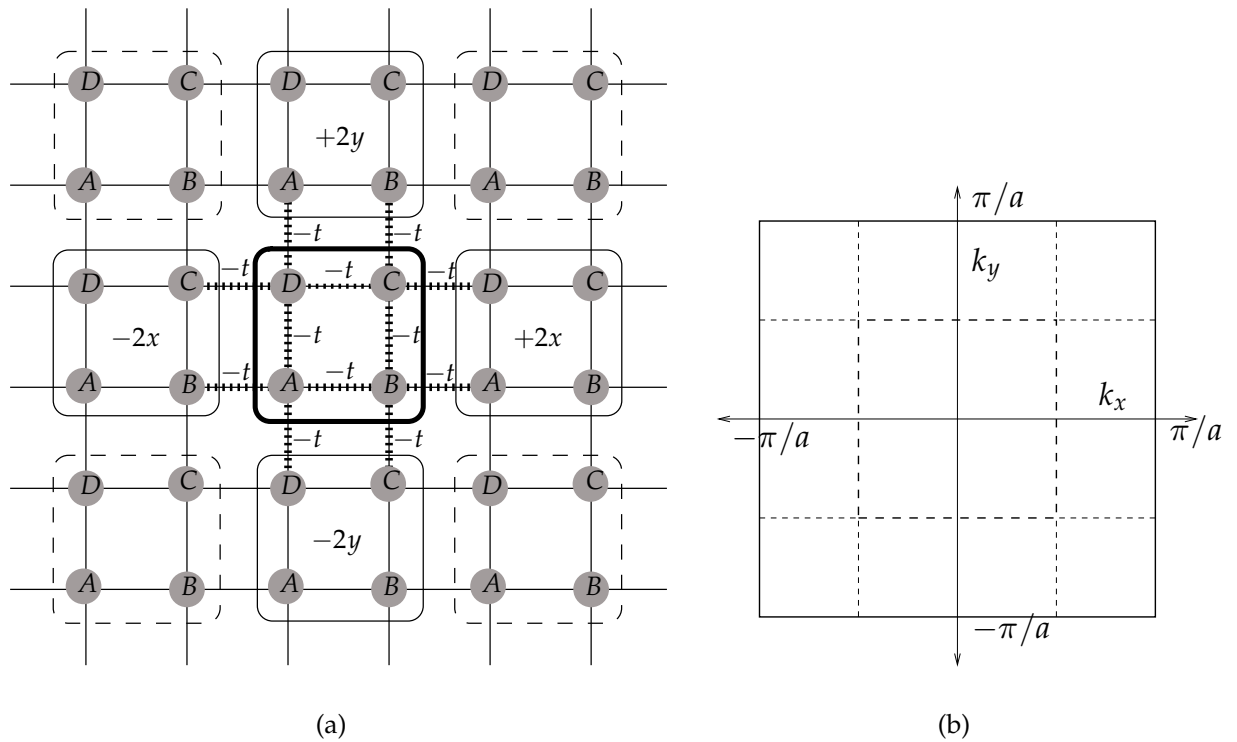(a)   (b)

Figure 5.5: (a) Division of the 2D square lattice into clusters consisting of four sites in a 2×2 arrangement. Each cluster has four neighbouring clusters, at displacements of $(\pm 2a, 0)$ and $(0, \pm 2a)$; care needs to be taken in establishing which cluster site of the neighbour is hopped to from each original cluster site. (b) All quantities in the Fourier-transformed quad-cluster model have momenta which live in the first reduced Brillouin zone, which is a smaller square, shown with a dashed line. Three other reduced Brillouin zones make up the rest of the original zone.

Figure 5.6: Impurity model used for quad-cluster two-site DMFT (*c.f.* Eqn 5.39). There are four impurity sites (with a Hubbard U interactions), connected together with $-t$ hopping elements from the original lattice; each is connected by various couplings $V_{...}$ to four bath sites with energies $\epsilon_{...}$.

forming the diagonal of D, and four eigenvectors making up

$$
\mathsf{J} = \frac{1}{2}
\begin{pmatrix}
1 & 1 & 1 & 1 \\
e^{-ik_x a} & -e^{-ik_x a} & -e^{-ik_x a} & e^{-ik_x a} \\
e^{-ik_x a - ik_y a} & e^{-ik_x a - ik_y a} & -e^{-ik_x a - ik_y a} & -e^{-ik_x a - ik_y a} \\
e^{-ik_y a} & -e^{-ik_y a} & e^{-ik_y a} & -e^{-ik_y a}
\end{pmatrix} .
\tag{5.38}
$$

The two-site impurity model with a bath site attached to each site in the cluster is illustrated in Fig. 5.6, and the non-interacting Hamiltonian in the matrix form of Eqn 5.14 has elements

$$
\mathsf{H}_{0,\text{imp}} =
\begin{pmatrix}
0 & -t & 0 & -t \\
-t & 0 & -t & 0 \\
0 & -t & 0 & -t \\
-t & 0 & -t & 0
\end{pmatrix}
\quad \text{and} \quad
\mathsf{V} =
\begin{pmatrix}
V_A & V_{AB} & V_{AC} & V_{AD} \\
V_{BA} & V_B & V_{BC} & V_{BD} \\
V_{CA} & V_{CB} & V_C & V_{CD} \\
V_{DA} & V_{DB} & V_{DC} & V_D
\end{pmatrix} .
\tag{5.39}
$$

As previously, the interacting impurity Hamiltonian is exactly-diagonalized to give the interacting impurity Green's function. According to Dyson's equation (Eqn 5.5), we can extract the 4×4 matrix self-energy, using the non-interacting Green's function (calculated using Eqn 5.18). Combining the self-energy with the matrix non-interacting lattice Green's function $\left[(\omega + \mu)\mathsf{I} - \mathsf{H}_0(\mathbf{k}) \right]^{-1}$ gives the lattice Green's function. Finally, this is compared with the impurity Green's function by means of fillings and the quasi-particle weight condition (Eqn 5.23).

(a) Spin-↑ electrons   (b) Spin-↓ electrons

Figure 5.7: Impurity model used for 2×2 cluster calculations, reduced to the minimal set of parameters to study antiferromagnetism.

However, in practice this gives a solution space with a large number of dimensions, and a greater mismatch of numbers of parameters and constraints than before. So, we look for a reduced implementation with the minimal possible number of variables that will permit self-consistency: as a first stage we just want greater flexibility in **k**-space than the 2×1 cluster.

In the implementation I have chosen, I choose to look only for antiferromagnetism and paramagnetism, and so take every quantity on site C to be the same as site A, and every quantity on site D to be the same as site B; and up spins on A sites are the same as down spins on B sites, and so on. Physically, this will also mean that x-y symmetry may not be broken (unlike the 2×1 cluster), although other momentum-space distortions will still be permitted. There are now just two different site energies (ϵ_A and ϵ_B) and six different couplings (V_A, V_B, V_{AB}, V_{BA}, V_{AC} and V_{BD}), which we constrain to real numbers for simplicity. This impurity model is illustrated in Fig. 5.7, and the matrices entering the Hamiltonian in Eqn 5.14 are

$$
\mathsf{V}_{0,\uparrow} = \begin{pmatrix} V_A & V_{AB} & V_{AC} & V_{AB} \\ V_{BA} & V_B & V_{BA} & V_{BD} \\ V_{AC} & V_{AB} & V_A & V_{AB} \\ V_{BA} & V_{BD} & V_{BA} & V_B \end{pmatrix} , \qquad \epsilon_\uparrow = \begin{pmatrix} \epsilon_A & 0 & 0 & 0 \\ 0 & \epsilon_B & 0 & 0 \\ 0 & 0 & \epsilon_A & 0 \\ 0 & 0 & 0 & \epsilon_B \end{pmatrix} ,
$$

$$
\mathsf{V}_{0,\downarrow} = \begin{pmatrix} V_B & V_{BA} & V_{BD} & V_{BA} \\ V_{AB} & V_A & V_{AB} & V_{AC} \\ V_{BD} & V_{BA} & V_B & V_{BA} \\ V_{AB} & V_{AC} & V_{AB} & V_A \end{pmatrix} , \qquad \epsilon_\downarrow = \begin{pmatrix} \epsilon_B & 0 & 0 & 0 \\ 0 & \epsilon_A & 0 & 0 \\ 0 & 0 & \epsilon_B & 0 \\ 0 & 0 & 0 & \epsilon_A \end{pmatrix} . \tag{5.40}
$$

The matrix impurity Green's functions now have certain symmetries, exhibiting

five degrees of freedom:

$$
\mathsf{G}_{\text{imp},\uparrow}^{-1} = \begin{pmatrix} G_A & G_{AB} & G_{AC} & G_{AB} \\ G_{AB} & G_B & G_{AB} & G_{BD} \\ G_{AC} & G_{AB} & G_A & G_{AB} \\ G_{AB} & G_{BD} & G_{AB} & G_B \end{pmatrix}, \qquad \mathsf{G}_{\text{imp},\downarrow}^{-1} = \begin{pmatrix} G_B & G_{AB} & G_{BD} & G_{AB} \\ G_{AB} & G_A & G_{AB} & G_{AC} \\ G_{BD} & G_{AB} & G_B & G_{AB} \\ G_{AB} & G_{AC} & G_{AB} & G_A \end{pmatrix} \tag{5.41}
$$

and for the non-interacting Green's function the elements are

$$
G_A = \omega + \mu - \frac{V_A^2 + V_{AC}^2}{\omega - \epsilon_A} - \frac{2V_{AB}^2}{\omega - \epsilon_B} , \qquad\qquad G_B = \omega + \mu - \frac{V_B^2 + V_{BD}^2}{\omega - \epsilon_B} - \frac{2V_{BA}^2}{\omega - \epsilon_A} ,
$$

$$
G_{AB} = t - V_{BA}\frac{V_A + V_{AC}}{\omega - \epsilon_A} - V_{AB}\frac{V_B + V_{BD}}{\omega - \epsilon_B} ,
$$

$$
G_{AC} = -\frac{2V_A V_{AC}}{\omega - \epsilon_A} - \frac{2V_{AB}^2}{\omega - \epsilon_B} \qquad \text{and} \qquad G_{BD} = -\frac{2V_B V_{BD}}{\omega - \epsilon_B} - \frac{2V_{BA}^2}{\omega - \epsilon_A} , \tag{5.42}
$$

using Eqn 5.18. The interacting Green's function is calculated by exact diagonalization, and inverted (taking advantage of the symmetry). From these two Green's functions the self-energy matrix can be calculated (which has the same symmetries as Eqn 5.41), and the lattice Green's function constructed: $\mathsf{G}_{\text{latt},\uparrow}^{-1}(\omega, \mathbf{k}) =$

$$
\begin{pmatrix} \omega + \mu - \Sigma_A & 2te^{ik_x}\cos k_x - \Sigma_{AB} & -\Sigma_{AC} & 2te^{ik_y}\cos k_y - \Sigma_{AB} \\ 2te^{-ik_x}\cos k_x - \Sigma_{AB} & \omega + \mu - \Sigma_B & 2te^{ik_y}\cos k_y - \Sigma_{AB} & -\Sigma_{BD} \\ -\Sigma_{AC} & 2te^{-ik_y}\cos k_y - \Sigma_{AB} & \omega + \mu - \Sigma_A & 2te^{-ik_x}\cos k_x - \Sigma_{AB} \\ 2te^{-ik_y}\cos k_y - \Sigma_{AB} & -\Sigma_{BD} & 2te^{ik_x}\cos k_x - \Sigma_{AB} & \omega + \mu - \Sigma_B \end{pmatrix} \tag{5.43}
$$

where each Σ depends on ω, and $k_x \to k_x a$, $k_y \to k_y a$. $\mathsf{G}_{0,\text{latt},\downarrow}$ is similar, with $\Sigma_A \leftrightarrow \Sigma_B$ and $\Sigma_{AC} \leftrightarrow \Sigma_{BD}$.

Moving on to self-consistency conditions, there are two fillings ($n_{A\uparrow} = n_{B\downarrow}$ and $n_{B\uparrow} = n_{A\downarrow}$) which must be the same for the impurity (*c.f.* Eqn 5.31) and lattice (Eqn 5.32, with G_{latt} from Eqn 5.43). For the quasiparticle residue conditions, we use Eqn 5.23 to determine

$$
V_A^2 + V_{AC}^2 + 2V_{AB}^2 = 2t^2 Z_B , \qquad V_B^2 + V_{BD}^2 + 2V_{BA}^2 = 2t^2 Z_A ,
$$

$$
V_{BA}(V_A + V_{AC}) + V_{AB}(V_B + V_{BD}) = t^2 Z_{AB} ,
$$

$$
2V_{AB}^2 + 2V_A V_{AC} = 0 \qquad \text{and} \qquad 2V_{BA}^2 + 2V_B V_{BD} = 0 , \tag{5.44}
$$

where Z_A, Z_B and Z_{AB} are elements of the Z matrix, labelled similarly to above; this set of equations is identical whether derived for $\uparrow$ or $\downarrow$ spins. Notice that we cannot now

choose $V_{AB} = V_{BA} = 0$ as we did for the 2×1 cluster.

Counting up, the problem is still underspecified: there are eight parameters (ϵ_A, ϵ_B, V_A, V_B, V_{AB}, V_{BA}, V_{AC} and V_{BD}) but only seven self-consistency conditions (n_A, n_B plus five in Eqn 5.44). We arbitrarily choose $V_{AB} = V_{BA}$; whilst there is no physical justification for this, we have just constrained the bath slightly more, and self-consistent solutions remain valid. In practice self-consistency is possible with this constraint, and moreover different relationships such as $V_{AB} = -V_{BA}$ could produce the same resulting state, indicating the choice really is somewhat arbitrary.

The last two equations of Eqn 5.44 are not dependent on any self-consistent quantities (*i.e.* Z) and thus constrain the impurity model from the outset — the equations are satisfied by choosing $V_{AC} = -V_{AB}^2/V_A$ and $V_{BD} = -V_{BA}^2/V_B$. The final number of degrees of freedom is thus five (plus one for n_total and μ), a number easily manageable computationally.

Expressions for the energy of a solution and quasiparticle Green's functions may be produced straightforwardly, similarly to the previous section (§5.3.1), making use of Eqn 5.36 and Eqn 5.43. The expressions are too long to quote, but it is worth noting

$$
\mathsf{JOJ}^\dagger = \begin{pmatrix} 1 & e^{ik_x a} & e^{ik_x a + ik_y a} & e^{ik_y a} \\ e^{-ik_x a} & 1 & e^{ik_y a} & e^{-ik_x a + ik_y a} \\ e^{-ik_x a - ik_y a} & e^{-ik_y a} & 1 & e^{-ik_x a} \\ e^{-ik_y a} & e^{ik_x a - ik_y a} & e^{ik_x a} & 1 \end{pmatrix} , \tag{5.45}
$$

which is to be used in Eqn 5.11 to calculate quasiparticle Green's functions. We can determine the momentum dependences that are permitted within the lattice Green's function:[4] its denominator is made up of a linear combination of the five functions

$$
\left\{ \cos^2 k_x a + \cos^2 k_y a, \quad \left[\cos^2 k_x a - \cos^2 k_y a \right]^2, \quad \cos^2 k_x a \cos 2k_x a + \cos^2 k_y a \cos 2k_y a, \right.
$$
$$
\left. \cos k_x a \cos k_y a \cos(k_x a + k_y a), \quad \cos k_x a \cos k_y a \cos(k_x a - k_y a) \right\} , \tag{5.46}
$$

the coefficient of each being ω-dependent. These constitute the shape of the dispersion for a single RBZ only (the first RBZ is the small square extending to $\mathbf{k} = (\pi/2a, \pi/2a)$, *c.f.* Fig. 5.5(b)).

The phase diagram and details of the ground state spectral functions for quadcluster two-site DMFT are presented in Chapter 7.

---

[4]For comparison with the pair-cluster lattice Green's function case, see the discussion following Eqn 5.35.

Next-nearest-neighbour hopping

A next-nearest-neighbour t' term in the lattice Hamiltonian allows study of the effects of geometrical frustration and changes in Fermi surface shape, and in particular separates half-filling from the van Hove points. In this section I shall describe how such a term can be implemented within two-site quad-cluster DMFT. The t' allows hopping diagonally on the square lattice, so that each site is additionally connected to four other sites on the same sublattice. The remaining zero off-diagonal elements of the non-interacting lattice Hamiltonian, Eqn 5.36, become terms with a form $-2t'e^{ik_x a + ik_y a}\cos k_x a \cos k_y a$, and its eigenstates (providing the bare dispersion) are of the form $-2t(\cos k_x a + \cos k_y a) - 2t'\cos k_x a \cos k_y a$, with changes of sign for $\cos k_x a$ and $\cos k_y a$ as Eqn 5.37. Calculations of the lattice Green's function, and hence lattice filling and quasiparticle Green's function must be altered to include these terms, although J remains the same as previously.

The non-interacting part of the impurity Hamiltonian has extra terms similarly, becoming

$$
\mathsf{H}_{0,\text{imp}} = \begin{pmatrix} 0 & -t & -t'/2 & -t \\ -t & 0 & -t & -t'/2 \\ -t'/2 & -t & 0 & -t \\ -t & -t'/2 & -t & 0 \end{pmatrix}
\tag{5.47}
$$

(note that an actual hopping of $t'/2$ gives the conventional definition of t' with complete frustration at $t' = t$). The self-consistency conditions for the reduced implementation (Eqn 5.44) are slightly altered, becoming

$$
V_A^2 + V_{AC}^2 + 2V_{AB}^2 = 2t^2 Z_B + \tfrac{3}{4}t'^2 Z_A + 2tt'Z_{AB}
$$
$$
V_B^2 + V_{BD}^2 + 2V_{BA}^2 = 2t^2 Z_A + \tfrac{3}{4}t'^2 Z_B + 2tt'Z_{AB}
$$
$$
V_{BA}(V_A + V_{AC}) + V_{AB}(V_B + V_{BD}) = (t^2 + \tfrac{1}{4}t'^2)Z_{AB} + \tfrac{1}{2}t't(Z_A + Z_B)
\tag{5.48}
$$

(the conditions that do not involve Z are unaltered).

5.4 Summary

Extending dynamical mean-field theory to cluster DMFT allows lattice geometry to play a rôle, so that magnetic phases may be compared consistently, and quantities are permitted a momentum dependence beyond that of the non-interacting dispersion — the theory is no longer restricted to infinite dimensions. Although cluster DMFT does not necessarily provide a rigorous extension to a finite number of dimensions, it is an

improvement upon DMFT, and the exact limit of infinite cluster size is approached. The self-consistency can be regarded as a rather sophisticated boundary condition on a cluster, which becomes increasingly unimportant as the cluster size is increased.

In this chapter, I have described cluster DMFT in detail, and presented for the first time a combination of two-site DMFT with cluster DMFT. The ease of solving the two-site DMFT equations means that cluster DMFT can be studied in reasonable time on a moderately-specified computer. Two-site cluster DMFT cannot generically provide enough constraints for all its input parameters, and in general we need to choose degrees of freedom to discard. We are already working in a reduced subspace of solutions to DMFT, so this is acceptable: there are already types of solutions which cannot be represented.

I have concentrated on two different shapes of small cluster. First, a 2×1 pair-cluster, as a minimum representation of a bipartite lattice, which has the potential to exhibit ferromagnetic, antiferromagnetic, ferrimagnetic and charge-ordered phases; results are presented in Chapter 6 and have been published [16]. Second, a 2×2 cluster formulation was described, necessary since the reduced symmetry of the 2×1 cluster produces artifacts. Such a quad-cluster has the potential to exhibit a wealth of symmetry broken phases (such as a spontaneous current around a plaquette), but I have restricted calculations to a minimal representation of antiferromagnetism, which has a more manageable number of degrees of freedom. Results for this cluster will be presented in Chapter 7.

There are endless possibilities for extending the work presented here. The cluster size could be increased and the model still remain solvable in a reasonable time. Two-site cluster DMFT could form the kernel of more advanced DMFT calculations, such as including orbital degrees of freedom to model real materials. And alternatively to such approaches focused on extending DMFT, two-site cluster DMFT could be used as an superior alternative to simple periodic boundary conditions for any many-body calculation on a finite-sized cluster.

Chapter 6

RESULTS: 2×1 PAIR-CLUSTER

Vér skulum gera elda þrjá. Skuluð þér heiðnir
menn vígja einn en eg annan en hinn þriðji
skal óvígður vera. En ef berserkurinn hræðist
þann einn eldinn er eg vígi en veður hina báða
þá skuluð þér taka við trú.

We shall kindle three fires. You heathen are to
hallow one of the fires, I shall hallow the second,
and the third fire is to remain unhallowed. If the
berserk is afraid of the fire I hallow, but walks
unscathed through your fire, then you must accept
the new faith.

NJAL'S SAGA [111]

6.1 Introduction

The previous chapter contained a description of the theory for two-site pair-cluster dynamical mean-field theory (§5.3.1), which is probably the simplest possible implementation of dynamical mean-field theory that can handle antiferromagnetic order consistently. This chapter presents results of a detailed investigation with this model of the phase diagram and quasiparticle properties of the single band Hubbard model (Eqn 1.1) on a square lattice. The work has been the subject of a recent publication [16].

At each point in the Hubbard model parameter space (U, n), there are in general several self-consistent solutions; locating these solutions initially is not straightforward. Often one must resort to beginning the self-consistency procedure with random (but sensible) bath parameters. Subsequently the parameters can seed the procedure for neighbouring points. When the full extent of each such phase has been found, the phase diagram is constructed by comparing the energy of every phase at each (U, n) and identifying the ground state.

There are several physical features which may then be used to distinguish the phases. First, the magnetic order — the pair-cluster can support paramagnetism, ferromagnetism, antiferromagnetism and ferrimagnetism. There are, however, phases with the same magnetic order that are distinct, and these must be distinguished with reference to the spectral function $A(\mathbf{k}, \omega)$. From this we can calculate, for example, the electron density across the Brillouin zone $n_{\mathbf{k}}$, from which the Fermi surface is visible, or the local density of states. Analysing these quantities may lead to physical interpretations of each of the phases, giving insight to the important physics. More importantly, expected experimental quantities can be calculated and comparison can be made with experiments such as photoemission spectroscopy. The two-site cluster DMFT method has the huge advantage that any such quantity can be calculated quickly and easily. We will be able to see complete details of a truly interacting system; we are not constrained to start out with a system with a Fermi surface, for instance, and could investigate how a Fermi surface could distort or even vanish, and what characterizes whatever is left behind.

In the next section (§6.2) I shall detail the phase diagram for two-site pair-cluster DMFT, and give the quasiparticle properties of each phase in terms of the spectral function $A(\mathbf{k}, \omega)$, density of states $\rho(\omega)$ and electron filling $n_{\mathbf{k}}$, objectively and without reference to the detailed theory behind the calculations (for this, see Chapter 5, §5.3.1). I shall discuss these results more subjectively in §6.3, providing an physical interpretation for each of the phases, and discussing a number of important issues. I shall compare with other theoretical models and relevant experiments. The results

give important insights into the Mott transition when antiferromagnetism is present — finally combining Slater's approach to the metal-insulator transition with that of Brinkman–Rice — and also into the strange pseudogap phase of the high-temperature superconducting cuprate materials.

6.2   Phase diagram

The 2D Hubbard model on a square lattice is investigated within two-site pair-cluster DMFT, for the Hubbard repulsion in the range $0 \leq U/t \leq 30$, and electron fillings $0.75 \leq n \leq 1$, where 1 is half-filling. Within the calculations (see also Appendix C), densities of states (to integrate for the electron filling or to plot spectral quantities) are evaluated as the imaginary part of a lattice Green's function with an analytic continuation $\omega \to \omega + i\delta$; typically $\delta \sim 0.005t$. **k**-space sums are carried out with $K = 120$ points across the Brillouin zone; the results are not sensitive to changes in either of these parameters.

The ground state phase diagram is shown in Fig. 6.1. Fillings above $n = 0.98$ are ignored since the **k**-space resolution is insufficient to give an accurate representation of the Fermi surface here, except at exactly half-filling where this is not an issue. For $n > 1$ the results will be the same ($n \to 2 - n$), since the model is particle-hole symmetric; and outside the region shown, the phase boundaries are expected to continue with little change. Self-consistent solutions for charge-ordered and ferrimagnetic phases were present, but never energetically favoured. Fig. 6.2(a) shows the variation of the quasiparticle weight z across the phase diagram, which is still very similar to the simple two-site DMFT picture of Fig. 4.3.

The phase diagram is demarcated by the regions where two different symmetries are each broken. First, antiferromagnetism is prominent, and there are three separate phases with this order. Fig. 6.2(b) shows how the sublattice magnetization varies across the phase diagram; the variation is comparable with that of non-cluster two-site DMFT (Fig. 4.8), and the extent of antiferromagnetism again very much less than that predicted by Hartree–Fock theory. The boundary between phase (b) and phase (c) is a second-order phase transition, in contrast to all the other boundaries which are first order and show a jump in magnetization — owing to a different phase becoming the ground state at that point.

Second, there is a breaking of x-y symmetry, which is like a Pomeranchuk instability, and can lead to quite severe Fermi surface distortions. Phases (b) and (c) have such a distortion, although all phases exhibit a slight distortion at very high U. The non-interacting model should exhibit a non-distorted Fermi surface, and indeed in phase (b) at very small U there is a smooth increase in the deviation from
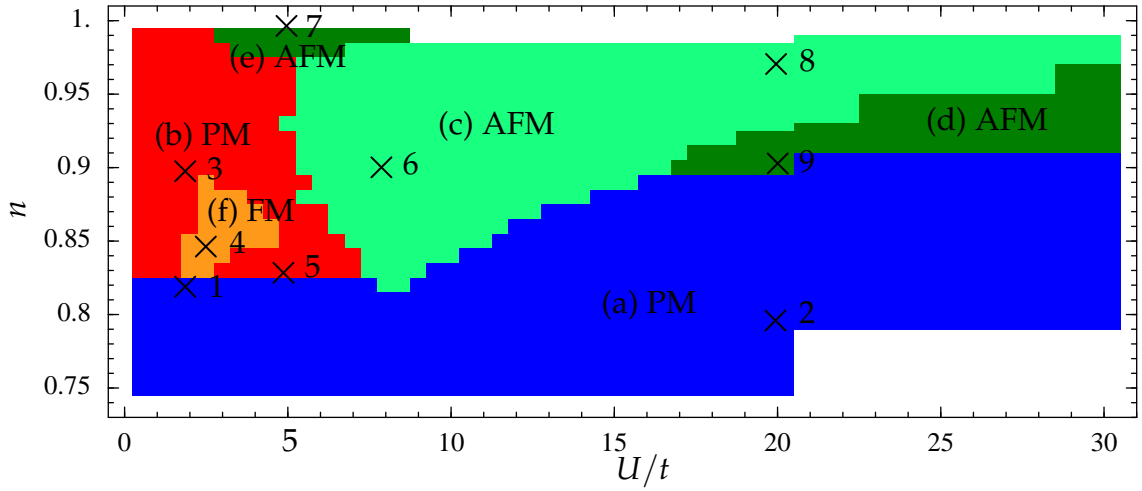
Figure 6.1: Ground state phase diagram $(U/t, n)$ for the 2D Hubbard model within two-site pair-cluster DMFT. Distinct solutions are different colours, and labelled (a) paramagnetism, (b) distorted paramagnetism, (c) distorted antiferromagnetism, (d) and (e) antiferromagnetism, and (f) ferromagnetism. At exactly half-filling the ground state is an antiferromagnet the same as phase (e). These phases characterized further in the text, and detailed spectra will be presented for the numbered points.
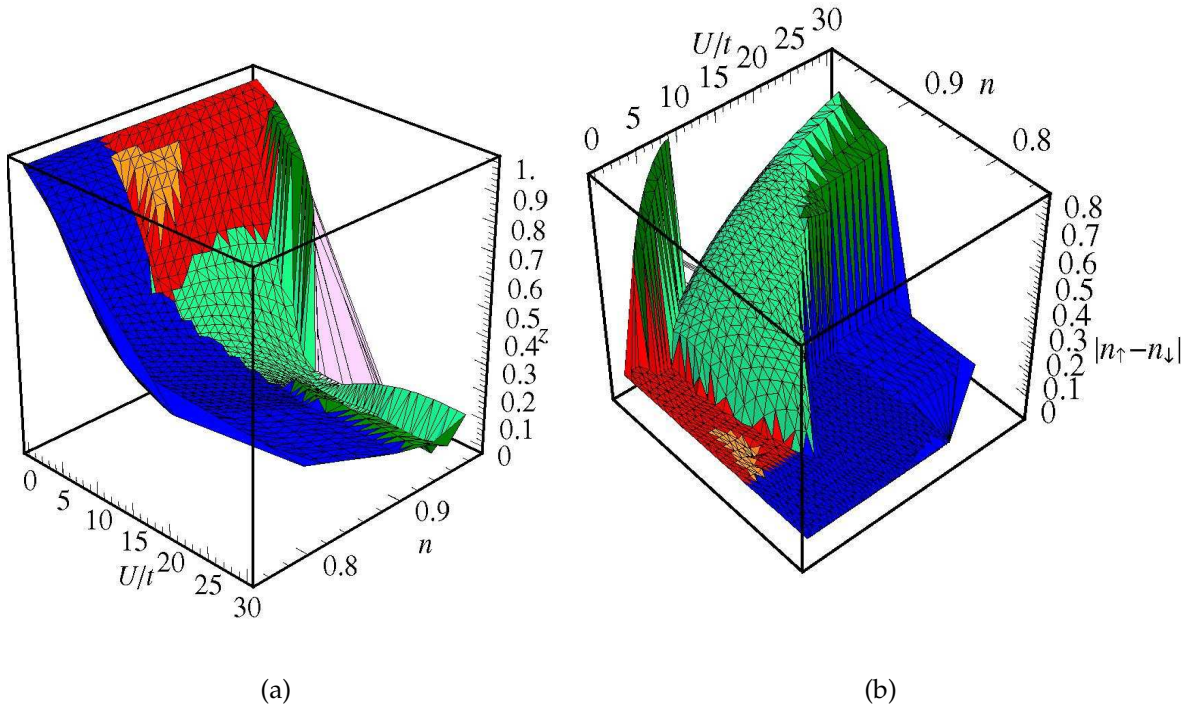
Figure 6.2: (a) Quasiparticle weight z (sublattice averaged) and (b) sublattice magnetization $|n_\uparrow - n_\downarrow|$ as a function of (U, n) for the ground state solutions of two-site pair-cluster DMFT. The quasiparticle weight behaves similarly to pure two-site DMFT (Fig. 4.3). In (b) ferromagnetic order is represented by a negative magnetization.
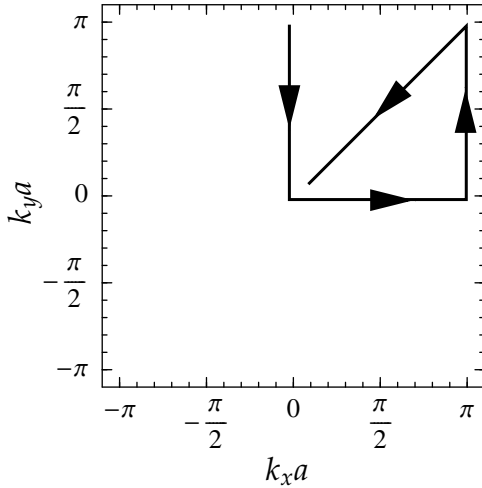
Figure 6.3: The arrow indicates the path $(0, \pi) \to (0,0) \to (\pi, 0) \to (\pi, \pi) \to (0,0)$ taken in **k**-space, that is used to present cross-sections of the spectral function and the electron filling.

symmetry. Quantitatively, we can define a r.m.s. deviation, D, as a normalized sum $D^2 = \sum_{k=0}^{\pi/a} [n_{(k,0)} - n_{(0,k)}]^2$, which can be used to define a phase boundary corresponding to $D \sim 0.1$ (an arbitrary choice which makes little difference); this reaches $U \sim 0.5t$ at $n = 0.83$. In contrast, the horizontal boundary between phases (a) and (b) corresponds to a first order transition with a jump in energy, as the distorted solution does not exist below $n \sim 0.83$. Points 3, 5, 6, 8 and 9 (*c.f.* Fig. 6.1) provide a comprehensive picture of the effects of the distortion, and the phenomenon will be discussed in detail in §6.3.4.

I shall now present details of the nine example points indicated in Fig. 6.1, by means of different perspectives on the spectral function $A(\mathbf{k}, \omega)$, which is the imaginary part of the quasiparticle lattice Green's function (Eqn 5.35), at a small analytical continuation $\omega \to \omega - i\delta$. When antiferromagnetic symmetry is broken, values of **k** plotted in the second reduced Brillouin zone (RBZ) actually represent the second band of quasiparticles from the first Brillouin zone, *i.e.* at $\mathbf{k} - (\pi, \pi)$.

The spectral function will be plotted directly, as a density plot with darker regions indicating greater spectral weight, along a cross-section following the path across the Brillouin zone shown in Fig. 6.3. The path includes the $(0, \pi)$ section in addition to the $(\pi, 0)$ section in order to illustrate the *x-y* symmetry breaking. To visualize features like the Fermi surface, a density plot of the electron filling across the Brillouin zone, $n_{\mathbf{k}} = \int_{-\infty}^{0} d\omega A(\mathbf{k}, \omega)$, is shown as a density plot. The scale 0 ▬▬ 1 is used, so that regions filled with electrons appear dark; a Fermi surface follows the discontinuities in $n_{\mathbf{k}}$, so the graph for non-interacting free electrons would be a sharply demarcated black circle. In some cases I also show $n_{\mathbf{k}}$ as a cross-section along the path of Fig. 6.3, similarly to the spectral function. The final quantity presented is the local density of states $\rho(\omega) = \sum_{\mathbf{k}} A(\mathbf{k}, \omega)$. All these quantities are normalized appropriately and, unless stated otherwise, have been averaged over both sublattice and spin.

6.2.1   Point 1: Paramagnetism at weak interactions

Point 1 (at $U = 2t$, $n = 0.82$, see graphs in Fig. 6.4), lying in phase (a), illustrates a conventional paramagnetic metal. A clear Fermi surface is visible: there is a discontinuity in $n_{\mathbf{k}}$ at the places where the dispersion crosses the chemical potential (*i.e.* $\omega = 0$), and here $n_{\mathbf{k}}$ jumps from almost unity to zero. A few flat (*i.e.* local) features in the spectrum show an initial signature of U. The density of states is almost the typical 2D tight-binding dispersion, with step-function edges and a singularity at the van Hove point.
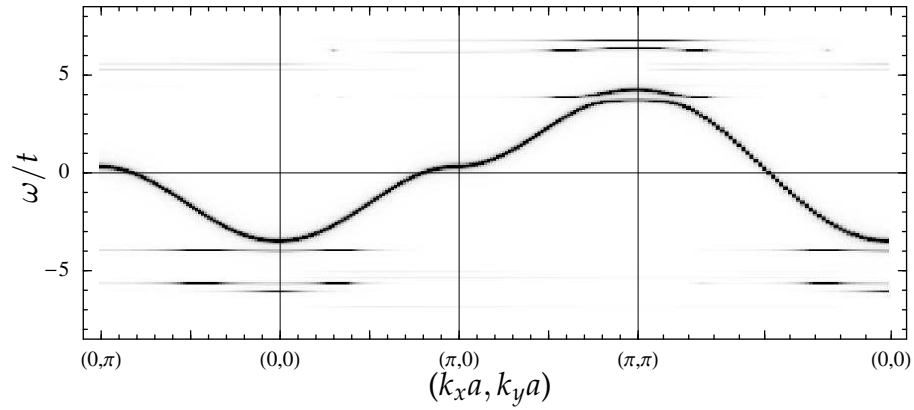
(a) Spectral function cross-section; dark ↔ greater spectral weight
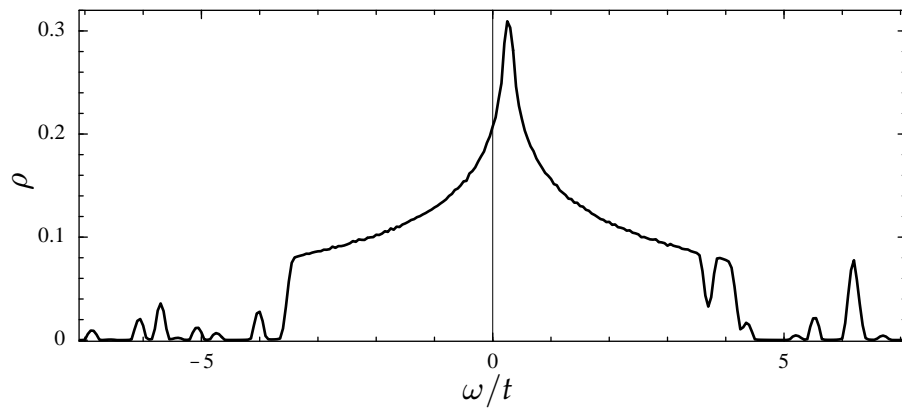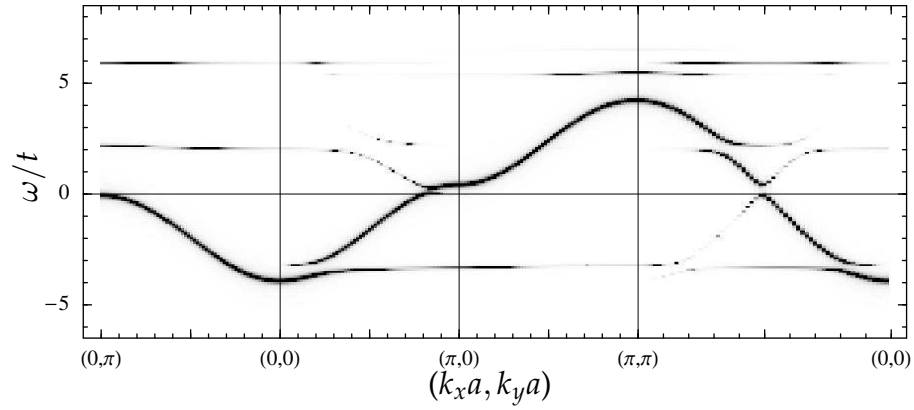

(b) Local density of states, smoothed
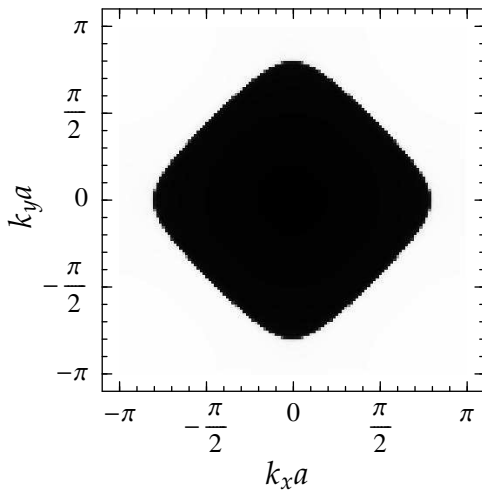
(c) $n_{\mathbf{k}}$ across Brillouin zone
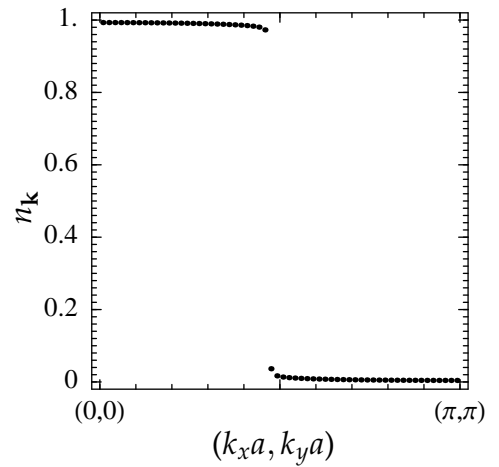
(d) $n_{\mathbf{k}}$ along cross-section in **k**-space

Figure 6.4: Point 1 ($U = 2t$, $n = 0.82$). Paramagnetism with weak interactions; see §6.2.1 for discussion.

6.2.2   Point 2: Paramagnetism at strong interactions

Point 2 ($U = 20t$, $n = 0.8$, see graphs in Fig. 6.5) illustrates a solution at a much greater interaction strength. Phase (a) is still a conventional metallic paramagnet, but effects of the local interaction have a significant effect and the metal is becoming "worse". The quasiparticle residue z of two-site DMFT has dropped — from $z = 0.972$ at $U = 2t$ to $z = 0.321$ at $U = 20t$, see also Fig. 6.2(a) — and in $n_{\mathbf{k}}$ a significant reduction of the Fermi surface discontinuity reflects this; the graph is taking on the curved form expected from Fermi liquid theory [4], and spectral weight is becoming distributed uniformly across the Brillouin zone, reflecting the local nature of the Hubbard U interaction. A very slight Pomeranchuk distortion is present.

In the density of states, upper and lower Hubbard bands can be seen together with a central quasiparticle peak. This peak is heavily renormalized (with a bandwidth of $\sim$ $3t$, reduced from the non-interacting bandwidth of $8t$), and the spectral function shows a flattened dispersion: the quasiparticles have become much heavier. The Hubbard bands have characteristics that reflect the non-interacting dispersion.
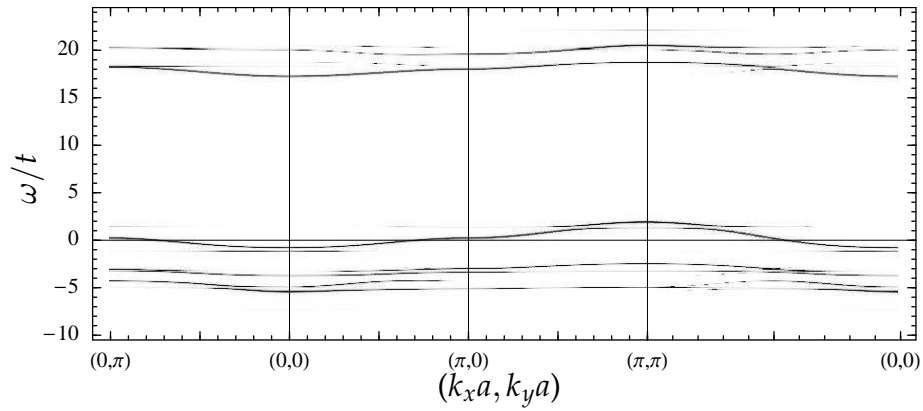
(a) Spectral function cross-section
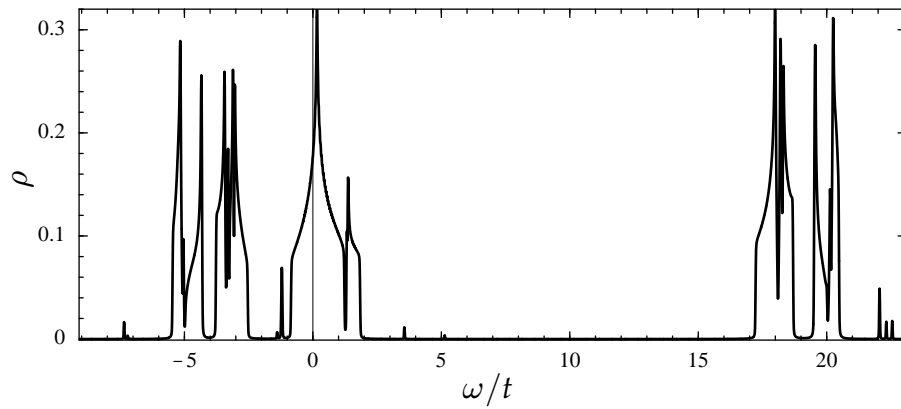
(b) Local density of states, smoothed
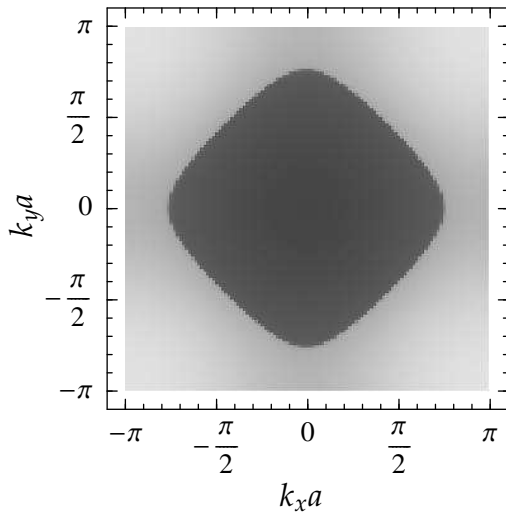
(c) $n_{\mathbf{k}}$ across Brillouin zone
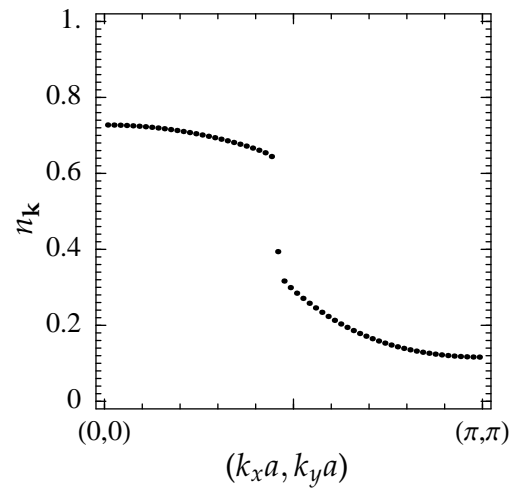
(d) $n_{\mathbf{k}}$ along cross-section in **k**-space

Figure 6.5: Point 2 ($U = 20t$, $n = 0.8$). Paramagnetism with strong interactions; see §6.2.2 for discussion.

6.2.3   Point 3: Paramagnetism with a distorted Fermi surface

Point 3 ($U = 2t$, $n = 0.9$, see graphs in Fig. 6.6) lies within the distorted paramagnetic phase. The distortion of the Fermi surface, discussed in detail in §6.3.4, is clear in the graph of $n_{\mathbf{k}}$, and in the spectral function the anisotropy is apparent in the x and y directions. Antiferromagnetic fluctuations (*c.f.* §6.3.1 and §6.3.3) are beginning to play a rôle: in $n_{\mathbf{k}}$ a ghost Fermi surface displaced by (π, π) is visible, gaps are appearing in the density of states, and reflected bands are apparent in the spectral function.

6.2.4   Point 4: Weak ferromagnetism

Enclosed within the distorted paramagnetic phase (b) is a small patch of low moment ferromagnetism, phase (f). Here the system is exploiting the soft Fermi surface near the van Hove points (*c.f.* §6.3.4 and Ref. [112]), and the Fermi surface for one spin species distorts more than the other. We believe this phase to be an product of the increased distortion tendency caused by the asymmetry of the 2×1 cluster.

(a) Spectral function cross-section
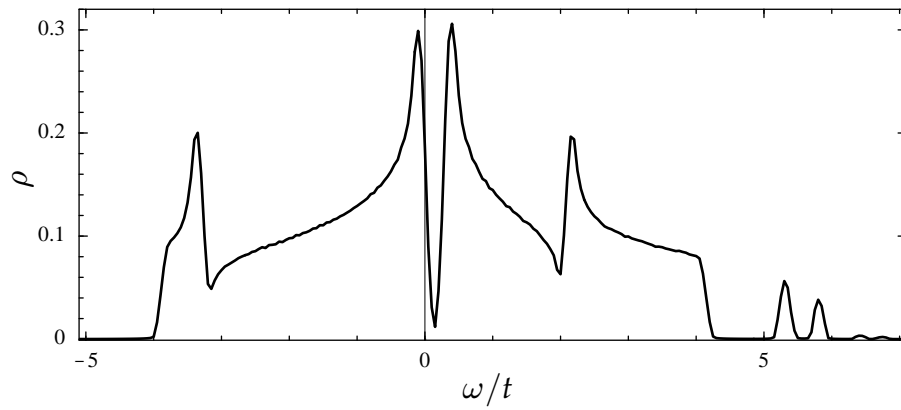
(b) Local density of states, smoothed
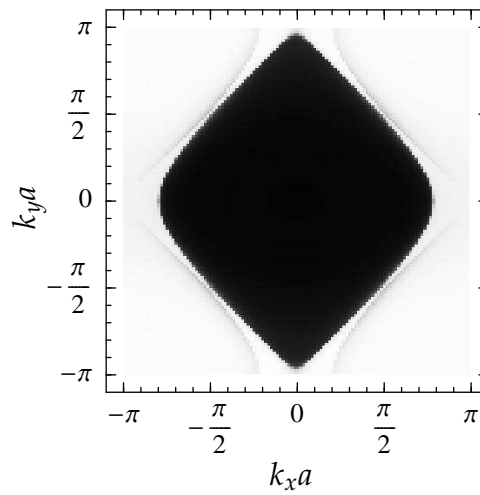
(c) $n_{\mathbf{k}}$ across Brillouin zone

Figure 6.6: Point 3 ($U = 2t$, $n = 0.9$). Paramagnetism with a distorted Fermi surface; see §6.2.3 for discussion.

6.2.5   Point 5: Paramagnetism with hole pockets

Increasing either the number of electrons or the interaction strength increases the distortion that was seen at Point 3, which has a dramatic effect by the time Point 5 is reached ($U = 5t$, $n = 0.83$, see graphs in Fig. 6.7). Where the distorted Fermi surface hits the reduced zone boundary at $(\pi/2, \pi/2)$, it vanishes: $n_\mathbf{k}$ shows a continuous decrease without a characteristic Fermi surface discontinuity (Fig. 6.7(d)). The remaining sections of Fermi surface are closed into hole pockets (visible in Fig. 6.7(c)) by a line with very small quasiparticle weight. This line has an origin connected with the antiferromagnetic fluctuations, as it comes from the (π, π)-displaced "ghost" Fermi surface mentioned above. The ghost Fermi surface is a feature of a ghost dispersion (*c.f.* the spectrum in Fig. 6.7(a) near (π, π)), which hybridized with the original dispersion. This created a gap, which is also apparent in the density of states. Further interpretation and the experimental relevance of these phenomena are discussed in §6.3.3 below.
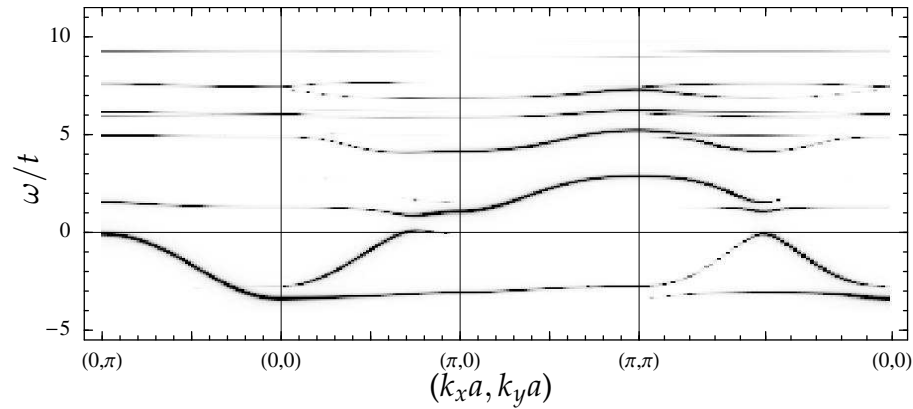
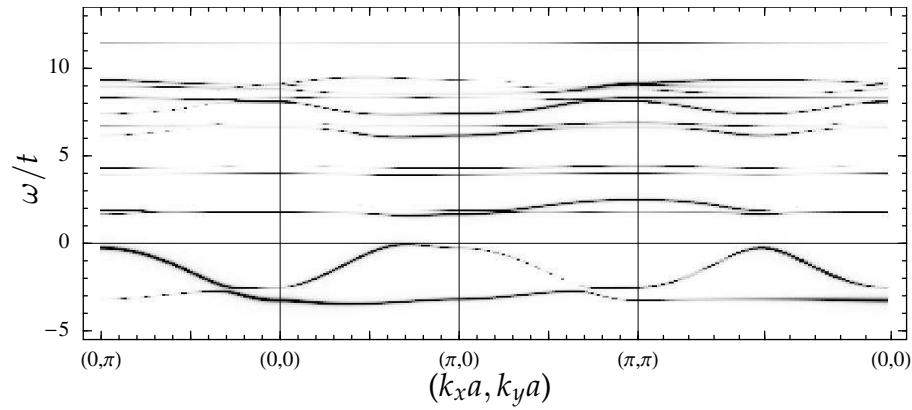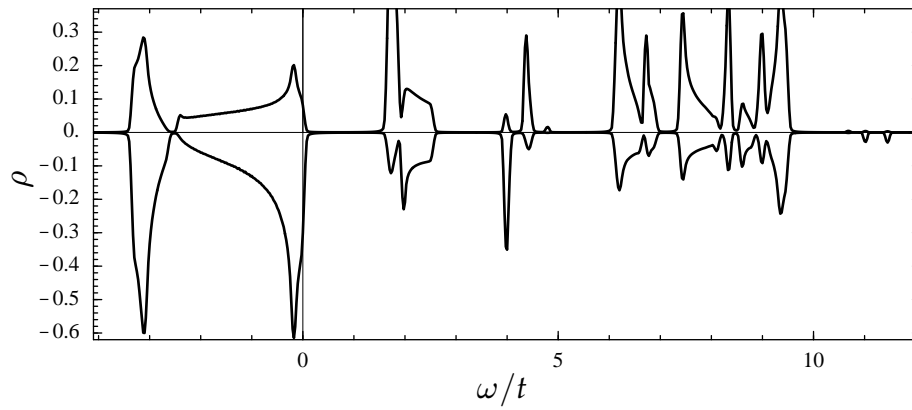(a) Spectral function cross-section
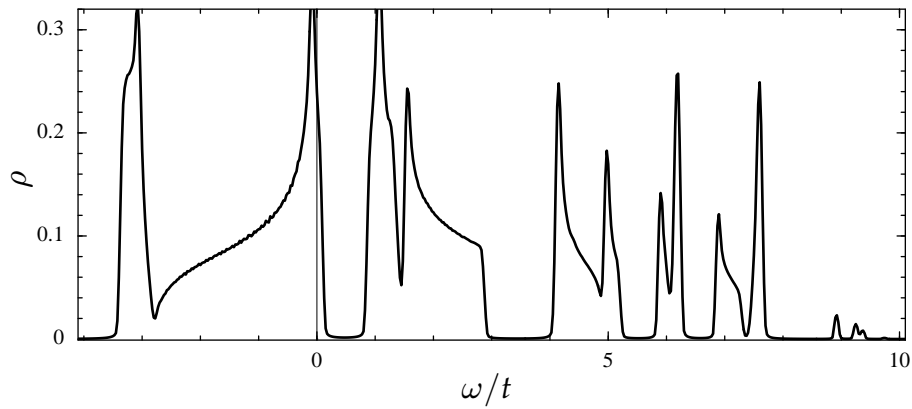
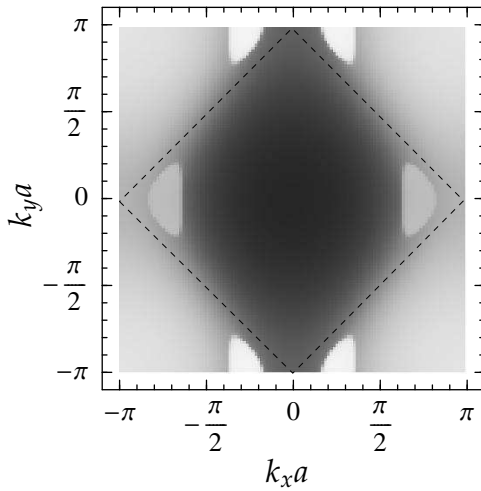(b) Local density of states, smoothed
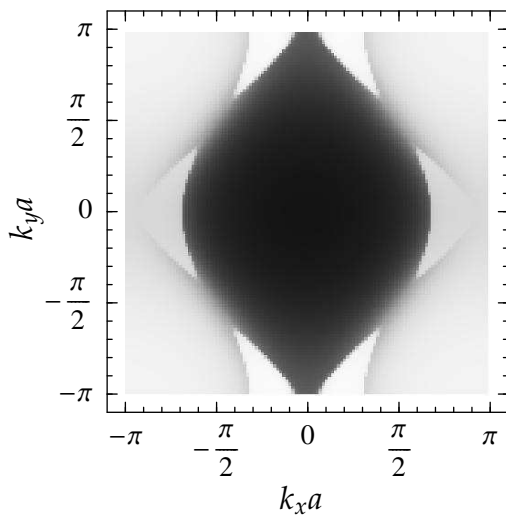
(c) $n_{\mathbf{k}}$ across Brillouin zone
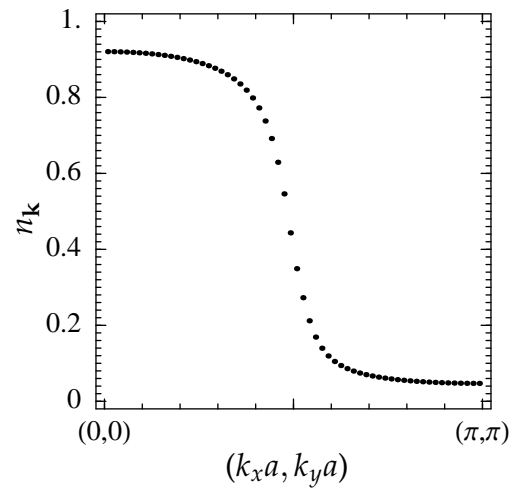
(d) $n_{\mathbf{k}}$ along cross-section in $\mathbf{k}$-space

Figure 6.7: Point 5 ($U = 5t$, $n = 0.83$). Paramagnetism with hole pockets; see §6.2.5 for discussion.

6.2.6 Point 6: Antiferromagnetism with hole pockets

On increasing the interaction strength from Point 5, there is a second order transition to an antiferromagnetic ground state, phase (c). There is virtually no change to any properties of the state apart from the broken magnetic symmetry. Point 6 ($U = 8t$, $n = 0.9$, see graphs in Fig. 6.8) lies well within phase (c), where increased U and n are having more effect. The hole pockets have shrunk, but the vague outer line originating from the ghost Fermi surface has increased in visibility: the whole pocket appears in Fig. 6.8(c), and a second step upwards can be seen in the $n_{\mathbf{k}}$ cross-section in Fig. 6.8(d).

(a) Spectral function cross-section
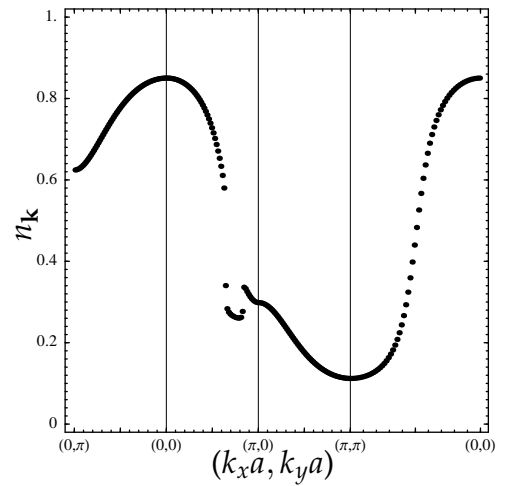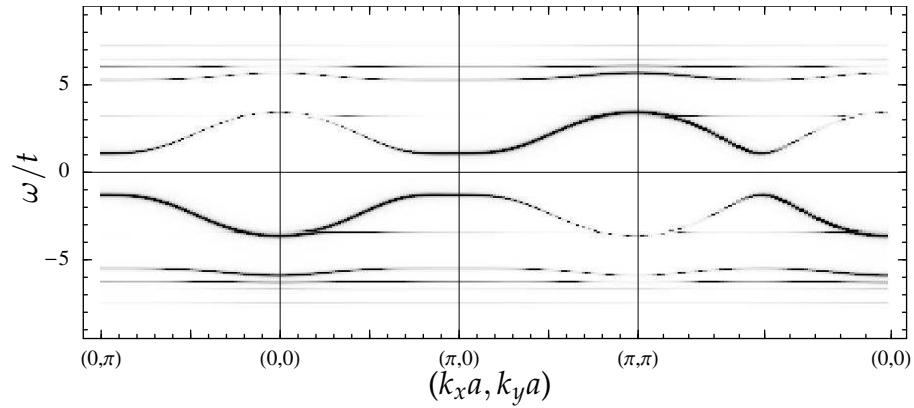

(b) Local density of states, smoothed

(c) $n_\mathbf{k}$ across Brillouin zone

(d) $n_\mathbf{k}$ along cross-section in $\mathbf{k}$-space

Figure 6.8: Point 6 ($U = 8t$, $n = 0.9$). Antiferromagnetism with hole pockets; see §6.2.6 for discussion. The density of states is plotted separately for each of the two sublattices, and the Brillouin zone is shown with the second quasiparticle band of states drawn in the second RBZ for convenience (the dashed line indicates the boundary).

6.2.7 Point 7: Antiferromagnetism at half-filling

Point 7 ($U = 5t$, $n = 1$, see graphs in Fig. 6.9) illustrates the antiferromagnetic insulating solution at exactly half-filling; phase (e), just off half-filling, has the same character. The ghost dispersion is clearly visible, together with the gaps caused by its hybridization with the original dispersion; in this case the gap occurs everywhere on the Fermi surface and causes the material to insulate. At very large U, a slight Pomeranchuk distortion becomes apparent in this phase.

(a) Spectral function cross-section
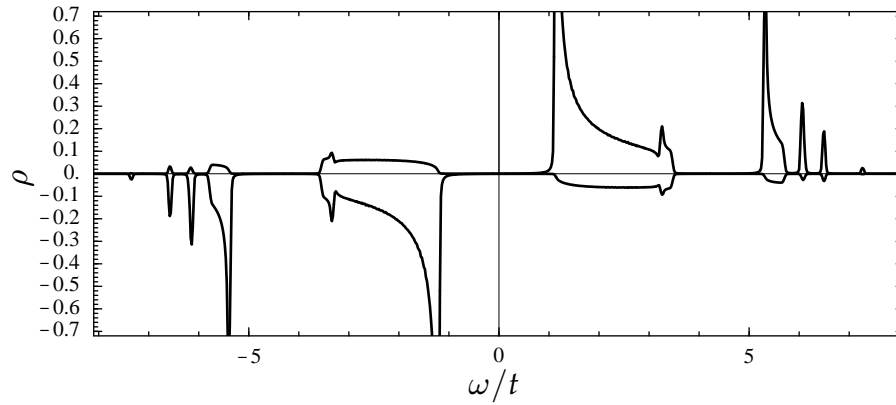
(b) Local density of states, smoothed
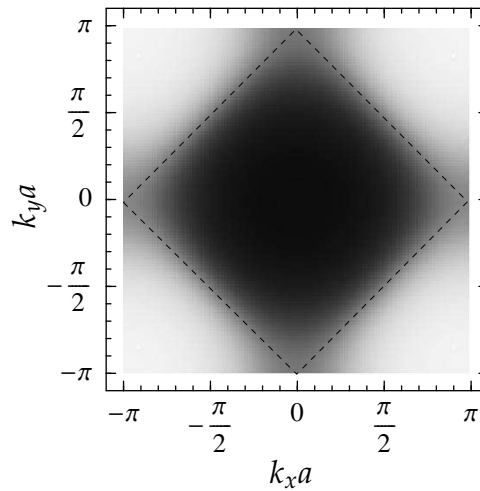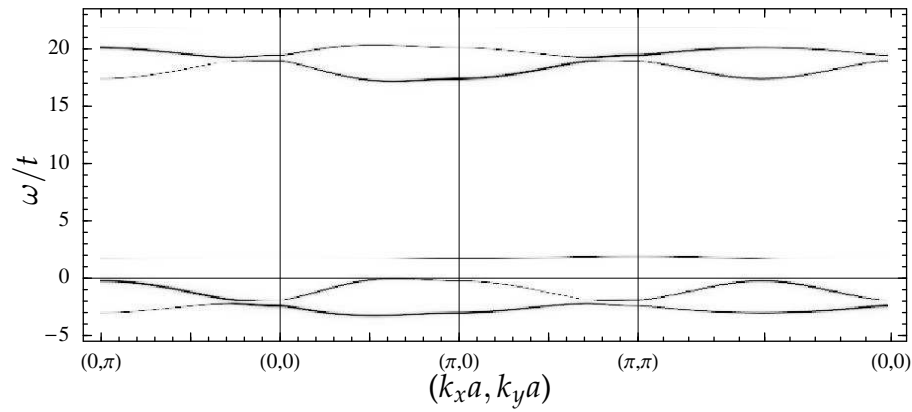

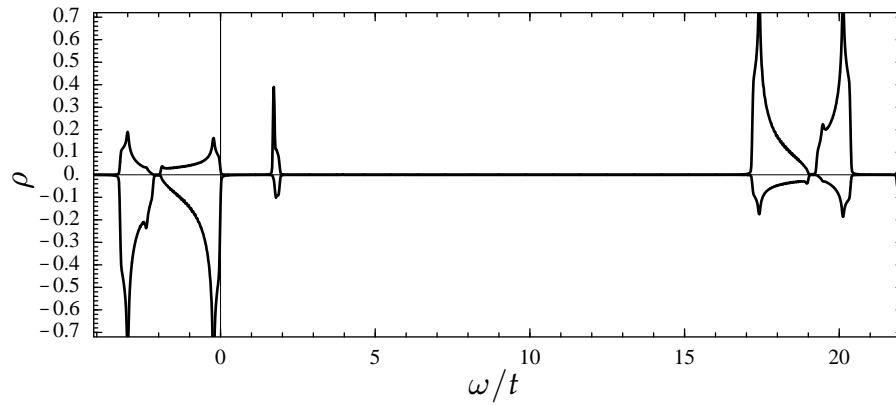(c) $n_{\mathbf{k}}$ across Brillouin zone

Figure 6.9: Point 7 ($U = 5t$, $n = 1$). Antiferromagnetism at half-filling; see §6.2.7 for discussion. The density of states is plotted separately for each of the two sublattices, and the Brillouin zone is shown with the second quasiparticle band of states drawn in the second RBZ for convenience (the dashed line indicates the boundary).

6.2.8 Point 8: Antiferromagnetism at strong interactions with hole pockets

Point 8 ($U = 20t$, $n = 0.97$, see graphs in Fig. 6.10), lies in the distorted antiferromagnetic phase (c) at U and n further increased from Point 6. Like Point 2 the strong interactions have caused an even distribution of the electrons across the Brillouin zone (uniform grey in Fig. 6.10(c)), reflecting the local nature of the Coulomb interaction. The hole pockets have shrunk to small circles — indicating how the Mott transition might happen in an antiferromagnetic material (see §6.3.2). There is a huge Slater gap, and unlike the paramagnetic Mott gap there are only two bands: it appears as if the central quasiparticle peak split into two magnetic bands which have fused with the Hubbard bands.

PSfrag replacements

(a) Spectral function cross-section

PSfrag replacements

(b) Local density of states, smoothed

PSfrag replacements
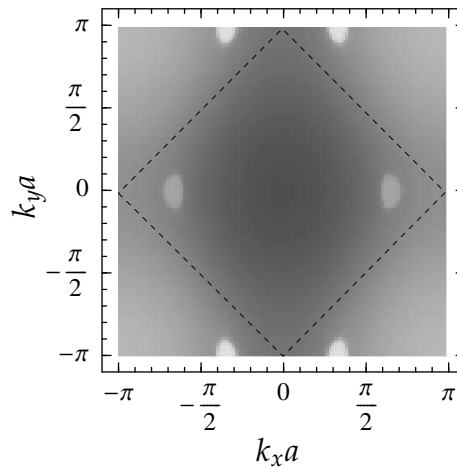
(c) $n_{\mathbf{k}}$ across Brillouin zone

Figure 6.10: Point 8 ($U = 20t$, $n = 0.97$). Antiferromagnetism at strong interactions with hole pockets; see §6.2.8 for discussion. The density of states is plotted separately for each of the two sublattices, and the Brillouin zone is shown with the second quasiparticle band of states drawn in the second RBZ for convenience (the dashed line indicates the boundary).
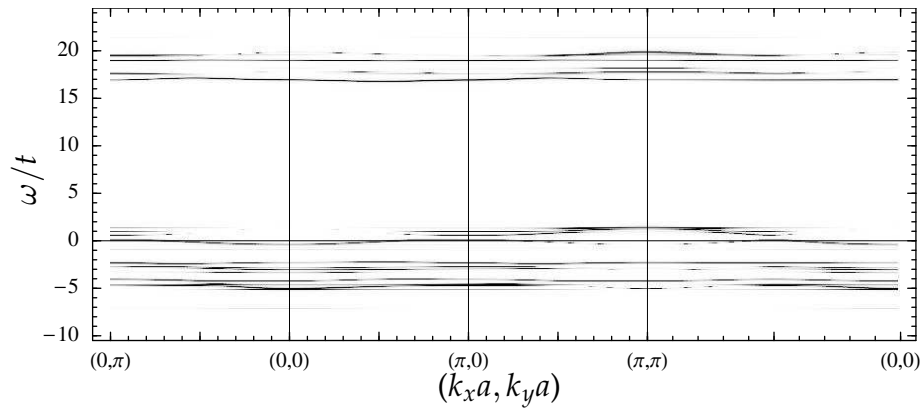
6.2.9 Point 9: Antiferromagnetism at strong interactions

Reducing the electron filling n from Point 8 causes the ground state to become an antiferromagnet of different character. This is phase (d), which Point 9 ($U = 20t$, $n = 0.9$, see graphs in Fig. 6.11) illustrates; it is a conventional antiferromagnet, and originates from the same self-consistent solution as phase (e).[1] The density of states has the familiar three-peak structure, with upper and lower Hubbard bands. The central quasiparticle peak has been renormalized by interactions (like Point 2), but here it is split by a Slater gap; in contrast to Point 8, the magnetism is occurring predominantly within this central renormalized band rather than across the whole spectrum. These antiferromagnetic phases are compared in more detail in §6.3.1.
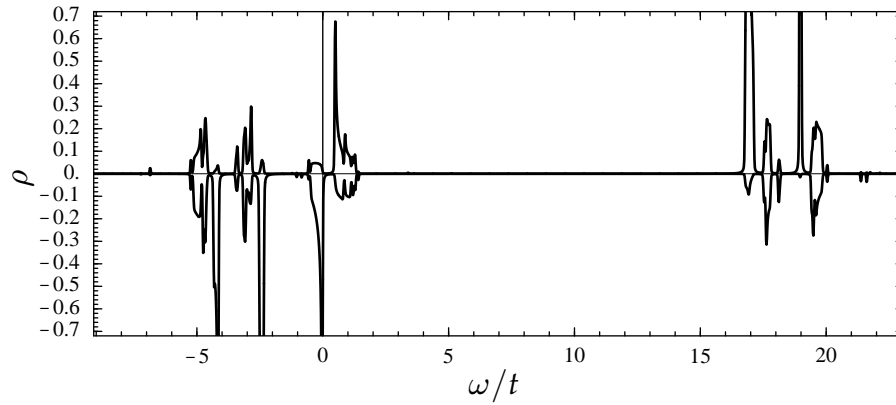
---

[1]In the intervening region, right across the phase diagram, its energy is greater than that of the ground state phase (c).

(a) Spectral function cross-section

(b) Local density of states, smoothed
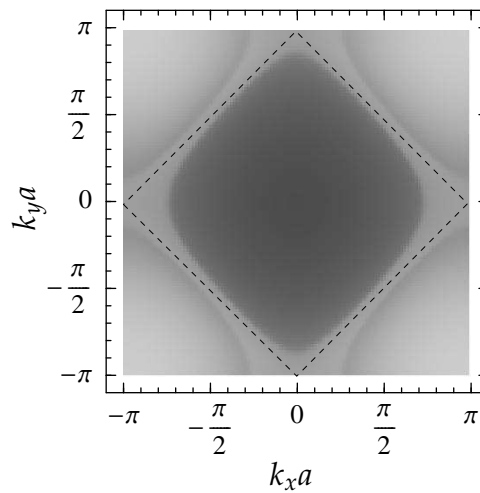

(c) $n_{\mathbf{k}}$ across Brillouin zone

Figure 6.11: Point 9 ($U = 20t$, $n = 0.9$). Antiferromagnetism at strong interactions; see §6.2.9 for discussion. The density of states is plotted separately for each of the two sublattices, and the Brillouin zone is shown with the second quasiparticle band of states drawn in the second RBZ for convenience (the dashed line indicates the boundary).

6.3 Discussion

In this section I will draw together, and discuss in detail, a variety of themes emerging from the diverse phases described above. Comparison will be made with other theoretical approaches in the literature, and relevant experimental quantities measured for various materials. Antiferromagnetism appears in several different guises, which I will interpret in §6.3.1. The progression across the phase diagram of various features gives insight to the Mott transition in the presence of antiferromagnetism (§6.3.2). Features have appeared which are intriguingly similar to phenomena observed in the normal state of the cuprate high-temperature superconductors, such as the pseudogap — see §6.3.3. Finally, many phases exhibit a Fermi surface distortion akin to that predicted by Pomeranchuk, which I will discuss in §6.3.4.

6.3.1 Slater antiferromagnetism

At half-filling, the square lattice is perfectly nested: the Fermi surface is a diamond shape and the wave-vector $\mathbf{Q} = (\pm\pi/a, \pm\pi/a)$ interconnects every point. In consequence, the susceptibility to magnetic order diverges for this wave-vector [113], and an infinitesimal local U causes an antiferromagnetic (sublattice) magnetization. A gap is formed at the Fermi energy and the state is an insulator [92] (see §6.3.2 for discussion of the metal-insulator transition). The results of the present calculation are consistent with this well-established picture: at exactly half-filling antiferromagnetism is observed (illustrated by Point 7, Fig. 6.9), with a moment exhibiting a similar variation with U to the Hartree-Fock form $m \propto e^{-\alpha/U}$ (see for example Ref. [114]), and very similar to that seen in unenhanced two-site DMFT (Fig. 4.6(a)). Spectral features are consistent with other studies, for example the separate high energy bands of Ref. [115].

However, at electron fillings different from $n = 1$, there is no theoretical consensus. The general extent of magnetic order that we observe away from half-filling is vastly smaller than predictions of Hartree–Fock theory, and furthermore in agreement quantitatively with the results of more sophisticated DMFT calculations. The possibility of *incommensurate* order is important off half-filling, but cannot be represented by our cluster DMFT approach. Our region of antiferromagnetism is divided into several different phases. Near to half-filling around $U = 5t$, there is a phase — labelled (e) on Fig. 6.1 — that is very similar to the half-filling solution, but metallic.

Further off half-filling, phase (e) is superseded by phase (c), which similarly exhibits a gap initially growing with U (for $U \lesssim 8t$), and also can be interpreted as a Slater antiferromagnet: a weak spin-density wave transition on a metallic state (see, for example, the mean-field theory of Schrieffer, Wen and Zhang [116]). At higher U,

114

the gap to the first available states above ϵ_F decreases again, indicated the appearance of Heisenberg-like physics (this is similar to phase (d) which will be discussed below). The density of states is quite complex (*e.g.* Fig. 6.8(b)) and its interpretation is difficult; the various gaps are the synthesis of Hubbard and Slater gaps.

The magnetism in phase (d) is somewhat easier to interpret: the density of states (Fig. 6.11(b)) and the spectrum (Fig. 6.11(a)) indicate that the magnetism is appearing as a spin-density wave transition — but for the renormalized quasiparticles. Just the central quasiparticle peak is exhibiting the Slater instability seen at Point 7 (Fig. 6.9(a) and (b)). The gap reduces as U is increased, and behaving consistently with the $\sim t^2/U$ scale expected of Heisenberg model physics. We interpret this phase as an antiferromagnetic metal in an effective t-J model, where $t_{\text{eff}} \ll t$ and $J_{\text{eff}} \sim t^2/U$. It is surprising that J appears to play a rôle in these materials, when U is a much larger energy scale; but this paradox is resolved now we see that U sets the scale for the outlying Hubbard bands, and renormalizes the quasiparticle peak such that a smaller J_{eff} may dominate. Such a separation of high and low energy scales is thought to be inherent to strongly correlated systems [117, 118].

Finally, in the conventional paramagnetic phase (a) at higher interaction strength, effects of antiferromagnetic fluctuations become apparent in the proximity of antiferromagnetic phases (*e.g.* near Point 2 but at larger n). There is a "ghost" Fermi surface, following the original Fermi surface shifted by $(\pi/a, \pi/a)$, similar to that visible at Point 3 (Fig. 6.6); see also §6.3.3. The electron liquid here could perhaps be described, at low energies, as a nearly-antiferromagnetic Fermi liquid. [34, 119]

6.3.2 Mott transition

In §3.5.1 I discussed how conventional (non-cluster) DMFT was able to combine the pictures of Mott–Hubbard and Brinkman–Rice to help understand the Mott transition. However, the mechanism for the metal-insulator transition proposed by Slater [92] has still to be fully integrated: if the lattice is not frustrated, the transition to antiferromagnetism will preempt any other metal-insulator mechanism [52]. The conventional DMFT studies, done within a paramagnetic picture, thus do not concern the true ground state, making their predictions physically doubtful (for $T = 0$); moreover, to include antiferromagnetism consistency, a cluster extension to DMFT is necessary.

One avenue of investigation [120, 74, 121, 64] is to remove the magnetic order with frustration, commonly as a t' next-nearest-neighbour hopping term in the Hamiltonian; and in Chapter 7 I will investigate some consequences of a t' term. Parcollet *et al.* [64] conclude that findings of DMFT for the paramagnetic metal–insulator transition

remain true. Others investigate the important question of temperature dependence (for example, Ref. [122]). Here I concentrate on a different question: how is the Mott insulating state approached from off half-filling, in the presence of antiferromagnetism?

Within my results, much of the metallic state does exhibit the characteristic three-peak structure of DMFT, for example Point 2 (Fig. 6.5(b)), even in an antiferromagnetic phase (Point 9, Fig. 6.11(b), where the central peak has a Slater gap). The quasiparticle weight decreases across the phase diagram regardless of the magnetic order (Fig. 6.2(a)), indicating a trend towards an insulator at half-filling for $U \gtrsim 12t$ (the expected Mott transition point of $\sim 1.5\times$ bandwidth $W = 8t$). Within conventional DMFT, the Mott transition is seen as the central quasiparticle peak sharpening and vanishing, but our results provide a contrasting picture of the transition. The Fermi surface *breaks up* into hole pockets separated by regions without free carriers (see Fig. 6.7(c) and Fig. 6.8(c)). As U increases, the quasiparticle residue in these pockets decreases and weight spreads across **k**-space, and with increased electron numbers the pockets shrink (see Fig. 6.10(c)) — suggesting that the mechanism for the metal-insulator transition is the shrinking and eventual vanishing of these pockets: at which point the material becomes an insulator.

Importantly, the hole-pocket features exist regardless of magnetic order, and off half-filling — two areas where the picture of conventional DMFT is unclear; we see now that this is because it cannot deal with **k**-space anisotropy. The phenomenon of the Fermi surface break-up into hole pockets provides an answer to another mystery: it describes how a state can transmute from a metallic state with a Fermi surface, to an insulating state without a Fermi surface at all.[2] Additionally, we have now combined Slater's approach to the metal insulator transition with the other two approaches: a Slater gap is formed but its effects are *anisotropic* (see below).

Luttinger volume   The strong correlations between electrons can be seen to be having a dramatic impact on the properties of the Fermi liquid: Luttinger's theorem [123], which states that the volume contained by the Fermi surface will remain constant, is violated for the states with a broken-up Fermi surface. Our results show that the Luttinger volume is enclosed instead by lines where the density of electrons falls off smoothly without the Fermi discontinuity.

---

[2]Although our limited **k**-space resolution means that we cannot approach very close to the transition, and we do not actually see the insulating state (except for the Slater antiferromagnet at half-filling).

Cuprates In the normal state of the cuprates, the number of holes seem to characterize physical properties (see, for example, Ref. [124]), which is consistent with our picture of the doped Mott insulator as a state with hole pockets. Additionally, photoemission observes disconnected sections of Fermi surface directly; this aspect is discussed further in the next section, and how the transition described above is inextricably linked with antiferromagnetism.

6.3.3 Pseudogap formation and arc-like Fermi surfaces

We can produce a unified picture of many of the phenomena discussed so far. Looking carefully at Fig. 6.6(c) reveals a "ghost" Fermi surface: low energy electron-like excitations appearing at the position of the original Fermi surface displaced by the antiferromagnetic wave-vector (π, π). These are antiferromagnetic fluctuations preceding the magnetic symmetry breaking. Looking at the complete spectral function (Fig. 6.6(a)) reveals that this "ghost" Fermi surface is a manifestation of a "ghost dispersion" — the original dispersion shifted by (π, π), but considerably weaker, having less spectral weight.

Nevertheless, the ghost dispersion hybridizes with the original dispersion to give the final electronic structure, giving rise to a gap in the spectrum (observable in the local density of states). The effects of this gap depend on whether the chemical potential μ falls within it, and how the gap evolves around the Fermi surface (*c.f.* Fig. 6.12). For Point 3 (Fig. 6.6), μ is below the gap everywhere (*c.f.* line (ii) in Fig. 6.12(b)), so the Fermi surface is similar to the non-interacting case; further out, the ghost dispersion crosses the Fermi level separately, and this leads to the ghost Fermi surface seen in Fig. 6.6(c).

If, however, μ is raised by increasing the filling n, or alternatively the hybridization gap is widened by increasing the interaction, μ can fall within the gap (*c.f.* line (i) in Fig. 6.12(b)). At half-filling (see Fig. 6.9), everywhere on the Fermi surface is affected in this way and there is a full gap, leading to an insulating state. But at Point 5 (Fig. 6.7), the Fermi surface is distorted, and the gap varies around the Fermi surface; the consequences are that near $(\pi/2, \pi/2)$, μ falls within the gap (seeFig. 6.7(a), *c.f.* line (i) in Fig. 6.12(b) again) and there is no Fermi surface here: $n_{\mathbf{k}}$ falls off smoothly towards (π, π), reflecting the reduced weight in the ghost band.

This gap is a *pseudogap* because there are other directions in which a well-defined Fermi surface remains. Along the line from $(0, 0)$ to $(\pi, 0)$ in Fig. 6.7(a), the chemical potential still cross the original dispersion, followed by the ghost dispersion (*c.f.* line (ii) in Fig. 6.12(b)). Here the ghost Fermi surface completes a closed *hole pocket* (see
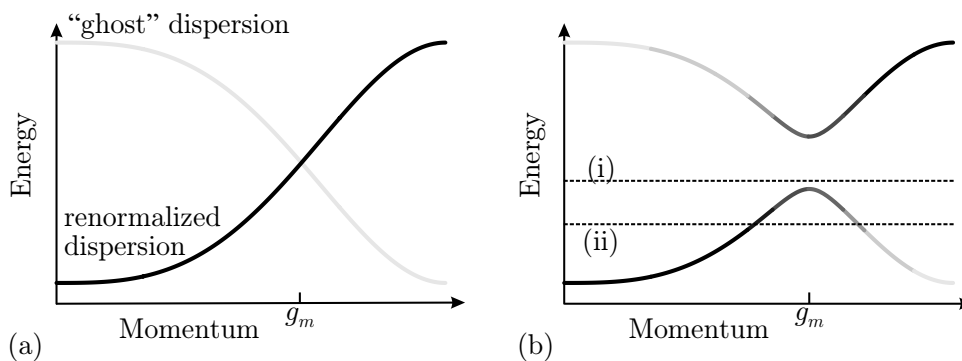
Figure 6.12: A schematic view (taken from Ref. [16]) of the origin of a pseudogap, as seen for example in the spectral function of Point 5, Fig. 6.7(a), near $(0.8\pi, 0)$ and near $(\pi/2, \pi/2)$; darker lines carry more spectral weight. (a) Distinct fluctuations on the A and B sublattices result in a second dispersion of low weight (a "ghost" dispersion). This is formed by the folding of the original, possibly renormalized, dispersion in the antiferromagnetic Brillouin zone (defining g_m). (b) Hybridization with the original dispersion forms a gap. Along directions in momentum space where the chemical potential lies within the gap [line(i)], there is a full gap in the excitation spectrum and no Fermi surface. Along directions where the chemical potential lies away from the gap it crosses the dispersion at two points [line (ii)]. A hole pocket forms with low spectral weight at the second crossing.

Fig. 6.7(a)), although with a much smaller quasiparticle residue than the original line, and the dominant feature is the arc-like remnant of the original Fermi surface. Hybridization with the ghost dispersion provides an intuitive explanation for origin of the hole pockets discussed in §6.3.2.

Chubukov [125, 126] first gave the argument detailing how hybridization with a (π, π)-shifted dispersion could give rise to hole pockets. In common with other studies in the literature, an initial finitesimal t' is required in the dispersion to generate an overlap with the ghost Fermi surface. Our calculations provide, novelly, a mechanism for the formation of pockets without such a parameter; one way of thinking about it is that the Σ_{AB} term provides an effective, if asymmetrical, t'.

The features described above are reminiscent of cuprate high-temperature super-conductors in their normal state, which are believe to have a Fermi surface consisting of arc-like segments separated by pseudogap regions [125, 127, 128]. There are important differences, however, between our results and what is seen in the cuprates, most significantly in the position of the arcs and the pseudogap regions. In the cuprates the Fermi surface arcs are seen at $(\pi/2, \pi/2)$ but appear near $(0.7\pi, 0)$ in our calculations, and the pseudogap occurs near $(\pi, 0)$ in the cuprates but near $(\pi/2, \pi/2)$ in our calculations. However, our small cluster severely constrains the momentum dependence of all quantities, and as will be discussed in the next section, the 2×1 cluster cannot admit the d-wave symmetry observed in the cuprates but only s- and p-wave configurations, which means for example that arcing can only happen near the van Hove points such as $(\pi, 0)$. Chapter 7 contains the results of calculations with a four site (2×2) cluster which permits d-wave symmetry, where a detailed comparison with the physics of the

cuprates will be made.

6.3.4   Pomeranchuk instability

It is the Fermi surface distortion that enables the emergence of pseudogap physics dis-
cussion in the previous section, and in this section I will discuss this distortion in more
detail. The breaking of x-y symmetry is apparent in the $n_{\mathbf{k}}$ electron density plots, and
also through differences between the $(0, \pi)$ and $(\pi, 0)$ segments of the spectral func-
tion. Across the phase diagram (see §6.2), its effect ranges from a small distortion —
at Point 3, see Fig. 6.6(c), and in all phases at high U, see *e.g.* Fig. 6.11(c) — through to
underlying the dramatic break-up of the Fermi surface into hole pockets discussed in
the previous section. Without the distortion, the Fermi surface could not overlap with
itself until diamond-shaped, when the hybridization creates a Slater insulating anti-
ferromagnet. Pomeranchuk [129] first showed that a Fermi liquid could be unstable
to a distortion of its Fermi surface. In more recent years such an effect has been found
within some renormalization group calculations, for example Refs [130, 131],[3] although
its existence remains controversial. Experimentally, it has very recently proposed that
$Sr_3Ru_2O_7$ near quantum critical point [132] might exhibit signs of a ferromagnetic dis-
tortion similar to phase (f) here.

The physical basis for the possibility of distortion is the flatness of the dispersion
near the van Hove points: the system can exploit the reduced Fermi velocity, and move
electrons from $(\pi, 0)$ to $(0, \pi)$ with little energy penalty. Similarly, in a phenomenolog-
ical Fermi liquid model, Metzner [112] regards the Pomeranchuk instability as an im-
portant manifestation of a "soft" Fermi surface in strongly correlated system, which
is unusually susceptible to many sorts of fluctuations. These might include those in-
vestigated by Schultz [133], and those causing non-Fermi liquid behaviour such as the
marginal Fermi liquid described in Chapter 2. Moreover, the peculiar patch of ferro-
magnetism constituting phase (f) of our phase diagram, is a further manifestation of
such a soft Fermi surface.

However, before drawing definitive conclusions we should note that a small cluster
means that there are severe restrictions on the Fermi surface shape. Looking at the
pair-cluster quasiparticle Green's function in Eqn 5.35, the only shapes possible are
the original dispersion $\epsilon_{\mathbf{k}}$, and $\epsilon_{\mathbf{k}} \cos k_x a$ which gives rise to the lemon-shaped Fermi
surfaces. The latter can only permit changes with opposite sign at $(\pi, 0)$ and $(0, \pi)$,
which means that if the Fermi surface has an inclination to distort, it can only do so by

---

[3]Competition with antiferromagnetic order is of concern to these authors; our calculations success-
fully address this issue.

breaking *x-y* symmetry in this way. The arcs (for example) discussed in the previous section can only appear in one place, within the cluster formulation.

Our model has broken *x-y* symmetry from the outset, because of the choice of 2×1 shape for the cluster, and this means that the tendency to distort will be enhanced; we cannot at this stage disentangle whether the phenomena described above are an artifact, or whether the Pomeranchuk distortions will still occur without the initial broken symmetry, or when other shapes are permitted. In Chapter 7, the cluster approach is extended to a 2×2 cluster, that preserves *x-y* symmetry and allows higher order distortions.

6.4 Summary

Within two-site pair-cluster DMFT, a decent phase diagram of the square lattice Hubbard model could be produced, which is much more satisfactory than the result from plain two-site DMFT. Even the small amount of momentum dependence permitted by a cluster consisting only of a pair of sites gave considerable insight into a variety of physical phenomena that many researchers are interested in.

The ground state phase diagram was divided into regions defined by two different kinds of symmetry breaking. First, magnetic symmetry: there was a region of antiferromagnetism which extends off half-filling to a band filling of 0.8, in good agreement with other modern approaches. Second, some phases exhibited a Pomeranchuk instability, where *x-y* symmetry is broken and the Fermi surface distorts. I have investigated the quasiparticle properties of each phase in detail, utilizing the complete spectral function that our technique allows access to, and reference was made to experimental quantities. Interpretations were given, although these are just one angle: there is a large amount of data available, and many alternative possibilities for analysis.

This investigation led to insights into several puzzling features of the Mott metal-insulator transition and how antiferromagnetism, proximity to van Hove points, and formation of the Mott gap compete with one another; all play a rôle in various regimes. The van Hove point means that the Fermi surface becomes soft, and can distort even at low U. Nesting causes Slater antiferromagnetism near half-filling, which can have some quite complex features. The Mott gap becomes significant at high U, but at the same time *t-J* model physics can be important through a small Slater gap in a highly renormalized quasiparticle band.

We saw also how the Mott metal-insulator transition might be approached, even within a magnetically ordered state: the Fermi surface evolves from a renormalized Fermi liquid obeying Luttinger's theorem, to a pseudogap state where a gap opens on

some parts of the Fermi surface, breaking it up into hole pockets separated by regions without free carriers. These pockets have a strongly momentum-dependent spectral density, being dominated by Fermi arcs, sections of the original Fermi surface. The Mott transition to an insulating state occurs by means of these pockets shrinking to points and vanishing: patterns in **k** space are absolutely essential for understanding it.

Many of these features, especially the pseudogap and the existence of Fermi arcs, are highly suggestive of features observed in the normal state of the cuprate super-conductors. However, the detailed match is not identical, and many features of the phases reflect the restrictions of the 2×1 cluster. The only distortions permitted will break *x*-*y* symmetry, and features are only allowed at certain places in the Brillouin zone; and it is not known if the distortions are real, but an over-emphasized artifact of the broken cluster symmetry. In the next chapter I will address these issues with a 2×2 cluster, which can permit the broken symmetries necessary to emulate the cuprates: increasing the cluster size allows access to higher Fourier components of the Fermi surface.

Still, the inclinations observed in the model are illuminating. The self-consistency procedure tried to drive electrons around the Fermi surface, exploiting the van Hove points — and this action was energetically favourable. We have also gained intuition on the formation of hole pockets and pseudogaps via hybridization, for example — useful progress, whether or not the details are correct. We achieved our aim of a quick investigation of features of the phase diagram and gained at the same time a surprising amount of other information.

Chapter 7

RESULTS: 2×2 QUAD-CLUSTER

Ant and Bee wrote the shopping list on a piece of paper that was square and flat.

ANGELA BANNER
Ant and Bee go Shopping [134]

7.1 Introduction

In this chapter I present the phase diagram of the square lattice Hubbard model under two-site quad-cluster DMFT, where a cluster that consists of four sites arranged in a 2×2 plaquette is used in combination with the "two-site" reduction of the DMFT self-consistency conditions (Chapter 4). The theory underlying the calculations was presented in Chapter 5 in §5.3.2. Chapter 6 investigated two-site pair-cluster DMFT, involving a 2×1 site cluster, and this chapter follows much the same pattern, but for a cluster double the size instead.

Much of the 2×1 pair-cluster phase diagram consisted of phases where x-y symmetry was broken and the Fermi surface had undergone a Pomeranchuk distortion, but it was not clear if this was just an artifact of the cluster shape. The cluster studied in this chapter is the simplest cluster that can represent antiferromagnetism without breaking x-y symmetry from the outset, but the implementation is somewhat restricted and cannot support broken x-y symmetry and so answer the question of whether the Pomeranchuk instability was real. However, what we wish to investigate instead is whether similar physical phenomena happen to those seen in the 2×1 cluster. For example, Chapter 6 showed how the Pomeranchuk-distorted Fermi surface could hybridize with itself and form hole pockets; we would like to know if a tetragonal distortion, permitted by the 2×2 cluster, is also favoured. This would be likely to give hole pockets in the vicinity of $(\pi/2, \pi/2)$ in the Brillouin zone, which would correspond better with observations of the normal state of the cuprate high-temperature superconductors.

As in Chapter 6, we explore the U-n phase diagram (see §7.2), identifying the ground state phase at each point. Much of the phase diagram indeed turns out to consist of phases with hole pockets near $(\pi/2, \pi/2)$, but these phases are generally antiferromagnetic, whereas the normal state of the cuprates is paramagnetic. There does exist a paramagnetic phase with hole pockets, but it is never energetically favoured. So, to encourage this phase, a negative next-nearest-neighbour hopping term (t') is added to the model (*c.f.* §5.3.2), which also means that the observed cuprate Fermi surface shape is better matched. A further advantage of studying such a *geometrically frustrated* model is that the effects of half-filling and the van Hove point are separated from each other, and now occur at different band fillings. The most part of this chapter (§7.3) is devoted to investigating the phase diagram when $t' = -0.5t$ (note that t' is defined here so that $t' = -t$ corresponds to full frustration).

The quad-cluster U-n phase diagram for $t' = -0.5t$ is presented in §7.3.1 and its general trends and features discussed, including the broad effects of the next-nearest-neighbour hopping term. Various representations of the spectral function (electron
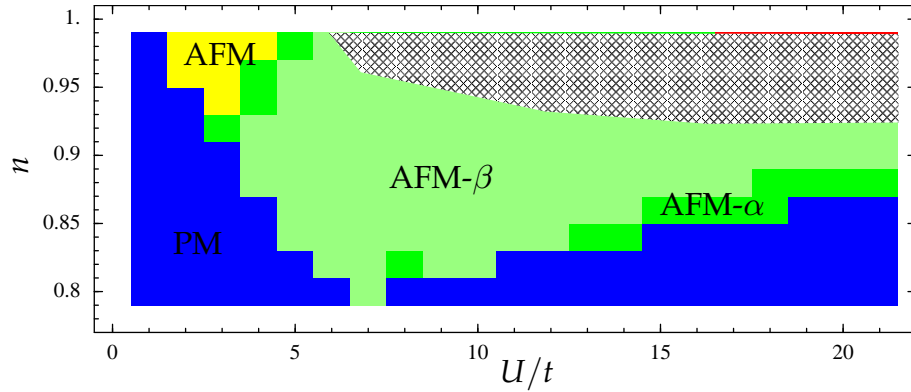
PSfrag replacements

Figure 7.1: Ground state phase diagram ($U/t, n$) for the 2D Hubbard model within two-site quad-cluster DMFT, with $t' = 0$. Distinct solutions are different colours, and labelled PM (conventional paramagnetism), AFM (conventional antiferromagnetism), AFM-α and AFM-β (both antiferromagnetism with hole pockets). Small gaps were tidied up. The hatched region is discussed in the text.

filling plus spectral density at the Fermi level across the Brillouin zone, cross-sections of the spectral function, and the local density of states) provide a detailed description of each of the phases: there are two paramagnetic phases (§7.3.2 and §7.3.3) and three antiferromagnetic phases (§7.3.4 and §7.3.5). The physical phenomena observed in these phases are then discussed and interpreted (§7.4). Comparisons are made with the conclusions from the pair-cluster model of §6.3, and also with a selection of experimental observations in the cuprates — particularly the pseudogap and the arc-like Fermi surfaces observed by angle-resolved photoemission spectroscopy (ARPES).

7.2   Results ($t' = 0$)

Fig. 7.1 shows the phase diagram for two-site cluster DMFT with no next-nearest-neighbour hopping ($t' = 0$); the underlying model is the same as for the phase diagram of Chapter 6 (Fig. 6.1), but the 2 × 2 cluster is used in place of the 2 × 1 cluster. The extent of antiferromagnetism is very similar, but the results differ in terms of symmetry in momentum space. The 2 × 1 cluster phase diagram exhibited a large region where x-y symmetry is broken, both in the antiferromagnetic region and continuing in to the adjoining paramagnetic region at low U. In contrast, our 2 × 2 cluster formulation cannot support such symmetry breaking; in §5.3.2 I described how only antiferromagnetic configurations are permitted, and so bonds in the x direction and the y direction have to be identical. Instead, most of the antiferromagnetic region of the 2 × 2 cluster phase diagram is dominated by phases distorted differently, and as dramatically, in momentum space: the Fermi surface vanishes near ($\pi, 0$) and equivalent points, and folds into four hole pockets centred at ($\pi/2, \pi/2$) etc. These two contrasting types of symmetry
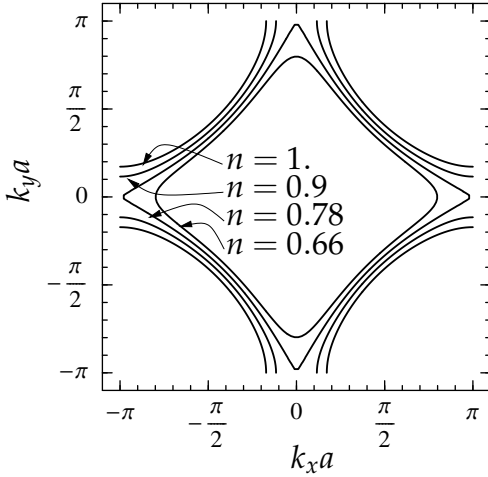
Figure 7.2: A set of non-interacting Fermi surfaces from a dispersion $\epsilon_{\mathbf{k}} = -2t(\cos k_x a + \cos k_y a - 0.5 \cos k_x a \cos k_y a)$ ($t' = -0.5t$), at four different electron fillings $n = 0.66, 0.78, 0.9, 1$.
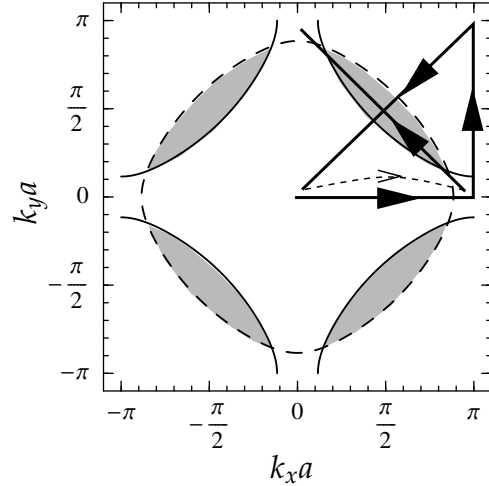
Figure 7.3: The arrow indicates the paths $(0,0) \to (\pi, 0) \to (\pi, \pi) \to (0,0)$ and $(\pi, 0) \to (0, \pi)$ that are taken in $\mathbf{k}$-space, used to present cross-sections of the spectral function. Also shown is a Fermi surface from Fig. 7.2 at $n = 0.9$, showing its (π, π) displacement (dashed) and the hole pocket regions (shaded).

breaking are discussed further in §7.4.2.

There are in fact two phases (AFM-α and AFM-β) with this type of distortion, which are differentiated by the precise details of their Fermi surface shape — although they are exceedingly close in energy. The phases of the same name in the following section (§7.3.1) are the same, and their properties shall be discussed further there (see Fig. 7.10 and Fig. 7.9 for AFM-α and AFM-β respectively). At high U, the site energies in the impurity model begin to diverge, and solutions are numerically difficult to find; this region is shown hatched in the phase diagram. There is an additional small patch of antiferromagnetism near half-filling at $U \sim 3$ that has more conventional character, the same as phase (e) of Fig. 6.1. Ferromagnetism is not permitted by the reduced quad-site implementation.

7.3   Results ($t' = -0.5t$)

Introducing next-nearest-neighbour hopping (*c.f.* §5.3.2) adds a further dimension to the phase diagram parametrized by t'. There will no longer be a $n \to 2 - n$ symmetry, but the halves are mirrored for $t' \to -t'$; *e.g.* $n > 1$ with $t' > 0$ is the same as $n < 1$ with $t' < 0$. I shall concentrate upon the case $t' = -0.5t$, leading to a non-interacting dispersion $\epsilon_{\mathbf{k}} = -2t(\cos k_x a + \cos k_y a - 0.5 \cos k_x a \cos k_y a)$. This value is close to the ARPES best fit Fermi surface shape [44] wherein $t' = -0.550t$. The van Hove point is separated from half-filling and now resides near $n = 0.78$, as shown in Fig. 7.2, which illustrates the non-interacting Fermi surface for this dispersion at various fillings.

125

7.3.1 Phase diagram

Fig. 7.4 shows the phase diagram for two-site quad-cluster DMFT with $t' = -0.5t$. The extent of antiferromagnetism has increased to $n = 0.74$, compared to $n = 0.8$ with $t' = 0$; and again there are several different antiferromagnetic phases, all of which exhibit the tetragonally-distorted Fermi surface with four hole pockets mentioned above. Two of these phases are the AFM-α and AFM-β phases observed at $t' = 0$; there is additionally a third phase labelled AFM-γ which has no $t' = 0$ equivalent. A further difference from $t' = 0$ is the emergence of a small patch of paramagnetism (δ-phase) with a similar hole pocket Fermi surface; this phase existed at $t' = 0$ but was never energetically favoured.

Fig. 7.5 shows the variation of (sublattice) magnetization and quasiparticle residue z across the phase diagram. Comparing with the 2×1 cluster equivalents in Fig. 6.2, the variations are very similar; although in Fig. 7.5(a) z can be seen to drop significantly on entering AFM-α or AFM-β — this is discussed in §7.4.2.

Proximity to the van Hove point at $n \sim 0.78$ presented numerical difficulties due to the cusp-like Fermi surface. At high U a slightly different solution (shown darker in Fig. 7.4), with a small antiferromagnetic moment, was possible in the region of $n = 0.78$; although this does not extend to low U, hence leaving a gap. Some of these features are probably artifacts of the limited **k**-space resolution at the cusps; we do not consider them further here. The phases with hole pockets do not show any signature of this particle-hole transition, as would be expected.

The remainder of this section is devoted to a more detailed, objective, analysis of the phases (interpretive discussion comes later in §7.4); various representations of the spectral function are presented for a number of demonstration points (§6.2 contained explanations of each of these representations). Calculations were again made using 120×120 points in the Brillouin zone, and a contour approach was used for integrating densities of states (*c.f.* Appendix C). Fig. 7.3 illustrates the path in momentum states used for cross-sections of the spectral function.
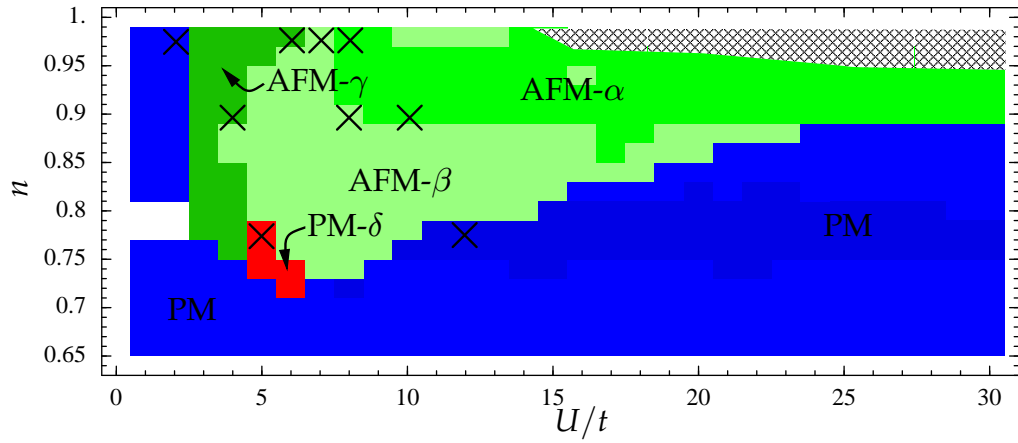
Figure 7.4: Ground state phase diagram ($U/t, n$) for the 2D Hubbard model within two-site quad-cluster DMFT, with $t' = -0.5t$. Distinct solutions are different colours, and labelled PM (conventional paramagnetism), PM-δ (paramagnetism with hole pockets), AFM-α, AFM-β, and AFM-γ (all antiferromagnetism with hole pockets). The phases are characterized further in the text (as is the band near $n = 0.78$), and detailed spectra will be presented for the indicated points. The diagram has been tidied up to extrapolate across a few points with numerical difficulties.
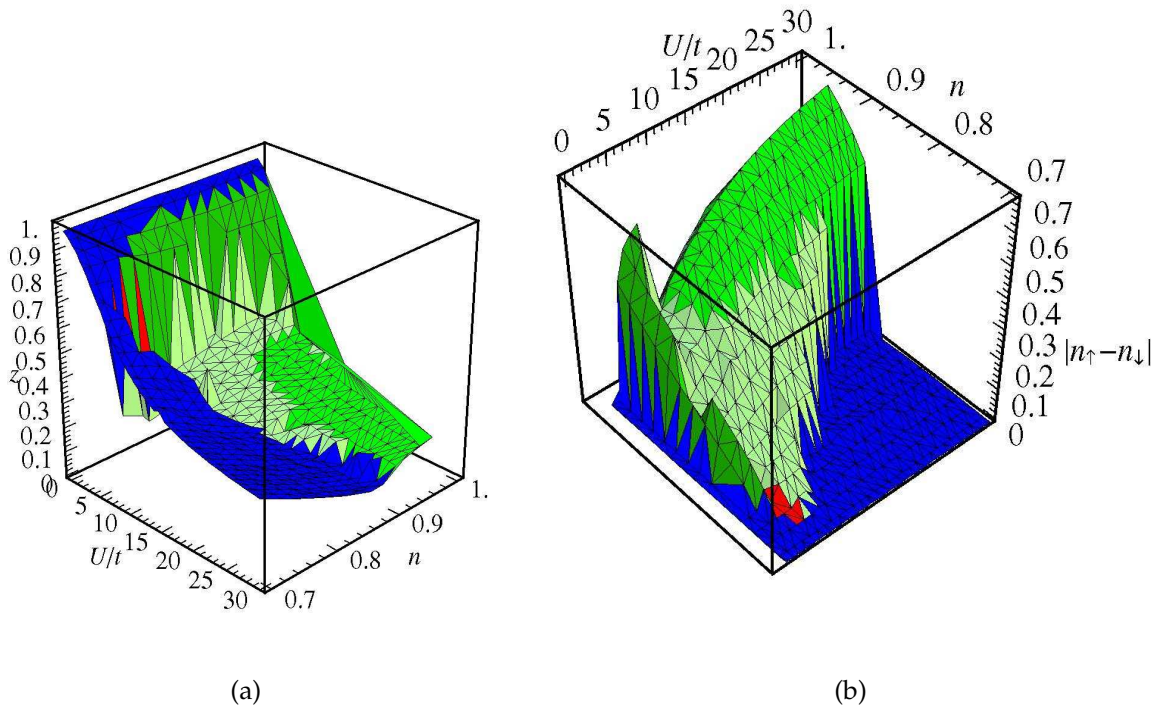

(a)   (b)

Figure 7.5: (a) Quasiparticle weight z (sublattice averaged) and (b) sublattice magnetization $|n_\uparrow - n_\downarrow|$ as a function of (U, n) for the ground state solutions of two-site quad-cluster DMFT with $t' = -0.5t$.

7.3.2 Paramagnetic phase

Fig. 7.6 illustrates points within the conventional paramagnetic phase (PM in Fig. 7.4). The Fermi surface encloses $(0,0)$ for $n < 0.78$ and (π, π) for $n > 0.78$, as shown in Fig. 7.6(a) and Fig. 7.6(b) respectively. The point at $(U = 12t, n = 0.78)$ is within the region exhibiting a small sublattice moment ($m \sim 0.01$), and cusps in the Fermi surface are slightly reduced. Fig. 7.6(c) and (d) show that the spectrum consists of a renormalized quasiparticle band (note the skewed density of states due to the t' term) together with Hubbard bands. The phase is indistinguishable from phase (a) of Fig. 6.1 for the 2×1 cluster (*e.g.* as illustrated in Fig. 6.5), except for the expected consequences of $t' < 0$, and the small distortion at high U in the pair-cluster solution that is not observed here.
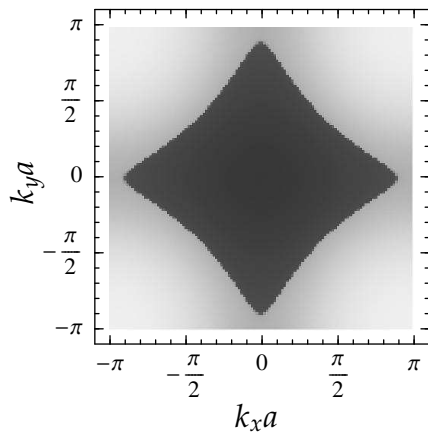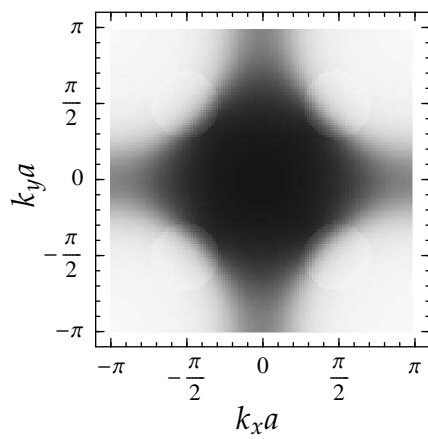
(a) $n_{\mathbf{k}}$ across Brillouin zone ($U = 12t$, $n = 0.78$)
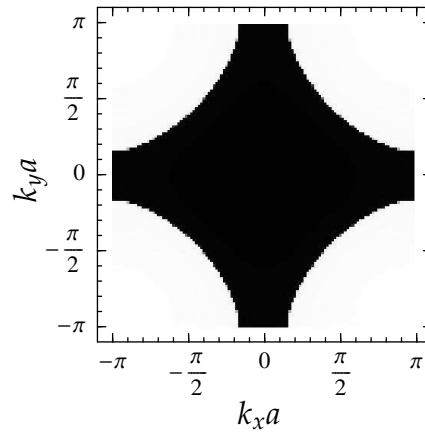
(b) $n_{\mathbf{k}}$ across Brillouin zone ($U = 2t$, $n = 0.98$)
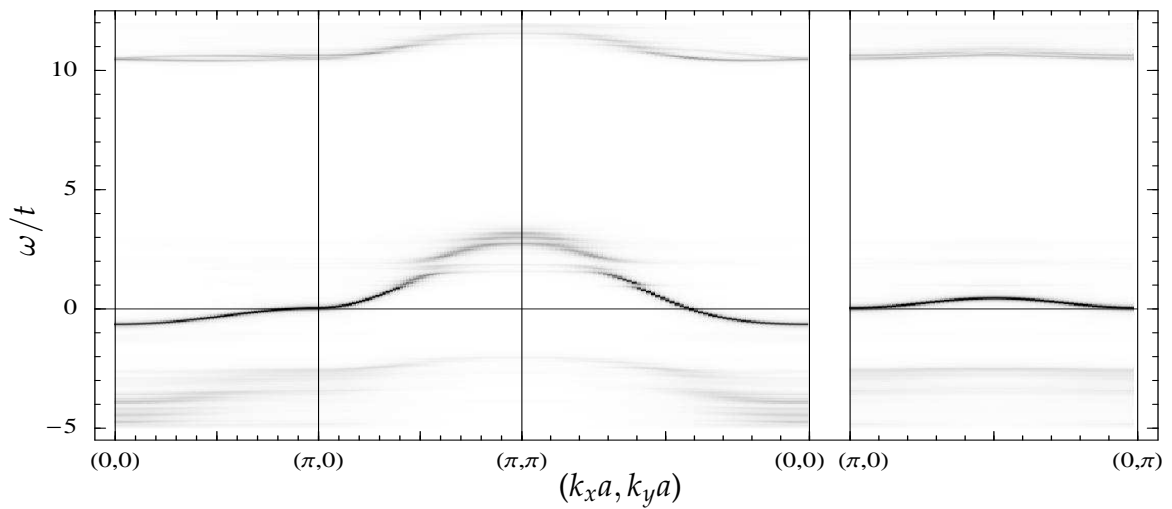
(c) Spectral function cross-section ($U = 12t$, $n = 0.78$); dark $\leftrightarrow$ greater spectral weight
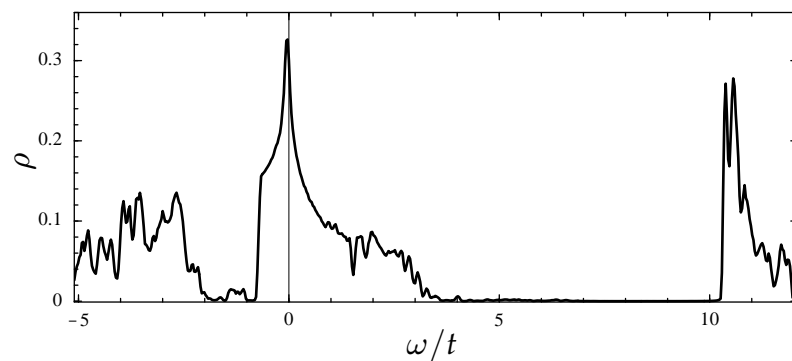
(d) Local density of states ($U = 12t$, $n = 0.78$), smoothed

Figure 7.6: Conventional paramagnetism ($U = 12t$, $n = 0.78$ and $U = 2t$, $n = 0.98$); see §7.3.2 for discussion.

129

7.3.3   Paramagnetism with hole pockets (δ-phase)

Fig. 7.7 illustrates the small region of paramagnetism with hole pockets, labelled PM-δ in Fig. 7.4. The density of states in Fig. 7.7(d) shows the formation of a gap at the Fermi level. This gap arises everywhere in the Brillouin zone apart from places near $(\pi/2, \pi/2)$: the spectral function — Fig. 7.7(c), $(\pi, 0) \to (0, \pi)$ section — shows a plume of low spectral weight branching off the main band and crossing the Fermi level. The result is a hole pocket that is almost circular, visible as a discontinuity in the electron density $n_{\mathbf{k}}$ in Fig. 7.7(a), and as the regions of high spectral density at the Fermi level in Fig. 7.7(b). The quasiparticle residue can be seen to vary around the hole pocket, being larger towards $(0, 0)$, where the original Fermi surface lay.

In the vicinity of $(\pi, 0)$ the dispersion is gapped and there is no Fermi surface. The non-interacting band is flat here due to the van Hove point (see Fig. 7.7(c)). Interactions cause it to split in two; each half expands over a larger region in momentum space whilst staying fairly flat, but neither cross the Fermi level anywhere now.

This phase is particularly interesting because of its relevance to the cuprates: it is a paramagnetic state that exhibits both a pseudogap and arc-like Fermi surfaces. In §7.4.3 below, this comparison with the normal state of the cuprates will be made in more detail.

(a) $n_\mathbf{k}$ across Brillouin zone
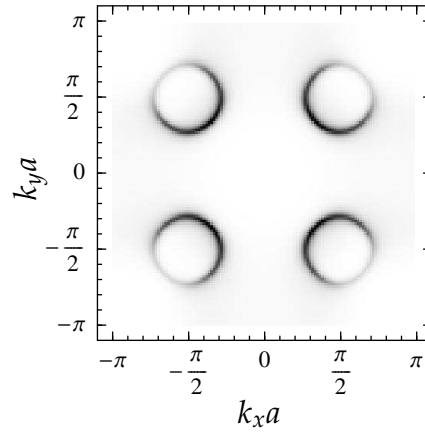
(b) Spectral density at ϵ_F across the Brillouin zone
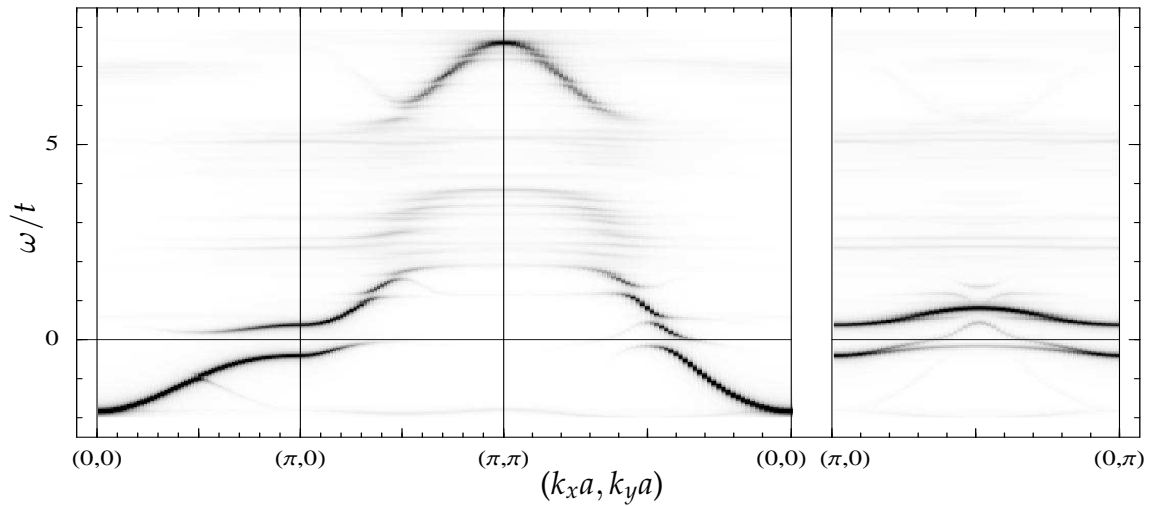
(c) Spectral function cross-section; dark $\leftrightarrow$ greater spectral weight
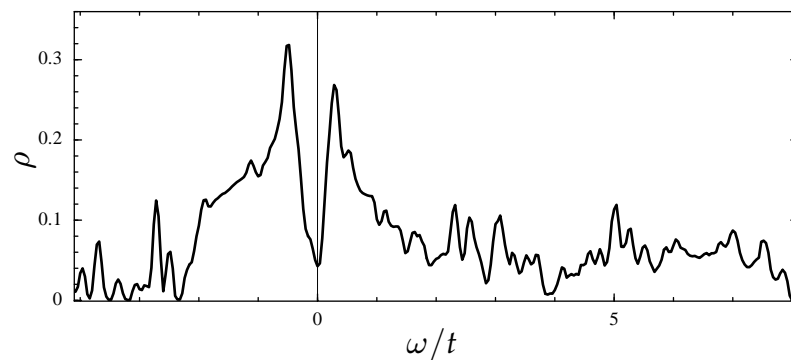
(d) Local density of states, smoothed

Figure 7.7: Paramagnetism with hole pockets ($U = 5t$, $n = 0.78$); see §7.3.3 for discussion. (b) shows $A(\mathbf{k}, \omega = 0)$ with a relative scale of spectral density.

7.3.4 Antiferromagnetism with hole pockets (γ-phase)

Fig. 7.8 illustrates two points within the antiferromagnetic γ-phase of Fig. 7.4. Clear hole pockets are visible near $(\pi/2, \pi/2)$ in Fig. 7.8(a), which become smaller and less distinct nearer the Mott transition (Fig. 7.8(b)). The spectral function in Fig. 7.8(c) shows bands crossing the Fermi level that give rise to these hole pockets. As usual, the hole pockets have a varying quasiparticle weight, becoming less distinct on the outer portion, where the band fades away along the $(0,0)$ to (π, π) spectral function cross-section.

Spectral features are generally similar to the PM-δ phase above, apart from the fact that the entire band is involved in the creation of a hole pocket, rather than a plume that branches off the main band.

(a) $n_{\mathbf{k}}$ across Brillouin zone ($U = 4t$, $n = 0.9$)

(b) $n_{\mathbf{k}}$ across Brillouin zone ($U = 6t$, $n = 0.98$)
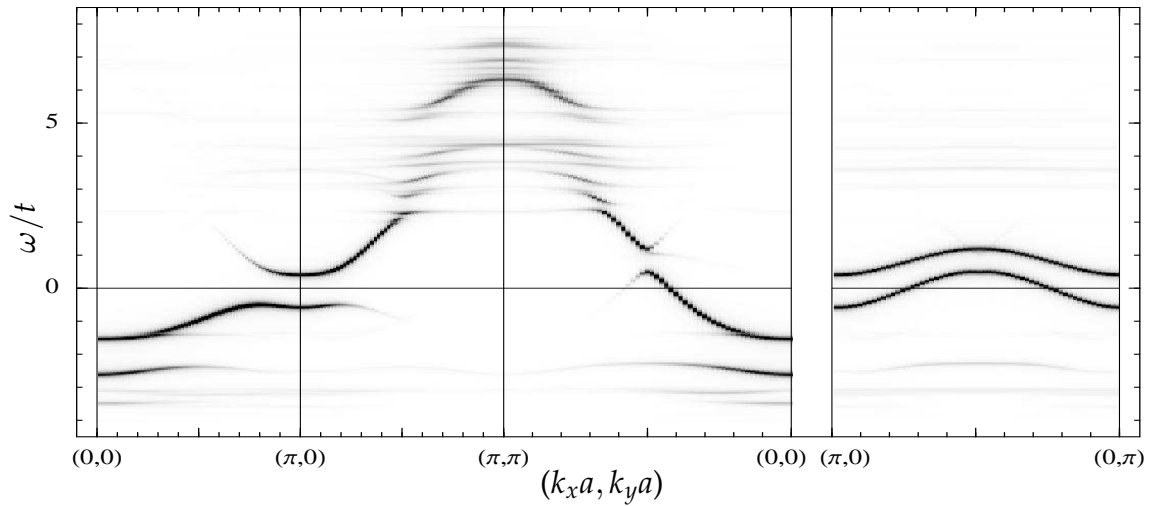
(c) Spectral function cross-section ($U = 4t$, $n = 0.9$); dark $\leftrightarrow$ greater spectral weight
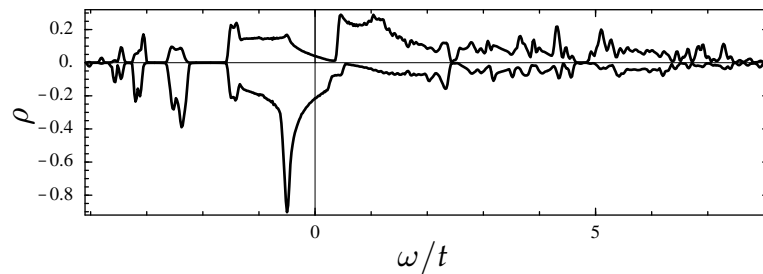
(d) Local density of states ($U = 4t$, $n = 0.9$), smoothed

Figure 7.8: Antiferromagnetism with hole pockets, γ-phase ($U = 4t$, $n = 0.9$ and $U = 6t$, $n = 0.98$); see §7.3.4 for discussion. The density of states is plotted separately for each of the two sublattices, and the Brillouin zone is shown with the second quasiparticle band of states drawn in the second RBZ for convenience (the dashed line indicates the boundary).

7.3.5 Antiferromagnetism with hole pockets (α- and β-phases)

Fig. 7.9 and Fig. 7.10 illustrate points within the antiferromagnetic β- and α-phases of Fig. 7.4 respectively. General spectral features are similar to AFM-γ and PM-δ discussed above: near $(\pi/2, \pi/2)$ etc. there are hole pockets where a band crosses and recrosses the Fermi level, and near $(\pi, 0)$ etc. there are gaps which split the dispersion into flattened, slightly expanded bands above and below the Fermi level.

Like the PM-δ phase, the spectral function is rather fragmented (in contrast to the AFM-γ phase). There is a floating narrow central band between the active bottom band and the upper Hubbard-like band, giving a spectrum reminiscent of the distorted phase (c) of the 2 × 1 cluster (see Fig. 6.8). The band that gives rise to the hole-pocket Fermi surface is somewhat separate from the main dispersion, particularly apparent in the AFM-β phase where only a weak plume crosses the Fermi level — exactly the same as in the PM-δ phase.

The antiferromagnetic α- and β-phases are exceedingly close to each other in energy and differ only by the orientation of the hole pockets; in the α-phase (Fig. 7.10) the hole pockets are aligned (conventionally) along the original Fermi surface line, like the γ-phase; but in the β-phase (Fig. 7.9) the pockets are aligned perpendicular to this. In this latter case (AFM-β), the quasiparticle residue is stronger on the *outer* side of the pockets (opposite the the other phases) and fades away completely on the inner side.
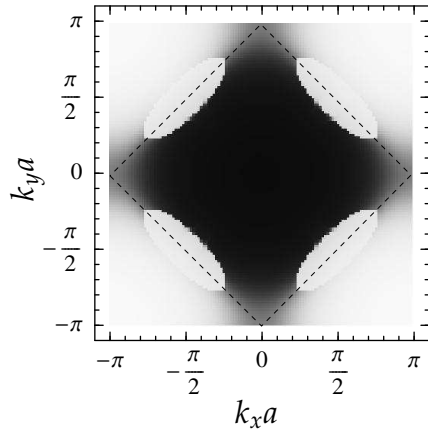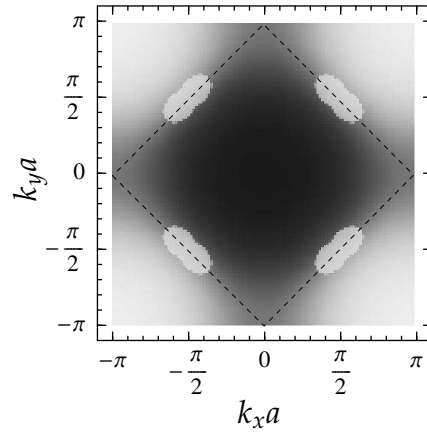
(a) $n_\mathbf{k}$ across Brillouin zone ($U = 8t$, $n = 0.9$)
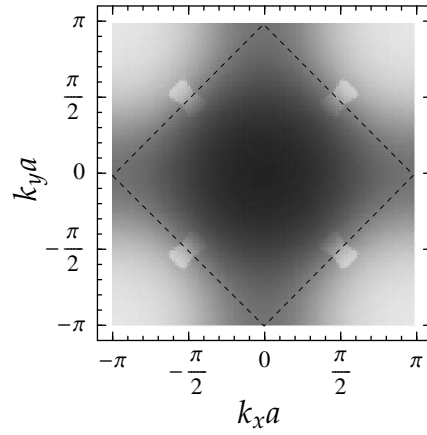
(b) $n_\mathbf{k}$ across Brillouin zone ($U = 7t$, $n = 0.98$)
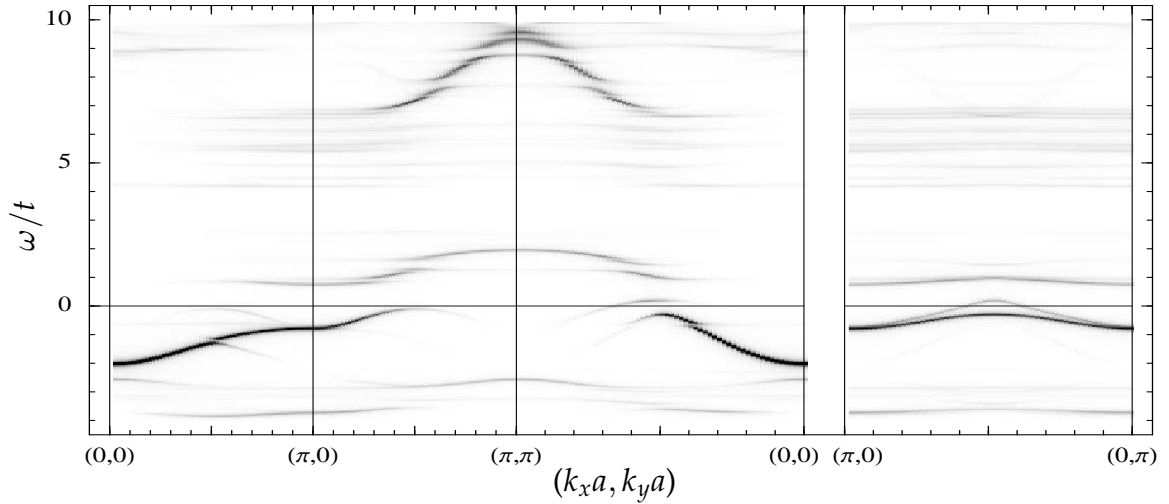
(c) Spectral function cross-section ($U = 8t$, $n = 0.9$); dark $\leftrightarrow$ greater spectral weight
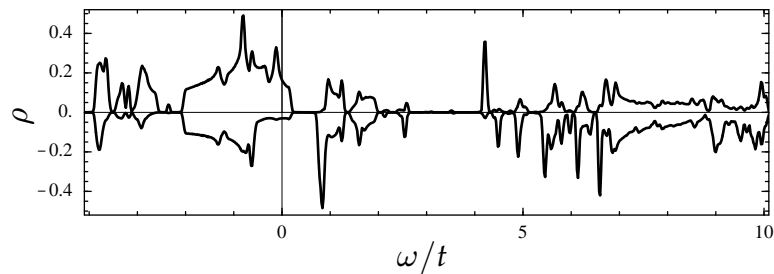
(d) Local density of states ($U = 8t$, $n = 0.9$), smoothed

Figure 7.9: Antiferromagnetism with hole pockets, β-phase ($U = 8t$, $n = 0.9$ and $U = 7t$, $n = 0.98$); see §7.3.5 for discussion. The density of states is plotted separately for each of the two sublattices, and the Brillouin zone is shown with the second quasiparticle band of states drawn in the second RBZ for convenience (the dashed line indicates the boundary).
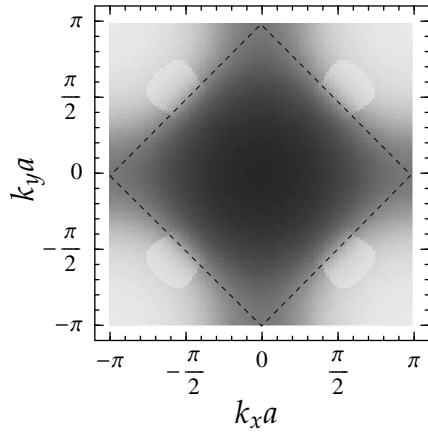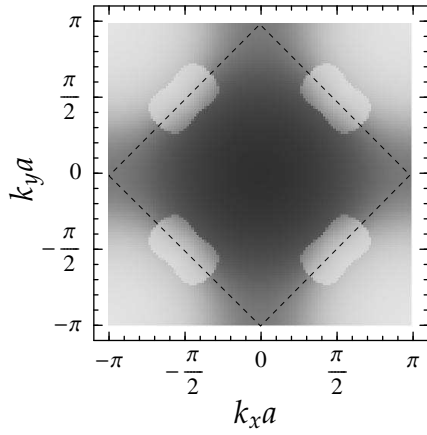
(a) $n_{\mathbf{k}}$ across Brillouin zone ($U = 10t$, $n = 0.9$)
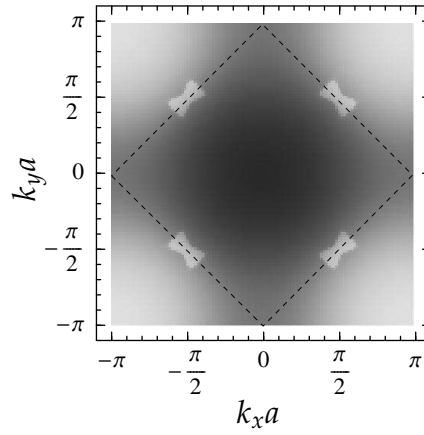
(b) $n_{\mathbf{k}}$ across Brillouin zone ($U = 8t$, $n = 0.98$)
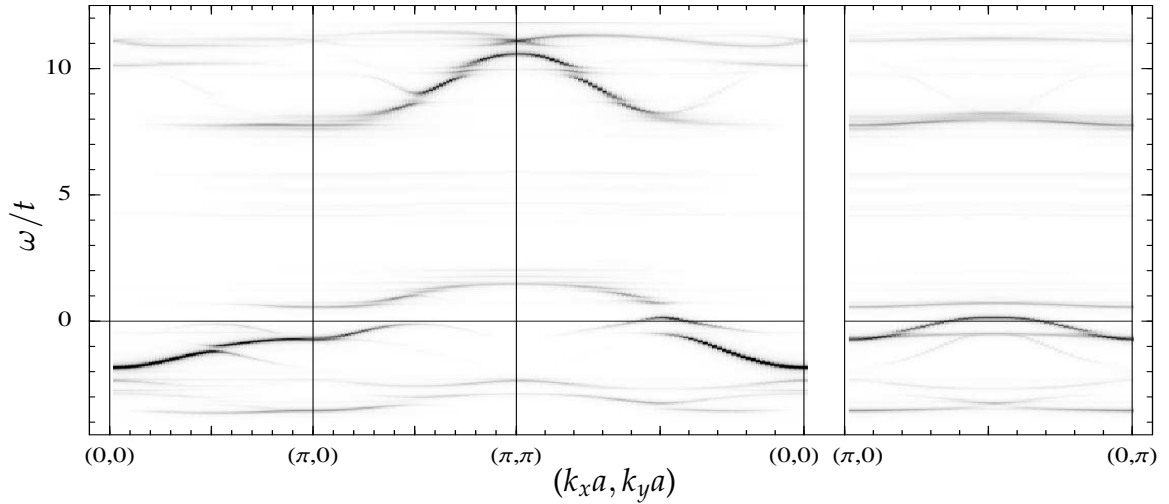
(c) Spectral function cross-section ($U = 10t$, $n = 0.9$); dark $\leftrightarrow$ greater spectral weight
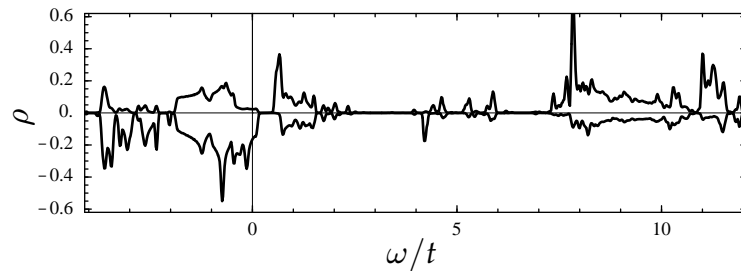
(d) Local density of states ($U = 10t$, $n = 0.9$), smoothed

Figure 7.10: Antiferromagnetism with hole pockets, α-phase ($U = 10t$, $n = 0.9$ and $U = 8t$, $n = 0.98$); see §7.3.5 for discussion. The density of states is plotted separately for each of the two sublattices, and the Brillouin zone is shown with the second quasiparticle band of states drawn in the second RBZ for convenience (the dashed line indicates the boundary).

136

7.4 Discussion

Many of the physical scenarios presented in Chapter 6 for the 2 × 1 cluster remain true for the 2 × 2 cluster. For example, the picture of the Mott transition (§6.3.2) is the same: the doped Mott insulator has a Fermi surface consisting of hole pockets, that are separated by regions where the electron density falls smoothly and there are no free carriers (breaking Luttinger's theorem). The hole pockets shrink as half-filling is approached, and become less distinct with increasing interaction strength U (see the $n_{\mathbf{k}}$ plots in Fig. 7.8, Fig. 7.9 and Fig. 7.10). The only difference from the pair-cluster is that the hole pockets are placed near $(\pm\pi/2, \pm\pi/2)$ for the quad-cluster.

The picture of Slater antiferromagnetism in §6.3.1 is generally accurate for the quad-cluster phases also; the AFM-α and AFM-β phases of this chapter are much like phase (c) of Fig. 6.1. Introducing the $t' < 0$ term leads to a suppression of the more conventional antiferromagnetic phases (d) and (e) of Fig. 6.1 for the quad-cluster, and enables the AFM-γ phase to emerge.

In the rest of this section I shall discuss several topics pertinent to the quad-cluster, beginning (in §7.4.1) with the effects that the t' term has upon the antiferromagnetism and Fermi surface shape within the phases, and on the hybridization of the dispersion with its (π, π)-displaced ghost. In §7.4.2 I examine the different Fermi surface distortions in each phase and those of Chapter 6, and finally experimental observations in the cuprates are compared with pseudogap and arc-like Fermi surface phenomena — now moved from the restricted positions of Chapter 6 to the correct places.

7.4.1 Next-nearest neighbour hopping (t') and hybridization

Introducing a next-nearest-neighbour hopping t' term to the lattice model has several effects. First, the half-filling point ($n = 1$) is now separate from the van Hove point, where the Fermi surface switches from enclosing $(0, 0)$ to enclosing (π, π) — this happens at $n \sim 0.78$ for $t' = -0.5$. It is useful to be able to distinguish the consequences of half-filling and the van Hove point: their coincidence in the Hubbard model is not necessarily reflected in real materials.

The second effect of t' is the creation of triangles on the lattice that will geometrically frustrate antiferromagnetism. Examining the sublattice magnetization, the effect can be seen: $|n_\uparrow - n_\downarrow|$ is typically 0.1 less in the frustrated model ($t' = -0.5$) than the unfrustrated one ($t' = 0$). The effect on the range of the antiferromagnetism off half-filling is somewhat surprising, though; at $U \sim 7t$, for example, the extent increases from $0.8 < n < 1$ when $t' = 0$, to $0.74 < n < 1$ when $t' = -0.5$ (see Fig. 7.1 and Fig. 7.4). However, the van Hove points — being flat regions all linked by (π, π) antiferromag-

(a)   (b)
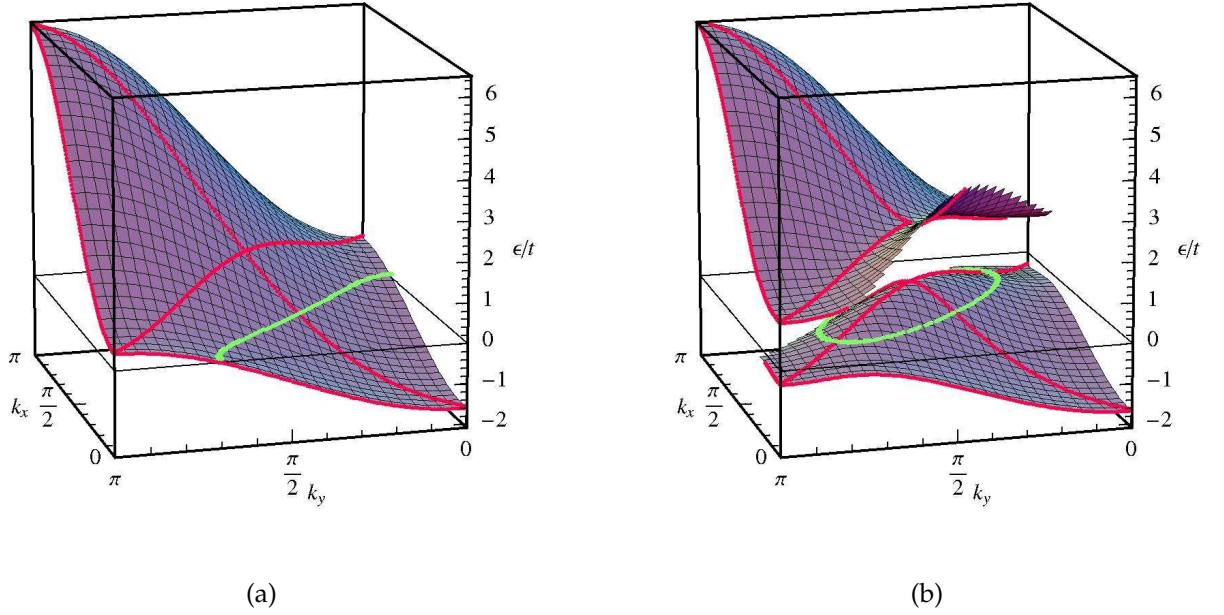
Figure 7.11: Schematic visualization of the formation of hole pockets. A non-interacting dispersion with $t' = -0.5$, shown in (a), hybridizes with a copy of itself displaced by a wave-vector (π, π). The result, with a hybridization gap of $1.5t$, is shown in (b). The "ghost" copy is weaker and is not visible except near the intersection. The Fermi surface is indicated with a green line, and the red lines show the cross-sections that are visible in the spectral function — *c.f.* Fig. 7.6(c) and Fig. 7.8(c), for example.

netic wave-vectors — encourage the antiferromagnetic instability, and have moved down to $n = 0.78$ from $n = 1$. It should also be noted that the antiferromagnetic phases consist of hole pocket phases, whose formation is encouraged by $t' < 0$ (see below). These two facts together can explain the increase in antiferromagnetic extent. At half-filling, one would expect less antiferromagnetism and for the order to appear above some finitesimal U instead of for $U > 0$.

Third, t' alters the Fermi surface shape, and this becomes important when the mechanism for self-hybridization is considered (*c.f.* §6.3.3) — *i.e.* how the dispersion $\epsilon_{\mathbf{k}}$ can overlap with the ghost dispersion $\epsilon_{\mathbf{k}+(\pi,\pi)}$ generated by antiferromagnetic fluctuations. If $t' = 0$, by the time the Fermi surface is large enough that it can overlap with itself, it has reached a diamond shape, which has flat bands along $(\pi, 0) \rightarrow (0, \pi)$ and cannot construct hole pockets. A negative t' causes the Fermi surface to bend inwards near $(\pi/2, \pi/2)$ etc., as shown in Fig. 7.2, and it never takes on a diamond shape. When the Fermi surface is large enough to enclose (π, π), it still has portions in the first reduced Brillouin zone, and hole pockets may be formed as shown in Fig. 7.3. A complete picture of the dispersion before and after this hybridization process is shown in Fig. 7.11, which will be useful for interpreting spectral function cross-sections.

In §6.3.3 I described the consequences of hybridization with a ghost dispersion for

the 2 × 1 cluster, and the general picture remains true for the 2 × 2 cluster. A gap is formed, but the chemical potential μ may or may not fall within it. At places in momentum space where it does, portions of the Fermi surface will disappear. Along the line $(\pi, 0) \to (0, \pi)$, the t' causes the band to curve, and additionally it is split by U; see Fig. 7.11(b). Near $(\pi, 0)$ etc. μ falls in the gap and there is no Fermi surface — but further along, the lower band crosses and recrosses μ, creating a hole pocket. In the $(0, 0) \to (\pi, \pi)$ direction Fig. 6.12 remains relevant: the original dispersion crosses the ghost dispersion near $(\pi/2, \pi/2)$, and when hybridized, the dispersion bends over and fades out because the ghost dispersion has less spectral weight (this is apparent in Fig. 7.8(c)).

7.4.2 Spontaneous distortions and soft Fermi surfaces

Whilst the picture above describes the state in the AFM-γ phase Fig. 7.8 (§7.3.4) well, there are rather more subtle effects in the AFM-α and AFM-β phases. However, the geometrical understanding of Fig. 7.11 is correct and remains useful; the bands are in effect just more fragmented by interactions.

First, we note that that hole pockets in AFM-α and AFM-β exist even when $t' = 0$ (see §7.2) — there is an effective t' *spontaneously* generated. This tetragonal distortion has the same underlying cause as the spontaneous Pomeranchuk (lemon-shaped) distortion in the 2 × 1 cluster (Chapter 6, *c.f.* §6.3.4): quasiparticles are easily displaced from the $(\pi, 0)$ etc. points because of their low Fermi velocity there. Here they move to the $(\pm\pi/2, \pm\pi/2)$ regions, but in Chapter 6 their redistribution was far more constrained.

The differences are due to the fact that the shape of the cluster determines the types of distortion permissible. For example, in §6.3.4 I noted for the pair-cluster that there could only be opposite changes to the points $(\pi, 0)$ and $(0, \pi)$. For the quad-cluster changes must have the same sign, and hence different distortions are observed. The 2 × 2 cluster permits tetragonal symmetry-breaking but does not permit distortions that break x-y symmetry. This is due to the restrictions put on the impurity model that the bonds between the A and B sites are identical in the x and y directions. The question of whether the Pomeranchuk instability of Chapter 6 is real (rather than an artifact of the broken symmetry of the 2 × 1 cluster) cannot be answered yet, but could be answered by an unrestricted 2 × 2 cluster.

Returning to the AFM-α and -β phases, it is apparent from the spectra (Fig. 7.10(c) and Fig. 7.9(c)) that the hole pockets are not just a result of simple hybridization: the Fermi surface is formed by plumes of spectral weight branching from the main bands

(although AFM-α). The same is true for the paramagnetic δ-phase; although here the t' is essential, as it encourages the formation of hole pockets and allows the paramagnetic state with hole pockets to become energetically favoured in a certain region. The quasiparticle residue for these three phases (see Fig. 7.5(a)) is reduced in comparison to the other phases, because of the weakness of these plumes.

These three phases have different shaped Fermi surfaces for the hole pockets: perpendicular orientations of ovals for AFM-α and AFM-β phases, and an almost circular shape for PM-δ. The exact shapes should not be given too much emphasis, since the 2×2 cluster can only support a limited number of shapes (*c.f.* Eqn 5.46 for $t' = 0$) — the important feature is the proximity to $(\pi/2, \pi/2)$. The crucial message from the results is the ease of distortion of the Fermi surface, from the Pomeranchuk phenomenon of Chapter 6 through to the evanescent plumes forming the variety of these hole pocket shapes (remember too that the AFM-α and AFM-β phases are exceedingly close in energy): everything fits the *soft Fermi surface* picture of Metzner [112].

7.4.3   The cuprates: pseudogap and Fermi arcs

In this section I will compare our results for the PM-δ hole pocket phase of Fig. 7.4 with experiments on the normal state of the cuprates. Note that the hole pockets in this phase are not just a result of hybridization of the Fermi surface containing a next-nearest neighbour hopping $t' < 0$, but exist when $t' = 0$ and are a rather more subtle interaction-caused momentum anisotropy. The t' is required, though, to make this phase energetically favoured: it encourages the hole pockets once they are already formed.

Angle-resolved photoemission spectroscopy (ARPES) experiments on the high temperature superconducting cuprates [127] observed that the superconducting gap appears to continue into the normal state, leaving a d-wave gap maximal in the $(\pi, 0)$ direction and nodal in the (π, π) direction [136]. It was suggested that the Fermi surface becomes gapped in the $(\pi, 0)$ regions (that are connected by (π, π) antiferromagnetic wave-vectors [119]) and disappears there. Marshall *et al.* [135] observed this effect in $Bi_2Sr_2CaCu_2O_{8-\delta}$ (see Fig. 7.12(b)), and more recently it was also observed in $La_{2-x}Sr_xCuO_4$ [128] (see Fig. 7.13(b)). Other experimental probes that cannot resolve momentum-space features show a gap near the Fermi level [136]. All these experimental observations coincide with the results of our calculations; Fig. 7.7(d) shows a significant reduction in the density of states near the Fermi level, and Fig. 7.7(a) and (b) demonstrate the lack of free carriers in the region of $(\pi, 0)$.

Spectrally, the band below the Fermi level near $(\pi, 0)$ is observed to be very flat

(a)   (b)
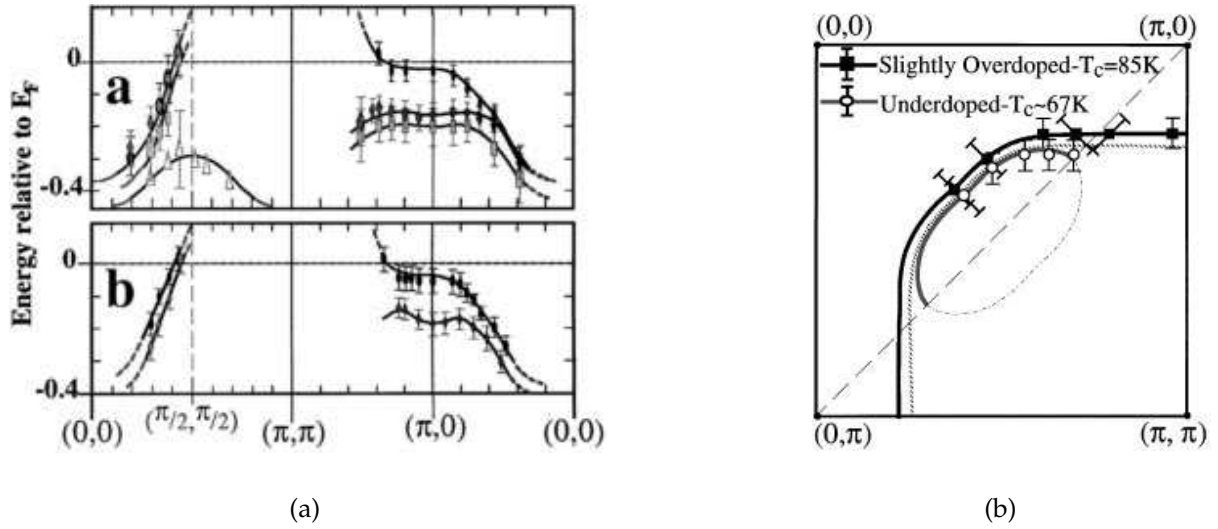
Figure 7.12: (a) Spectrum and (b) Fermi surface from ARPES measurements on $Bi_2Sr_2CaCu_2O_{8-\delta}$, taken from Figs 3 and 4 of Ref. [135]. (a) is constructed from a variety of samples; the lower curves are more underdoped.
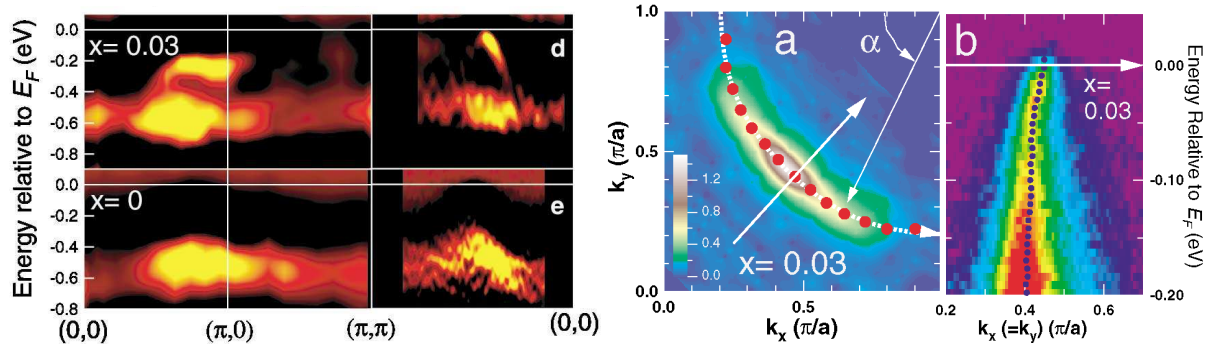
Figure 7.13: Spectral density (a) as a cross-section and (b) near the Fermi level from ARPES measurements on $La_{2-x}Sr_xCuO_4$, taken from Figs 1 and 2 of Ref. [128] The compound is very underdoped; when $x = 0$ it is a anti-ferromagnetic insulator and when $x = 0.03$ it is just in the insulating spin-glass phase. In (a), note the flat band near $(\pi, 0)$ and the sharp feature near $(\pi/2, \pi/2)$, and the lower Hubbard band at -0.6eV. (b) shows the arc-like Fermi surface, and the band that gives rise to it.

(see Fig. 7.12(a) and Fig. 7.13(a)), and again our calculations show the same things — see Fig. 7.7(c). Note that ARPES cannot observe the unfilled bands above the Fermi level included in this graph. The modulation near $(\pi, 0)$ in Fig. 7.12(a) for underdoped cuprates is tantalisingly similar to Fig. 7.8(c), although the latter is from an antiferromagnetically ordered state.

According to ARPES experiments, the Fermi surface is thus eroded near $(\pi, 0)$ etc., and only remains in *arc-like* segments near $(\pi/2, \pi/2)$ etc. — see Fig. 7.12(b) and Fig. 7.13(b). It has been variously suggested in the past (*e.g.* Refs [135] and [125]) that these arcs originate from portions of hole pockets; but signatures of the other side have never been observed, in spite of ARPES workers directly searching for them [137]. Our calculations predict completed hole pockets, like the other theories, but we can go further and explain why only an arc is observed by ARPES. The outer portion, coming from the weaker "ghost" dispersion, has a smaller spectral weight (see Fig. 7.7(b)), and is likely to be too weak for ARPES to observe. PM-δ solutions at lower n have an even more uneven distribution of spectral weight, and the hole pocket is larger, giving a curvature more like Fig. 7.13(b) (though in any case, we should not take too much notice of the exact momentum space shapes as the 2×2 cluster gives limitations on shapes as discussed above).

Spectrally, the band bending over that causes the far side of the hole pocket is visible near $(\pi/2, \pi/2)$ — see Fig. 7.13(a), top right, agreeing with Fig. 7.7(c). In the underdoped cuprates, which are nearer the antiferromagnetic region of their phase diagram, there is a band very reminiscent of the hybridization effect described above — see Fig. 7.12(a), top left. In fact, the sample in Fig. 7.13 is quite close to being antiferromagnetic, so comparison may be made with Fig. 7.8 also, which gives excellent agreement on Fermi surface shape and spectra.

The phenomena discussed above have been intensely studied theoretically, and I shall now mention a sample of the literature; however few (if any) authors have produced complete pictures that are directly relevant. The idea of hybridization to produce hole pockets is well established (see *e.g.* Ref. [125]) and others have suggested that the far side of the hole pocket may not be experimentally observable [138]. Various renormalization group approaches [139, 140] have shown how portions of the Fermi surface disappear near $(0, \pi)$ etc. These places are the *hot spots* that were mentioned in Chapter 2: at high temperatures quasiparticles can exist here but have short lifetimes. Recent theoretical approaches that produce hot spots include that of Sénéchal *et al.* [141] who use a cluster perturbation theory approach (but require second and third neighbour hopping, and the pockets are not clear). The Dynamical Cluster Approximation can produce hot spots without including a t' term [142], and another CDMFT

approach [64] also gets hot spots (with a t'); but neither of these give very clear results about the Fermi surface.

7.5 Summary

The 2×2 quad-cluster investigated in this chapter is the last, and most sophisticated, application of two-site cluster DMFT to be studied in this thesis. It allowed antiferromagnetism and a range of momentum-dependent phenomena to be investigated coherently within dynamical mean-field theory. I have presented results for the the phase diagram of the 2D Hubbard model, with and without a t' next-nearest-neighbour hopping term. The detailed properties of the electronic spectral function and quasiparticles gave some fascinating results, and reproduced features of the normal state of the cuprates that have not been understood.

The phase diagram is demarcated by borders between paramagnetism and antiferromagnetism, and also by the Fermi surface shape. Some regions do not have a conventional Fermi surface but instead a dramatically different shape consisting of four hole pockets centred at $(\pm\pi/2, \pm\pi/2)$. Generally, the distortion that is necessary to give rise to this shape occurs spontaneously from the effects of electronic interactions. The many-body Hamiltonian generates an effective t' necessary to create hole pockets, and the direct t' we add enhances the effect, and allows a paramagnetic phase exhibiting hole pockets to emerge. The spectral shapes can be well understood by visualizing a non-interacting dispersion, with a direct t', hybridizing with a (π, π)-displaced "ghost" caused by antiferromagnetic fluctuations. A good subject for future study would be the completion of the other half ($n > 1$) of the phase diagram, and then progressing towards a full picture of the effects of varying amounts of next-nearest-neighbour hopping and higher order terms.

Several crucial features of the normal state of the cuprate high-temperature superconductors are reproduced in the paramagnetic phase that we discovered with a Fermi surface consisting of hole pockets, and we hope to publish these results. We observe the formation of a pseudogap, by the erasure of Fermi surface in the region of $(\pi, 0)$. ARPES observations show a Fermi surface consisting of arcs, which are matched well by the hole pockets seen in our calculations that show one side with very small spectral weight that would probably be unobservable.

Spectral features are broadly similar to those seen in the results for the 2×1 paircluster (Chapter 6). The mechanism for the approach to the Mott transition in an antiferromagnetic environment, that emerged from the 2×1 cluster, remains true in the 2×2 cluster: hole pockets form, and increasing the number of electrons and the inter-

action strength U cause them to shrink and become less distinct. The difference is the position of the hole pockets; for the 2×1 cluster, the positions of features within the Brillouin zone were severely constricted, but the 2×2 cluster model allows the hole pockets to exist in their natural $(\pi/2, \pi/2)$ position. Also, an asymmetrical cluster encouraged x-y symmetry to be broken, a feature prohibited within the 2×2 cluster we used. Whilst it is useful to have separated the effects of this instability from other Fermi surface distortions, we still do not know if it is just an artifact of the cluster shape. To answer this question, a 2×2 cluster should be studied with free bath parameters that are not antiferromagnetically constrained; as well as allowing both types of symmetry breaking, this would permit different types of magnetic order and more exotic phases (such as spontaneous currents round a plaquette), and all could be studied on an equal footing.

Chapter 8

CONCLUSIONS

Who can say how long the eye of the vulture
or the lynx requires to grasp the totality of a
landscape, or whether in a comprehensive
instant the seemingly inexhaustible confusion
of detail falls upon their eyes in an ordered
and intelligible series of distances and shapes,
where the last detail is perceived in relation to
the corporate mass?

MERVYN PEAKE
Titus Groan [143]

Many approaches to strongly correlated electron systems in the past have neglected momentum anisotropy, yet experiments on materials such as the cuprate high temperature superconductors have observed significantly anisotropic features. In this thesis, I have investigated both the cause and effect of anisotropy in momentum-space through two separate calculations, illustrating two complementary approaches to strongly correlated electron systems.

The first concerns magnetotransport properties (Hall effect and magnetoresistance) arising from a particular model of electron scattering within the normal state of the cuprates. The project is phenomenological and experimentally oriented: photoemission measurements observed "hot spots" at particular places in momentum space, where the electrons have a significantly shorter lifetime. The calculations explored the *consequences* of this anisotropy for magnetotransport in the copper oxide layer of these compounds.

In contrast, the approach of the second project is microscopic: we investigate, mathematically and computationally, a many-body model within a sophisticated approximation scheme. Specifically, we study the phase diagram and quasiparticle properties of the square lattice Hubbard model within a minimal implementation of cluster dynamical mean-field theory, at zero temperature. The calculations show that one consequence of electron-electron interactions is the spontaneous break up of the Fermi surface. The result is a state with four hole pockets separated by regions without free carriers: thus providing an *origin* for the momentum anisotropy observed in the planes of the cuprates.

I shall now discuss the conclusions from each of the two projects in more detail.

8.1 Phenomenological model for magnetotransport

The aim of Chapter 2 was to investigate the model proposed by Varma and Abrahams, invoking *anisotropic small-angle scattering* to attempt to explain the anomalous magnetotransport properties of the high-temperature superconducting cuprate materials in their normal state. They find that, given the marginal Fermi liquid linear temperature (T) dependence of the resistivity, small-angle scattering processes can give rise to a quadratic T^2 dependence of the Hall angle, as is observed in experiments.

In this thesis, I have presented results of calculations for a large variety of Fermi surfaces, scattering rates and other parameters, using a numerical technique, which can provide a completely independent check on the calculations of Varma and Abrahams. The conclusion from these calculations is that the T^2 dependence of the Hall angle is only possible for Fermi surfaces which are specially tuned to be *particle-hole*

symmetric, where the conventional Hall effect vanishes and the Hall angle is dominate by a higher order term which has the necessary unconventional T^2 dependence. Small deviations from particle-hole symmetry result in significant deviations from this law, whereas experimentally there is only a small change in the temperature exponent with doping. However, it is possible that correlations between electrons subtly pin the system very close to particle-hole symmetry regardless of doping, so we cannot rule out the model on this basis.

I show here that the key to resolving the issue is the *magnetoresistance*. Conventional metals obey Kohler's rule, which related the temperature dependences of the resistivity and the magnetoresistance, but measurements on the cuprates show a violation of Kohler's rule and suggest a modified Kohler's rule which relates the temperature dependence of the magnetoresistance to that of the Hall angle. Varma and Abrahams do not directly calculate the magnetoresistance predicted by their model, and we calculate it for the first time. I find that Kohler's rule is not broken by the small-angle scattering model: no combination of parameters can generate significant deviations, and certainly nothing like the modified Kohler's rule observed experimentally.

Thus we conclude that small-angle scattering does not underlie the anomalous normal state transport properties of the cuprates, and the explanation most likely does not lie within a Fermi liquid picture. The question remains the subject of active research, and more recent experiments on phenomena such as the optical Hall effect have enabled progress in our understanding of the electron relaxation rates in the cuprates.

8.2   Two-site cluster DMFT

Dynamical mean-field theory (Chapter 3) is one of the most exciting new techniques for strongly correlated electron systems from the last decade. A major insight from DMFT is how the Mott transition takes place via a three peak structure, that comprises two Mott–Hubbard bands existing simultaneously with an increasingly heavy central quasiparticle peak. DMFT has aided progress with many other phenomena, for example understanding of real materials through combination with density functional theory.

In conventional implementations, DMFT requires considerable computational resources, and cannot represent momentum-dependent effects of correlations. In this thesis I address these issues simultaneously with the development of *two-site cluster DMFT*. Within two-site DMFT (Chapter 4), the self-consistent bath of DMFT is represented by just a single site in an impurity model, but physically-motivated concepts are used to determine self-consistency conditions. Many-body dynamical effects are

retained; two-site DMFT is probably the simplest model that can reproduce all the key features of the Mott transition.

Two-site DMFT, being computationally straightforward, constitutes an ideal kernel for DMFT self-consistency calculations in situations where we wish to concentrate on further degrees of freedom. In this thesis, I combine two-site DMFT with cluster DMFT for the first time (Chapter 5). Cluster DMFT involves a cluster of several sites, instead of the single site of conventional DMFT, connected to some self-consistent bath. Now, different types of local magnetic order may be compared confidently, and the quantities calculated by cluster DMFT are permitted some momentum-dependence.

Our aim is to investigate the phase diagram and quasiparticle properties of the 2D Hubbard model within two-site cluster DMFT, at zero temperature. The simplicity of two-site DMFT is necessary for a comprehensive survey of the phase diagram — it is too computationally expensive within conventional DMFT. The cluster approach is not only essential to represent antiferromagnetism, but we also find that there are some fascinating momentum-space features of electronic correlations.

Understanding of the phase diagram was built up through three increasingly complex models; firstly within two-site DMFT without a cluster (Chapter 4), secondly with a 2×1 pair-cluster (Chapter 6), and thirdly with a 2×2 quad-cluster (Chapter 7). Here I shall predominantly focus on the last.

Conventional DMFT showed how the pictures of the Mott transition proposed by Hubbard and Brinkman–Rice could be synthesized, and our cluster approach allows the third picture of the Mott transition proposed by Slater (antiferromagnetism) to be incorporated simultaneously. We observe two predominant features in our phase diagram: *antiferromagnetism* (ubiquitous at half-filling, and maximally extends to 80% filling), and regions where the Fermi surface is distorted and forms *hole pockets*, located near $(\pi/2, \pi/2)$ in the Brillouin zone. The hole pockets provide a mechanism for how the Fermi surface can disappear through the Mott transition: as the insulating state is approached, the pockets shrink and become less distinct; the combined quasiparticle residue reduces, and the pockets will become points and vanish at the point the material becomes an insulator. Simultaneously, we observed a complex spectral picture of how the the Hubbard bands and quasiparticle peak coexist with these hole pockets. The Slater gap is present, but its consequences are *anisotropic*.

The distortion of the Fermi surface into hole pockets is demonstrative of another general feature: a *soft Fermi surface*. In the pair-cluster model, we observed a spontaneous Pomeranchuk lemon-shaped distortion of the Fermi surface, with hole pockets in corresponding places, and in the quad-cluster model we observed a variety of hole pocket shapes in phases close in energy. Our approach did not allow a direct com-

parison — we leave it as a future exercise to determine if there are circumstances in which the Pomeranchuk distortion remains favourable. But the overall conclusion is that there will be a number of closely competing distortions of the Fermi surface that are significant departures from the non-interacting shape. Shape is just one possible manifestation of this softness: it is indicative of more exotic phases such as supercond-uctivity, and the fluctuations could lead to a breakdown of Fermi liquid theory.

Introducing a next-nearest-neighbour hopping t' term increases the favourability of a paramagnetic state containing hole pockets, that reproduces many phenomena that have been observed in the normal state of the cuprate high-temperature superconduct-ors. We observe the formation of a *pseudogap*, where a partial gap is formed and regions of the Brillouin zone near $(\pi, 0)$ etc. are bereft of quasiparticles. The spontaneous for-mation of hole pockets explains why transport properties depend on the doping $1 - n$ rather than the Luttinger volume n. We predict a scenario where the Hall coefficient changes sign, as the Fermi surface goes from particle-like to consisting of hole pockets, which is probably simultaneous with the metal becoming antiferromagnetic. Finally, the hole pockets that we observe exhibit a rather asymmetrical distribution of spectral weight: one side is very weak, and photoemission experiments would only be able to observe the other side — they indeed see only *arcs* of Fermi surface. We predict that with high enough resolution and sensitivity, and close enough to the Fermi level $(\epsilon_F - \delta)$, the other half of the pockets will become visible.

Self-consistent mean-field theory has some dangers. A wealth of phases are pro-duced, and whilst we can compare the energies of these phases to identify the ground state, we can never be sure that there is not an additional, lower-energy phase that has been missed. A simple example is how conventional DMFT is not able to support antiferromagnetism, which is lower in energy than paramagnetism. Phases also try to exploit the detailed features of the model (such as the broken symmetry in the pair-cluster), and further study has to be made to distinguish how much properties are real of artifacts of the model. The work in this thesis has been entirely restricted to zero temperature, and it would be interesting to establish how thermodynamics alters the ground state picture.

The models studied in this thesis can be viewed from many different perspectives, and there are a vast number of possible extensions. The general picture of the 2D Hubbard model phase diagram from a genuine many-body theory is a useful resource, providing guidance for what more sophisticated DMFT representations (for example) should look for.[1] It is an achievement to see so many phenomena emerge from just one relatively simple model; its features that have been studied in the past have all been

---

[1]And indeed, other researchers have already used my work in this way.

investigated within different, specialized models.

I have demonstrated that two-site cluster DMFT is an interesting technique that should provide an effective "impurity solver" for many more complex problems, such as looking for Fermi surface features and antiferromagnetism in multiple-orbital models of real materials. Larger clusters and extended Hubbard models could be investigated, and more detailed physical properties of phases extracted, such as conductivity and the effects of a magnetic field; the possibility of superconductivity could be included through the appropriate anomalous Green's functions. Finally, I would promote two-site DMFT as a sophisticated boundary condition for any cluster approach to interacting electron systems: as a vastly superior alternative to periodic boundary question, single sites are just added to the edge of the cluster and constrained self-consistently, and many-body effects will be included reliably.

Appendix A

BOLTZMANN TRANSPORT FORMULATION

> God keep me from ever completing anything.
> This whole book is but a draught — nay, but
> the draught of a draught. Oh, Time, Strength,
> Cash, and Patience!
>
> _____
> HERMAN MELVILLE
> *Moby Dick* [144]

The basis of our calculations in Chapter 2 is classical Boltzmann transport theory [24, 29]. Here I reproduce the derivation of the linearized Boltzmann equation. We consider the steady state equation for the distribution function $f_\mathbf{k}$. We have no diffusion (spatial homogeneity is assumed) and therefore the only processes altering the distribution in $\mathbf{k}$-space are those due to applied electric and magnetic fields, and a generalized scattering. The $\mathbf{k}$-vector of each carrier is changed according to

$$\hbar\dot{\mathbf{k}} = e(\mathbf{E} + \mathbf{v_k} \times \mathbf{B})$$

(where e is negative for an electron) and the first order contribution to the distribution is

$$\frac{\partial f_\mathbf{k}}{\partial t}\bigg|_{\text{fields}} = -\frac{d\mathbf{k}}{dt} \cdot \frac{\partial f_\mathbf{k}}{\partial \mathbf{k}} = -\frac{e}{\hbar}(\mathbf{E} + \mathbf{v_k} \times \mathbf{B}) \cdot \frac{\partial f_\mathbf{k}}{\partial \mathbf{k}} .$$

For a steady state we require that the combined change in $f_\mathbf{k}$ due to contributions from the fields and scattering is zero; hence

$$-\frac{e}{\hbar}(\mathbf{E} + \mathbf{v_k} \times \mathbf{B}) \cdot \frac{\partial f_\mathbf{k}}{\partial \mathbf{k}} + C_\mathbf{k} = 0 ,$$

where $C_\mathbf{k}$ is the rate of change of the state $\mathbf{k}$ due to scattering.

We would like to look at the departure from equilibrium so we write $f_\mathbf{k} = f_\mathbf{k}^0 + g_\mathbf{k}$, where $f_\mathbf{k}^0 = (\exp\{\beta(\epsilon_\mathbf{k} - \mu)\} + 1)^{-1}$, the plain Fermi distribution. We note that

$$\frac{\partial f_\mathbf{k}^0}{\partial \mathbf{k}} = \frac{\partial \epsilon_\mathbf{k}}{\partial \mathbf{k}} \frac{\partial f_\mathbf{k}^0}{\partial \epsilon_\mathbf{k}} = \hbar \mathbf{v_k} \frac{\partial f_\mathbf{k}^0}{\partial \epsilon_\mathbf{k}} ,$$

and so the cross-product causes the term with $\mathbf{B}$ and $f_\mathbf{k}^0$ to vanish. We also assume that non-linear E^2 contributions are small and neglect the term $\mathbf{E} \cdot \nabla_\mathbf{k} g_\mathbf{k}$, giving the linearized Boltzmann equation

$$e\mathbf{E} \cdot \mathbf{v_k} \frac{\partial f_\mathbf{k}^0}{\partial \epsilon_\mathbf{k}} + \frac{e}{\hbar}\mathbf{v_k} \times \mathbf{B} \cdot \frac{\partial g_\mathbf{k}}{\partial \mathbf{k}} = C_\mathbf{k} . \tag{A.1}$$

In future calculations I shall choose units such that $e = 1$ and $\hbar = 1$.

Appendix B

BETHE LATTICE

Bring us in no egges,
      for ther are many schelles;
But bring us in good ale,
      and give us nothing elles;
And bring us in good ale.

ANONYMOUS [145]

The Bethe lattice, in which every lattice point is connected to a number z of others which do not themselves interconnect (see Fig. B.1), is often used as the underlying lattice for DMFT calculations since its self-consistency condition turns out to be simple.[1] Here I shall derive the Green's function and density of states for the Bethe lattice in infinite dimensions, including the case when there is broken bipartite symmetry; I show also how the Bethe lattice is useful for the dynamical mean-field theory (DMFT) self-consistency equations.
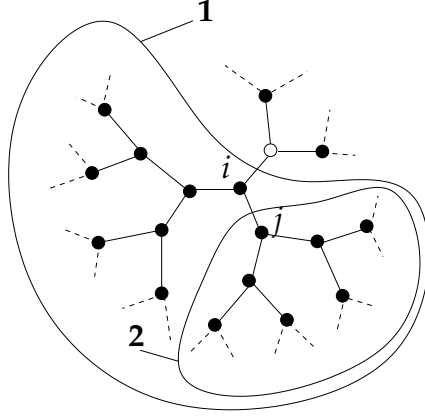

Figure B.1: A portion of a Bethe lattice with coordination number number $z = 3$. For an infinitely extended Bethe lattice, expunging site 0 leaves a lattice subset (**1**, connected to site i), that is identical to the subset (**2**, connected to site j) left when site i is additionally expunged. Hence the Green's functions $G_{ii}^{(0)} = G_{jj}^{(0,i)}$ are equivalent.

B.1 Green's function

First we derive the non-interacting Green's function and hence the density of states. Following Georges *et al.* [52] we take a "cavity" approach, as no simple Fourier transform is possible. The action is divided into several parts

$$S = \int_0^\beta d\tau \underbrace{\left[c_0^\dagger(\partial_\tau - \mu)c_0 \right.}_{S_0} - \underbrace{\left. \sum_i t_{i0}(c_i^\dagger c_0 + \text{h.c.}) \right]}_{\Delta S} + S^{(0)} , \tag{B.1}$$

where sites $\{i\}$ are the z neighbours of the cavity site 0, S_0 is the action of site 0, and $S^{(0)}$ is the action in the presence of the cavity (*i.e.* when site 0 has been removed). Suppose we integrate out all sites except site 0 and those connected to it; sites not connected to any of $\{0, i\}$ will disappear into the determinant and cancel out, and the action is left

---

[1]A Lorentzian density of states yields a simpler condition — but one in which the Green's functions $\mathscr{G}_0$ and G_{local} are no longer connected, which is not terribly useful.

in the form

$$S = S_0 + \Delta S - \sum_i \int_0^\beta d\tau \int_0^\beta d\tau' c_i^\dagger(\tau') G_{ii}^{(0)}{}^{-1}(\tau' - \tau) c_i(\tau) , \tag{B.2}$$

where we have introduced the Green's function $G^{(0)}$ in the presence of the cavity, when $S = S^{(0)}$. Let us now integrate out the sites $\{i\}$ by a completing-the-square identity

$$S = \int_0^\beta d\tau \left[c_0^\dagger(\partial_\tau - \mu) c_0 - \sum_i t_{i0}^2 \int_0^\beta d\tau' c_0^\dagger(\tau') G_{ii}^{(0)}(\tau' - \tau) c_0(\tau) \right] ; \tag{B.3}$$

we have used here the Bethe lattice property that none of the i are connected to each other. Hence we can relate the on-site Green's function to the Green's functions in the presence of the cavity: $G_{00}{}^{-1}(i\omega_n) = i\omega_n + \mu - \sum_i t_{i0}^2 G_{ii}^{(0)}(i\omega_n)$. If we are comparing lattices with different coordination numbers z, we must scale the hopping such that the electrons' kinetic and potential energies are in proportion; hence we choose $t_{ij} = t/\sqrt{z}$, and noting that all sites i are identical

$$G_{00}{}^{-1} = \zeta - t^2/z \sum_i G_{ii}^{(0)} = \zeta - t^2 G_{ii}^{(0)} , \tag{B.4}$$

where $\zeta = i\omega_n + \mu$. We can now further remove a site i, and exactly the same equation will result for nearest neighbours j of i, except there are only $z - 1$ of them since site 0 was already removed; hence

$$G_{ii}^{(0)}{}^{-1} = \zeta - \frac{z-1}{z} t^2 G_{jj}^{(0,i)} . \tag{B.5}$$

In the limit of an infinitely extended Bethe lattice, we can argue that these two Green's functions are identical, as illustrated in Fig. B.1. So, taking the limit of infinite dimensions $z \to \infty$, gives the on-site Green's function:

$$\zeta = t^2 G_{\text{Bethe}} + G_{\text{Bethe}}^{-1} \tag{B.6}$$

$$G_{\text{Bethe}} = \frac{\zeta - \sqrt{\zeta^2 - 4t^2}}{2t^2} . \tag{B.7}$$

Taking care with the analytic structure of this function (there is a branch cut from $\zeta = -2t$ to $\zeta = 2t$), its imaginary part yields a *semi-circular* density of states:

$$D(\epsilon) = \frac{\sqrt{4t^2 - \epsilon^2}}{2\pi t^2} \quad (|\epsilon| < 2t) , \qquad D(\epsilon) = 0 \quad (|\epsilon| > 2t) . \tag{B.8}$$

For two-site DMFT, we require the second moment of this density of states

$$\sum_{\mathbf{k}} \epsilon_{\mathbf{k}}^2 = \int d\epsilon \, \epsilon^2 D(\epsilon) = t^2 . \tag{B.9}$$

B.2   DMFT self-consistency

The local non-interacting Green's function is defined to be $G_{0,\text{local}}(\omega + \mu) = \sum_{\mathbf{k}} \frac{1}{\omega + \mu - \epsilon_{\mathbf{k}}}$, and so Eqn 3.7 can be written

$$G_{\text{local}}(i\omega_n) = G_{0,\text{local}}(i\omega_n + \mu - (\mathscr{G}^{-1}(i\omega_n) - G_{\text{local}}^{-1}(i\omega_n))) . \tag{B.10}$$

This form is only useful if we know the local Green's function explicitly; for most lattices, we cannot carry out the **k**-sum analytically. But for the Bethe lattice, we can write (using Eqn B.6)

$$\mathscr{G}^{-1}(i\omega_n) = i\omega_n + \mu - t^2 G_{\text{local}}(i\omega_n) . \tag{B.11}$$

This gives an explicit prescription for reconstructing a new function $\mathscr{G}$ from the interacting Green's function G_{local} such that they are self-consistent on a Bethe lattice; this is equivalent to matching on-site and lattice Green's functions.

B.3   Two-sublattice symmetry breaking

We can derive directly the Green's function for a Bethe lattice where alternate sites are different — this is relevant for the study of antiferromagnetism, and provides a double check on the equations produced for antiferromagnetic DMFT self-consistency (*c.f.* §4.4.1). In infinite dimensions, Eqn B.5 above becomes

$$G_{ii}^{(0)}{}^{-1} = \zeta - t^2 G_{jj}^{(0,i)} . \tag{B.12}$$

If symmetry is broken an A-type Green's function must be related to a B-type Green's function by this relation, and vice versa. Also, some intrinsic property of the A-site must be different from that on the B site, so there are now two different ζ_A, ζ_B. So we have

$$G_{A,ii}^{(0)}{}^{-1} = \zeta_A - t^2 G_{B,jj}^{(0,i)}; \qquad G_{B,jj}^{(0,i)}{}^{-1} = \zeta_B - t^2 G_{A,kk}^{(0,i,j)} ; \tag{B.13}$$

combining these to eliminate G_B gives

$$t^2 \zeta_A G_A^2 - \zeta_A \zeta_B G_A + \zeta_B = 0 \qquad \Rightarrow \qquad G_A = \frac{1}{2t^2} \sqrt{\frac{\zeta_B}{\zeta_A}} \left(\zeta_A \zeta_B \pm \sqrt{\zeta_A \zeta_B - 4t^2} \right) . \quad \text{(B.14)}$$

In DMFT, the difference between A and B is given by the self-energy, and we have $\zeta_{A,\sigma} = \omega + \mu - \Sigma_\sigma$, $\zeta_{B,\sigma} = \omega + \mu - \Sigma_{\bar{\sigma}}$; Eqn 4.26 can be reproduced using Eqn B.14.

Appendix C

COMPUTATIONAL TECHNIQUES

Life is easy to chronicle, but bewildering to practise...

E. M. FORSTER
A Room with a View [146]

In this Appendix the computational and numerical techniques utilized in each part of this thesis are outlined, and the root-finding procedure used to solve the two-site DMFT self-consistency equations is discussed in detail in §C.1. Mathematica was used for many of the calculations for Chapter 2; its `LinearSolve` routine generally dealt well with the badly-conditioned scattering matrix (despite complaining). The core of two-site dynamical mean-field theory (DMFT) parts was done using programs written in C. In addition, Perl was used to manage exploration of the (U, n) phase diagram (interfaced to C using SWIG [147]) and for data collection, and Mathematica for some algebra and the presentation of data (phase diagrams and other graphs).

Diagonalizing the DMFT impurity model was done directly with routines from LA-PACK [148] (*e.g.* `dsyev`) for plain two-site DMFT and for the 2×1 cluster. For the 2×2 cluster a Lanczos approach is necessary, and to calculate the ground state I used the `dnlaso` routine from LASO [149]. Lanczos is used to calculate the zero temperature Green's function [150]. Identifying convergence of the Green's function is tricky, and I probed it near the ground state eigenvalue and at nearby poles (identified using the LAPACK routine `dstevx` to find eigenvalues of a tridiagonal matrix).

Numerical integration of the density of states is required to evaluate the lattice filling (and also the energy and $n_{\mathbf{k}}$), and for this I used routines from QUADPACK [151] within the GNU Scientific Library (GSL) [152]. For earlier calculations, on the Bethe lattice, it is necessary to identify the singularities on the edges of the square root (*e.g.* where $\omega + \mu - \Sigma_\sigma(\omega) = 2t$ for Eqn 4.18); these can be calculated by finding the roots of polynomials, when $\Sigma_\sigma(\omega)$ is expressed as Eqn 4.14, using the GSL routine `gsl_poly_complex_solve`.

When $\mathbf{k}$-dependence is included explicitly, the $\mathbf{k}$-sum was done as a simple sum (with look-up tables for all possible quantities), and prior to the numerical integration (*i.e.* for each ω point). Densities of states were calculated from the imaginary parts of a Green's function, with an analytic continuation $\omega \to \omega + i\delta$ to broaden the delta functions. All poles lie on the real axis, and so we can choose any contour which encloses the lower half of the real axis and goes through zero, begin careful of preserving the measure of distance along the contour. The contour is chosen to be a considerable distance away from the real axis to make the function smooth and easily integrated numerically; for this I used infinite range functions such as `gsl_integration_qagil`.

In later stages, numerical differentiation is required to calculate Z, and I used the `gsl_diff_central` routine. For the 2×2 clusters, it is necessary to carry out operations (such as inversion) on a 4×4 matrix, for which I code the algebra directly.

C.1   Multidimensional root-finding

At the core of two-site DMFT is a set of self-consistent equations that I solve by means of multi-dimensional root-finding, to find the parameters of the dynamical field that cause the self-consistent equations to be satisfied. The alternative (often used for conventional DMFT) is to obtain explicit analytical expressions for these parameters from the self-consistency equations, and iterate; but in general, this is not possible, and iteration is less reliable than root-finding.

Matching Green's functions (*e.g.* Eqn 4.4) gives a number of self-consistency constraints, which must be equal to the number of impurity model parameters, and the problem can be rewritten in the form $\mathbf{F}(\mathbf{x}) = \mathbf{0}$ (*c.f.* §4.3.2). $\mathbf{x}$ is the vector of input parameters (characterizing the dynamical field), from which we can calculate the vector function $\mathbf{F}$ that gives the distance from self-consistency for each of the equations.

We wish to find the best way to treat this problem computationally, regarding the function $\mathbf{F}$ as a black box. Calculating $\mathbf{F}$ is computationally expensive (for two-site DMFT it will involve large matrix diagonalization and numerical integration); and we certainly do not know its gradients analytically. This means that the best approach is the *Broyden method* [153], which is based upon Newton's method for the calculation of the optimal step $\delta\mathbf{x}$:

$$\mathbf{F}(\mathbf{x} + \delta\mathbf{x}) \simeq \mathbf{F}(\mathbf{x}) + \nabla\mathbf{F}(\mathbf{x}) \cdot \delta\mathbf{x} \quad \Rightarrow \quad \delta\mathbf{x} = -(\nabla\mathbf{F})^{-1} \cdot \mathbf{F}(\mathbf{x}) \quad \text{for} \quad \mathbf{F}(\mathbf{x} + \delta\mathbf{x}) = \mathbf{0} \quad \text{(C.1)}$$

where $\nabla\mathbf{F}$ is the Jacobian matrix. Although the *direction* given by this $\delta\mathbf{x}$ is guaranteed to decrease $|\mathbf{F}|^2$, it may have too large a magnitude and extend beyond the region where the approximation is valid; hence we may need to backtrack, and a line search should be used to find the optimal step size quickly [153].

Evaluation of the Jacobian matrix $\nabla\mathbf{F}$ is not possible analytically for DMFT, and in larger dimensions, evaluation by finite differences is costly. Broyden [154] derived the optimal way of *updating* the Jacobian, from how the function $\mathbf{F}$ has changed in the previous Newton step:

$$\mathbf{J}_{i+1} = \mathbf{J}_i + \frac{(\delta\mathbf{F}_i - \mathbf{J}_i \cdot \delta\mathbf{x}_i) \otimes \delta\mathbf{x}_i}{\delta\mathbf{x}_i \cdot \delta\mathbf{x}_i} \, , \tag{C.2}$$

where $\mathbf{J}$ is the *approximate* Jacobian. The initial Jacobian has to be calculated by finite differences; and the approximate Jacobian gradually deteriorates, so occasionally (when the line search fails to provide a suitably good step) it needs to be reinitialized by finite differences. In practice, the algorithm has proved very reliable, and convergence is rapid once the minimum is reasonably proximate (even in nine dimensions).

List of references

[1] G. Eliot. *Middlemarch* (1873). Epigraph to Chapter 51.

[2] D. Pines and P. Noziéres. *The Theory of Quantum Liquids*. Addison Wesley Advanced Book Classics 1989 (1966).

[3] R. B. Laughlin and D. Pines. Proc. Natl Acad. Sci. U.S.A. **97**, 28 (2000).

[4] A. J. Schofield. Contemporary Physics **40**, 95 (1999).

[5] F. D. M. Haldane. J. Phys. C: Solid State Phys. **14**, 2585 (1989).

[6] P. Coleman, C. Pepin *et al.* J. Phys.: Condens. Matter **13**, 723 (2001).

[7] P. W. Anderson. Phys. Rev. Lett. **67**, 2092 (1991).

[8] T. R. Chien, Z. Z. Wang *et al.* Phys. Rev. Lett. **67**, 2088 (1991).

[9] R. W. Hill, C. Proust *et al.* Nature **414**, 711 (2001).

[10] C. Pfleiderer, S. R. Julian *et al.* Nature **414**, 427 (2001).

[11] S. A. Grigera, R. S. Perry *et al.* Science **294**, 329 (2001).

[12] M. Vojta. Rep. Prog. Phys. **66**, 2069 (2003).

[13] F. C. Zhang and T. M. Rice. Phys. Rev. B **37**, 3759 (1988).

[14] C. M. Varma and E. Abrahams. Phys. Rev. Lett. **86**, 4652 (2001).

[15] E. C. Carter and A. J. Schofield. Phys. Rev. B **66**, 241102 (2002).

[16] E. C. Carter and A. J. Schofield. Phys. Rev. B **70**, 045107 (2004).

[17] W. S. Gilbert. *The Mikado, or The Town Of Titipu* (1885). From the song "A more humane Mikado never, did in Japan exist".

[18] C. M. Varma and E. Abrahams. Phys. Rev. Lett. **88**, 139903(E) (2001).

[19] V. M. Yakovenko (August 2002). Private communication.

[20] R. Hlubina. Phys. Rev. B **64**, 132508 (2001).

[21] E. Abrahams and C. M. Varma. Phys. Rev. B **68**, 094502 (2003).

[22] K. G. Sandeman and A. J. Schofield. Phys. Rev. B **63**, 094510 (2001).

[23] Y.Nakajima, K.Izawa *et al.* J. Phys. Soc. Jpn **73**, 5 (2003).

[24] J. M. Ziman. *Theory of Solids*. Cambridge University Press.

[25] M. Gurvitch and A. T. Fiory. Phys. Rev. Lett. **59**, 1337 (1987).

[26] T. Valla, A. V. Fedorov *et al.* Science **285**, 2110 (1999).

[27] C. M. Varma, P. B. Littlewood *et al.* Phys. Rev. Lett. **63**, 1996 (1989).

[28] A. Carrington, A. P. Mackenzie *et al.* Phys. Rev. Lett. **69**, 2855 (1992).

[29] J. M. Ziman. *Electrons and Phonons*. Oxford University Press. (Oxford Classics Series 2001).

[30] J. M. Harris, Y. F. Yan *et al.* Phys. Rev. Lett. **75**, 1391 (1995).

[31] A. Malinowski, M. Z. Cieplak *et al.* Phys. Rev. B **66**, 104512 (2002).

[32] T. Valla, A. V. Federov *et al.* Phys. Rev. Lett. **85**, 828 (2000).

[33] E. Abrahams and C. M. Varma. Proc. Natl. Acad. Sci. **97**, 5714 (2000).

[34] P. Monthoux and D. Pines. Phys. Rev. B **49**, 4261 (1994).

[35] R. Hlubina and T. M. Rice. Phys. Rev. B **51**, 9253 (1995).

[36] B. P. Stojkovic and D. Pines. Phys. Rev. Lett. **76**, 811 (1996).

[37] A. Perali, M. Sindel *et al.* Eur. Phys. J. B (2001).

[38] L. B. Ioffe and A. J. Millis. Phys. Rev. B **58**, 11631 (1998).

[39] N. Hussey. Eur. Phys. J. B (2003).

[40] H. Kontani. J. Phys. Soc. Japan **70**, 1873 (2001).

[41] P. Coleman, A. J. Schofield *et al.* Phys. Rev. Lett. **76**, 1324 (1996).

[42] D. K. K. Lee and P. A. Lee. J. Phys. Cond. Mat. **9**, 10421 (1997).

[43] G. Kotliar, A. Sengupta *et al.* Phys. Rev. B **53**, 3573 (1996).

[44] M. R. Norman, M. Randeria *et al.* Phys. Rev. B **52**, 615 (1995).

[45] Y. Ando and T. Murayama. Phys. Rev. B **60**, R6991 (1999).

[46] Y. Wang and N. P. Ong. Proc. Natl Acad. Sci. USA **98**, 11091 (2001).

[47] N. P. Ong. Phys. Rev. B **43**, 193 (1991).

[48] S. I. Woods, A. S. Katz *et al.* Phys. Rev. B **66**, 014538 (2002).

[49] M. Grayson, L. B. Rigal *et al.* Phys. Rev. Lett. **89**, 037003 (2002).

[50] D. Schmadel, J. Tu *et al.* `cond-mat/0210304`.

[51] J. Joyce. *A Portrait of the Artist as a Young Man* (1916). Chapter 5.

[52] A. Georges, G. Kotliar *et al.* Rev. Mod. Phys. **68**, 13 (1996).

[53] W. Metzner and D. Vollhardt. Phys. Rev. Lett. **62**, 324 (1989).

[54] A. C. Hewson. *The Kondo Problem to Heavy Fermions*. Cambridge University Press (1993).

[55] J. W. Negele and H. Orland. *Quantum Many-Particle Systems*. Perseus Books (1998).

[56] G. D. Mahan. *Many Particle Physics*. Kluwer Academic/Plenum, third edition (2000).

[57] G. Santoro, M. Airoldi *et al.* Phys. Rev. B **47**, 16216 (1993).

[58] A. Schiller and K. Ingersent. Phys. Rev. Lett. **75**, 113 (1995).

[59] X. Y. Zhang, M. J. Rozenberg *et al.* Phys. Rev. Lett. **70**, 1666 (1993).

[60] M. Jarrell. Phys. Rev. Lett. **69**, 168 (1992).

[61] M. J. Rozenberg, X. Y. Zhang *et al.* Phys. Rev. Lett. **69**, 1236 (1992).

[62] A. Georges and W. Krauth. Phys. Rev. Lett. **69**, 1240 (1992).

[63] J. E. Hirsch and R. M. Fye. Phys. Rev. Lett. **56**, 2521 (1986).

[64] O. Parcollet, G. Biroli *et al.* `cond-mat/0308577`.

[65] M. Caffarel and W. Krauth. Phys. Rev. Lett. **72**, 1545 (1994).

[66] Q. Si, M. J. Rozenberg *et al.* Phys. Rev. Lett. **72**, 2761 (1994).

[67] R. Bulla, A. C. Hewson *et al.* J. Phys. Cond. Mat. **10**, 8365 (1998).

[68] R. Bulla. Phys. Rev. Lett. **83**, 136 (1999).

[69] M. Potthoff. Phys. Rev. B **64**, 165114 (2001).

[70] J. K. Freericks and M. Jarrell. Phys. Rev. Lett. **74**, 186 (1995).

[71] J. Wahle, N. Blümer *et al.* Phys. Rev. B **58**, 12749 (1998).

[72] K. Byczuk and D. Vollhardt. Phys. Rev. B **65**, 134433 (2002).

[73] M. Fleck, A. I. Liechtenstein *et al.* Phys. Rev. Lett. **80**, 2393 (1998).

[74] R. Chitra and G. Kotliar. Phys. Rev. Lett. **83**, 2386 (1999).

[75] R. Zitzler, T. Pruschke *et al.* Eur. Phys. J. B **27**, 473 (2002).

[76] V. I. Anisimov, A. I. Poteryaev *et al.* J. Phys. Cond. Mat. **9**, 7359 (1997).

[77] A. I. Lichtenstein and M. I. Katsnelson. Phys. Rev. B **57**, 6884 (1998).

[78] S. Y. Savrasov, G. Kotliar *et al.* Nature **410**, 793 (2001).

[79] A. I. Lichtenstein, M. I. Katsnelson *et al.* Phys. Rev. Lett. **87**, 067205 (2001).

[80] N. F. Mott. *Metal–insulator transitions*. Taylor & Francis, second edition (1990).

[81] P. Limelette, A. Georges *et al.* Science **302**, 89 (2003).

[82] J. Hubbard. Proc. R. Soc. Lond. A **281**, 401 (1964).

[83] A. Fujimori, I. Hase *et al.* Phys. Rev. Lett. **69**, 1796 (1992).

[84] W. F. Brinkman and T. M. Rice. Phys. Rev. B **2**, 4302 (1970).

[85] A. Georges and G. Kotliar. Phys. Rev. B **45**, 6479 (1992).

[86] S.-K. Mo, J. D. Denlinger *et al.* Phys. Rev. Lett. **90**, 186403 (2003).

[87] A. Y. Matsuura, H. Watanabe *et al.* Phys. Rev. B **58**, 3690 (1998).

[88] G. Kotliar. Science **302**, 67 (2003).

[89] J. Schlipf, M. Jarrell *et al.* Phys. Rev. Lett. **82**, 4890 (1999).

[90] M. J. Rozenberg, R. Chitra *et al.* Phys. Rev. Lett. **83**, 3498 (1999).

[91] W. Krauth. Phys. Rev. B **62**, 6860 (2000).

[92] J. C. Slater. Phys. Rev. **82**, 538 (1951).

[93] U. Brandt and C. Mielsch. Z. Phys. B **79**, 295 (1990).

[94] B. Bairnsfather. *Fragments from France*. Cartoon caption (1915).

[95] E. Lange. Mod. Phys. Lett. B **12**, 915 (1998).

[96] Q. Si and G. Kotliar. (private communication).

[97] M. Potthoff, T. Herrmann *et al.* Phys. Status Solidi B **210**, 199 (1998).

[98] V. M. Galitskii and A. B. Migdal. Sov. Phys.-JETP **7**, 96 (1958).

[99] A. L. Fetter and J. D. Walecka. *Quantum Theory of Many-Particle Systems*. McGraw-Hill (1971). Eqn (9.36).

[100] W. von der Linden and D. M. Edwards. J. Phys.: Condens. Matter **3**, 4917 (1991).

[101] M. Potthoff. Eur. Phys. J. B **32**, 429 (2003).

[102] A. P. Mackenzie, Y. Maeno *et al.* Rev. Mod. Phys. **75**, 657 (2003).

[103] A. Koga, N. Kawakami *et al.* Phys. Rev. Lett. **92**, 216402 (2004).

[104] W. Shakespeare. *The Tragedy of Hamlet, Prince of Denmark* (1603).

[105] G. Biroli, O. Parcollet *et al.* `cond-mat/0307587`.

[106] M. H. Hettler, A. N. Tahvildar-Zadeh *et al.* Phys. Rev. B **58**, R7475 (1998).

[107] M. H. Hettler, M. Mukherjee *et al.* Phys. Rev. B **61**, 12739 (2000).

[108] G. Kotliar, S. Y. Savrasov *et al.* Phys. Rev. Lett. **87**, 186401 (2001).

[109] G. Biroli and G. Kotliar. Phys. Rev. B **65**, 155112 (2002).

[110] C. J. Bolech, S. S. Kancharla *et al.* Phys. Rev. B **67**, 075110 (2003).

[111] anon. *The Story of Burnt Njal (Njal's Saga)*. Icelandic (13th century). Translated by M. Magnusson and H. Pálsson, Penguin (1960). §103.

[112] W. Metzner, D. Rohe *et al.* Phys. Rev. Lett. **91**, 066402 (2003).

[113] D. R. Penn. Phys. Rev. **142**, 350 (1966).

[114] Y. Kakehashi and J. H. Samson. Phys. Rev. B **33**, 298 (1986).

[115] C. Dahnken, M. Aichhorn *et al.* `cond-mat/0309407`.

[116] J. R. Schrieffer, X. G. Wen *et al.* Phys. Rev. B **39**, 11663 (1989).

[117] T. D. Stanescu and P. Phillips. Phys. Rev. Lett. **91**, 017002 (2003).

[118] T. R. Kirkpatrick and D. Belitz. `cond-mat/0303151`.

[119] D. Pines. Z. Phys. B **103**, 129 (1997).

[120] D. Duffy and A. Moreo. Phys. Rev. B **55**, R676 (1997).

[121] R. Zitzler, N. Tong *et al.* `cond-mat/0308202`.

[122] S. Moukouri and M. Jarrell. Phys. Rev. Lett. **87**, 167010 (2001).

[123] J. M. Luttinger. Phys. Rev. **119**, 1153 (1960).

[124] Y. J. Uemura, G. M. Luke *et al.* Phys. Rev. Lett. **62**, 2317 (1989).

[125] A. V. Chubukov and D. K. Morr. Phys. Reports **288**, 355 (1997).

[126] A. Abanov, A. V. Chubukov *et al.* Advances in Physics **52**, 119 (2003).

[127] A. Damascelli, Z. Hussain *et al.* Rev. Mod. Phys. **75**, 473 (2003).

[128] T. Yoshida, X. J. Zhou *et al.* Phys. Rev. Lett. **91**, 027001 (2003).

[129] I. I. Pomeranchuk. J. Exptl. Theoret. Phys. (U.S.S.R.) **25**, 524 (1958).

[130] C. J. Halboth and W. Metzner. Phys. Rev. Lett. **85**, 5162 (2000).

[131] V. Hankevych, I. Grote *et al.* Phys. Rev. B **66**, 094516 (2002).

[132] R. A. Borzi, S. A. Grigera *et al.* `cond-mat/0403390`.

[133] H. J. Schulz. Phys. Rev. B **39**, 2940 (1989).

[134] A. Banner. *Ant and Bee go Shopping*. Kaye and Ward (1972).

[135] D. S. Marshall, D. S. Dessau *et al.* Phys. Rev. Lett. **76**, 4841 (1996).

[136] T. Timusk and B. Statt. Rep. Prog. Phys. **62**, 61 (1999).

[137] M. R. Norman, H. Ding *et al.* Nature **329**, 157 (1998).

[138] E. Altman and A. Auerbach. Phys. Rev. B **65**, 104508 (2002).

165

[139] N. Furukawa, T. M. Rice *et al.* Phys. Rev. Lett. **81**, 3195 (1998).

[140] A. A. Katanin and A. P. Kampf. `cond-mat/0310112`.

[141] D. Sénéchal and A.-M. S. Tremblay. Phys. Rev. Lett. **92**, 126401 (2004).

[142] T. A. Maier, T. Pruschke *et al.* Phys. Rev. B **66**, 075102 (2002).

[143] M. Peake. *Titus Groan* (1946). 'Near and Far'.

[144] H. Melville. *Moby Dick* (1851). Chapter 32.

[145] anon. *No. 159*. In M. S. Luria and R. L. Hoffman, editors, *Middle English Lyrics*, page 143. W W Norton & Company (1974).

[146] E. M. Forster. *A Room with a View* (1908). Chapter 14.

[147] *Simplified Wrapper and Interface Generator (SWIG)*. `http://www.swig.org/`.

[148] E. Anderson, Z. Bai *et al.* *LAPACK Users' Guide*. SIAM, third edition (1999). `http://www.netlib.org/lapack/`.

[149] D. S. Scott. *LASO*. `http://www.netlib.org/laso/`.

[150] R. Haydock, V. Heine *et al.* J. Phys. C: Solid State Phys. **8**, 2591 (1975).

[151] R. Piessens, E. de Doncker *et al.* *Quadpack*. `http://www.netlib.org/quadpack/`.

[152] M. Galassi, J. Davies *et al.* *GNU Scientific Library Reference Manual*. Network Theory Ltd., second edition (2003). `http://www.gnu.org/software/gsl/`.

[153] W. H. Press, S. A. Teukolsky *et al.* *Numerical Recipes in C*. Cambridge University Press (1992). § 9.7.

[154] C. G. Broyden. Mathematics of Computation **19**, 577 (1965).